

**Construction of binary protein
superlattices composed of inorganic
nanoparticles and fluorophores**

Dissertation

zur Erlangung der Würde des Doktors der Naturwissenschaften der
Fakultät für Mathematik, Informatik und Naturwissenschaften,
Fachbereich Chemie der Universität Hamburg

vorgelegt von

Michael Rütten

aus Viersen

Hamburg 2022

Gutachter der Dissertation Prof. Dr. Tobias Beck
Prof. Dr. Alf Mews

Gutachter der Disputation Prof. Dr. Tobias Beck
Prof. Dr. Arwen Pearson
Dr. Tobias Vossmeier

Tag der Disputation 17.02.2023

Datum der Druckfreigabe 02.03.2023

The work presented in this thesis was carried out at the Institute of Inorganic Chemistry of the RWTH Aachen University between October 2018 and December 2019 and at the Institute of Physical Chemistry of the University Hamburg January 2020 and December 2022.

Publications

Parts of this thesis are in the process of being published:

- I. Construction of Highly Ordered Fluorophore and Gold Nanoparticle Superlattices based on novel Hetero Binary Protein Assemblies, *in preparation*.
- II. Highly Ordered Protein Cage Assemblies Loaded with Plasmonic Gold Nanoparticles, *in preparation*.

The author has also contributed to the following related publications:

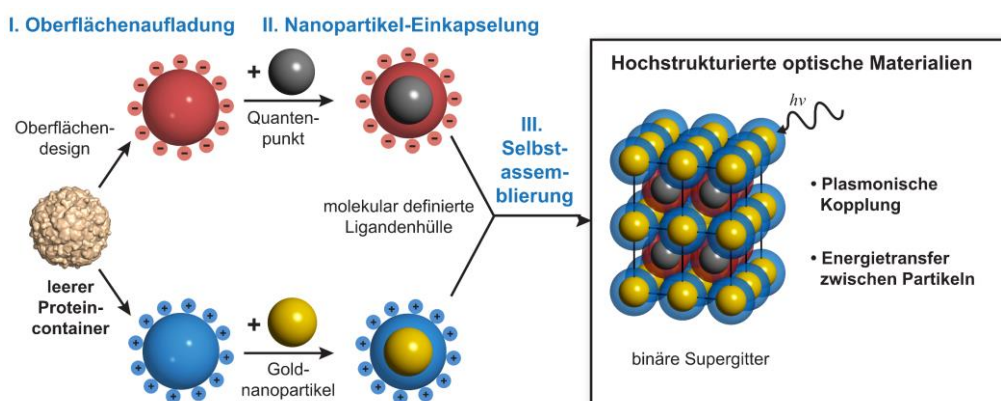
- III. Optical Properties of Proteincage-based Metacrystals, *in preparation*.
- IV. Surface Functionalization of Plasmonic Gold Nanoparticle-Loaded Protein Cages with Fluorescent Antennas, *in preparation*.
- V. Böhler, H.; Rütten, M.; Lang, L.; Beck, T., Crystalline Biohybrid Materials based on Protein Cages in *Methods in Molecular Biology*, Springer Nature, *in Press*.

Conference contributions:

- Talk: “Encapsulation of inorganic nanoparticles into surface charged protein containers.” *Nanotage*, Aachen, Germany **2019**.
- Poster: “Encapsulation of inorganic nanoparticles into protein containers towards highly ordered biohybrid materials.” *Joint Polish-German Crystallographic Meeting*, Wrocław, Poland **2020**.
- Talk and poster: “Encapsulation of inorganic nanoparticles into novel *T. maritima* encapsulin variants.” *29th Annual Meeting of the German Crystallographic Society*, virtual event **2021**. *Poster prize*.
- Poster: “Encapsulation of inorganic nanoparticles into novel *T. maritima* encapsulin variants.” *120th Bunsen-Tagung*, virtual event **2021**.
- Poster: “Crystalline materials based on *T. maritima* encapsulin variants.” *14th International Conference on Synchrotron Radiation Instrumentation*, virtual event **2021**.
- Poster: “Crystalline materials based on *T. maritima* encapsulin variants.” *GRC Bioinspired Materials*, Les Diablerets, Switzerland **2022**.
- Talk: “Construction of binary protein superlattices composed of inorganic nanoparticles and fluorophores” *NANOHYBRID - Hamburg Conference on Complex Nanostructures*, Hamburg, Germany **2022**.

Zusammenfassung

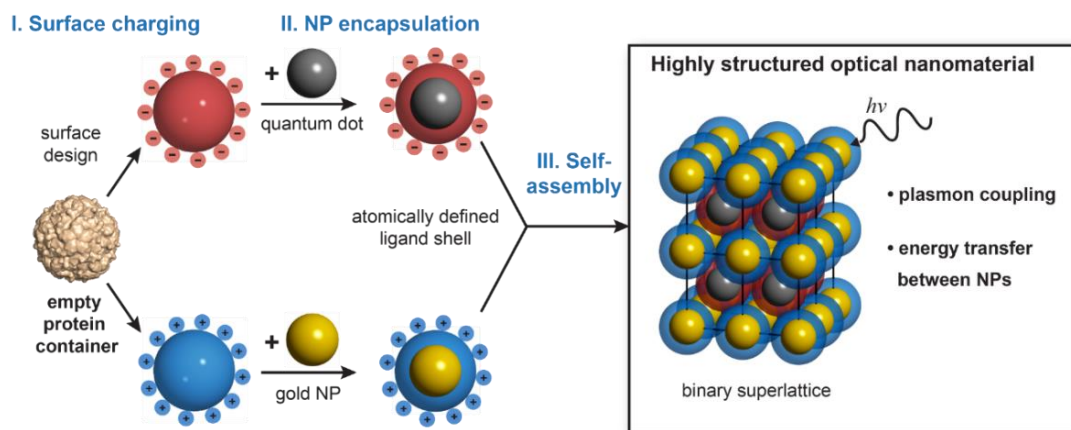
Proteincontainer haben als Bausteine für den Aufbau neuartiger biohybrider Materialien an Interesse gewonnen. Sowohl die Beladung als auch der Aufbau der Proteincontainer können verändert werden, wodurch verschiedene Materialien mit neuartigen Eigenschaften entstehen. Mit Proteincontainern lassen sich leicht hochgradig geordnete Assemblierungen erreichen, wodurch die größten Herausforderungen bei den Assemblierungen von Nanopartikeln überwunden werden. Nanoskalige biohybride Materialien, die auf mit Nanopartikeln beladenen Proteincontainern basieren, werden durch einen innovativen Designansatz mit entgegengesetzt geladenen Proteincontainern als Bausteine geschaffen.



In dieser Arbeit wurden die Kristallisationsbedingungen für neuartige geladene Proteincontainer untersucht und optimiert. Abhängig von der Proteinvariante und den Kristallisationsbedingungen, wurden unterschiedliche Zusammensetzungen gefunden und im Rahmen dieser Arbeit diskutiert. Außerdem wurde der Einfluss der Temperatur auf die Kristallisationsexperimente untersucht. Die Proteincontainer wurden mit Nanopartikeln über einen Dis- und Reassemblierungsansatz beladen. Mit Goldnanopartikeln beladene Proteine wurden zu biokompatiblen Substraten für künftige Anwendungen wie oberflächenverstärkte Raman-Streuung kristallisiert. Proteincontainer unterschiedlicher Größe wurden zu neuartigen heterobinären Strukturen zusammengesetzt. Beide Container wurden mit Nanopartikeln beladen, was zu dicht gepackten Nanopartikel-Übergittern führte. Die Nanopartikel-Übergitter könnten zukünftig Anwendung in der verfolgbaren Katalyse oder der Magneto-Plasmonik finden. Darüber hinaus wurden neue Ansätze zur Strukturbestimmung auf der Grundlage von Nanopartikel-Supergittern auf proteinbasierte Assemblierungen angewandt. In Fällen, in denen die Auflösung eines Proteinkristalls aus Röntgenbeugungsexperimenten nicht ausreichte, konnte die Beugung an den Nanopartikelübergittern untersucht werden. Darüber hinaus wurde eine hocheffiziente Fluorophor-Markierung von Proteincontainer erreicht. Fluoreszierende Proteincontainer wurden als neuartiger Baustein für den Aufbau von fluoreszierenden Proteinkristallen verwendet. Schließlich wurden die Wechselwirkungen zwischen Goldnanopartikeln und Fluorophoren mittels Konfokalmikroskopie untersucht.

Abstract

Protein containers have gained interest as building blocks for the assembly of novel biohybrid materials. The cargo loading as well as the assembly of the protein containers can be altered, resulting in various materials with novel emerging properties. Highly ordered assemblies can easily be achieved with protein containers, overcoming major challenges in nanoparticle assemblies. Nanoscale biohybrid materials based on nanoparticle loaded protein containers are created by an innovative design approach with oppositely charged protein containers as building blocks.



In this work, crystallization conditions for novel supercharged protein containers were screened and optimized. Depending on the protein variant and crystallization condition, different assemblies were found and discussed within this work. Moreover, the influence of temperature on the crystallization was observed. Protein containers were loaded with nanoparticles via dis- and reassembly approach. Gold nanoparticle loaded proteins were crystallized towards biocompatible substrates for future applications such as surface enhanced Raman scattering. Protein containers of different sizes were assembled into novel hetero binary structures. Both containers were loaded with nanoparticles, resulting in densely packed nanoparticle superlattices. The nanoparticle superlattices might give access to future applications in traceable catalysis or magneto-plasmonics. Moreover, new approaches for structure determination based on nanoparticle superlattices were applied on protein-based assemblies. In cases, where the resolution of a protein crystal from X-ray diffraction experiments was not sufficient, diffraction of the nanoparticle superlattices could be investigated. In addition, highly efficient fluorophore labeling of protein containers was achieved. Fluorescent protein containers were used as a novel building block for the assembly of fluorescent protein crystals. In the end, interactions between gold nanoparticles and fluorophores were investigated in confocal microscopy.

Table of contents

1 Introduction	1
2 Theoretical background	2
2.1 Plasmonic nanoparticles.....	2
2.1.1 Synthesis and functionalization	2
2.1.1.1 Gold nanoparticles	4
2.1.2 Optical properties of plasmonic nanoparticles	5
2.1.3 Applications based on plasmonic nanoparticles	6
2.2 Fluorescence	7
2.2.1 Fluorophores	8
2.2.1.1 Protein labeling with fluorophores	9
2.3 Quantum dots	10
2.4 Protein containers.....	13
2.4.1 Encapsulins	14
2.4.1.1 <i>T. maritima</i> encapsulin	16
2.5 Assembly of nanoscale building blocks	18
2.5.1 Plasmonic nanoparticle superlattices	18
2.5.2 Superfluorescent nanocrystal superlattices	20
2.5.3 Protein container assemblies	22
3 Basis of the present work	28
3.1 Supercharging of the protein container encapsulin	28
3.2 Nanoparticle synthesis and encapsulation	29
3.3 Positively charged ferritin variant.....	30

4 Concept and aim of this thesis	32
5 Results	34
5.1 Generation of novel protein building blocks	34
5.1.1 Supercharging of <i>T. maritima</i> encapsulin	34
5.1.2 Site-directed mutagenesis of the protein container encapsulin	36
5.1.2.1 Mutagenesis to supercharge encapsulin	36
5.1.2.2 Elimination of flavin binding-site	36
5.1.3 Production and purification of encapsulin variants	37
5.1.3.1 Production and purification of negatively charged encapsulin variants ..	37
5.1.3.2 Production and purification of positively charged encapsulin variants....	40
5.1.3.3 Flavin-free encapsulin variants.....	44
5.1.4 Positively charged ferritin with additional cysteine.....	49
5.2 Encapsulation of cargo into protein containers.....	51
5.2.1 Encapsulin dis- and reassembly.....	51
5.2.2 Gold nanoparticle encapsulation	53
5.2.2.1 AuNP synthesis.....	53
5.2.2.2 Functionalization and characterization of AuNPs	55
5.2.2.3 Scale-up of AuNP encapsulation.....	59
5.2.2.4 Encapsulation of small AuNPs	61
5.2.2.5 Purification of AuNP-loaded Encapsulin.....	63
5.2.3 Quantum dot encapsulation.....	66
5.2.3.1 Encapsulation of gQDs functionalized with small organic ligands	67
5.2.3.2 Encapsulation of gQDs functionalized with PEG ligands	74
5.2.4 Protein functionalization	80
5.2.4.1 Integration of fluorophores into positively charged ferritin	80

5.2.4.2 Purification of fluorophore-loaded positively charged ferritin.....	81
5.2.4.3 Determination of degree of fluorophore labeling	83
5.3 Protein crystallization towards binary superlattices	86
5.3.1 Crystallization of negatively charged encapsulin	87
5.3.1.1 AuNP-loaded Enc ^(neg) crystals.....	93
5.3.2 Crystallization of positively charged encapsulin	95
5.3.3 Crystallization of negatively and positively charged encapsulin variants	98
5.3.4 Negatively charged encapsulin and positively charged ferritin	100
5.3.4.1 NP-loaded hetero binary crystals	100
5.3.4.2 AuNP and fluorophore-loaded hetero binary crystals.....	105
5.3.5 Protein cross-linkers and their influence on crystal properties.....	107
5.3.6 Optical properties of nanoparticle – fluorophore loaded protein crystals	109
6 Summary and perspective	116
7 Experimental part.....	119
7.1 General	119
7.2 <i>E. coli</i> strains	119
7.3 Chemicals	120
7.4 Analytical methods.....	120
7.4.1 Transmission electron microscopy	120
7.4.2 Scanning electron microscopy.....	120
7.4.3 Electrospray ionization mass spectrometry	120
7.4.4 Matrix-assisted laser desorption/ionization mass spectrometry.....	121
7.4.5 SDS-Page and native PAGE	121
7.4.6 UV-Vis spectroscopy	122
7.4.7 Dynamic light scattering	122

7.4.8 Zeta potential.....	123
7.4.9 Atomic absorption spectroscopy.....	123
7.4.10 Optical microscopy	123
7.4.11 Confocal imaging.....	123
7.5 Gold nanoparticle synthesis	124
7.5.1 Improved TURKEVICH synthesis	124
7.5.2 PENG synthesis.....	124
7.5.3 Calculation of gold nanoparticle concentration	124
7.6 Ligand exchange	125
7.6.1 Citrate stabilized AuNPs.....	125
7.6.2 Oleyl amine stabilized AuNPs	125
7.6.3 Giant core/shell QDs	126
7.7 Protein related protocols.....	126
7.7.1 QuikChange™ site-directed mutagenesis	126
7.7.2 Protein production and purification	128
7.7.2.1 Negatively charged Enc	128
7.7.2.2 Positively charged Enc.....	129
7.7.2.3 Positively charged Ftn with additional cysteine	129
7.7.3 Encapsulin dis- and reassembly.....	130
7.7.4 Nanoparticle encapsulation	130
7.7.5 Fluorophore functionalization	131
7.7.6 Determination of flavin content	131
7.8 Protein crystallography	131
7.8.1 Hanging drop vapor diffusion.....	131
7.8.2 Stabilization of protein crystals	131
7.8.2.1 Glutaraldehyde.....	131

7.8.2.2 Alternative cross-linkers	132
7.8.2.3 Structure determination and refinement	132
8 Appendix	133
9 Bibliography	159
10 Abbreviations	173
11 List of figures	177
12 List of tables.....	182
13 List of chemicals.....	184
Danksagung	188
Eidesstattliche Erklärung.....	190
Curriculum Vitae	191

1 Introduction

Over the last decades, nanoparticles have moved into the focus of research due to their physical and chemical properties. Depending on their size and surface area, different properties are reported.^[1,2] Precise nanoparticle arrangements into well-defined structures are desired to enable effects such as strong plasmon coupling between plasmonic particles. In general, nanoparticle superlattices are promised to feature e.g. magnetic or optical properties single particles do not. Moreover, superlattices composed of two different kinds of nanoparticles (binary superlattices) facilitate the possibility combining effects. The combination of for example plasmonic and magnetic nanoparticles may lead to the emerge of novel properties. Many possible applications such as catalysis,^[3] imaging,^[4] data storage,^[3] drug-delivery^[5] and optics^[6] are in application or discussion.

For the assembly of nanoparticles, many approaches focus on the assembly based on complex nanoparticle ligand shells. Very monodisperse nanoparticles are desired to assemble in materials with distinct properties. On the other hand, inhomogeneous particles lead to a decrease in high order. In conclusion, new approaches are mandatory. In nature, protein containers are used to encapsulate and protect proteins or enzymes.^[7,8] Protein containers can also be exploited to feature non-native cargo.^[9,10] In addition, biological structures can also be used as a template for bioconjugation to combine biocompatibility and physical properties that were not possible before.^[11,12]

Protein containers can act as a novel building block and can be assembled into three dimensional assemblies via protein crystallization. After finding suitable crystallization conditions, the protein assemblies must be characterized. With one protein container variant, a variety of crystal structures can be achieved. Some of them feature either a close packing or high porosity. It's not that easy to assemble nanoparticles to form a different structure. Various protein containers materials have been reported, that enable unusual properties for nanoscale assemblies.^[13,14] In general, protein container assemblies facilitate the control over the positioning and combination of nanoparticles or fluorophores in an highly ordered material.^[15]

In this work, an innovative strategy for the construction of biohybrid materials composed of nanoparticles and fluorophores based on supercharged protein containers is presented. Supercharged encapsulin and ferritin protein containers loaded with nanoparticles and fluorophores were chosen as building blocks for the assembly of novel hetero binary protein container assemblies. These novel binary assemblies loaded with gold nanoparticles and fluorophores were characterized via confocal imaging.

2 Theoretical background

In the following chapters the theoretical background for this work is presented. First, the focus is on the synthesis and optical properties of plasmonic gold nanoparticles. Afterwards, fluorophores and their application for protein labeling are explained and followed by semiconductor nanoparticles, in detail quantum dots. Protein containers in general but especially the *Thermotoga maritima* encapsulin are introduced. In the end, the assembly of previously shown nanoscale building blocks and their applications are discussed.

2.1 Plasmonic nanoparticles

Nanoparticles are a compound structure of atoms and defined as particles with characteristic dimensions from 1 nm to 100 nm.^[16-19] Therefore, nanoparticles are classified between atomic and bulk matter. The physical and chemical properties of nanoparticles are highly dependent on their size and shape and not shared with particles above the nanoscale.^[3,16,20] In comparison to bulk matter, single nanoparticles feature a higher surface to volume ratio. The higher ratio leads to an enhanced reactivity based on an increased number of reactive centers on the nanoparticle surface.^[21] Depending on the nanoparticle size, different properties are observed, for example change in redox states or adsorption capacity.^[22,23] Furthermore, the size-dependent electronic properties of nanoparticles result in quantum size effects.^[3] By increasing the size of nanoparticles, the position of the localized surface plasmon resonance (LSPR) (chapter 2.1.2) is shifted to a higher wavelength.^[24] Additionally, the ligand shell composition influences the position of the LSPR of nanoparticles of the same size.^[10,13,24] Noble metal atoms such as gold and silver are usually used for plasmonic nanoparticles. Novel materials based on plasmonic nanoparticles are of interest for applications such as sensing^[25-27], bio-imaging^[28-30] and energy transfer^[31-33].

2.1.1 Synthesis and functionalization

Nanoparticles can be synthesized in different sizes and with a large variation of ligands attached to the surface. Since the size influences the particle's properties, several requirements are needed for the synthesis to achieve monodisperse size distributions and the targeted size. In addition, the nanoparticle shape contributes to the particle's properties. A spherical gold nanoparticle is expected to feature different plasmonic properties than for example a star-shaped gold nanoparticle.^[34] Furthermore, a specific control over the nanoparticle surface functionality and uniformity should be given.

The synthesis of nanoparticles is based on 'bottom-up' or 'top-down' strategies.^[35] In the 'top-down' approach physical methods like laser or thermal ablation, sputtering or mechanical

milling are used.^[35] For example, through mechanical milling, bulk material is milled to smaller particles. As a drawback from of the mechanical process, erosion occurs and impurities form. One further disadvantage of this approach are broad size distributions. On the other hand, large scale production of nanoparticles can be achieved.^[36,37] The 'bottom-up' approach covers the chemical synthesis of nanoparticles. For this approach, nanoparticles are constructed from atoms or molecules in liquid phase through chemical reduction methods.^[38-40] The nanoparticle size and shape can be controlled very precisely.^[41,42]

The theory and mechanism of nanoparticle formation by liquid phase reduction was originally investigated by VICTOR K. LAMER.^[43] The model introduced by LAMER is most commonly used to describe nanoparticle growth.^[44-46] In detail, the LAMER model can be divided into three phases (Figure 2.1). First, a rapid increase in concentration of free monomer leads to a saturation (c_s) of the solution (I). After passing the critical level of supersaturation (c_{min}), the monomer faces a burst of nucleation (II). The nucleation process leads to a significant decrease in monomer concentration until the critical level of supersaturation (c_{min}) is reached. At that point, no further nucleation occurs due to the low monomer concentration. In the last phase, the particle growth starts (III). Monomers are further consumed, and particles grow until the saturation concentration (c_s) is reached again.^[43,44] After all particles are formed, the ripening process is taking place. The ripening process was first described in 1900 by WILHELM OSTWALD and is called the OSTWALD ripening.^[47] Small particles feature high solubility and surface energy within a solution. Therefore, smaller particles tend to redissolve and allow larger particles to grow even further.^[45,48]

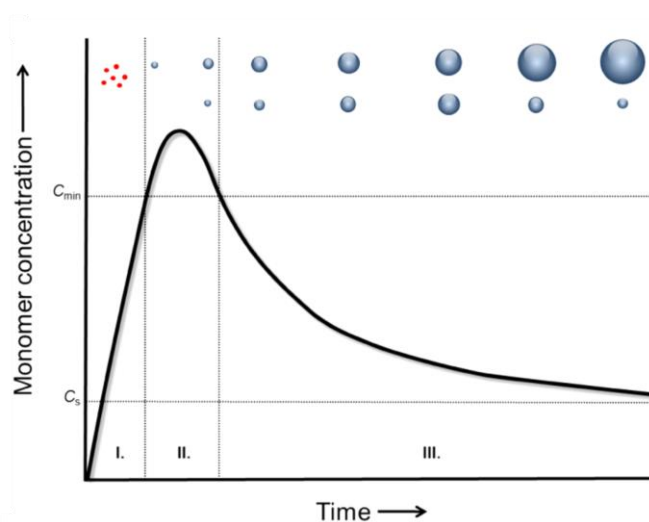


Figure 2.1: LAMER model for nanoparticle growth. Diagram of the three phases of nanoparticle growth and dependence of monomer concentration over time. Figure adopted from reference VREELAND *et. al*^[44] with permission from American Chemical Society, copyright 2015.

As a result of the large nanoparticle surface area and therefore their high surface energy, nanoparticle agglomeration and oxidation through their high reactivity are problematic.

Nanoparticles without any stabilizing agents are only stable under ultra-high vacuum conditions.^[49] As a result, some sort of stabilization is needed in the solution. For stabilization three approaches based on electrostatic, steric and their combination can be applied.^[49] In aqueous or polar solvents, positively or negatively charged ligand molecules on the nanoparticle surface will lead to repulsion with same charged nanoparticles. Due to this electrostatic repulsion, particles with the same charge will not agglomerate. The increase of the number of ligands enhances the nanoparticle stabilization.^[50] The surface charge depends on the pH value of the solution and therefore influences the nanoparticle interaction. Dependent on the nanoparticle ligand, additional electrolytes present in the nanoparticle solution might weaken the stabilization and lead to particle agglomeration.^[51-54] Large molecules that act as ligands for nanoparticles lead to steric stabilization. Typically, long alkyl chains are used as steric stabilizers for nanoparticles in apolar organic solvents.^[42,49] Amphiphilic ligands based on polyethylene glycol (PEG) derivatives allow nanoparticles to be soluble in various solvents.^[55,56] A combination of both steric and electrostatic approaches leads to electrosteric stabilization. One example are polymer-stabilized nanoparticles.^[57-61] Furthermore, the nanoparticle functionalization with different kind of molecules influences the solubility or binding affinity of the nanoparticles.^[62-64] Molecules that act as a nanoparticle ligand bind to the nanoparticle surface by an anchoring group. Typically, anchoring groups are based on thiols^[10,55,63] or amines^[1,65-67]. Ligands with weak binding to the nanoparticle surface can be exchanged with ligands with higher affinity to the nanoparticle surface.^[68,69] Furthermore, a ligand exchange can include the phase transfer of nanoparticles.^[13,70] The choice of ligands does not only contribute to the stabilization of the nanoparticle. Moreover, the morphology of the nanoparticles can be controlled during synthesis to achieve various shapes.^[71] Next to spheres, shapes such as rods, plates, cubes, wires and stars can be synthesized.^[71-76]

2.1.1.1 Gold nanoparticles

The interest of the synthesis of monodisperse gold nanoparticles (AuNP) started decades ago and is still ongoing.^[41,77-79] Next to gold nanoparticles, the synthesis of other noble metal nanoparticles such as silver gained interest.^[74,75,80] Some of the best-known synthesis of gold nanoparticles are based on experiments by JOHN TURKEVICH.^[41,81] The synthesis for gold nanoparticles by TURKEVICH is expected to follow the mechanism proposed by LAMER. In aqueous solution, the gold precursor is reduced with sodium citrate, which acts as both a reducing and a stabilizing agent (Figure 2.2).^[77]

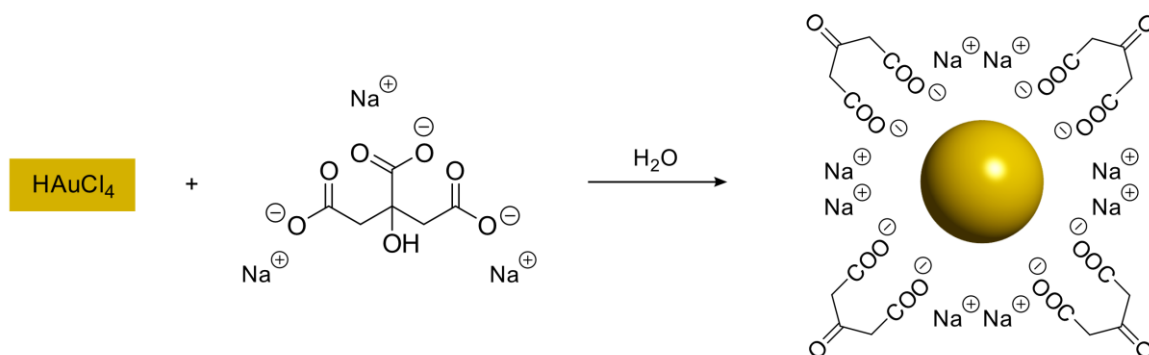


Figure 2.2: Gold nanoparticle synthesis based on the TURKEVICH method. Schematic reaction of tetrachloroauric acid and citrate to form citrate-stabilized AuNPs. Figure adapted from ZHAO *et. al.*^[82]

Over the last years, the gold nanoparticle synthesis proposed by TURKEVICH was improved by further investigating the synthesis.^[41] Here, the citrate acts as an reducing agents. Also, the citrate ligand adsorbs to the gold nanoparticle surface through its carboxyl anchoring group. Moreover, citrate influences the pH of the solution. To gain control over the pH of the reaction and in conclusion the nanoparticle size, citrate buffer instead of citrate solution was introduced.^[40] Additionally, ethylenediaminetetraacetic acid (EDTA) was introduced to achieve a narrower size distribution and increase particle uniformity. The influence of EDTA is not yet revealed, but it is assumed that the pH-dependent stabilization of certain crystal facets of the AuNPs leads to less anisotropic growth.^[41] Due to the negative charge of the citrate, particle stability is given through electrostatic repulsion. Based on the weak binding of the citrate to the nanoparticle surface, a ligand exchange with ligands of higher surface affinity can be performed.^[1,10,83,84]

2.1.2 Optical properties of plasmonic nanoparticles

Various different kinds of nanoparticles are presently investigated.^[1,19,85] Nanoparticles offer properties such as magnetic^[5,86] or mechanical^[87,88] features. Furthermore, optical properties of plasmonic nanoparticles are of high interest.^[24,89-93] Centuries ago, colloidal gold was integrated within objects, such as ruby glass or the famous LYCURGUS CUP.^[94,95] In 1857, MICHAEL FARADAY was the first who published the relation between gold and its optical properties. FARADAY proposed an influence of the optical properties based on the nanoparticle diameter. Colloidal dispersions of gold were prepared by reducing an aqueous solution of a gold precursor until a deep red color was observed.^[79]

Optical properties of plasmonic nanoparticles are based on the local surface plasmon resonance (LSPR). The LSPR is described by the collective oscillation of the electron cloud of a metal nanoparticle excited by an electric field (Figure 2.3).^[73,96]

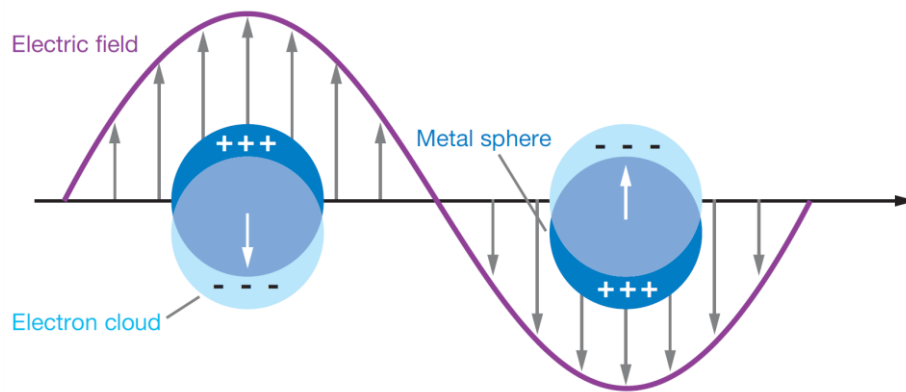


Figure 2.3: Schematic diagram of localized plasmon resonance in nanoparticles. Figure adopted from reference WILLETS *et. al*^[96] with permission from Annual Reviews, Inc., copyright 2007

Light is an electromagnetic wave and interacts with particles smaller than the incident wavelength.^[73,96,97] The electric field leads to an accumulation and displacement of electrons from their equilibrium position. The displacement creates uncompensated charge at the metal nanoparticle and results into a polarization of the nanoparticle surface. Due to Coulomb attraction, the electrons are dragged back to the equilibrium position, which leads to an oscillation of the electrons. Changes in the local dielectric environment influence the LSPR. These changes can be detected through an LSPR wavelength-shift measurement.^[97,98] Furthermore, the metal itself, the particle size and shape influence the position of the plasmon resonance peak.^[73,97,99-102] In 1908, GUSTAV MIE described the extinction spectra of spherical particles. MIE presented a solution for the Maxwell equations for the optical response of spherical particles of arbitrary size.^[103]

2.1.3 Applications based on plasmonic nanoparticles

The optical properties of plasmonic nanoparticles sparked interest to investigate their possible applications. A few selected examples of applications are presented in this chapter, but further details are reported elsewhere.^[100,104]

Due to the notable interaction of plasmonic nanoparticles with light, these particles can be applied for photoacoustic imaging.^[105,106] The photoacoustic (PA) effect describes the conversion of light to sound using a pulsed laser. An optical active material absorbs electromagnetic radiation, resulting into a localized thermal deposition and production of a pressure wave.^[107] Several material properties such as the absorption coefficient, thermal expansion coefficient or specific heat capacity influence the conversion of optical energy to pressure waves.^[108] Based on the tunability of the LSPR, highly stable gold nanoparticles are suitable imaging agents for PA.^[105-109]

The interaction between plasmonic nanoparticles and light results in highly confined electric fields.^[110] For methods such as surface-enhanced Raman scattering (SERS), highly confined electric fields are of interest. At very short distances, strong near-field coupling between plasmonic nanoparticles facilitate intense electromagnetic hot-spots. To achieve short distances, plasmonic nanoparticles can either be assembled in 2D or 3D.^[111-113] The Raman intensity is amplified by the resulting hot-spots between closely assembled plasmonic nanoparticles.^[110,114-117] Assemblies of plasmonic nanoparticles show coupling effects and therefore interactions of electromagnetic fields of single nanoparticles.^[25,111,112,118,119]

Besides using plasmon coupling to enhance Raman signals, it can be used to monitor distances between plasmonic nanoparticles or DNA hybridization. Furthermore, plasmon coupling can be applied to detect conformational changes or distances of biomolecules.^[120-122] A different method to detect these changes in distances is to use Förster resonance energy transfer (FRET). In comparison to 'molecular rulers' based on fluorophores and FRET, plasmonic nanoparticle-based 'molecular rulers' do not suffer from low and fluctuating signal intensities or have a distance limit of around 10 nm. Additionally, no photobleaching occurs and therefore the observation time is not limited.^[6,32,120,123] Another strategy is based on the combination of FRET and plasmonic nanoparticles. The fluorescence emission intensity of fluorophores can be enhanced by coupling with the noble metal electric field. Next to enhancing fluorescence emission, quenching of the emission is possible as well.^[4,13,122,124-128]

2.2 Fluorescence

Luminescence is the emission of light from a substance and is based on electronically excited states. Depending on the nature of the excited states, luminescence can be subdivided into two classes: phosphorescence and fluorescence. The emission of light from triplet excited states (T_1) to ground states (S_0) is called phosphorescence. Prior to the phosphorescence, intersystem crossing between excited singlet state (S_1) and triplet state (T_1) occurs. This is a transition to a state with a different spin multiplicity. Since the transition from triplet to the ground state is forbidden emission rates are slow ($10^3 - 10^0 \text{ s}^{-1}$) and common lifetimes are milliseconds to seconds. The lifetime describes the average time between excitation and return to ground state. In contrast, fluorescence emission rates are typically faster (10^8 s^{-1}) since a transition from excited singlet state (S_1) to ground state (S_0) is taking place. Lifetimes near 10 ns or even below are observed.^[129] The processes of absorption, fluorescence and phosphorescence are illustrated by a simplified JABLONSKI diagram^[129,130] (Figure 2.4).

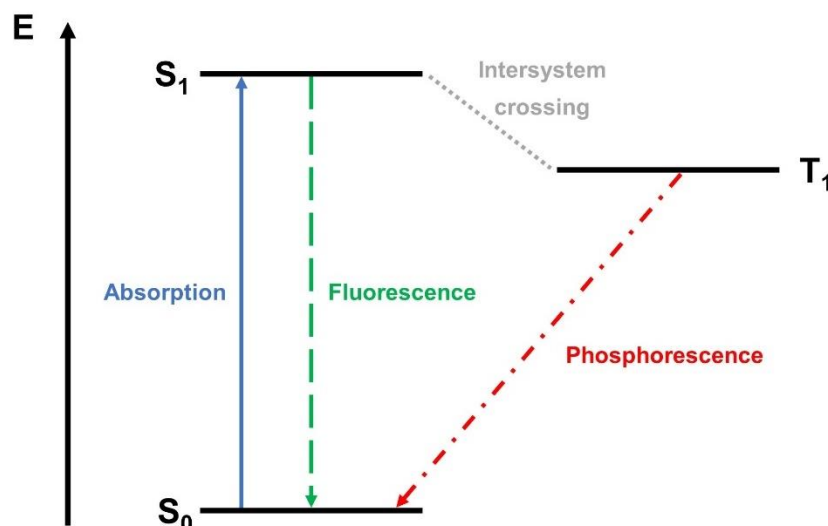


Figure 2.4: Schematic JABLONSKI diagram used to illustrate electronic states of a molecule and the transition between them. The absorption of energy leads to the transition from ground state (S_0) to excited singlet state (S_1). Energy can be emitted directly via the transition from excited to ground state (S_1 to S_0). The process is called fluorescence. Alternatively, a triplet state is achieved by intersystem crossing. The process of energy release from a triplet (T_1) to ground state (S_0) is called phosphorescence.

Fluorescence can be affected by the interaction of a fluorophore and quencher. Based on the contact time between both objects, two different kinds of quenching are possible. For static quenching, the contact time between fluorophore and quencher is significantly longer than the excitation decay time, resulting in the fluorescence being quenched. Dynamic quenching is based on the coupling between fluorophore and quencher, leading to an energy or charge transfer towards the quencher. The fluorescence intensity and decay time are decreased since the energy or charge transfer competes with the fluorescence.^[131,132]

2.2.1 Fluorophores

A fluorescent chemical compound that absorbs light of a specific wavelength and re-emits light at a longer wavelength is called a fluorophore. Typically, fluorophores are organic molecules with molecular weights up to 1,000 Dalton (Da). They contain aromatic groups, or planar or cyclic regions with several π -bonds. The fluorophore's structure and its chemical environment influence the energy transfer efficiency, quantum yield and lifetime since the excited fluorophore interacts with neighboring molecules. Fluorophores feature excitation and emission spectra with maxima for each fluorophore at specific wavelengths.^[129]

One of the most popular fluorophores is fluorescein. Fluorescein belongs to the family of xanthenes and can be used for labeling purposes.^[133] Other popular fluorophores are rhodamine derivatives, also part of the xanthene family (Figure 2.5). Rhodamines exhibit high

photostability and photophysical properties. Consequently, rhodamines are used as laser dyes^[134], fluorescence standards for quantum yields^[135], single-molecule imaging^[136] or imaging in living cells^[137]. Furthermore, enzymes^[138], antibodies^[139] or other biomolecules can be labeled with various fluorophores^[140]. In detail, the fluorescence can be used, for example, to monitor and image specific protein interactions at cell membranes^[141] or measure protein-protein interactions or conformation changes by FRET^[142]. Moreover, fluorophore-labeled bioconjugates are discussed to feature properties such as superfluorescence (chapter 2.5.2).^[11]

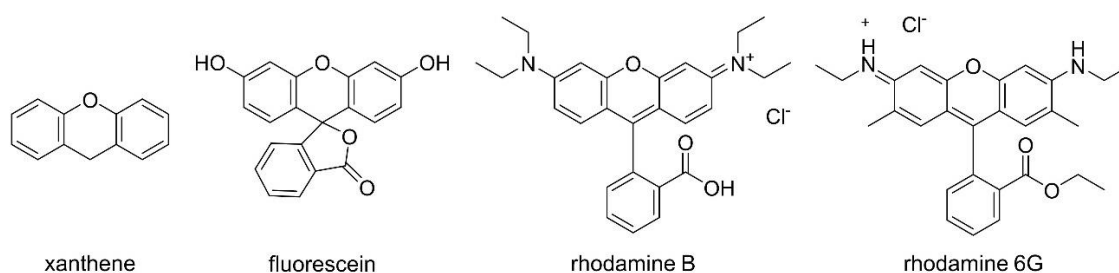


Figure 2.5: Overview of certain fluorophores of the xanthene family. From left to right: xanthene as a reference, fluorescein, rhodamine B, rhodamine 6G.

2.2.1.1 Protein labeling with fluorophores

The labeling of biomolecules such as proteins can be achieved by the coupling of selected fluorophores with certain amino acid residues of the protein. Amino acids such as lysine can be coupled with succinimidyl ester, glutamic and aspartic acid with amines and cysteines with maleimides. Cysteine is a proteinogenic amino acid with a thiol-containing side chain. The combination and reaction of a thiol and maleimide is one of the most efficient MICHAEL-type additions.^[143,144] The MICHAEL addition can be carried out under relatively mild reaction conditions and achieves highly stereo- and regiospecific products.^[145,146] The reaction is simple, robust and highly effective and fulfills the criteria of a modular 'click' reaction.^[143] As a result, thiol-maleimide reactions are very reliable and have gained ongoing interest for bioconjugation a long time ago.^[147-149]

The mechanism of the thiol-maleimide reaction is shown in detail in Figure 2.6. In terms of bioconjugation, R–SH equals the protein with a functional cysteine residue, while R¹–maleimide corresponds to a maleimide-functionalized fluorophore. The catalytic cycle of the formation of product requires an initial nucleophilic thiolate anion (Figure 2.6A). Two routes to form initial thiolate anions are described.

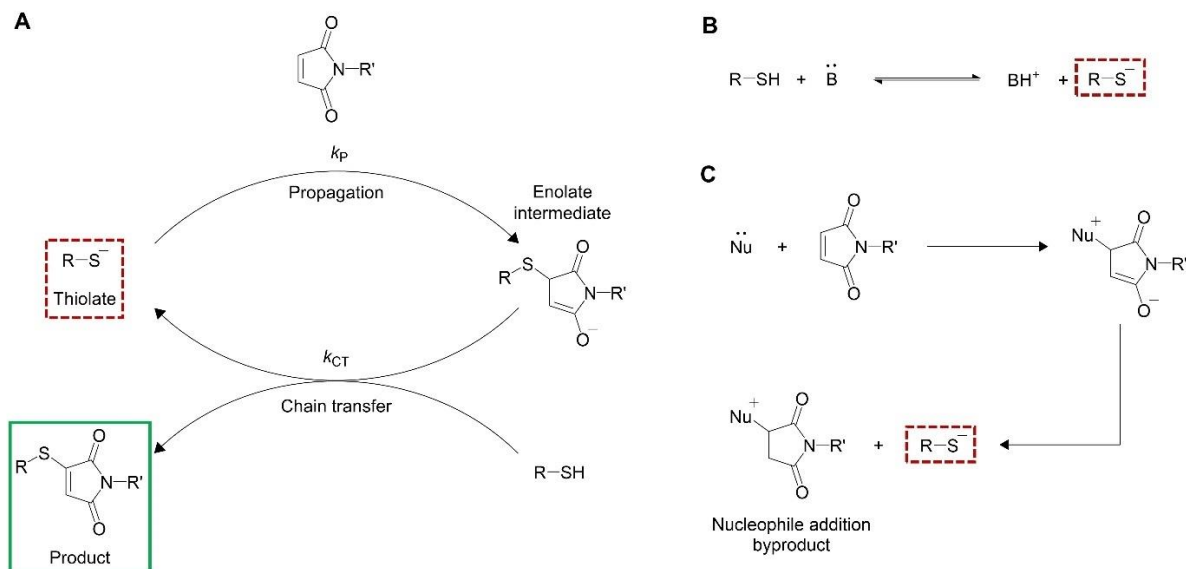


Figure 2.6: Schematic thiol-maleimide reaction pathway. (A) Mechanism for the thiolate-catalyzed addition to an *N*-substituted maleimide. (B) Formation of thiolate anion based on acid-base equilibrium. (C) Nucleophile-initiated pathway towards thiolate anion formation. Adopted from CHOUHARY *et. al.*^[150] with permission from Royal Society of Chemistry, copyright 2010.

The first route requires a base, while the second one is initiated by a nucleophile. The base-initiated mechanism is based on a weak base to deprotonate the initial thiol (Figure 2.6B). In consequence, the initially formed thiolate anion acts as a strong nucleophile, attacks the π-bond of a maleimide and forms a strongly basic enolate intermediate. The basic enolate intermediate deprotonates an equivalent of thiol, resulting in new thiolate and the final product. The second route is based on a nucleophile attacking the π-bond of the maleimide, resulting in a zwitterionic enolate intermediate (Figure 2.6C). This step is followed by the deprotonation of a thiol forming the initial thiolate anion. A nucleophile addition byproduct is formed, but since the thiol-maleimide reaction takes place very fast, the amount of byproduct is negligible (< 1 %).^[150-152]

2.3 Quantum dots

In the solid state, materials are classified as insulators, conductors and semiconductors (Figure 2.7). Their electrical properties can be explained by the band model. For insulators, the band gap is large (> 4 eV) and no charge transport can take place from valence to conduction band. In contrast to a large band gap, electrically conductive materials feature an overlap of the valence and the conduction band. Band gaps between 0.1 eV and 4.0 eV are typical for semiconductors.^[153] In semiconducting materials, electrons can overcome the band gap by absorbing energy and move into the conduction band, while leaving a positive hole in the valence band. Despite the band gap, electrons are still attracted to their corresponding positive

holes. The relation between the attracted pair of an electron and its corresponding hole is referred to as an exciton.^[154] The recombination of this exciton results in an outgoing electromagnetic radiation based on the energy difference between the valence and the conduction band in the form of fluorescence.^[153,155]

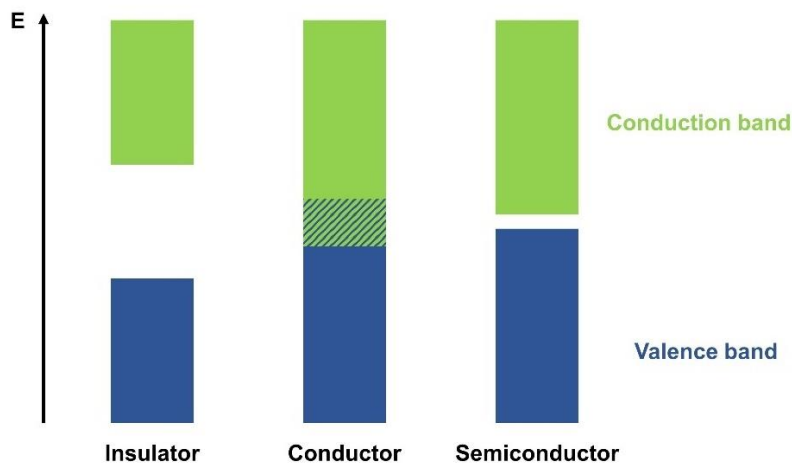


Figure 2.7: Schematic comparison between insulator, conductor and semiconductor based on the energy gap between conduction and valence band. The gap between conduction and valence band varies between insulator, conductor and semiconductor. Large band gaps are observed for insulators, while the bands overlap in conductors. In semiconductors, small band gaps between valence and conduction band are found. Blue: valence band; green conduction band.

If semiconductor bulk material is compressed to the nanoscale, it results in an increase of the band gap energy and therefore the optical and electronic properties change. This observation is called the size quantization effect. Due to the particle size, the exciton is locally confined. Fluorescent semiconductors that feature the size quantization effect are called quantum dots (QDs) and have special optical properties.^[155] Small changes to the few nanometers large QDs results in significant changes in the fluorescence. This implies a direct link between size and optical properties (Figure 2.8).^[156]

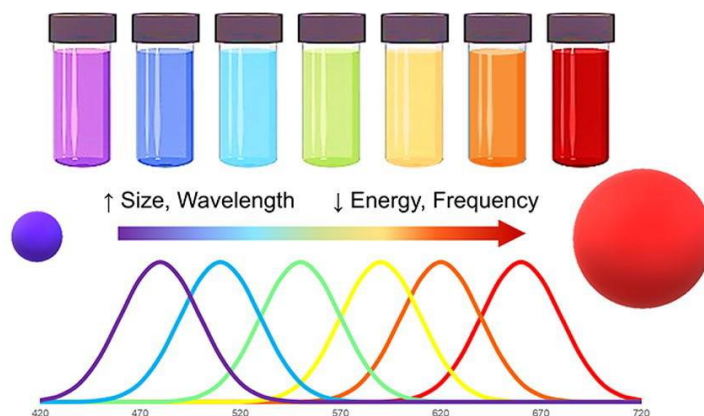


Figure 2.8: Illustration of the size dependent optical properties of QDs. With increasing size, the emission wavelength also increases, while the energy and frequency of the QD drop. Figure adopted from reference MOZAFARI *et. al*^[156] with permission from John Wiley and Sons, copyright 2020.

Next to the absorbed energy and the resulting fluorescence, the ratio of absorbed to emitted photons plays a significant role for the QDs properties. The ratio between absorbed to emitted photons is defined as the fluorescence quantum yield. A quantum yield (QY) of 1 means that all absorbed photons are emitted.^[157-159]

Traditionally, semiconductor QDs are synthesized by fast injection of the precursor into a hot solvent solution. The reaction is taking place in a three-neck flask under inert atmosphere (N₂). High temperatures are common for these reactions.^[160,161] Nucleation and growth of the semiconductor QDs can be described by the LAMER model (Chapter 2.1.1). Alternatively, all reagents can be mixed in a three-neck flask and nucleation and growth is induced either chemically or thermally.^[162] Based on the synthesis, native ligands can be trioctylphosphine oxide (TOPO), octadecane (ODE) or oleic acid (OA).^[160,163,164] Native QD ligands from the synthesis can be exchanged to achieve, for example, water solubility.^[165-168]

Usually, a QD core features defects on the outer surface, in which electrons can be trapped (trap states). Due to the interaction between electron and defect, energy is transferred into the crystal lattice (vibrational transition) instead of contributing to fluorescence. Therefore, a shell is grown around the QD core to remove traps and enable higher quantum yields.^[169] In the end, the growth of a shell around the QD core yields in brighter particles, due to the significant increase in their absorption cross-section.^[170] A variety of core-shell particles with different geometries or shell thicknesses are achievable and lead to different quantum yields and photostability.^[161,171,172] Common spherical core-shell QDs are composed of inorganic compounds such as cadmium selenide / cadmium sulfide (CdSe/CdS) or cadmium selenide / zinc selenide (CdSe/ZnSe). CdSe/CdS core-shell particles are reported to achieve fluorescence quantum yields up to 97 %.^[173] For higher stability of optical properties against photodegradation or photoblinking, zinc sulfide (ZnS) is suggested as a shell material.^[161] The emission wavelength can even be tuned by changing the composition in, for example, Cd_{1-x}Zn_xSe QDs. On such a Cd_{1-x}Zn_xSe core, a ZnS shell can be grown. These core-shell particles show fluorescence in the blue-green spectral range and achieve very high QYs up to 100 %.^[174-176] Typically, the shell around the core is up to a few nanometers thick. The shell thickness can even be increased up to 10 nm or more as shown for giant core/shell QDs.^[177,178] Even these giant core/shell particles can be synthesized very monodisperse and can achieve high QYs of 98 %.^[171]

Since QDs show significant optical properties, such as a size-dependent and narrow emission band with a high QY, they have gained interest for commercial applications.^[179] Furthermore, QDs are discussed for applications such as photocatalysis^[180], energy harvesting^[181] or lasing^[182]. To achieve higher biocompatibility of QDs, the incorporation in protein-based assemblies will be investigated in this work.

2.4 Protein containers

A protein container is a precise assembly of protein subunits into polyhedral shell-like structures.^[183,184] In most cases, each subunit is composed of the same amino acid sequence. Most protein containers adopt sphere-like morphology, but rods, rings and more complex geometries are also found.^[183,185-189] Moreover, protein containers can be subdivided into two classes: non-viral and viral containers. If the latter are just composed of their protein capsid shell without their genetic material, they are referred to as virus-like particles (VLP). The icosahedral symmetry is the most common one for spherical virus containers. The smallest possible icosahedral container is constructed out of 60 identical subunits. Viral containers benefit from icosahedral symmetry due to the higher volume in comparison to smaller assemblies such as octahedral ferritins composed of 24 subunits. In 1962 CASPAR and KLUG demonstrated that the triangulation number T is useful to describe the container morphology with discrete values such as 1, 3, 4 or 7.^[184,190]

In general, the focus of this thesis lies on spherical protein containers with icosahedral, tetrahedral or octahedral symmetry^[190]. A small selection of common protein containers is visualized in Figure 2.9. All these differently shaped protein containers have in common that they have precisely defined outer, inner and inter-subunit surfaces. The outer surface is mainly responsible for the interaction with the container environment. On the other side, the inner surface determines the properties of the cavity. The inter-subunit surface is crucial for the protein container assembly.^[191,192] All these surfaces can be redesigned to manipulate the protein container's native properties. With the change of amino acids, it is possible to trigger protein container assembly with metal ions.^[191,193] Modifications of the inner or outer surface affect the encapsulation of cargo^[194,195] or enable the targeting of the protein container towards cells^[196,197]. Furthermore, small pores are usually found between subunits. These pores often play an important role for small molecules or ions to enter the cavity, while larger molecules are not able to pass.^[198,199] Based on their amino acid composition, protein container pores may be charged or hydrophobic. Therefore, certain pores are permeable specifically for distinct molecules with a certain charge or polarity.^[198,200-202] The molecular flux into protein containers can even be enhanced by altering the amino acid composition of the pore.^[198,200]

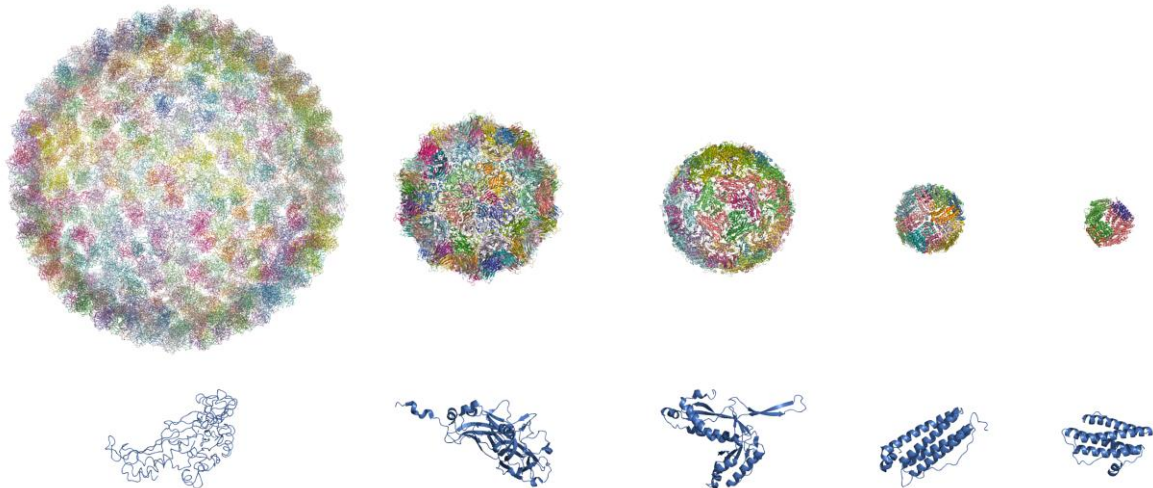


Figure 2.9: Examples of protein containers with different sizes and morphology. From left to right: P22 procapsid (diameter: 56 nm, PDB: 3IYI), cowpea mosaic virus (diameter: 30 nm, PDB: 1NY7), encapsulin (diameter: 24 nm, PDB: 3DKT), ferritin (diameter: 12 nm, PDB: 2FHA), Dps (diameter: 9 nm, PDB: 1QGH). The corresponding subunit is shown below each container.

Most of the hollow protein containers shown in Figure 2.9 encapsulate functional cargo inside their cavity. Next to their native cargo, protein containers were exploited to encapsulate non-native cargo.^[9,203,204] They can act as delivery vehicles for more than their natural cargo, even for vaccines or drugs. The encapsulation of cargo is one way to increase the cargo's stability and lifetime.^[10,13,205,206] Protein containers are also used as nanoreactors and templates for controlled synthesis of nanoparticles.^[207-209] The application of biological scaffolds conjugated with fluorophores for developing non-classical light sources as photonic probes for medical imaging was recently investigated. Moreover, an icosahedral virus template is conjugated with many fluorophores and excited by ultrafast laser pulses. Properties such as superfluorescence or superradiance are discussed.^[11] Based on recent results using biological templates to accurately define the chemical environment, orientation and position of fluorophores seem to enable properties which are not imaginable with randomly distributed fluorophores.

2.4.1 Encapsulins

Almost three decades ago, encapsulins were originally discovered. Initially, high-molecular-weight aggregates were found in bacteriostatic culture supernatants of *Brevibacterium linens* (*B. linens*) M18 via transmission electron microscopy (TEM) imaging. At that time, the author's research concluded that this high-molecular-weight aggregate must be a bacteriocin, a proteinaceous toxin produced by bacteria.^[210] Some decades later, it was shown that the high-molecular-weight aggregates were wrongly characterized in being titled bacteriocins. In fact, this led to the discovery and later characterization of the *B. linens* encapsulin.^[7,211] Further research led to a still increasing number of thousands of encapsulins. Recently, encapsulins

have been grouped into four distinct families, each reflecting differences in structure, sequence and operon organization.^[7,212] The first family of encapsulins is probably the best-studied and widespread family. The key characteristic of the first family is the operon organization: the encapsulin protein is almost directly followed by a single primary cargo protein.^[212,213] In comparison to the first family of encapsulins the other three families do not yet play such a significant role in research and are not discussed here.

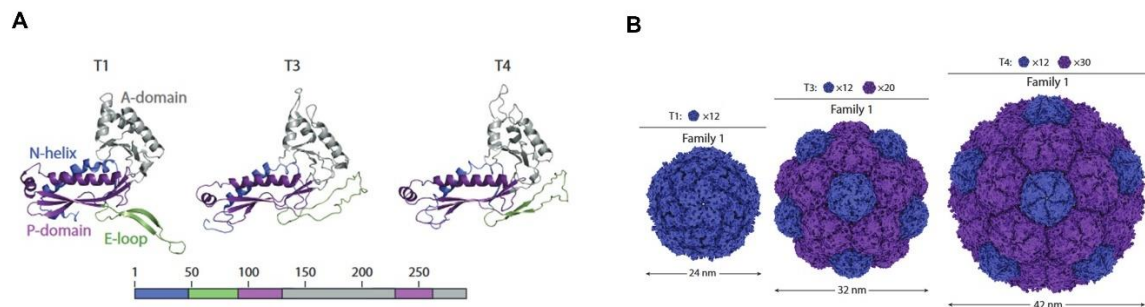


Figure 2.10: Overview of structural features of encapsulin of the first family. (A) and (B) from left to right: $T = 1$ (PDB: 3DKT), $T = 3$ (PDB: 4PT2) and $T = 4$ (PDB: 6NJ8) encapsulins. Figure adapted from reference GIESSEN^[7] with permission from Annual Reviews, Inc., copyright 2022.

Encapsulins are hollow protein containers with icosahedral symmetry with diameters between 24 and 42 nm and with triangulation numbers of $T = 1$, $T = 3$ or $T = 4$ (Figure 2.10).^[214,215] All known encapsulins share structural similarities with the shell protein gp5 of the Hong Kong 97 (HK97) bacteriophage. This finding hints towards an evolutionary connection.^[216] The HK97-fold is named after the gp5 shell protein and is unusual for known cellular proteins. This led to a misunderstanding of its molecular and physiological functions until further research was carried out.^[7,217] For viruses, the HK97-fold is frequently found, but outside of viruses it is only present in bacterial and archaeal encapsulins.^[212] Encapsulin subunits similar to HK97-fold have three structural domains: the axial domain (A-domain), peripheral domain (P-domain) and the extended loop (E-loop). Additionally, encapsulins of the first family feature a unique N-terminal helix (Figure 2.10A), which interacts with the P-domain and is crucial for the formation of the cargo-loading peptide (CLP) binding site.^[217,218] The E-loop arrangement dominates the assembly mode. An extended E-loop results in $T = 1$ assemblies, whereas a compact E-loop enables $T = 3$ and 4 assemblies. For each of the three assemblies, differently sized protein containers with icosahedral symmetry have been reported (Figure 2.10B). The encapsulin container surface consists of pentameric and hexameric facets along the icosahedral fivefold and threefold symmetry axes, respectively. As usual for proteins in general, pores between subunits are formed. The pores are symmetrically distributed over the protein shell at their two, three and fivefold symmetry axes.^[214,217] In currently discovered encapsulins, the pores are charged or uncharged and differ in size.^[7,9,214,215]

Naturally, encapsulins encapsulate cargo proteins like peroxidases^[212], ferritin-like proteins (FLPs)^[219] and desulfurases^[220]. Based on their cargo, encapsulins are suggested to play roles in iron storage or oxidative stress resistance.^[214,215] The encapsulation of cargo is mostly mediated by cargo-loading peptides.^[9,194] Further details about general cargo encapsulation are provided in the following chapter. Next to the encapsulation of cargo into the encapsulin container, the mineralization inside certain encapsulins was investigated.^[221,222]

2.4.1.1 *T. maritima* encapsulin

The focus of this work is based on the *T. maritima* encapsulin. Therefore, additional information will be presented in this chapter. This encapsulin is found in the hyperthermophilic bacterium *T. maritima* and is a 24 nm sized protein container assembled out of 60 identical subunits via icosahedral symmetry with $T = 1$. The cavity of this encapsulin is approximately 20 nm large. For this encapsulin, the natural cargo is an FLP, the function of which is to sequester soluble iron as Fe(II) by oxidation and mineralization as Fe(III).^[9] Furthermore, it was suggested that this encapsulin may be a flavoprotein. Flavoproteins typically possess a yellow coloration, due to bound flavins like riboflavin, flavin mononucleotide (FMN) and flavin adenine dinucleotide (FAD).^[223] Exactly this yellow coloration was found for the *T. maritima* encapsulin. Two concurrent structural studies independently came to conclusion that this encapsulin is a flavoprotein. Both studies inspected the independently determined cryo-EM structures (PDB: 7MU1; 7KQ5) of the *T. maritima* encapsulin and concluded that the flavin is bound via π -stacking to the tryptophan at position 90 (W90). The mutation of tryptophan at position 90 to glutamic acid (W90E) or to alanine (W90A) led to a loss of the yellow coloration. Characterization of these new encapsulin variants showed no typical features of flavins. Furthermore, the role of the flavin in combination with the natural FLP cargo is discussed. Typically, the oxidation of iron requires the transfer of an electron from iron to an acceptor. The flavin could serve as an electron acceptor, but iron storage and release assays showed no difference between the wild type and W90E encapsulin. The flavin's role is not yet finally revealed entirely.^[219,224]

Based on the crystal structure of the *T. maritima* encapsulin (PDB: 3DKT), SUTTER *et. al* observed electron density of the cargo close to the encapsulin inner surface. The electron density could be attributed to the cargo protein with its C-terminus binding to the encapsulin. Each subunit has a binding site for the CLP, meaning that a maximum of 60 cargo proteins could be loaded. SILVER and GIESSEN investigated the CLP-shell interactions in *T. maritima* encapsulins. They highlighted that the CLP-shell interactions are based on hydrophobic and ionic interactions. Furthermore, a certain flexibility is necessary for efficient cargo loading.^[194] SAVAGE *et. al* showed that the CLP can be fused with a green fluorescent protein (GFP) to

function as non-native cargo. The encapsulation of the CLP-modified GFP into the *T. maritima* encapsulin was successful.^[9] Moreover, it was possible to encapsulate inorganic nanoparticles into *T. maritima* encapsulin. In this previous work of our group, plasmonic gold nanoparticles were functionalized with CLPs and encapsulated with high efficiency (Figure 2.11).^[10]

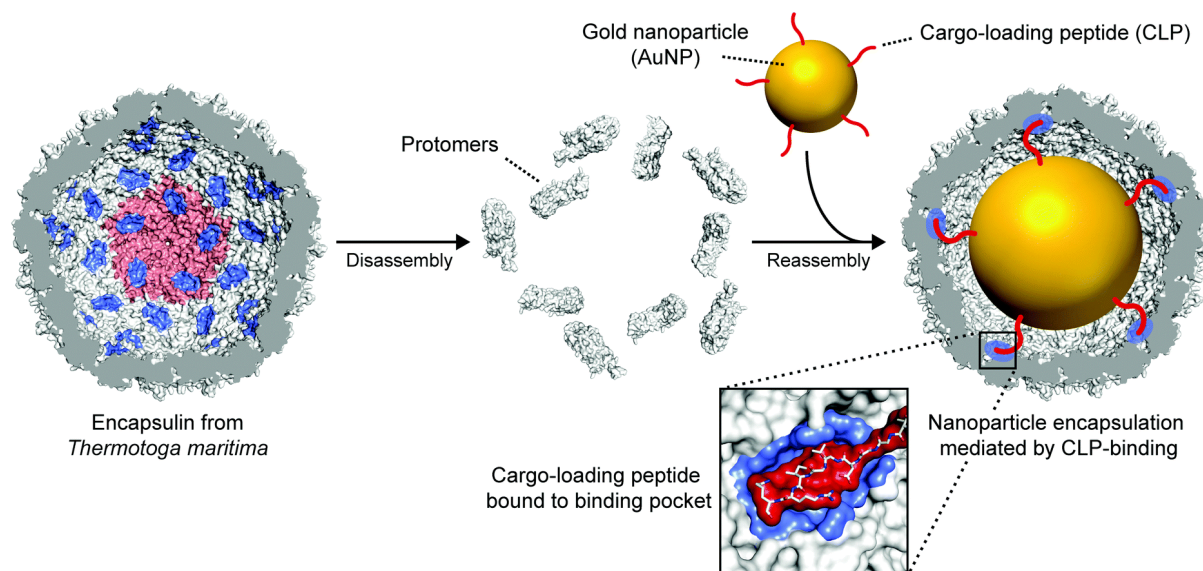


Figure 2.11: Schematic illustration visualizing the peptide-directed encapsulation of gold nanoparticles into *T. maritima* encapsulin. One out of 12 pentamers is highlighted in light red. The protein container is disassembled into protomers. Gold nanoparticles functionalized with a cargo-loading peptide (CLP) are added to the disassembled protein container while the reassembly is initiated. Afterwards, the gold nanoparticle is encapsulated into the protein container. The cargo-loading peptide is bound to the binding pocket (inset). Each of the 60 monomers features one CLP-binding pocket, as highlighted in blue. Figure adopted from reference BECK *et. al*^[10] with permission from Royal Society of Chemistry, copyright 2009.

The encapsulation process is based on the disassembly of a protein container followed by the reassembly of the subunits, while cargo of interest is added (Figure 2.11). The disassembly is induced if the pH is either very acidic or basic or chaotropic agents such as guanidine hydrochloride are added, while the protein is incubated at 4 °C for 1 h. Reassembly is initiated by diluting the sample with a buffer of neutral pH.^[9,10] Recently, a study investigated the dis- and reassembly for three different encapsulins. The timescale of encapsulin reassembly was up to a few hours, depending on the encapsulin variant. Thermal encapsulin disassembly at temperatures up to 90 °C is investigated. In contrast to other encapsulins, the *T. maritima* encapsulin showed high stability and no disassembly at higher temperatures, which is consistent with it being derived from thermophilic bacteria.^[217,225]

For smaller protein containers such as ferritin, it was shown that protein containers can act as a size-constrained template for nanoparticle formation.^[205,226] Similarly, SILVER and GIESSEN successfully synthesized silver nanoparticles (AgNPs) inside the encapsulin container.^[222] A mineralization peptide was fused to the N-terminus of *T. maritima* encapsulin, which is exposed

to the container cavity. The AgNP mineralization peptide was already used beforehand to synthesize AgNPs inside ferritin.^[227,228]

Both, the size and charge of the pores, are crucial aspects for mineralization or reactions inside protein containers, due to molecules diffusing through the pores. The *T. maritima* encapsulin has pores at its two-, three and fivefold symmetry axes, which are negatively charged, uncharged and positively charged, respectively. LUTZ *et. al* investigated the molecular flux of *T. maritima* encapsulin and modified the 3 Å large pore along the fivefold axis. Via a stepwise deletion of amino acids, the pore-forming loop region was decreased, leading into larger pores of up to 11 Å.^[198]

Protein containers have been used as templates for nanoparticle synthesis or catalysis, but also genetically modified to alter structures. Moreover, protein containers can act as building blocks for the assembly of biohybrid nanomaterials, as shown in the following chapter.

2.5 Assembly of nanoscale building blocks

Over the last decades, research focused on methods to self-assemble nanoscale building blocks such as nanoparticles with distinct properties into organized 2D or 3D materials. The organization of objects from a disordered state to an ordered structure is called self-assembly. Self-assembled structures of nanoscale building blocks show emergent properties single particles do not feature.^[111,229,230] The final structures can be based on nanoparticles or biomolecules such as proteins.^[231,232] Based on the fact that both nanoparticles and protein containers can be assembled individually, the combination of both types has gained interest.^[13,15] Therefore, the following chapters will highlight current approaches for the self-assembly of nanoscale building blocks towards novel biohybrid materials.

2.5.1 Plasmonic nanoparticle superlattices

The nanoparticle ligand shell plays a significant role for the assembly, since the ligands interact with the environment. Additionally, the ligand shell can be altered through changing the ligand systems.^[1,25,233,234] External stimuli such as solvent, pH or temperature affect the ligand interactions.^[1,233-235] By controlling the ligand interactions, assemblies of interest can be achieved. Here ligands can be either small molecules or DNA.^[229,236-238]

Since gold nanoparticles show interesting optical properties, research on their assembly possibilities and properties started years ago and is still ongoing.^[25,112,239,240] MURRAY and co-workers described a method to synthesize nanoparticle crystals. Organic solvent containing nanoparticles was placed on a diethylene glycol surface in a Teflon well. The well was covered

with a glass slide and the organic solvent could evaporate through the gaps between the well and the glass. After complete evaporation, a solid membrane formed and was characterized via transmission electron microscopy (TEM) and scanning electron microscopy (SEM).^[241] The basic procedure was transferred for the synthesis of gold nanoparticle monolayers and crystals.^[112,242] Figure 2.12a depicts a TEM image of polystyrene-stabilized nanoparticles assembled into hexagonally packed monolayers. Repulsive forces from the polystyrene ligands and van-der-Waals attraction between the gold nanoparticles lead to small gaps between the nanoparticles.^[111,243] By increasing the nanoparticle concentration and decreasing the reaction rate during self-assembly, face-centered cubic crystals were obtained and imaged via SEM (Figure 2.12b). For further characterization the optical response of such gold nanoparticle crystals was examined.^[112]

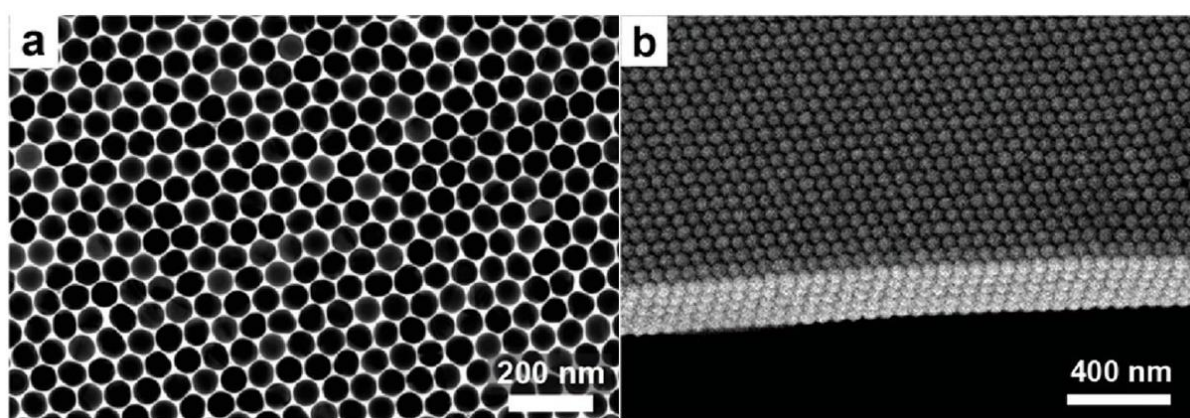


Figure 2.12: Electron microscopy images of assembled gold nanoparticles. (a) Transmission electron microscopy image of gold nanoparticle monolayer. (b) Scanning electron microscopy image of gold nanoparticle crystal. Figure adopted from reference MUELLER *et. al.*^[25], copyright 2021.

As mentioned in chapter 2.1.3, SERS is one application of interest for plasmonic nanoparticles. MUELLER *et. al.* investigated plasmonic gold nanoparticle crystals via simulations and experimental measurements.^[25] Finite-difference time-domain (FDTD) simulations were carried out to analyze the distribution of the electric field and resulting field enhancement inside plasmonic gold nanoparticle crystals. In Figure 2.13a, the electric field amplitude of an *fcc* crystal composed of plasmonic gold nanoparticles is visualized. Six layers of gold nanoparticles of a size of 60 nm and with 1.5 nm interparticle gaps were used to calculate the electric field amplitude at four excitation energies where polaritons are resonantly excited (Figure 2.13c). An increased excitation energy corresponds to an increase in effective refractive index. If the excitation energy equals the polaritonic band gap, light cannot enter the plasmonic crystal and the electric field is only enhanced in top layers (Figure 2.13a, 2.11 eV). As shown in literature and by MUELLER *et. al.* light is strongly confined inside a plasmonic crystal.^[25,244-246] In Figure 2.13c, the electric field intensity as a function of excitation energy of the bulk and the top layer of a plasmonic crystal is illustrated. The enhancement of the bulk (crystal) is based on the mean value of the enhancement of hot spots from all layers (Figure

2.13c, red line). To calculate the plasmonic crystal surface enhancement, only hot spots of the top nanoparticle layer were considered (Figure 2.13c, blue line). In both cases the strongest enhancement was calculated at the resonance energy of the polaritons (Figure 2.13c, dashed lines). In comparison, for the enhancement of the bulk and surface it was stated that the optical properties of the bulk mainly determine the field enhancement at the surface of the crystal. The field enhancement at the surface plays a significant role for measurements where analyte is drop cast on the surface.

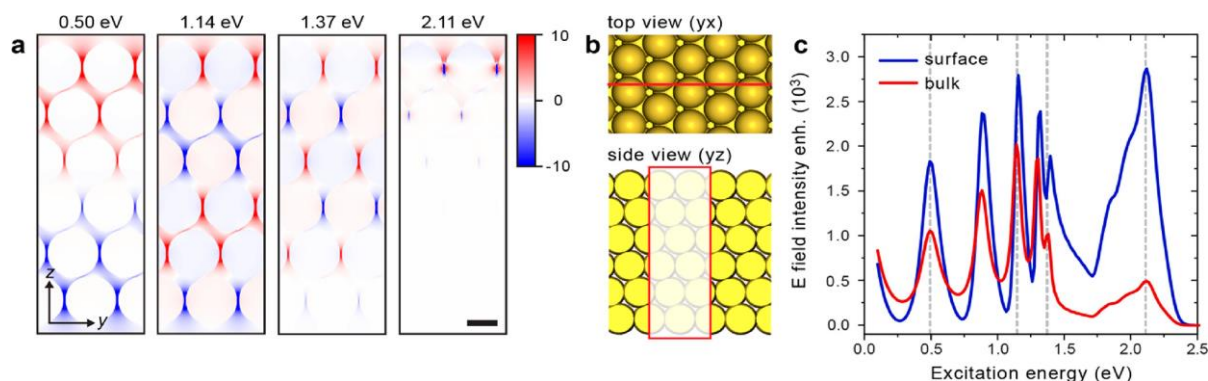


Figure 2.13: FDTD simulated field enhancement of 3D gold nanoparticle crystals. (a) Field amplitude enhancement as a function of position inside gold nanoparticle crystal within six layers. Excitation energy range visualized for four cases (0.50 eV, 1.14 eV, 1.37 eV and 2.11 eV). The polarization of the incident light was set along y. Scale bar is 30 nm. (b) Schematic top and side view of *fcc* gold nanoparticle crystal. The plane of simulation is highlighted with red lines. (c) Electric field intensity enhancement in the hot spots of the plasmonic crystal. The surface (top nanoparticle layer) electric field intensity enhancement (blue) and the mean value of the enhancement of all layers (red, bulk) was calculated. The polarization of the incident light was set along x. Figure adopted from reference MUELLER *et. al.*^[25], copyright 2021.

In addition to FDTD simulations, experimental measurements were carried out by MUELLER *et. al.* The observed SERS enhancement factors agreed with the FDTD based factors. Therefore, both simulation and experiment highlight that plasmonic crystals are promising platforms for quantitative and repeatable SERS detection.^[25]

2.5.2 Superfluorescent nanocrystal superlattices

Assembled plasmonic particles show different properties as single particles. The same observations were found for an ensemble of emitters. An individual emitter like an excited atom or ion behaves differently than its ensemble. The excitation of such an ensemble leads to spontaneous emission. The individual atoms couple and become synchronized after a system specific delay time (τ_D). After a characteristic decay time (τ_{SF}), a collective emission as a short, intense burst of light is the result (Figure 2.14). The process itself is called superfluorescence.^[247] To achieve superfluorescence some requirements such as close positions of the individual emitters and decoupling from the environment are needed.

Superfluorescence differs from superradiance, since the latter occurs in systems that initially feature a macroscopic dipole by the excitation process.

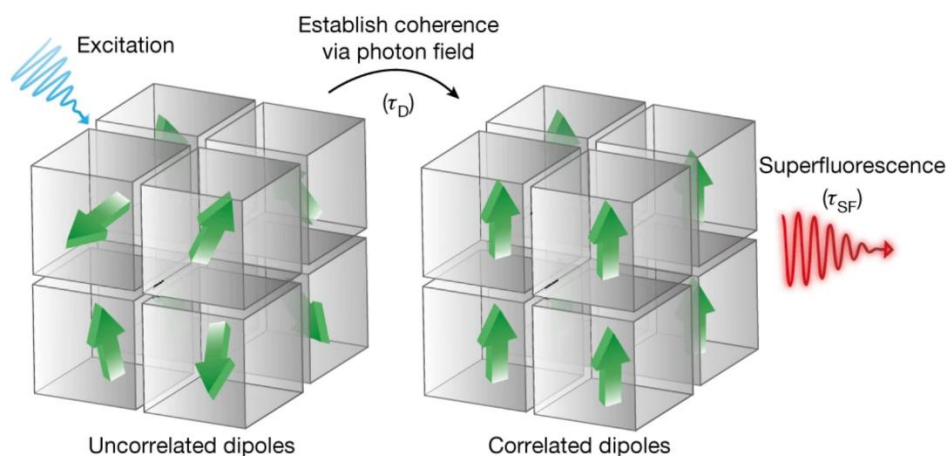


Figure 2.14: Illustration of the superfluorescence mechanism. The excitation of an assembly of uncorrelated dipoles leads to correlated dipoles inside the assembly and results in collective emission called superfluorescence. Figure adopted from reference STÖFERLE *et. al.*^[248] with permission from Springer Nature, copyright 2018.

Superfluorescence has been observed for certain gases and solid-state systems.^[249-253] In recent years, perovskite nanocrystals (NC) gained interest. Their three-dimensional assemblies feature optical properties such as superfluorescence.^[248,254-256] One example for perovskite NCs are caesium lead halides (CsPbX_3 , $X = \text{Cl, Br}$). These perovskite NCs can be self-assembled via solvent drying into superlattices (Figure 2.15a-d).^[248,257,258]

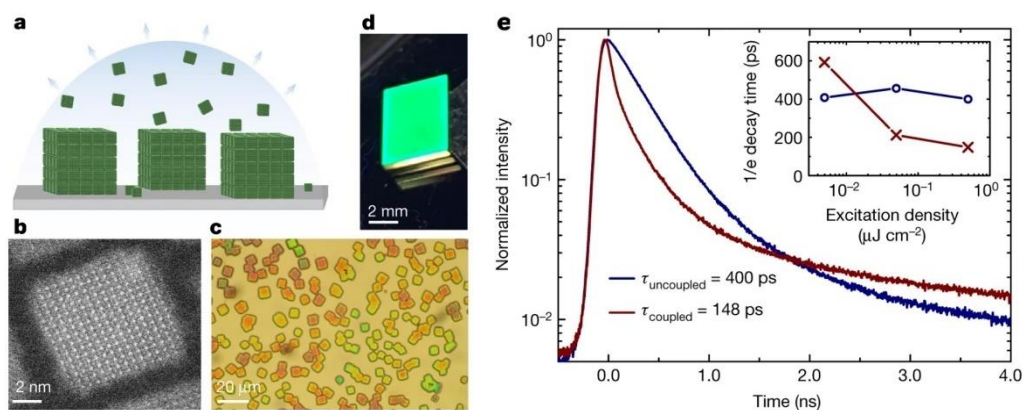


Figure 2.15: Assembled lead halide perovskite nanocrystal superlattices and their fluorescence lifetime. (a) Illustration of the assembly of single lead halide perovskite nanocrystals into superlattices via solvent evaporation. (b) High resolution TEM image of a single lead halide perovskite nanocrystal. (c) Photograph of micrometre-sized nanocrystal superlattice assemblies. (d) Optical microscope image under ultraviolet light of three dimensional, cuboidal-shaped nanocrystal superlattices. (e) Two time-resolved photoluminescence decays are visualized. The uncoupled and coupled superlattice decay times are shown in blue and red, respectively. Inset indicates the power-dependence of the decay times of both components. Figure adapted from reference STÖFERLE *et. al.*^[248] with permission from Springer Nature, copyright 2018.

Investigation of the optical properties of certain perovskite NC superlattices by KOVALENKO and co-workers show that the optical properties of the superlattices differ between coupled and uncoupled systems. If the system is coupled, superfluorescence with a characteristic decay time can be observed. The decay time of the uncoupled system is longer (Figure 2.15e). Additionally, the decay time was strongly affected by the excitation power (inset Figure 2.15e). A diluted nanocrystal sample did not lead to any superfluorescence. Therefore, superfluorescence was only observed for perovskite NC superlattices, since an ensemble of emitters is needed.^[247,248,250,254]

2.5.3 Protein container assemblies

In general, proteins are atomically defined and produced by nature with specific amino acid sequences, which can be altered if needed. Protein containers are structurally well-defined spherical objects, which can be used for mixed assemblies with nanoparticles. Containers such as CCMV and ferritin have been used to construct superlattices based on electrostatic interactions between protein containers and oppositely charged synthetic nanoparticles.^[188,259,260] Altering the nanoparticle ligand shell resulted in differently ordered binary ferritin–nanoparticle structures.^[261] Ideally the crystalline material can be tuned to achieve structural, chemical or physical properties of interest. For a controlled assembly of protein building blocks into three dimensional materials, several aspects must be addressed. As shown for the assembly of binary ferritin–nanoparticle structures, electrostatic interactions play a significant role. To achieve electrostatic attraction between protein containers, the surface can be engineered by changing amino acids into positively or negatively charged amino acids (Figure 2.16). Moreover, the assembly can be mediated by changing the salt concentration. In the case of oppositely charged ferritin containers, a high Mg^{2+} concentration resulted in a unitary lattice, whereas a low Mg^{2+} concentration resulted in a binary lattice.^[15,262]

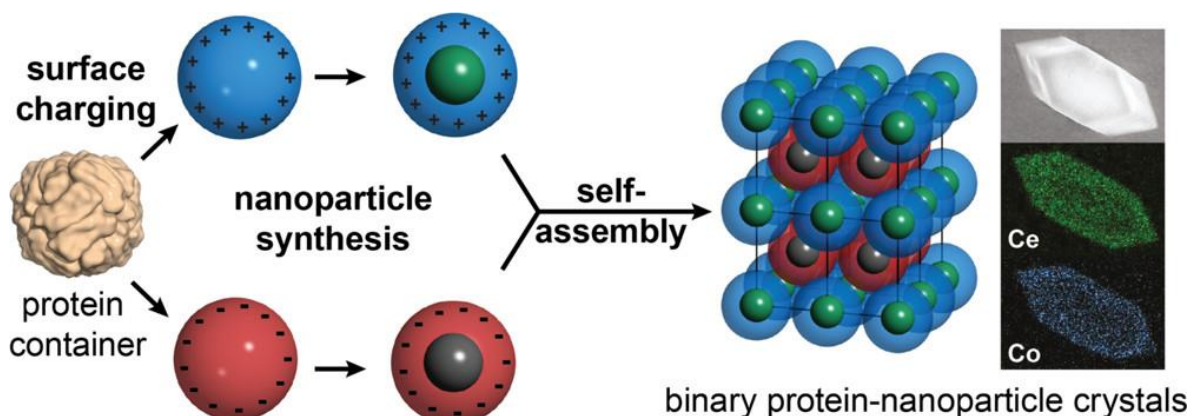


Figure 2.16: A general strategy to assemble binary protein-nanoparticle crystals. The surface charging of a protein container leads to either positively or negatively surface charged protein containers. After nanoparticle synthesis inside the containers, self-assembled structures can be achieved. These binary protein-nanoparticle

crystals can be analyzed via energy dispersive X-ray (EDX) mapping to visualize the elemental distribution of the nanoparticle. Figure adapted from reference BECK *et. al*^[15] with permission from American Chemical Society, copyright 2016.

TEZCAN and co-workers focused on the structural variation of ferritin assemblies through the creation of protein–metal–organic frameworks.^[232,263] The construction principles of metal–organic frameworks (MOFs) were transferred to design a 3D crystalline protein lattice. Ferritin acts as a node with a metal ion coordination site. The metal ion coordination site was introduced at the threefold axis pore through mutation of amino acids. Coordinated metal ions were then linked by organic linkers to assemble the protein containers. Lattice type and dimensions were dictated by changing both the metal and linker (Figure 2.17).^[232]

For the generation of hybrid protein-nanoparticle materials, prior to the assembly of protein containers, nanoparticles can be incorporated. The incorporation can be achieved by either dis- and reassembly while encapsulating cargo or by mineralization inside the container. These nanoparticle-loaded protein containers can be crystallized just as empty containers, because the protein container is the primary building block that defines the crystal lattice and not the nanoparticle cargo. The nanoparticle cargo is still accessible within the protein container crystal and can be used to catalyze the conversion of dye substrates. Substrates diffuse through the crystal channels and through the container.^[205]

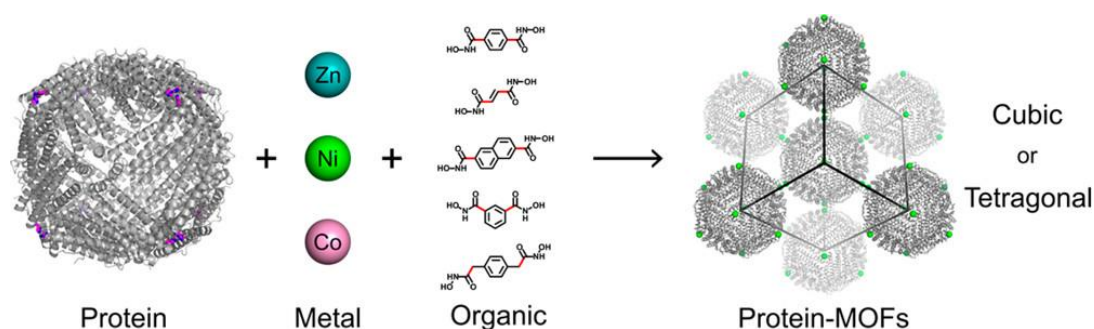


Figure 2.17: General strategy for the assembly of protein-MOFs based on protein container, metal ions and organic linker. A variety of metal ions and organic linkers are shown. Depending on the composition cubic or tetragonal structures can be achieved. Figure adopted from reference TEZCAN *et. al*^[232] with permission from American Chemical Society, copyright 2017.

CORNELISSEN and co-workers fabricated thin films of viral protein containers based on a biphasic system. In detail, CCMV protein containers were used and loaded with gold nanoparticles or enzymes.^[264] On the CCMV surface, there are plenty of amine groups present that enable the interfacial cross-linking of protein containers.^[265,266] Both, CCMV and cross-linker molecules diffuse towards the interfacial surface. The thickness of the obtained films could be controlled by the reaction conditions. Gold nanoparticle-loaded CCMV protein films were still catalytically active at the reduction of 4-nitrophenol (4-NP) to 4-aminophenol (4-AP). The reaction was monitored through the decrease of the absorption of 4-NP at 400 nm and

increase at 292 nm due to the generation of new product, 4-aminophenol (Figure 2.18).^[264] AuNP-loaded CCMV was not assembled into a highly ordered structure. Still, the assembly showed feasible properties for SERS and analyte detection and further highlighting the possibility to assemble NP-loaded proteins. Based on these findings, highly ordered assemblies might feature even stronger enhancements.

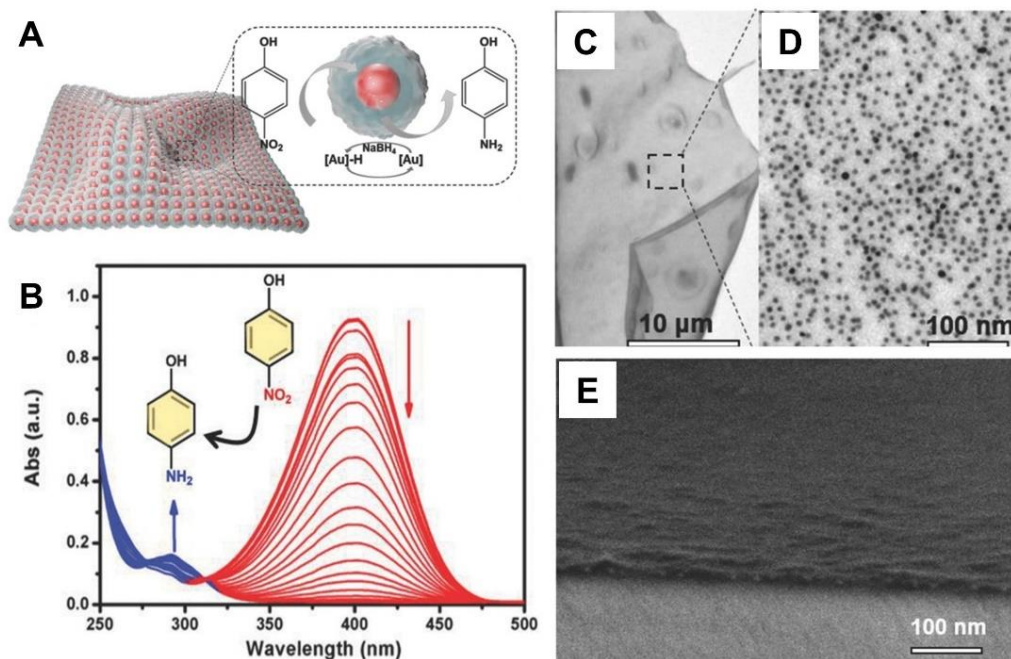


Figure 2.18: Schematic illustration of thin CCMV films loaded with gold nanoparticles and their catalytic activity to reduce 4-nitrophenol. (A) General scheme to highlight the catalyzed reaction of 4-nitrophenol (4-NP) by CCMV-AuNP films. (B) The reduction of 4-NP to 4-aminophenol (4-AP) is monitored through the decrease of the absorption at 400 nm and increase at 292 nm. (C) and (D) Low and high magnification TEM images of CCMV-AuNP films. (E) SEM image of CCMV-AuNP film. Figure adopted from reference CORNELISSEN *et. al*^[264] with permission from John Wiley and Sons, copyright 2018.

Recently, BECK *et. al* assembled redesigned ferritin (Ftn) containers for binary superlattices composed of fluorophores and gold nanoparticles instead of metal oxide nanoparticles (Figure 2.16). In detail, prior to protein crystallization cargo was encapsulated into the protein containers via dis- and reassembly approach. Two oppositely charged Ftn variants were used. Ftn^(neg) was loaded with rhodamine fluorophores (RhFtn^(neg)), while Ftn^(pos) was loaded with gold nanoparticles (AuFtn^(pos)). Additionally, the gold nanoparticle loading was altered to investigate the influence of the amount of gold on the fluorescence lifetime. First, empty crystals, crystals with only one component and binary crystals were examined via confocal microscopy and excitation at 405 nm. Empty protein crystals (eFtn^(pos)/eFtn^(neg)) showed green fluorescence with a maximum at 560 nm (Figure 2.19A, B). The green fluorescence is caused by the cross-linking agent glutaraldehyde^[267], which is used to stabilize the protein crystal. In comparison, crystals loaded with rhodamine B showed strong yellow fluorescence with a maximum at

580 nm (Figure 2.19A, B). $\text{AuFtn}^{(\text{pos})}/\text{eFtn}^{(\text{neg})}$ crystals featured fluorescence around 470 nm. Moreover, the green fluorescence of the glutaraldehyde is not observed, indicating that almost all fluorescence is quenched by AuNPs (Figure 2.19B). In contrast, $\text{AuFtn}^{(\text{pos})}/\text{RhFtn}^{(\text{neg})}$ crystals showed very weak fluorescence, even at higher excitation power. Further investigation was carried out via fluorescence lifetime imaging (FLIM). In comparison between $\text{AuFtn}^{(\text{pos})}/\text{RhFtn}^{(\text{neg})}$ and $\text{eFtn}^{(\text{pos})}/\text{RhFtn}^{(\text{neg})}$ a large decrease in lifetime is observed if AuNPs are present (Figure 2.19C). The decrease in lifetime is caused by the quenching of fluorescence by AuNPs.

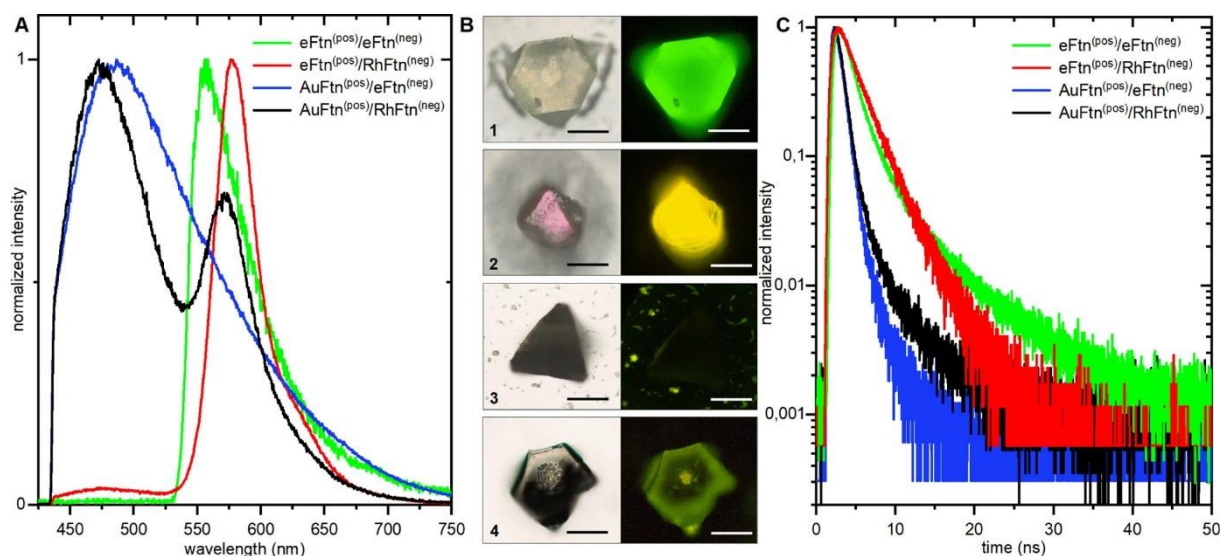


Figure 2.19: Fluorescence spectra, decay curves and images of binary protein crystals. (A) Fluorescence spectra of crystals with empty protein container ($\text{eFtn}^{(\text{pos})}/\text{eFtn}^{(\text{neg})}$), fluorophore filled ($\text{eFtn}^{(\text{pos})}/\text{RhFtn}^{(\text{neg})}$), AuNPs filled ($\text{AuFtn}^{(\text{pos})}/\text{eFtn}^{(\text{neg})}$) and a combination of both cargo ($\text{AuFtn}^{(\text{pos})}/\text{RhFtn}^{(\text{neg})}$). (B) Brightfield (left) and fluorescence (right) microscopy images of empty (1), filled with fluorophore (2) or AuNP (3) and a combination of fluorophore with AuNP (4). Scale bars equal 25 μm . (C): Fluorescence decay curves of the binary protein samples described in A and B. Figure adopted from reference BECK *et. al*^[13] with permission from American Chemical Society, copyright 2022.

In a second experiment by BECK *et. al*, the fluorophore is changed from rhodamine B with an emission maximum at 580 nm to rhodamine 6G with an emission maximum at 550 nm, to achieve a higher spectral overlap between the plasmon band (514 nm). Furthermore, the loading of protein containers was switched. $\text{Ftn}^{(\text{neg})}$ is filled with AuNPs ($\text{AuFtn}^{(\text{neg})}$), while $\text{Ftn}^{(\text{pos})}$ is loaded with rhodamine 6G ($\text{RhFtn}^{(\text{pos})}$). For binary $\text{RhFtn}^{(\text{pos})}/\text{AuFtn}^{(\text{neg})}$ crystals almost no fluorescence was detected (Figure 2.20A). The loss of detected fluorescence is caused by strong interactions between the excitons in rhodamine molecules and plasmon in the AuNPs. For such a substantial drop in fluorescence intensity, the fluorescence lifetime is still significant. Strong non-radiative decay channels in AuNPs dissipate the energy transferred from rhodamine to gold plasmons via exciton-plasmon coupling. Since this interaction is based on AuNPs, the interaction strength of the AuNP density was studied. The gold loading was altered

from 100 to 50, 25, 10 and 0 %. Via confocal FLIM it was possible to investigate the spatial distribution of interaction strength in the RhFtn^(pos)/AuFtn^(neg) crystal with different AuNP loadings (Figure 2.20).^[13]

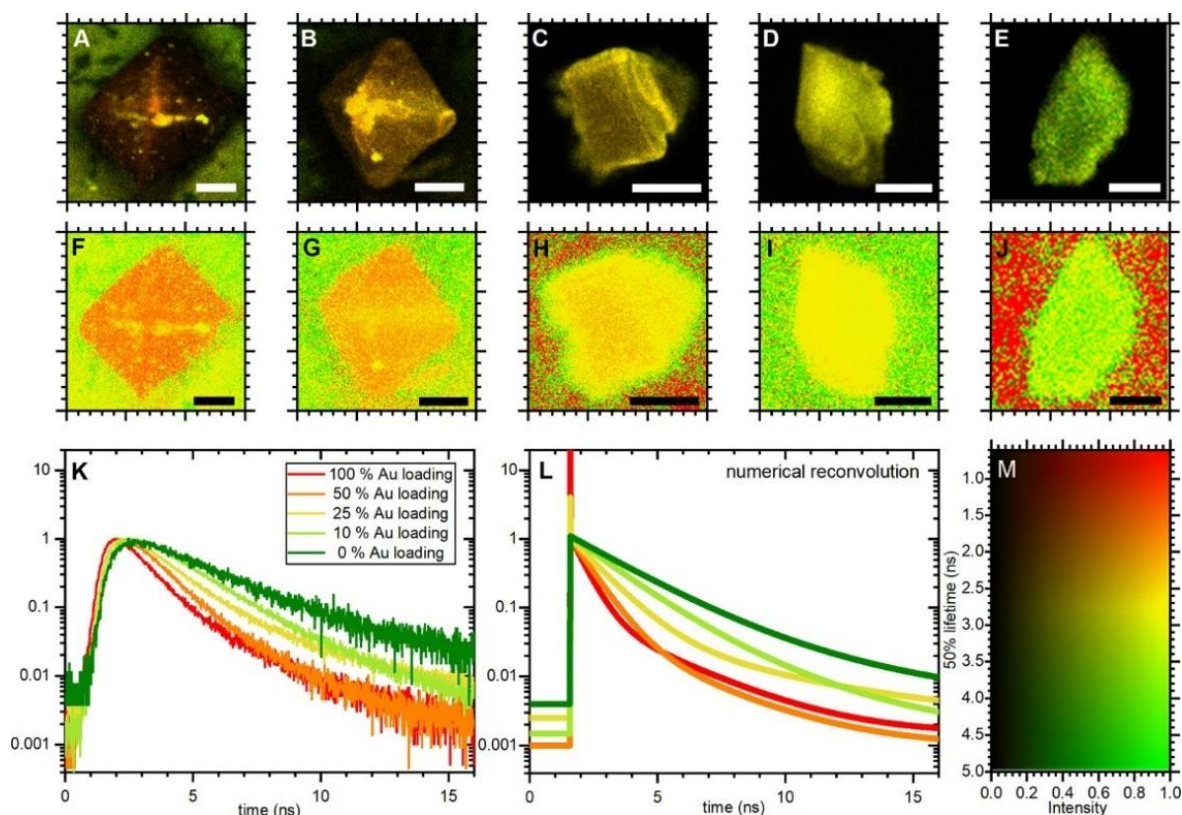


Figure 2.20: Confocal lifetime analysis of binary protein crystals with different AuNP loading. (A) to (E) Confocal fluorescence lifetime images of protein crystals with different AuNP loading. (A) to (E): 100 %, 50 %, 25 %, 10 % and 0 % gold loading. (F) – (J): Confocal fluorescence lifetime images with lifetime contrast of protein crystals visualized in (A) to (E). (K): Fluorescence lifetime decay curves integrated over the protein crystal region for crystals with different AuNP loadings. (L): Theoretical modelling of fluorescence decay curves. Modelled decay curves are obtained by fitting to the experimental data with numerical reconvolution. (M): Color coding for intensities and lifetimes. Scale bars are 25 μm . Figure adopted from reference BECK *et. al*^[13] with permission from American Chemical Society, copyright 2022.

In Figure 2.20A-E, double-encoded images are shown for the different AuNP loadings. Low intensity is indicated by dark areas, whereas bright areas represent high intensity. Additionally, red and green color coding indicate short and long lifetimes, respectively. For each image, the intensity is normalized to their maximum. Protein crystals with the lower AuNP loading (Figure 2.20E) show stronger fluorescence than crystals with higher AuNP loading (Figure 2.20A). In Figure 2.20A, the background fluorescence is visible since the fluorescence of the crystal is almost nonexistent due to quenching. For the crystal with the lowest AuNP concentration (Figure 2.20E), no background fluorescence was visible, due to the strong fluorescence of the crystal in comparison to the background. With a decrease of AuNP loading a decrease in coupling of rhodamine with AuNPs was observed. Interestingly, corners, edges and local spots

featured high emission intensity, while plane facets showed shorter lifetimes (Figure 2.20F-J). One explanation for this is that less AuNPs are coordinated to rhodamine molecules at corners and edges. Moreover, the local coordination of dye molecules within the crystal also changes with altered AuNP concentrations inside the crystal. The effect of the coordination on the fluorescence decay was further investigated by modeling. In the end, it was noted that the fluorophore, in this case the acting dipole, was encapsulated statistically and therefore without a fixed position and orientation. Bringing the excitonic dipole to high-symmetry locations and controlling its orientation was stated as a favorable goal, since both the location and orientation play a significant role for the interaction between dipole and plasmon. Further knowledge about the gold-only superlattice is needed, to understand the plasmon modes of the AuNP superlattice.^[13]

Altogether, protein containers are versatile building blocks. These building blocks can be used for the assembly of nanoparticles or other cargo into binary superlattices. Potential applications such as catalysis, coating of sensitive cargo, fluorescence enhancement or quenching are addressed within the last chapters (2.5.1 and 2.5.2).

3 Basis of the present work

In this chapter, the basis of the present work is presented. Therefore, essential results of the BECK group will be summarized. The main protein scaffold used for the assembly of binary superlattices is the *T. maritima* encapsulin. As already shown in chapter 2.5.3 (Protein container assemblies, Figure 2.16) two oppositely supercharged ferritin protein containers have previously been used as building blocks. To achieve a similar approach with encapsulin, the protein surface of the encapsulin needed a surface redesign. Unpublished work by MATTHIAS KÜNZLE that focused on the surface redesign of the encapsulin container will be discussed in chapter 3.1, since parts of this work are based on these results. The synthesis, ligand exchange and encapsulation of gold nanoparticles from previous publications^[10,13] into protein containers are an important starting point for this thesis. Recent results are highlighted in chapter 3.2. Additionally, the human heavy chain ferritin protein container was used to assemble novel hetero binary protein lattices. In detail, the positively surface charged ferritin was either used loaded with nanoparticles or with fluorophores. The latter one was established for the positively supercharged ferritin in this work, but the design of the novel ferritin variant for fluorophore functionalization was done in unpublished works by HENDRIK BÖHLER and MADE BUDIARTA. The design approach of the novel ferritin variant and how to load nanoparticles into ferritin will be described in chapter 3.3.

3.1 Supercharging of the protein container encapsulin

In early reports of the BECK group, the positively supercharged ferritin Ftn^(pos) was introduced.^[195] The template for surface redesign was a model derived from the crystal structure of the human heavy chain ferritin (PDB: 2CEI). The design was carried out with the *Rosetta molecular modelling software*^[268] and based on a method originally published by MIKLOS *et al.*^[269] Without going into much detail, the procedure for surface redesigning is described. For the surface redesign, a fixed backbone protocol was used. Side chains can be altered without harming structural features of the protein. Only residues on the outer surface were allowed to be mutated. During simulations, the native amino acid, lysine or arginine were allowed. Weights of the energy function for the reference energies of the desired amino acids gradually changed to favor positively charged amino acids. Additionally, the surface redesign was carried out to negatively supercharge the ferritin surface. In this case, instead of lysine or arginine the negatively charged amino acids glutamic and aspartic acid were allowed. These novel ferritin variants were produced, purified and were suitable to be crystallized. The resulting novel protein lattices of high order highlight the success of this procedure (Figure 2.16).^[15]

The same procedure as described above and depicted in Figure 3.1 was carried out by MATTHIAS KÜNZLE for the *T. maritima* wild type encapsulin (Enc^{wt}). As a model, the Enc^{wt} crystal structure was used (PDB: 3DKT). The weights used for the surface charging are listed in the appendix (Table 8.1). Two individual simulations for both negatively and positively supercharged encapsulin (Enc) variants were carried out. The results of these simulations are shown in the appendix (Figure 8.1, Figure 8.2, Figure 8.3 and Figure 8.4).

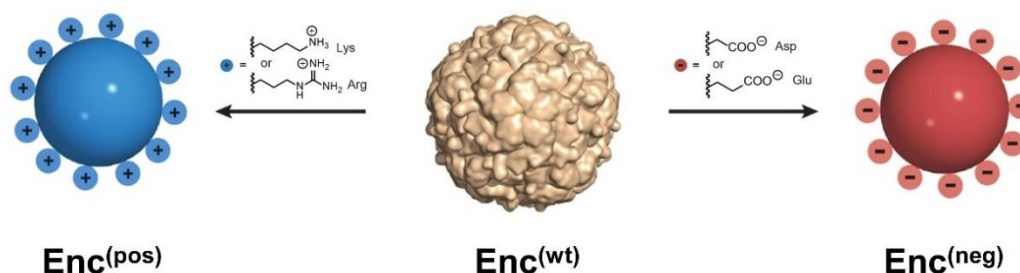


Figure 3.1: Schematic visualization of encapsulin surface supercharging based on the crystal structure model. By either altering the amino acids to lysine (Lys) or arginine (Arg) positively charged residues are introduced. For negatively charged residues aspartic (Asp) or glutamic acid (Glu) are chosen. Enc^{wt} surface model based on crystal structure (PDB: 3DKT). Blue or red indicate positively or negatively supercharged protein containers, respectively.

3.2 Nanoparticle synthesis and encapsulation

The synthesis and encapsulation of AuNPs into Enc^{wt} or supercharged ferritin variant $\text{Ftn}^{\text{(pos)}}$ and $\text{Ftn}^{\text{(neg)}}$ have already been shown by the BECK group.^[10,13] As shown in Figure 2.11 AuNPs can be encapsulated via electrostatic interactions or with higher efficiency into Enc^{wt} supported by a cargo-loading peptide (CLP). In detail, 11 nm or 13 nm large AuNPs were encapsulated into Enc^{wt} . The AuNP loaded protein was purified via size-exclusion chromatography (SEC) and transmission electron microscopy (TEM) images were taken (Figure 3.2).

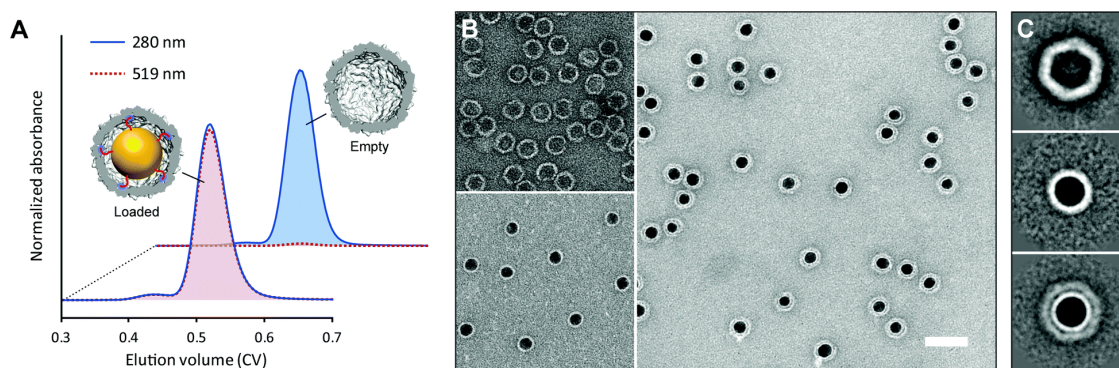


Figure 3.2: Analytical data for the CLP-mediated encapsulation of gold nanoparticles. (A) Size-exclusion chromatogram of empty and gold nanoparticle-loaded encapsulin. Absorbance at 519 nm indicates successful encapsulation. Elution volumes of both samples are nearly the same. (B) Negatively stained TEM images: (top left) empty encapsulin containers; (bottom left) CLP-functionalized gold nanoparticles with visible ligand shell; (right)

Encapsulated gold nanoparticles. Scale bar is 50 nm. (C) Class-averages of empty encapsulin containers (top), gold nanoparticles (middle) and AuNP-loaded encapsulin containers (bottom). Figure adopted from reference BECK *et. al.*^[10] with permission from Royal Society of Chemistry, copyright 2009.

Furthermore, smaller AuNPs of around 3 nm were encapsulated into supercharged Ftn variants. The nanoparticle loaded protein containers were also purified, but in this case via ion-exchange chromatography (IEC) to separate free AuNPs from the protein containers. The encapsulation of AuNPs into supercharged Ftn variants is not based on a CLP encapsulation approach, but on electrostatic interactions.^[13]

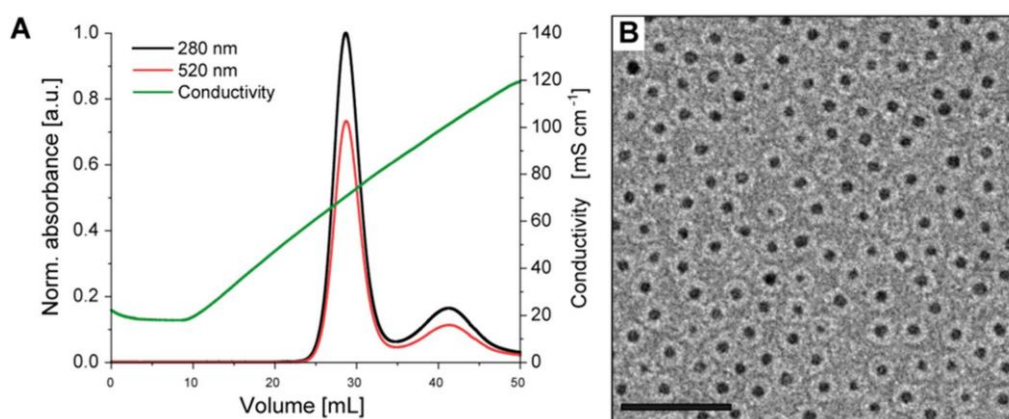


Figure 3.3: Purification and TEM images of gold nanoparticle-loaded ferritin. (A) Ion-exchange chromatogram of AuNP loaded ferritin. Absorbance at 520 nm indicates the presence of gold nanoparticles. (B) TEM image to visualize gold nanoparticle loaded protein containers. Scale bar is 50 nm. Figure adopted from reference BECK *et. al.*^[13] with permission from American Chemical Society, copyright 2022.

3.3 Positively charged ferritin variant

As mentioned in chapter 3.1 the BECK group has already established supercharged Ftn variants. In a recent publication, the encapsulation of fluorophores into both, Ftn^(pos) and Ftn^(neg) was established. In detail, the encapsulation of fluorophores into Ftn^(pos) was performed by diffusion through pores. On the other hand, fluorophores were encapsulated by chemical conjugation into Ftn^(neg). The basic idea was to conjugate a fluorophore on the inner surface. Therefore, two mutations were carried out. First, a surface exposed cysteine (Cys) residue at position 130 was mutated to alanine (C130A). Otherwise, this Cys residue would be accessible for fluorophore labeling. Additionally, position 130 is close to the pore along the three-fold axis. Based on symmetry, three fluorophores would be very close together and might quench each other.^[270] Labeling the protein at this point might influence the container stability since it is close to the protein-protein interface. Secondly, a cysteine residue was introduced at position 53 (K53C). The native lysine (Lys) was determined to be very solvent accessible. For each amino acid at the inner surface the *GetArea*^[271] software was used to differentiate between buried and accessible amino acids. The software compares the accessibility of a single amino acid of

a protein by setting up a theoretical tripeptide. The tripeptide starts and ends with glycine (Gly) while the amino acid of interest (X) is in the middle (Gly-X-Gly). A specific solvent accessible surface area is calculated for each amino acid and listed as a value in percentage. Based on these results, lysine at position 53 was chosen, since it was the most solvent accessible amino acid at the inner surface. The resulting $\text{Ftn}^{(\text{neg})}$ with additional cysteine ($\text{Ftn}^{(\text{neg})}\text{-Cys}$) was successfully labeled with several fluorophores.^[12] In detail, the protein is first disassembled and then labeled. Afterwards the reassembly was triggered, and the protein purified. Unpublished work by MADE BUDIARTA focused on the addition of the K53C mutation in $\text{Ftn}^{(\text{pos})}$ to create $\text{Ftn}^{(\text{pos})}\text{-Cys}$. The primer design and mutagenesis were carried out (Table 8.3), but no labeling with high efficiency was achieved before this work.

In chapter 2.4, it was briefly mentioned that protein containers can be applied as a template for nanoparticle synthesis. The BECK group has already published work, in which cerium oxide nanoparticles and magnetic iron oxide nanoparticles were synthesized inside supercharged ferritin variants. Ions or small molecules diffuse through the protein pores and nanoparticles can be synthesized inside the protein container (Figure 3.4A). Since the protein cavity has a defined size, the maximum nanoparticle size is limited to the cavity size. Protein containers loaded with metal oxide nanoparticles can still be crystallized into highly ordered protein lattices (Figure 3.4B).^[205] For the assembly of novel binary protein lattices, cerium oxide and iron oxide nanoparticle-loaded $\text{Ftn}^{(\text{pos})}$ samples were kindly provided by MARCEL LACH.

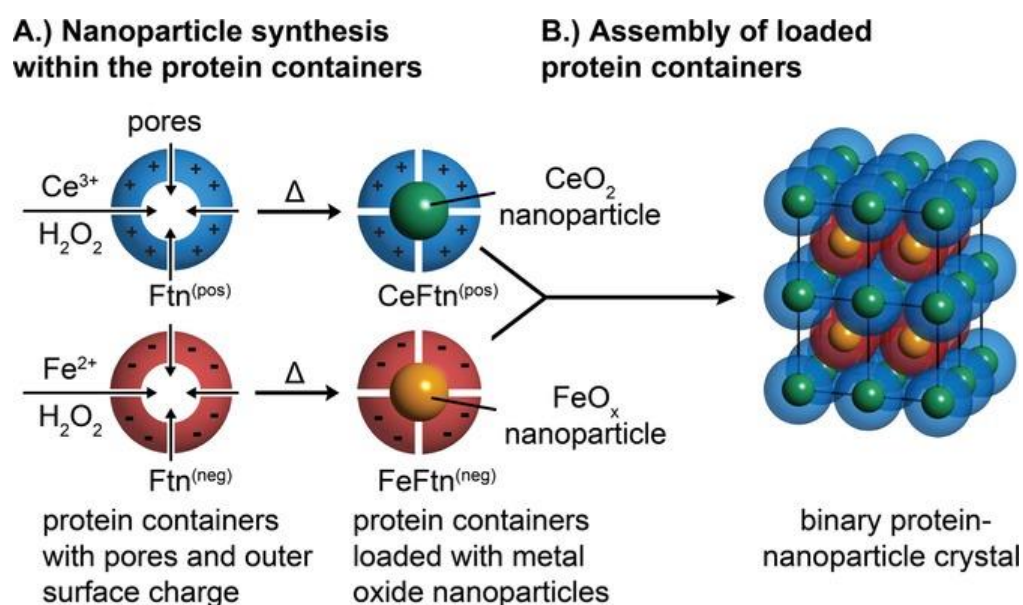


Figure 3.4: General strategy for the assembly of binary metal oxide nanoparticle-loaded protein crystals. (A) Nanoparticle synthesis is carried out inside the ferritin container. Ions and small molecules diffuse through the protein pores. (B) Nanoparticle-loaded protein containers form highly ordered binary nanoparticle superlattices. Figure adopted from reference BECK *et. al.*^[205] with permission from John Wiley and Sons, copyright 2017.

4 Concept and aim of this thesis

The overall aim of this thesis is the assembly of novel binary superlattices and their characterization towards application. For this approach, the *T. maritima* encapsulin container is used as a main building block. As described in detail in chapter 2.4.1.1, the *T. maritima* encapsulin container is 24 nm in diameter and features a 20 nm large cavity. The protein container has gained interest as a template for nanoparticle synthesis inside the cavity^[222] or a modular platform for tagging on the outer surface^[272]. The BECK group has already established the encapsulation of gold nanoparticles into the wild type encapsulin Enc^(wt).^[10] Gold nanoparticles are not only used for catalysis.^[273] Moreover, they are favored for their plasmonic properties.^[118] As discussed in the theoretical background, applications such as SERS are under research (chapter 2.1.2).^[25] Therefore, one goal was to establish the crystallization of first empty and then AuNP-loaded encapsulin to create highly structured plasmonic biohybrid materials. Initial investigations will be evaluated to discuss the feasibility of these plasmonic biohybrid materials for SERS.

To create a binary encapsulin protein crystal, supercharged encapsulin variants will be investigated. A binary protein crystal allows for the implementation of a second kind of cargo. Different combinations are theoretically possible, like AuNPs in both Enc^(neg) and Enc^(pos) or AuNPs in Enc^(pos) and a new kind of cargo in Enc^(neg). The general strategy for the assembly of binary protein crystals is based on two oppositely charged protein containers as building blocks for the assembly. In detail, the strategy can be subdivided into three sections (Figure 4.1). First, the surface redesign of the protein container is carried out. In a second step, nanoparticles such as AuNPs or QDs are encapsulated in one supercharged protein variant. Now, the protein container is the atomically defined ligand shell. These protein containers are then assembled via protein crystallization. In the end, the goal is to build highly structured optical nanomaterials with desired properties such as plasmon coupling or energy transfer between nanoparticles.

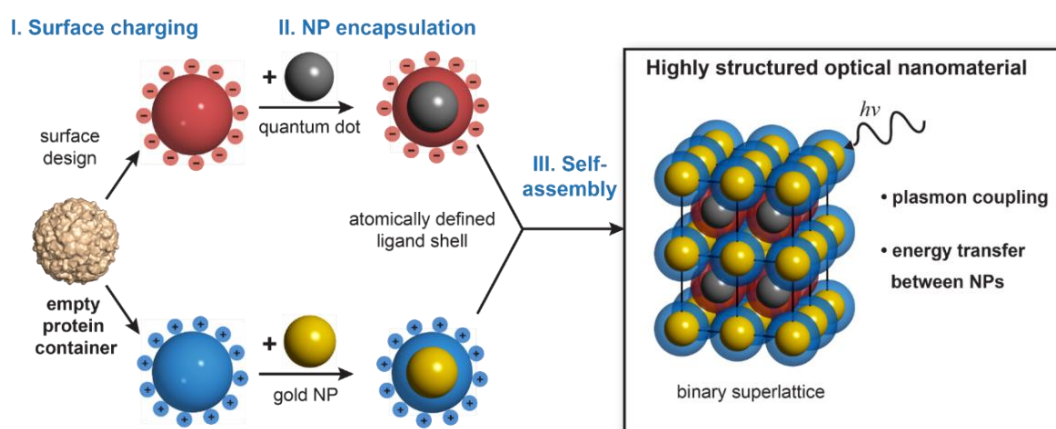


Figure 4.1: Schematic overview of the fabrication of nanomaterials composed of gold nanoparticles and quantum dots.

An additional cargo of interest are semiconductor nanoparticles. In detail, giant core/shell quantum dots (gQDs) were chosen due to their high photostability and quantum yield.^[171] Moreover, these gQDs offer a similar size to the already established AuNPs and possible compatibility to the AuNP ligand system based on thiols as anchoring group. For single particles, it is already known that decay rates and corresponding quantum efficiencies can be influenced by exciton-plasmon interactions.^[274] Interactions between a fluorescent (QD) and plasmonic material (AuNP) might demonstrate novel optical effects mediated by collective contributions of particles in lattices. In literature, binary superlattices from AuNPs and QDs were achieved e.g. via DNA-based assembly.^[275] These established DNA-based assemblies are sensitive against heating and not suitable for applications with elevated temperatures, since these small DNA-linkers have a specific melting temperature starting at around 50 °C. Additionally, DNA-linkage is easily disrupted by the influence of salt and shows stability issues under certain conditions.^[276,277] The encapsulin protein container is not only extremely thermostable but also stable against strong changes in salt concentrations.^[217,225] Therefore, the encapsulin container was aimed to as a novel building block to create stable binary superlattices composed of QDs and AuNPs. As already shown, ferritin can be used as building blocks for the assembly of binary nanoparticle superlattices.^[205] As a first step towards this goal, the encapsulation of gQDs into the encapsulin container was investigated.

An alternative approach based on binary protein crystals composed of plasmonic AuNPs and fluorophores instead of quantum dots was applied. An already established system of the BECK group based on protein containers with fluorophores and plasmonic AuNPs was already described in chapter 2.5.3. The system previously used by the BECK group was based on Ftn samples, in which the fluorophores were encapsulated either by dis- and reassembly or via diffusion through pores. Both methods lead to a statistic encapsulation of fluorophores without fixed orientation or position. Fixed orientation and position of fluorophores are desired since the coupling in the system is based between dipoles and plasmons. The dipole-dipole interaction, even in a highly ordered system, might play a significant role.^[11,278] In this work, the establishment of a positively supercharged ferritin Ftn^(pos) that is capable of acting as a template to fix various fluorophores in an ordered fashion will be analyzed. In addition, this ferritin variant was suitable for the assembly of novel binary protein crystals composed of fluorophores and plasmonic gold nanoparticles. To study the optical properties, confocal lifetime imaging will be utilized.

5 Results

The results are based on protein container nanomaterials loaded with non-native cargo or further modifications on either the outer or inner surface. For the assembly, supercharged protein containers are used. The structural and functional characterizations of these materials are described. This chapter can be subdivided into three parts. The first part includes the generation of novel protein building blocks (chapter 5.1). In the second part, the encapsulation of cargo into these protein containers is discussed. Moreover, the functionalization of the inner surface of protein containers with fluorophores is addressed (chapter 5.2). After presenting these building blocks with cargo inside, the proteins were assembled via protein crystallization to fabricate biohybrid nanomaterials (chapter 5.3). This chapter also discusses the structural characterization of nanoparticle loaded protein crystals followed by a discussion on optical properties of novel biohybrid assemblies based on initial results.

5.1 Generation of novel protein building blocks

For the overall aim to create novel protein assemblies, the corresponding buildings blocks need to be designed. First, the previously simulated data for the supercharging of the *T. maritima* encapsulin by MATTHIAS KÜNZLE were analyzed. Based on the analyzed data, mutagenesis of the wild type encapsulin Enc^(wt) was carried out. In the beginning of this work, several experiments were carried out with encapsulin variants featuring a flavin attached to the outer surface. At a certain point in time, researchers published an approach to remove the flavin, which was adapted for this work.^[219] Therefore, some protocols initially established for proteins with flavin were adapted to protein variants without flavin without any problems. Moreover, the positively supercharged ferritin variant with additional cysteine Ftn^(pos)-Cys was added as a new building block. Consequently, all these proteins were produced, purified and characterized.

5.1.1 Supercharging of *T. maritima* encapsulin

In order to achieve a binary protein crystal, the protein's outer surface needs to be supercharged: one variant with positive and one with negative surface charge. The general procedure of the redesign is described in chapter 3.1. The simulation results are shown in the appendix (Figure 8.1 to Figure 8.4). *Rosetta* simulations were carried out to determine at which positions mutations to positively charged amino acids are favored. As an input, the encapsulin crystal structure (PDB: 3DKT) and the protein sequence (Table 8.5) was provided. Some mutations already appear in early runs, indicating that these mutations are energetically favored. A mutation appearing in a later run does not mean that this position should not be

mutated. Rather, this is an indication that a higher 'weight' value (Table 8.1) is required and results in overwriting other interactions in *Rosetta*. After several runs, it was observed that with a higher change in energy, the suggested amino acid might change e.g. from lysine (K) to arginine (R) or glutamic (E) to aspartic acid (D). In such a case, the first suggested amino acid is chosen since this amino acid was already energetically favored at a lower change in energy. Suitable positions for the supercharging are listed in Table 8.2.

Only relying on a computational approach and introducing all suggested mutations might lead to a completely unstable protein that cannot be produced at all. Some native amino acids might be involved in intramolecular interactions which should not be harmed. For charging the outer surface, mainly oppositely charged amino acids should be considered, since a change from e.g. a negative to a positive residue has a higher impact on the surface charge compared to a change of an uncharged residue. Additionally, it was avoided to introduce too many mutations in one area, because the surface charge should be well distributed over the container surface. These aspects were considered for choosing final positions to mutate.

First, the electrostatic potential for the wild type encapsulin was analyzed. Since Enc^(wt) is already negatively charged, only the results for the design of the positively charged Enc were processed. The final chosen positions are highlighted blue in Table 8.2. As introduced in chapter 2.4.1.1, encapsulin is a protein container consisting of 60 subunits. Therefore, seven mutations per subunit lead to a total change of 420 amino acids on the outer surface. One additional mutation at position 90 was introduced into both variants (chapter 5.1.2.2). The electrostatic surface potential of novel encapsulin variants described in this work are shown in Figure 5.1.

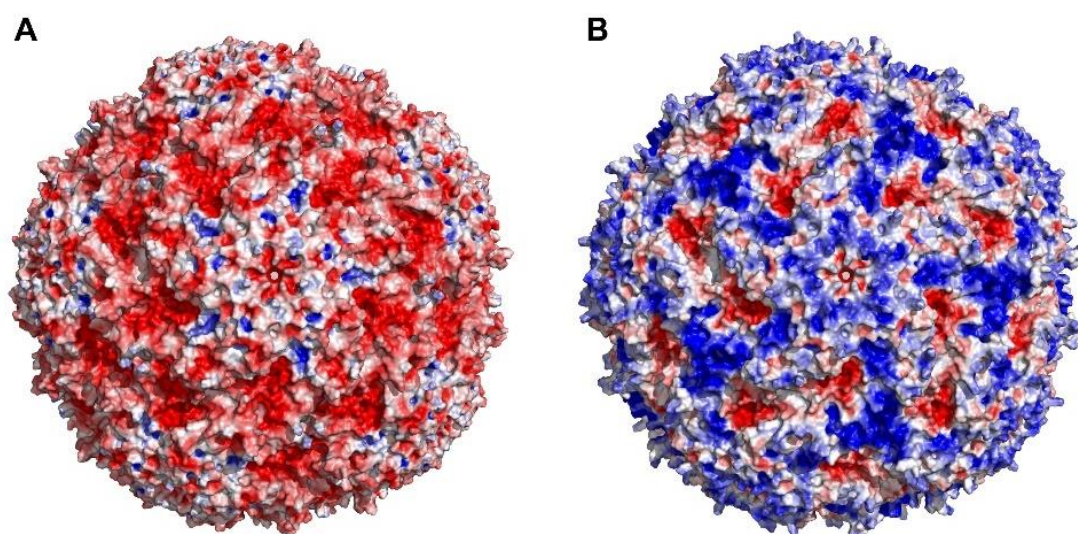


Figure 5.1: Electrostatic surface potential of oppositely charged Enc variants. Negative (A) and positive Enc (B) containers. The surface charge was increased by replacing amino acids on the outer surface. Colors are from red (-5 kT/e) to blue (+5 kT/e).

5.1.2 Site-directed mutagenesis of the protein container encapsulin

For the implementation of mutations based on *Rosetta* calculations, primers for site-directed mutagenesis were designed. A primer is a short nucleic base sequence that provides a starting point for DNA synthesis. Without going into detail, primers were designed according to the *QuikChange* protocol's requirements. A minimal GC content of 40 %, primer length between 25 to 45 bases, the desired mutation in the middle of the primer, a melting temperature ≥ 78 °C and the primer should terminate in one or more G or C bases. The designed primers were synthesized by *Eurofins Genomics*. The purchased primers were used in a *QuikChange* two-step PCR^[279] established within the BECK group. The complete polymerase chain reaction (PCR) protocol is shown in Table 7.3.

5.1.2.1 Mutagenesis to supercharge encapsulin

As shown in Table 8.2, seven positions were chosen to positively supercharge encapsulin. Each mutation was carried out one by one. Therefore, several sequential PCR runs were performed. After performing individual PCR runs, the sequence of the gene was sequenced to verify the introduction of the mutation. The sequence of the final positively charged encapsulin gene variant featuring seven mutations is aligned with the $\text{Enc}^{(\text{wt})}$ genetic sequence in Figure 8.5.

5.1.2.2 Elimination of flavin binding-site

In chapter 2.4.1.1, structural features of the $\text{Enc}^{(\text{wt})}$ are described in-depth. In cryo-EM structures of two concurrent structural studies, the flavin binding site was determined at the tryptophan (Trp/W) at position 90 (W90).^[219,224] To remove the binding site, SAVAGE *et al.* mutated W90 to alanine (W90A) or glutamic acid (W90E).^[219] Both mutations were carried out in this work on $\text{Enc}^{(\text{wt})}$ since the flavin adds an absorption at around 450 nm to the protein sample. This additional absorption is not desired due to the fact that the protein will be used for the assembly of binary materials with optical properties. Any additional molecule that absorbs or shows fluorescence is not desired in such a material. In conclusion, the flavin binding-site must be removed for the positively charged encapsulin variant. W90 was not only mutated to alanine, but also to arginine to introduce an additional positive charge on the outer surface. Mutagenesis on both protein genes were carried out. The sequence was verified by genetic sequencing. For further clearance, these protein variants will be named differently, as listed in Table 5.1. The verified sequences are aligned in Figure 8.6 and Figure 8.5.

Table 5.1: Overview of protein variants with or without flavin binding-site with their corresponding names.

Protein	Mutations
Enc ^(wt)	-
Enc ^(neg)	W90E
Enc ^(neg) -Ala	W90A
Enc ^(pos) -Fla	D63K+T86R+E116R+E127K+E143K+E186K+E241R
Enc ^(pos)	D63K+T86R+W90R+E116R+E127K+E143K+E186K+E241R
Enc ^(pos) -Ala	D63K+T86R+W90A+E116R+E127K+E143K+E186K+E241R

5.1.3 Production and purification of encapsulin variants

The introduced proteins with a negative surface charge from previous chapters were produced based on an adapted protocol published by the BECK group.^[10] The protocol had to be adjusted to establish the production of positively charged encapsulin variants. The detailed protocols are described in chapter 7.7.2. In general, *E. coli* strain C43(DE3) was chosen as expression host. Protein expression was induced by the addition of isopropyl- β -D-1-thiogalactopyranoside (IPTG) to the culture medium.

5.1.3.1 Production and purification of negatively charged encapsulin variants

Cells containing the plasmid with the Enc^(wt), Enc^(neg) or Enc^(neg)-Ala gene were grown according to an established protocol, summarized in chapter 7.7.2.1.^[280] The purification of negatively charged encapsulin variants was carried out using established protocols with minor changes. Residual proteins or impurities from production are removed via ion-exchange chromatography (IEC). Afterwards, the SEC is carried out to separate aggregated from pure protein.

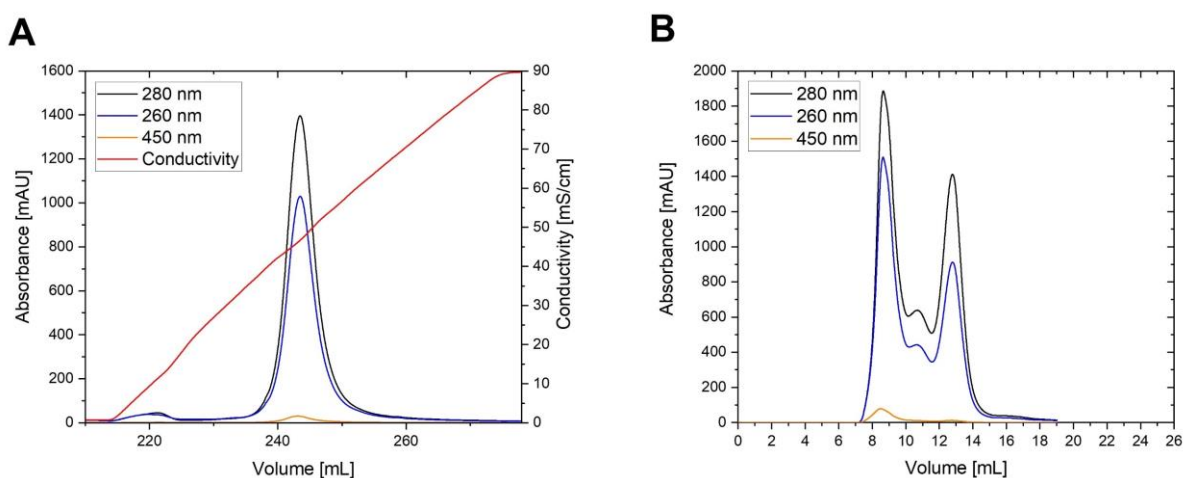


Figure 5.2: Ion-exchange and size-exclusion chromatograms for negatively surface charged encapsulin. (A) IEC chromatogram for Enc^(neg). Protein elution at 46 mS/cm. (B) SEC chromatogram for Enc^(neg). Absorbance was monitored at 280 nm (black), 260 nm (blue) and 450 nm (orange). Conductivity is shown in red.

Exemplary IEC and SEC chromatograms for Enc^(neg) are shown in Figure 5.2. Chromatograms for Enc^(wt) and Enc^(neg)-Ala are shown in the appendix (Figure 8.10 and Figure 8.11). In IEC, negatively surface charged Enc elutes at 46 mS/cm. In SEC, larger species elute at small elution volumes. In this case, an elution at 8.2 mL indicates the elution of protein aggregates, while at 12.8 mL pure protein containers are expected (Figure 5.2B). To achieve a sample that contains almost no aggregates and is suitable for e.g. protein crystallization, the protein purification was optimized. Usually, only MgCl₂ as supplement is used for purification, but here additional CaCl₂ is added to the solution after cell lysis. Mg²⁺ and Ca²⁺ ions act as stabilizers and enhancer for DNase activity.^[281,282] Both bivalent ions may not only support the enzymatic process, but also bind residual nucleic acids. Still, too high concentrations of ions may decrease the digestion efficiency. The effect of both bivalent ions in previous purification steps can be observed in SEC (Figure 5.3A). The optimized protocol leads to a decrease of protein aggregates (8.2 mL). To remove residual aggregates two additional SEC runs are carried out. The effect of the removal of residual aggregates is shown in Figure 5.3B. Nevertheless, an improvement could be observed and more experiments must be done to investigate the influence of both ions to further improve the purification.

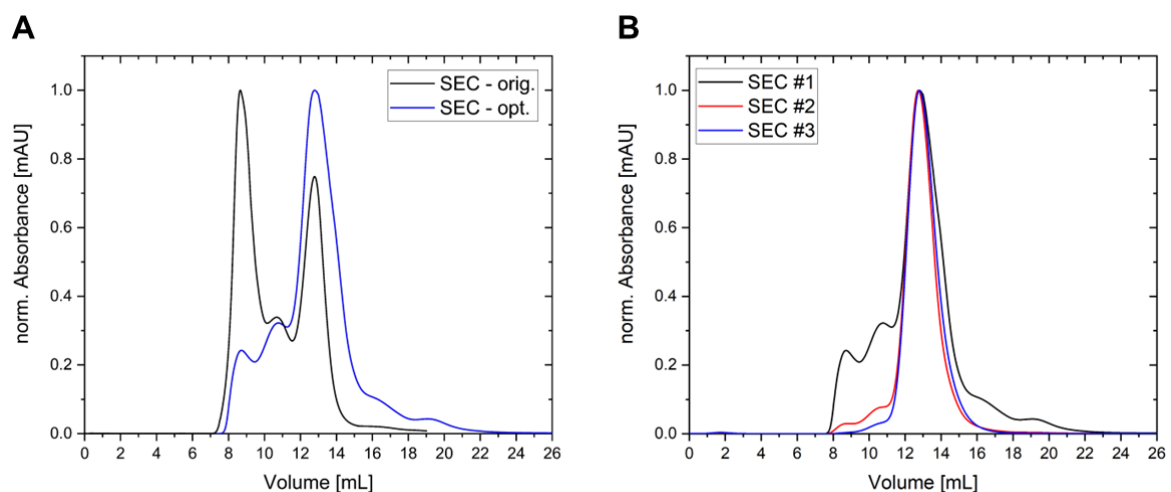


Figure 5.3: Overlay of three subsequent SECs of Enc^(neg). (A) Comparison between two SEC runs based on either the original purification protocol (SEC - orig.) or the optimized protocol containing bivalent ions (SEC - opt.) (B) The first SEC run is shown in black, the second in red and the third run in blue. Absorbance was measured at 280 nm.

The purified protein variants were characterized by several methods to verify the successful production of the proper protein container. Since the Enc^(wt) was already characterized in detail in literature^[10,217], the focus is laid on the novel negatively supercharged protein variants, especially Enc^(neg). The proteins only differ in the mutation at position 90. Typically, a sodium dodecyl sulfate polyacrylamide gel electrophoresis (SDS-PAGE) is carried out to prove if protein of the right mass is produced. SDS gel with Enc^(neg) and Enc^(neg)-Ala is shown in the appendix (Figure 8.7). In both cases, a protein with a mass below 34000 Da was detected. Since SDS gels does not feature such a high resolution, small differences and exact masses

cannot be detected. Nevertheless, the production and purification of the correct protein was verified.

To verify the purification of the correct protein with higher accuracy Electrospray ionization (ESI) mass spectrometry (MS) was used. The calculated molecular masses determined via MS are listed in Table 5.2. Corresponding MS-spectra can be found in the appendix (Figure 8.8). The molecular masses based on ESI-MS fit very well with the calculated numbers.

Table 5.2: Molecular mass determined via ESI MS for negatively supercharged encapsulin variants.

Molecular mass [g/mol]	Enc ^(neg)	Enc ^(neg) -Ala
Calculated	30765.18	30707.14
ESI	30764.76	30707.04

The MS results verify the production of the proper protein, while the SEC (Figure 5.2B) already indicates the formation of a protein container at an elution volume typical for the already established Enc^(wt) container. TEM is used to visualize the protein container. Negatively stained TEM images of Enc^(neg) are shown in Figure 5.4A. TEM images of Enc^(neg)-Ala are found in the appendix (Figure 8.9). The container size was determined via *ImageJ* and visualized in the corresponding histogram (Figure 5.4B). A size distribution of 23.99 nm with a standard deviation of 0.86 nm was determined. This value fits very well with the diameter of wild type encapsulin of around 24 nm.

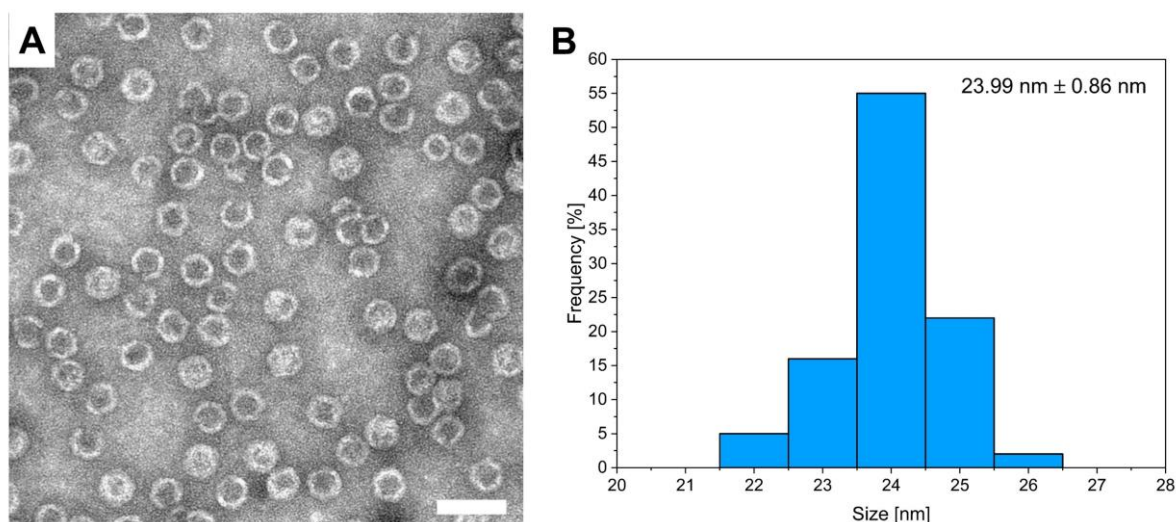


Figure 5.4: TEM images of Enc^(neg) and corresponding histogram with size distribution. (A) Negative stained TEM image of Enc^(neg). Scale bar is 50 nm. (B) Histogram and size distribution with standard deviation for Enc^(neg). 100 protein containers were measured to determine size distribution.

Dynamic light scattering (DLS) was carried out to determine the hydrodynamic diameter of the protein container. As described in chapter 7.4.7, for each sample two measurements with three runs each were performed at 20 °C. Additionally, the surface ζ -potential of the protein samples

was determined. These measurements were carried out at 25 °C. Both proteins were measured in a 10 mM phosphate pH 6.0 buffer. The data is shown Table 5.3.

Table 5.3: Hydrodynamic diameters and ζ -potential of negative encapsulin variants.

Sample	D _{DLS} [nm]	PDI	ζ -potential [mV]
Enc ^(wt)	28.17	0.167	- 28.60
Enc ^(neg)	24.04	0.039	- 24.50

In this case, only Enc^(wt) and Enc^(neg) were compared because the wild type features the flavin on the outer surface, which might influence the ζ -potential and hydrodynamic diameter. Interestingly, in the same condition the ζ -potential is around 4 mV more negative for Enc^(wt). The surface bound flavin probably causes this increased value. The flavin backbone is bound to the surface tryptophan and only the side chain might affect the ζ -potential. Flavin mononucleotide features a side chain with several hydroxy groups and a phosphate head group, which might add additional negative charge to the outer Enc^(wt) surface. The riboflavin side chain lacks a phosphate group and mostly consists of hydroxy groups (Figure 5.7). Via DLS the hydrodynamic diameters for encapsulin samples could be determined. A size of 24.04 nm for Enc^(neg) fits very well to the TEM based value of 23.99 nm (Figure 5.4B). On the other hand, a size of around 28 nm for Enc^(wt) deviates strongly in comparison to Enc^(neg). A PDI of 0.167 indicates a less monodisperse sample. Values below 0.1 are expected for protein samples, since protein containers are identical to each other without change in size or shape resulting in very monodisperse samples. In this case, Enc^(wt) either does not seem to be as stable as Enc^(neg) in 10 mM phosphate buffer pH 6.0 or the sample investigated contained smaller protein agglomerates which were not completely removed via protein purification. Moreover, the influence of the surface bound flavin must not be disregarded and is most likely responsible for the observed deviation in size and PDI.

In conclusion, novel negatively charged encapsulin variants without flavin attached to the outer surface were designed, purified and characterized.

5.1.3.2 Production and purification of positively charged encapsulin variants

For negative Enc variants the production is carried out at 37 °C. In early experiments, the production of positive Enc variants was also done at 37 °C, but almost no protein was purified (data not shown). Consequently, a first step to improve protein yield was to change the temperature. A decrease in temperature goes along with a decrease of protein expression. The decrease to lower temperatures facilitates the production of folded, soluble protein.^[283] In this case, the temperature was decreased to 18 °C. To overcome the reduced protein

expression the time for protein production was increased from several hours to days (chapter 7.7.2.2). With this novel protocol, it was possible to produce positively charged encapsulin in high yield.

As described in the following section, several parameters of the Enc^(neg) protocol were adjusted to establish the purification of novel positive Enc variants. To a certain extent, some knowledge of purifying positively supercharged Ftn was transferred. Ftn^(pos) is purified at a pH value of 6, while negative Enc and Ftn variants are purified at a pH value of 9. Therefore, the pH for the positive Enc purification was changed to 6. Due to the more acidic pH, Enc^(pos) becomes more positively charged and the binding strength to ion exchange column is increased. Typically, Ftn^(pos) is purified with a buffer containing 1 M NaCl in comparison to 0.15 M used for negative Enc variants. The high amount of salt is necessary to keep the positive Ftn in solution. Otherwise, interactions between negatively charged RNA and DNA with the positively charged protein container are not prevented. Subsequently, the purification of positive Enc was directly carried out in a buffer with high NaCl concentration. Moreover, the purification of Ftn^(pos) is carried out with RNase only, while for negative Enc variants DNase and RNase are feasible. DNase is excluded since DNA is digested into smaller negatively charged parts which might be small enough to stick to the positive container surface. Larger negatively charged constructs are easier to remove than smaller molecules directly attached to the surface. To summarize, a purification at pH = 6 with RNase only and high salt concentration was chosen. The final protocol to purify positive Enc variants is described in detail in chapter 7.7.2.2.

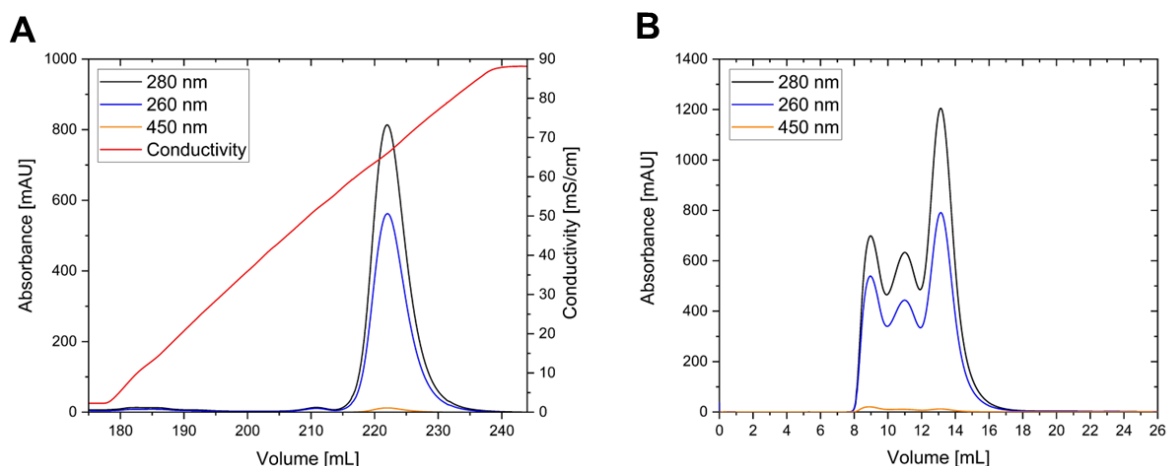


Figure 5.5: Ion-exchange and size-exclusion chromatograms for positively surface charged encapsulin. (A) IEC chromatogram for Enc^(pos). Protein elution at 65 mS/cm. (B) SEC chromatogram for Enc^(pos). Absorbance was monitored at 280 nm (black), 260 nm (blue) and 450 nm (orange). Conductivity is shown in red.

For the new purification process, also the IEC and SEC were adjusted for positive encapsulin. Both methods were carried out to remove residual proteins or impurities from production and larger protein aggregates. IEC and SEC chromatograms for Enc^(pos) are shown in Figure 5.5. Positively supercharged Enc elutes at 65 mS/cm. The protein specific elution volume for SEC

is 12.9 mL. In comparison, the elution volume for Enc^(neg) is 12.8 mL (Figure 5.2). The elution volume of Enc^(pos) indicates no significant change in size. Chromatograms for Enc^(pos)-Fla and Enc^(pos)-Ala are found in the appendix (Figure 8.13 and Figure 8.12).

Purified Enc^(pos) variants were characterized by the same techniques as mentioned for Enc^(neg) variants. The proteins listed in Table 5.4 only differ in one single mutation at position 90, as discussed earlier (Table 5.1). Prior to further characterization, gel electrophoresis was carried out. For all three protein variants, bands at the expected range can be seen in the SDS gel (Figure 8.7). In detail, the protein bands are at the same level as for negative Enc variants and indicate the purification of a protein in the same mass range. Since SDS gels lack in higher resolution, ESI MS was carried out (Figure 8.8). In Table 5.4 the measured molecular masses are given. Via ESI MS, the molecular masses of Enc^(pos) and Enc^(pos)-Ala were determined very accurately. Surprisingly, it was not possible to access the molecular mass of Enc^(pos)-Fla via ESI MS. A less ionizable protein is less likely, because other Enc variants could be characterized via ESI. Insufficient sample preparation or residual salt in solution might be the reason for unsuccessful ionization in ESI. As seen for Enc^(neg) variants, ESI-MS results in molecular masses very similar to the expected mass.

Table 5.4: Molecular masses determined via ESI MS for positively supercharged encapsulin variants.

Molecular masses [g/mol]	Enc ^(pos)	Enc ^(pos) -Ala	Enc ^(pos) -Fla
Calculated	30911.74	30825.69	30941.76
ESI	30910.32	30826.19	-

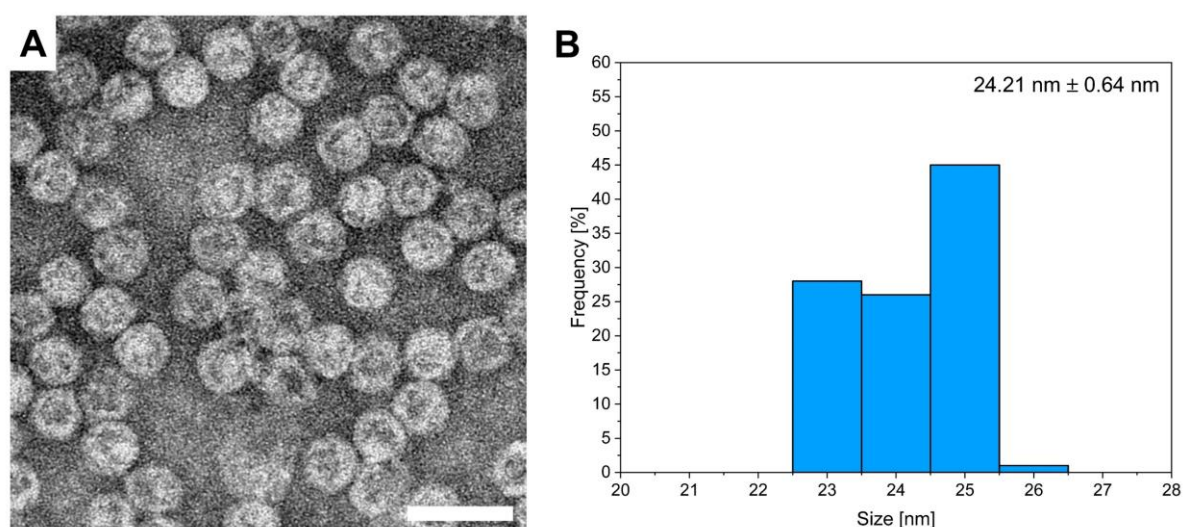


Figure 5.6: TEM images of Enc^(pos) and corresponding histogram with size distribution. (A) Negative stained TEM image of Enc^(pos). Scale bar is 50 nm. (B) Histogram and size distribution with standard deviation for Enc^(pos). 100 protein containers were measured to determine size distribution.

Via MS the production of the proper protein is verified. The following step is to check if the protein subunits form a fully assembled container. In Figure 5.6A negatively stained TEM images are shown. Spherical structures can be observed and confirm an assembled protein container. Due to a staining or imaging artefact, some protein containers appear to be filled, but in several TEM images such artefact is observed either strong or weak (Figure 5.4, Figure 5.12). In a second step, the protein containers are measured to determine a size distribution. For Enc^(pos), a size distribution of 24.21 nm with a standard deviation of 0.64 nm is found. This size distribution features no significant deviation to neither the reported size of Enc^(wt) nor Enc^(neg) with around 24 nm. In fact, Enc^(pos) seems to be larger with 24.21 nm than Enc^(neg) with 23.99 nm, but the container size was measured by hand via *ImageJ*. Since protein containers do not yield a high contrast in negative stained TEM images, it is currently not possible to automatically process these images with higher precision.

For further characterization, DLS and ζ -potential measurements were carried out. The results are listed in Table 5.5. In this case, two positively supercharged protein variants are compared with each other. In detail, the positive Enc variants with flavin (Enc^(pos)-Fla) and without flavin (Enc^(pos)) are compared. To compare the ζ -potential of two oppositely charged protein variants Enc^(neg) is listed.

Table 5.5: Hydrodynamic diameters and ζ -potential of positive encapsulin variants. For comparison between oppositely charged variants Enc^(neg) is listed.

Sample	D _{DLS} [nm]	PDI	ζ -potential [mV]
Enc ^(pos) -Fla	25.45	0.031	-
Enc ^(pos)	27.23	0.026	19.30
Enc ^(neg)	24.04	0.039	- 24.50

The hydrodynamic diameter for Enc^(pos) is significantly larger than for Enc^(pos)-Fla. Despite the deviation, in both cases a low PDI is achieved and indicates monodisperse samples. One reason for a larger D_{DLS} value might be caused by residual salt in the solution. The salt concentration has a sizeable impact on the hydrodynamic diameter. In theory, with higher salt concentration a greater extent of charged ions bind to the protein surface resulting in more arranged water molecules around the protein surface and larger hydrodynamic diameters. Typically, positive Enc variants are stored in a buffer containing 1 M NaCl. Residual salt might not have been properly removed and causes a larger diameter in DLS. After all, the actual protein diameter is determined via TEM (Figure 5.6), while DLS determines the hydrodynamic diameter in solution. The ζ -potential of Enc^(pos) with 19.30 mV shows that this variant is not exactly oppositely charged to Enc^(neg) with - 24.50 mV. But nevertheless, a significant change in ζ -potential occurred, since the original template for supercharging was a negatively charged

Enc variant. This change is supposed to enable and support strong electrostatic interactions in protein crystallization.

In the end, novel positively supercharged encapsulin variants with and without flavin attached to the outer surface were successfully designed, purified and characterized.

5.1.3.3 Flavin-free encapsulin variants

For the assembly of nanoparticle loaded protein crystals with optical properties, any contamination such as the flavin bound to the encapsulin surface is undesirable. SAVAGE *et al.* mutated W90 to alanine (W90A) or glutamic acid (W90E) to remove the flavin.^[219] As described in detail in the previous chapters, it was not only possible to adopt this mutation to Enc^(wt), but also to apply the mutation into the novel positively supercharged Enc. At the time of this work, it is still not fully clear which flavin is bound to the outer surface. Three flavins that are found in protein production via *E. coli* are shown in Figure 5.7A.

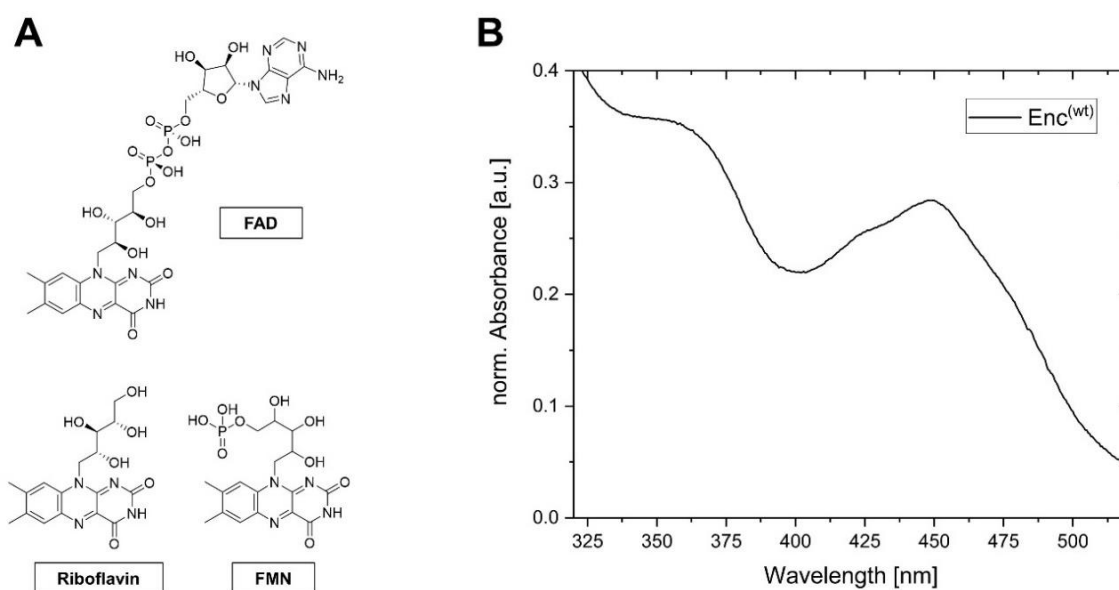


Figure 5.7: Overview of possible surface bound flavins and characteristic absorbance. (A) Chemical structures. (B) UV-Vis spectra of Enc^(wt).

All three of these flavins feature an absorbance maxima at 350 nm and 450 nm.^[219] When the flavin is attached to the outer protein surface of the wild type encapsulin, maxima at around 350 nm and 450 nm can be observed (Figure 5.7B).

Based on the absorbance spectra it is not clear which flavin might be bound to the encapsulin. One study carried out mass spectrometry of the protein sample to determine the mass of the flavins. The protein sample was analyzed via liquid chromatography MS. For that experiment, the sample was eluted with a gradient of water to acetonitrile. Both solutions were supplemented with formic acid. The organic solvent denatures the encapsulin on the column

to induce the release of bound flavin. Riboflavin and FMN were found, but no FAD.^[219] Reports in literature discuss which flavin might fit into their corresponding cryo-EM data. Either riboflavin or FMN are modelled into the electron density found at the binding site, but the flavin side chain is flexible and not preserved.^[219,224] Therefore, it is still unclear which of the two flavins is bound because both might be possible.

For this work, ESI MS was carried out to get further details about the possible flavin. Since the flavin is not removed via protein purification steps, the bond to the outer surface seems to be quite strong. Therefore, a harsh procedure was performed to separate flavin and encapsulin. In detail, the protein was incubated for 30 min at 4 °C with trichloroacetic acid (TCA). TCA is widely used in biochemistry to precipitate macromolecules. In this case, TCA is supposed to precipitate the encapsulin but not the flavin. After incubation the sample is centrifuged for 10 min at 13000 g at 4 °C to pellet precipitated protein. The resulting pellet is of white color while the supernatant stays yellow. Typically, proteins are not colored and appear white. The coloring already indicates that the protein is found in the pellet and the flavin remains in solution. The supernatant is then used for ESI MS measurements (Figure 5.8). For reference, untreated FAD and riboflavin are also characterized via ESI MS and to check if possible degradation products are found. In Figure 5.8A, an m/z value corresponding to riboflavin (377.14 Da) was found. In the region around 450 Da, low intensity for a mass of 452.72 Da can be observed. This mass is close to the expected value of 456.56 Da for FMN. No mass for FAD (786.17 Da) is found. Other expected m/z ratios from the reference data do not appear in the supernatant MS data (Figure 5.8B+C). Detected m/z ratios with higher values are degraded fragments of residual protein since they do not appear in the reference data and are too high for any flavin molecules. Detected m/z values of around 127 Da and 138 Da fit to degradation products of TCA into dichloroacetic acid and formic acid, respectively.^[284] Riboflavin degradation products such as lumichrome at 243 Da, lumiflavin at 259 Da and carboxymethylflavin at 301 Da are observed.^[285,286] Most of the degradation products do not appear in the reference data since they were not chemically treated with TCA. Only lumichrome, a typical flavin photodegradation product is observed. To check the suitability of this experiment and if the amount of sample was just too low to detect other flavins, it was repeated but with a higher concentrated sample of Enc^(wt). Additionally, Enc^(pos)-Fla was also treated with TCA. In both cases, the yellow-colored supernatant was analyzed via ESI MS (Figure 8.14). Again, a very intense signal for riboflavin mass and an almost vanishing signal for FMN mass is found. This result indicates that mostly riboflavin is bound to the encapsulin surface. On the other hand, it might be possible that FMN is less ionizable and therefore not observed with high intensity as riboflavin in ESI MS. In comparison, SAVAGE and co-workers detected significantly more FMN than riboflavin ions in liquid chromatography MS.^[219] The procedure to separate protein and flavin carried out in this work is based on the precipitation of proteins. It is not expected that FMN would precipitate

Results

and therefore appear with lower intensity. Even if both molecules react with each other, resulting products would be detected, but this is not the case. There are no m/z values that might fit to thinkable reaction products. In fact, it seems that almost no FMN is present in these encapsulin samples.

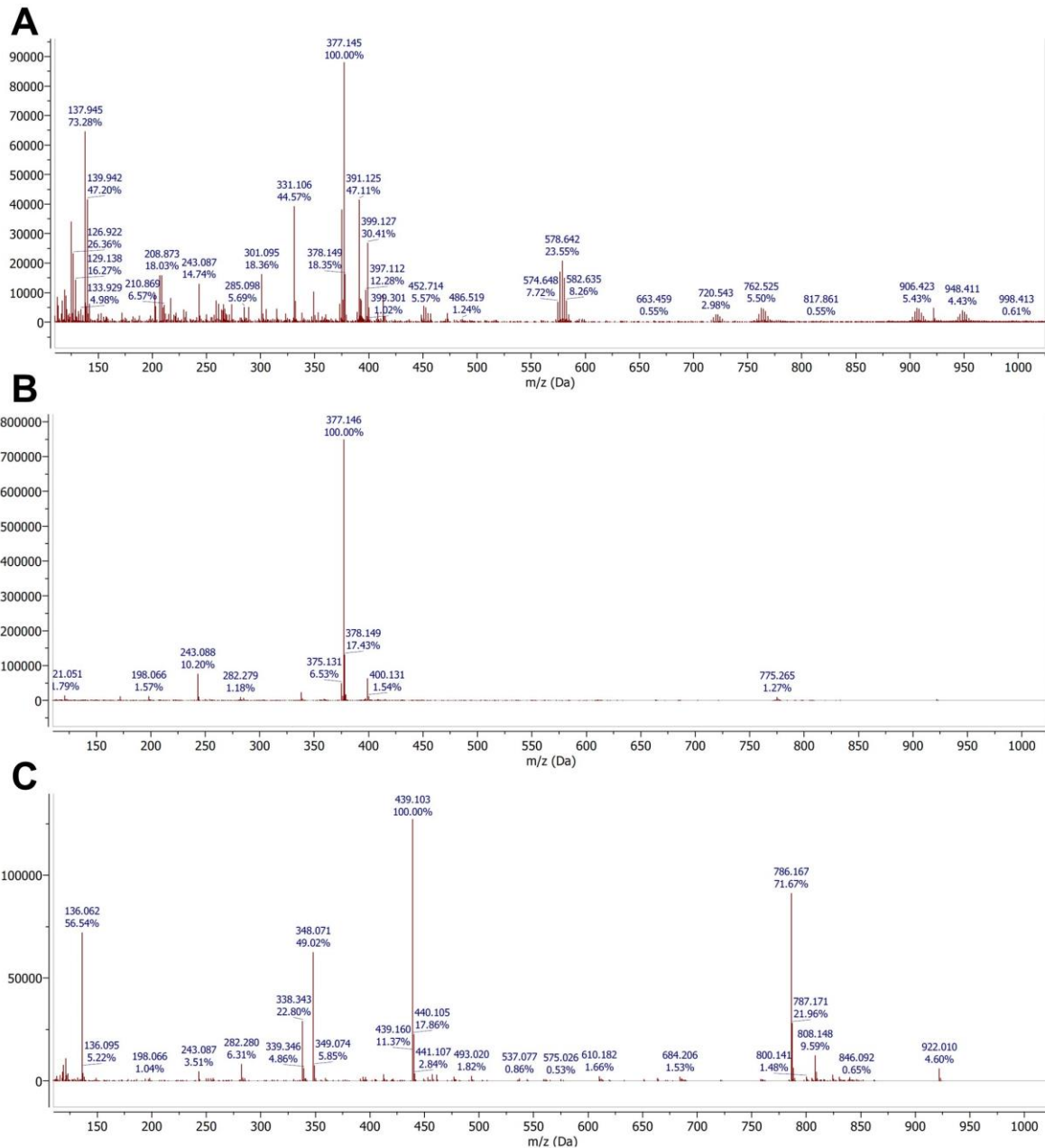


Figure 5.8: ESI MS spectra to distinguish which flavin is bound to encapsulin. Enc^(wt) (A), riboflavin (B) and FAD (C) ESI MS spectra with m/z range from 110 Da to 1025 Da.

A comparison of the protein purification steps between this work and published by SAVAGE *et al.* results in no difference with large impact. SAVAGE and co-workers dialyzed the protein sample prior to SEC, while in this work IEC is carried out prior to SEC. Basically, both methods should lead to the same result, having a protein sample separated from smaller molecules. It is unlikely that surface bound FMN interacts with the chromatography column used for IEC, is

removed from the encapsulin surface and irreversibly bound. One step before protein purification is protein production. SAVAGE *et al.* induce the protein production with IPTG at an OD₆₀₀ of 0.3 and expression takes place at 18 °C.^[219] For this experiment, protein expression is induced at OD₆₀₀ of 0.7 and is carried out at 37 °C. Especially the temperature might influence the production and use of riboflavin and FMN inside the *E. coli* cell. Here, further research is needed to investigate the influence of the temperature and inducing time, but this is not part of the works scope.

In previous chapters encapsulin variants with and without flavin are introduced. For Enc variants with flavin the question emerged how many flavins are attached to the protein surface? To resolve this question, a method already used to determine the loading of fluorophores in ferritin is used.^[12] Experimental details are found in chapter 7.7.6. Since it is presumably riboflavin that is bound to the encapsulin surface, a riboflavin stock solution was used to prepare a concentration row. For each measurement point, the absorption at 280 nm and 450 nm was measured (Figure 8.15). Based on these calibrations, the ratio of riboflavin to encapsulin is determined (Table 5.6).

Table 5.6: Calculation of the number of riboflavin molecules attached to the encapsulin surface.

Protein	Riboflavin/Enc
Enc ^(wt)	34.90
Enc ^(pos) -Fla	46.86

Based on this method, it was possible to determine that roughly 35 and 47 riboflavin molecules are attached to Enc^(wt) and Enc^(pos)-Fla, respectively. The encapsulin container is constructed out of 60 subunits, thus 60 binding sites are present. Due to 60 binding sites up to 60 riboflavin molecules can bind to the surface and indicate that this result is reasonable. Interestingly, the positively supercharged Enc^(pos)-Fla features roughly 12 additional riboflavin molecules on the outer surface. The major difference between both variants is the surface charge. In detail, additional cationic amino acids are added in close range to the aromatic residue tryptophan at position 90 into Enc^(pos)-Fla at position 86 and 241. In structural biology cation- π interactions are well known.^[287,288] In this case, the cationic residues might act as catchers and improve flavin binding. Moreover, the change of time and temperature in protein production might also influence the flavin amount.

Currently the only method to avoid flavin binding to encapsulins is the mutation at position 90 to remove the aromatic amino acid. To further characterize encapsulins with and without flavin, the absorption ratios of A260/280 and A450/280 are compared (Table 5.7). Since flavins feature a characteristic absorbance at 450 nm, this value is compared with the protein

absorbance maximum at 280 nm. The ratio of A260/280 is used to evaluate the purity of the protein sample. The values listed below are extracted from protein purification via SEC.

Table 5.7: Comparison of absorption ratios of encapsulin variants with and without flavin. Protein variants without flavin are marked with an asterisk.

	Enc ^(wt)	Enc ^{(neg)*}	Enc ^{(neg)-Ala*}	Enc ^{(pos)-Fla}	Enc ^{(pos)-Ala*}	Enc ^{(pos)*}
A260/280	0.694	0.646	0.647	0.733	0.693	0.657
A450/280	0.065	0.009	0.009	0.107	0.010	0.010

In every protein variant with a mutation at position 90, the absorbance ratio of A260/280 and A450/280 decreases, indicating the removal of bound flavin. For Enc^{(pos)-Fla} the ratio at A450/280 is higher than for Enc^(wt), indicating that a higher amount of flavin is bound to Enc^{(pos)-Fla}, due to the increase in absorption at 450 nm. This result agrees with the conclusion from the previous experiment (Table 5.6), in which Enc^{(pos)-Fla} binds more flavin molecules than Enc^(wt).

For an additional characterization, the absorbance spectra of Enc^{(pos)-Fla} and Enc^(pos) are measured and shown in Figure 5.9. The characteristic flavin absorbance at around 350 nm and 450 nm can be observed for Enc^{(pos)-Fla}. For Enc^(pos) the absorbance at 450 nm is absent. The leftover absorbance at around 350 nm can be attributed to the protein. Even by eye the significant change in color can be seen (Figure 5.9 - inset). The same behavior can be observed for negatively charged Enc variants (data not shown). The loss of the characteristic flavin absorbance furthermore indicates the successful removal of the flavin.

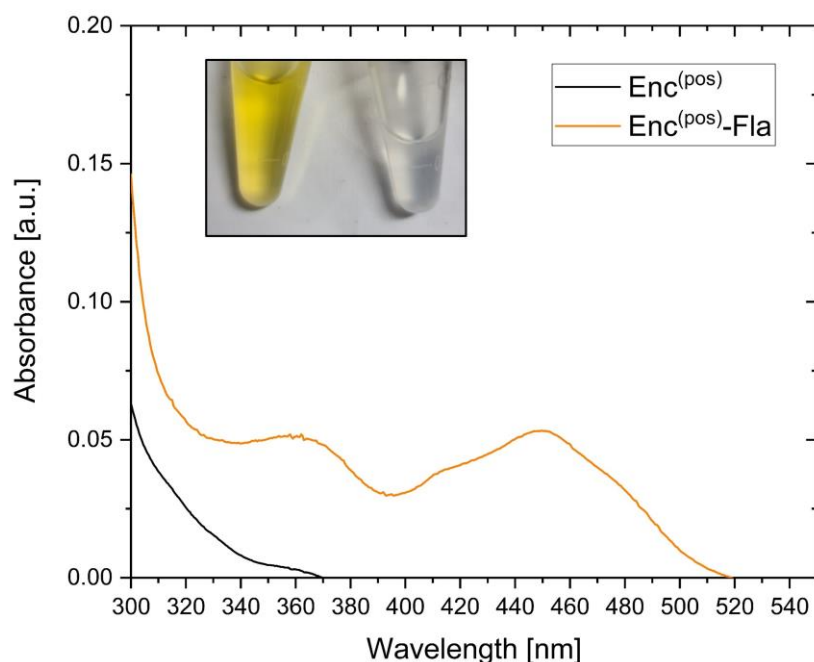


Figure 5.9: Absorption spectra of Enc^{(pos)-Fla} and Enc^(pos). Absorbance spectra were recorded at the same protein concentration. Inset: Visual comparison between Enc^{(pos)-Fla} (left) and Enc^(pos) (right) samples.

In conclusion, Enc variants with flavins were characterized by MS and absorbance spectra. Possibly riboflavin is the main flavin bound to the Enc surface, while positive Enc binds significantly more flavin to its surface than negative Enc.

5.1.4 Positively charged ferritin with additional cysteine

In a recent study, BECK *et al.* investigated the interactions between AuNPs and fluorophores loaded in a Ftn protein crystal (chapter 2.5.3).^[13] One of the latest statements in their study highlighted the interest of enabling a system with a defined chemical environment, orientation and position of fluorophores as shown with a fluorophore-conjugated icosahedral virus template by DRAGNEA.^[11,289] For this purpose, a positively supercharged ferritin variant with additional cysteine is used. The Ftn^(pos)-Cys variant labeled with various fluorophores is supposed to be used as a novel building block for the assembly of binary protein lattices.

Initially MADE BUDIARTA carried out the mutagenesis of Ftn^(pos)-Cys. This work continued his approach: Here the new protein variant is produced for the first time and characterized. Ftn^(pos)-Cys is produced and purified after an already established protocol for Ftn^(pos) (chapter 7.7.2.3).^[205] Corresponding IEC and SEC chromatograms for Ftn^(pos)-Cys are shown in Figure 5.10.

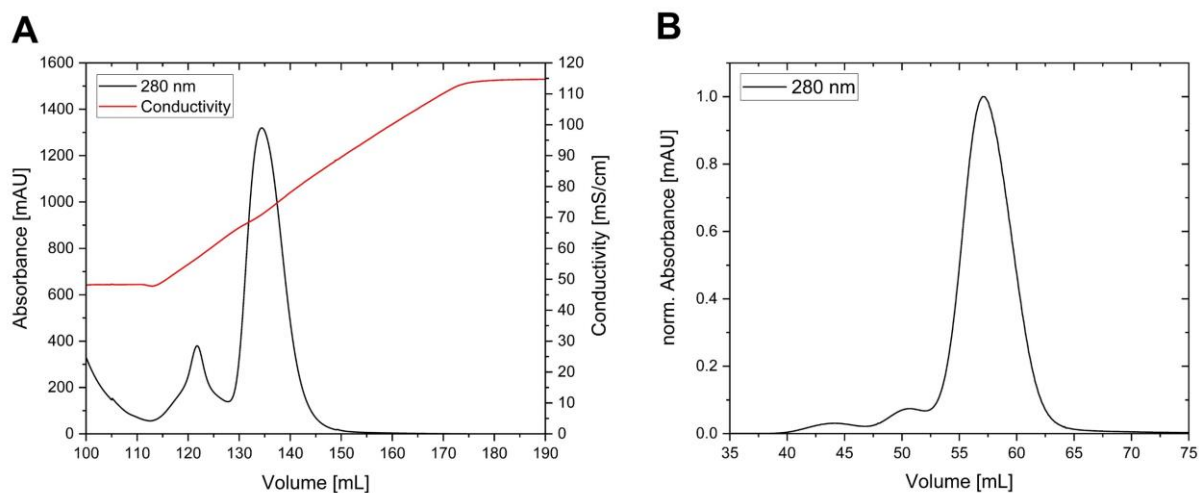


Figure 5.10: Ion-exchange and size-exclusion chromatograms for positively supercharged ferritin with additional cysteine. (A) IEC chromatogram for Ftn^(pos)-Cys. Protein elution at 71 mS/cm. (B) SEC chromatogram for Ftn^(pos)-Cys. Absorbance was monitored at 280 nm (black). Conductivity is shown in red.

The elution volume of Ftn^(pos)-Cys in SEC (Figure 5.10B) fits very well to the reported value of Ftn^(pos) with around 57 mL and indicates the elution of a protein container with the correct size. To verify the purification of a protein with the correct mass, ESI MS is carried out. In Figure 5.11 the ESI MS spectrum is presented.

5.2 Encapsulation of cargo into protein containers

The encapsulation of cargo into protein containers was described in detail in chapter 2.4 and its sub-chapters. First, the protein container is disassembled and then reassembled while cargo is added. As shown for encapsulin a cargo-loading peptide (CLP) can be exploited to encapsulate non-native cargo such as AuNPs into a protein container. Another possibility is to use electrostatic interactions for cargo encapsulation if CLP functionalization cannot be carried out. Along these lines, two goals were envisioned: First, optimization of the AuNP encapsulation. Secondly, encapsulation of novel cargo such as quantum dots.

5.2.1 Encapsulin dis- and reassembly

Initial encapsulation trials were carried out to reproduce the encapsulation of AuNPs into Enc^(wt) according to already established protocols.^[10] Surprisingly, it was not possible to reproduce the encapsulation based on the established procedures. To further investigate this problem, first the disassembly of encapsulin was investigated. In general, the disassembly is triggered by strong acidic or basic pH or high concentration of guanidine hydrochloride (Gua).^[9,225] Only the acidic approach was of interest, because it was already possible to achieve high encapsulation efficiencies with the acidic disassembly condition.^[10] In our protocol, the protein dissolved in ultrapure water is diluted ten times with 10 mM phosphate buffer pH 2.0 to induce disassembly. Moreover, in a work by SAVAGE *et. al* the disassembly is carried out at pH 1.0. SAVAGE and co-workers adjust the pH of the buffered protein solution with the addition of HCl to pH 1.0, because at pH 2.0 the protein disassembly was not complete.^[9] The question arises why the disassembly at pH 2.0 and high encapsulation efficiency into Enc^(wt) were possible in previous works and what has changed. The protein present in water and being diluted with a buffer of pH 2.0 should not result in a significant difference in pH than adjusting the buffered protein solution to pH 2.0 with HCl. The main deviation in both approaches might be the final volume of the disassembly solution. The ten times dilution might result in a larger sample volume than adding small volumes of a concentrated HCl solution. The difference of sample volume might indicate that a sample with lower protein concentration in a larger volume is able to disassemble at pH 2.0. Therefore, additional experiments were carried out to analyze this observation.

As a first experiment, Enc^(wt) and Enc^(pos)-Fla were disassembled in 10 mM phosphate pH 1.0 and pH 2.0. After incubation at 4 °C for 1 h, negatively stained TEM samples were prepared. For disassembly at pH 1.0, no protein containers can be observed (Figure 5.12B+E). Remarkably, at pH 2.0 protein containers are still present (Figure 5.12C+F). In these experiments, the disassembly was carried out by diluting the protein dissolved in 20 mM Tris pH 7.5, 0.3 M NaCl ten times with 10 mM phosphate buffer of pH 1.0 or 2.0. The final pH was

verified via pH electrode, indicating the dilution process with the disassembly buffer is sufficient to change the solution's pH. Additionally, the idea that protein disassembly occurs in less concentrated solutions at pH 2.0 was disproved. Consequently, it is not clear why high encapsulation efficiencies were possible based on a disassembly at pH 2.0.

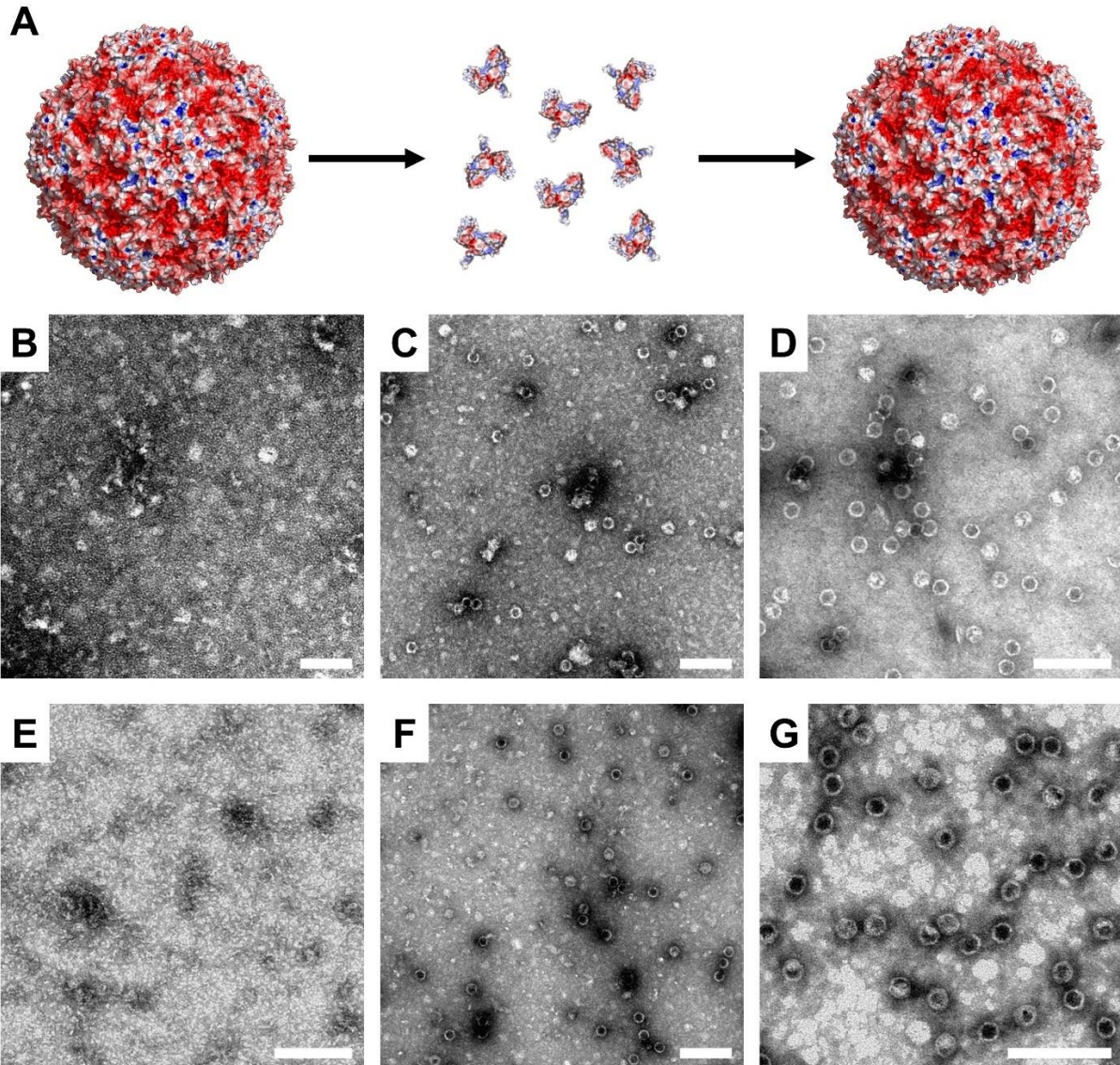


Figure 5.12: Investigation of the encapsulin disassembly via negative stained TEM images. (A) General scheme for protein dis- and reassembly. Proteins incubated at pH 1.0 in (B) and (E) and at pH 2.0 in (C) and (F). Disassembled proteins at pH 1.0 were reassembled at pH 7.0 in (D) and (G). TEM images for *Enc*^(wt): (B), (C) and (D). TEM images for *Enc*^(pos)-Fla: (E), (F) and (G). Scale bars are 100 nm.

Based on TEM images it is not clear if no disassembly occurs at pH 2.0 or whether it is only partial. To address this question, a native gel was prepared (Figure 8.17). Native gels are also known as non-denaturing gels and make it possible to analyze proteins in their folded state. *Enc*^(wt) was incubated for 1 h at 4 °C in pH 1.0, 1.5 and 2.0. At pH 2.0 the disassembly is incomplete, because both protomer and container bands are visible. Already at pH 1.5 no protein containers are observed anymore.

To check if Enc^(wt) and Enc^(pos)-Fla disassembled at pH 1.0 still reassemble, the original reassembly protocol is carried out. After reassembly, negative stained TEM samples were prepared (Figure 5.12D+G). In both cases reassembled protein containers are observed. At this point flavin-free variants were not yet discovered and only Enc^(wt) and Enc^(pos)-Fla were available for investigation (Figure 5.12). Nevertheless, it was possible to show that the positively supercharged Enc^(pos)-Fla can also be dis- and reassembled. Due to the change to more positive amino acids on the outer surface it was not clear if the reassembly still occurs. The container cavity is negatively charged while the new variant is positively charged. Electrostatic interactions could lead to stacking between protein subunits and no successful reassembly, but this does not seem to be the case.

After investigating the disassembly mechanism via negative stained TEM samples and native gel, it is possible to distinguish the problem of no encapsulation. Based on these results, the disassembly of Enc variants will only be carried out at pH 1.0.

5.2.2 Gold nanoparticle encapsulation

In chapter 2.4.1.1 *T. maritima* encapsulin, the possibility to encapsulate AuNPs is described and visualized (Figure 2.11). In previous work, only a few micro grams of protein were used for the encapsulation of AuNPs. Since larger amounts of protein are needed for the assembly, one task of this work was to investigate the upscaling of the AuNP encapsulation. Furthermore, the encapsulation of a single and multiple smaller AuNPs into Enc was examined.

5.2.2.1 AuNP synthesis

As described in detail in chapter 2.1.1.1, the improved TURKEVICH method makes use of EDTA to achieve very monodisperse AuNPs of desired sizes. The synthesis was already applied in previous works of the BECK group to synthesize AuNPs that fit into the Enc^(wt) cavity,^[10] but was not yet applied to supercharged flavin free Enc variants. In another work smaller AuNPs were encapsulated into supercharged Ftn variants.^[13] It was planned to also encapsulate these smaller gold nanoparticles into the Enc container. Therefore, both types of AuNPs had to be synthesized.

The synthesis with the goal of making 13 nm large particles was achieved with a protocol (chapter 7.5.1) based on the improved TURKEVICH synthesis of AuNPs by SCHULZ *et. al.*^[41] Smaller gold nanoparticles of around 3 nm are synthesized by another established protocol (chapter 7.5.2) based on PENG *et. al.*^[294]

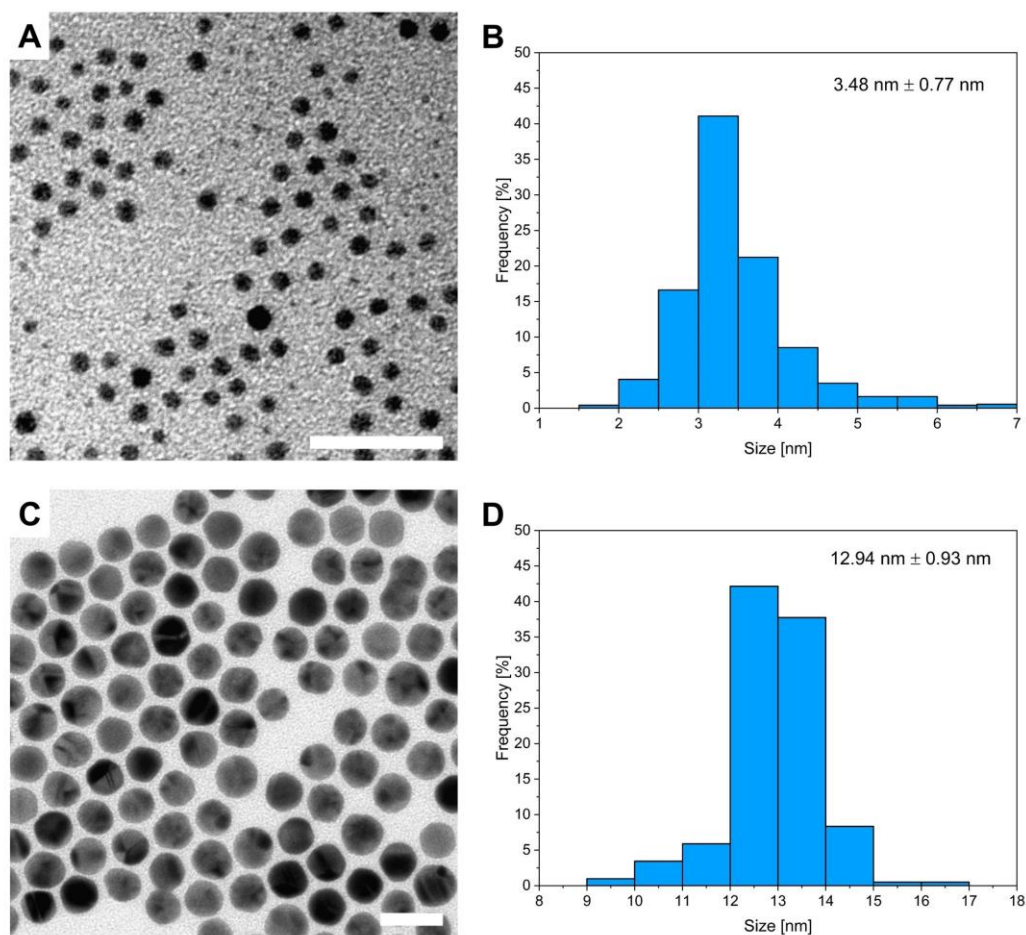


Figure 5.13: TEM images and histograms of synthesized AuNPs. TEM images of AuNPs synthesized based on (A) PENG and (C) TURKEVICH protocols. Histograms of (B) PENG and (D) TURKEVICH AuNPs based on TEM images. Scale bars are 20 nm.

In both cases, it was possible to synthesize AuNPs with desired sizes (Figure 5.13). However, for the encapsulation of AuNPs into Enc variants, it is important to determine the exact particle concentrations to achieve high encapsulation efficiency. Based on the Au precursor amount, Au density and size of AuNPs determined by TEM, it is possible to calculate a particle concentration. Nevertheless, such a calculation assumes a 100 % conversion of nanoparticle precursor. To determine the Au content of an improved TURKEVICH synthesis and take possible losses through synthesis and purification into account, atomic absorption spectroscopy (AAS) was used (Table 5.9). Typical AuNP concentration of a PENG AuNP synthesis was already determined by MARCEL LACH.^[295] In general values for $c_{\text{AAS}}(\text{Au})$ are slightly higher than estimated. Due to heating the aqueous solution, water evaporates, and the Au concentration is higher than expected. The estimated $c_{\text{calc}}(\text{Au})$ is based on the initial synthesis volume, which is slightly larger. Moreover, the yield of each synthesis seems to be rather high since no strong loss can be observed. Based on the nanoparticle size and Au concentration it is possible to determine the AuNP concentration.

Table 5.9: Atomic absorption spectroscopy results to determine Au concentrations. Three samples from different TURKEVICH AuNP syntheses were analyzed. For each sample three AAS measurements were carried out. Mean values are listed for $c_{\text{AAS}}(\text{Au})$.

Sample	$c_{\text{calc}}(\text{Au})$ [mg/L]	$c_{\text{AAS}}(\text{Au})$ [mg/L]
1	145.63	146.35
2	145.63	147.62
3	40.42	42.45

Initially, the aim was to synthesize AuNPs of two different sizes and determine their particle concentrations. The determination of the particle concentration established within this work, enables the encapsulation of synthesized AuNP without assuming particle concentrations based on theoretical calculations.

5.2.2.2 Functionalization and characterization of AuNPs

After synthesis, AuNPs are functionalized with an already established ligand system composed of oleyl amine or citrate. The native ligands of 3.5 nm and 13 nm AuNPs are not suitable for encapsulation due to their hydrophobicity or strong negative charge. Prior to encapsulation, a ligand exchange must be carried out. For high nanoparticle encapsulation efficiencies into Enc, AuNPs were functionalized with a positively charged ligand called (11-mercaptoundecyl)-N,N,N-trimethylammonium bromide (MUTAB) and CLP.^[10] In both cases, the anchoring group is a thiol functionality (Figure 5.14). The CLP-mediated encapsulation of AuNPs will also be applied on novel supercharged Enc variants. Therefore, AuNPs of 3.5 nm and 13 nm were chosen for functionalization.

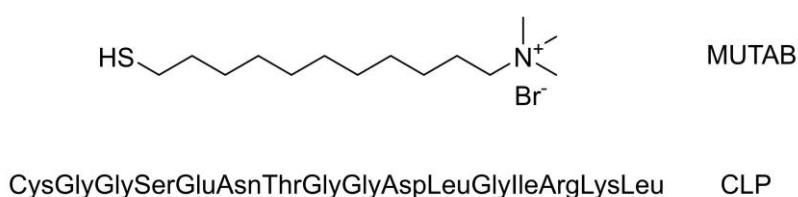


Figure 5.14: Ligands applied on AuNPs for peptide-mediated encapsulation. For convenience, only amino acid three letter code is used to describe the CLP.

For AuNPs of both sizes, established protocols were applied for ligand exchange (chapter 7.6.1 and 7.6.2). Originally, for the small AuNPs smaller ligands were used, but it was also shown that MUTAB can be applied.^[13] In this work, the small AuNPs are functionalized with MUTAB and CLP just as the large AuNPs. In previous results, it was shown that roughly half of the added amount of CLP binds to the NP surface. For larger AuNPs 20 CLP molecules per NP were added, but roughly 9 CLPs bond to the NP surface.^[10] To establish the CLP-functionalization of smaller AuNPs, different amounts of CLP were added to the ligand

exchange. In detail, 10 and 40 CLP molecules per NP surface were chosen. It is assumed that in this case also only half of the CLP molecules end up at the AuNP surface. Therefore, two sets of AuNPs with estimated 5 and 20 CLPs per NP were prepared. Since the surface of 3.5 nm large AuNPs is significantly smaller than for 13 nm large AuNPs, it is assumed that less CLPs per NP surface are needed for efficient encapsulation. Furthermore, too many CLPs on the NP surface might decrease the NP stability. To distinguish the exact number of CLPs bound to the NP surface, further research is needed. In previous works, BECK and co-workers have already shown how to determine the amount of bound CLPs.^[10] Here, after successful ligand exchange, nanoparticles are washed with ultrapure water and taken for characterization. First, UV-Vis measurements were used to characterize the AuNPs and determine their plasmonic resonance maximum (Figure 5.15). Only water soluble AuNPs with citrate, MUTAB or mixed MUTAB-CLP ligand shells were analyzed.

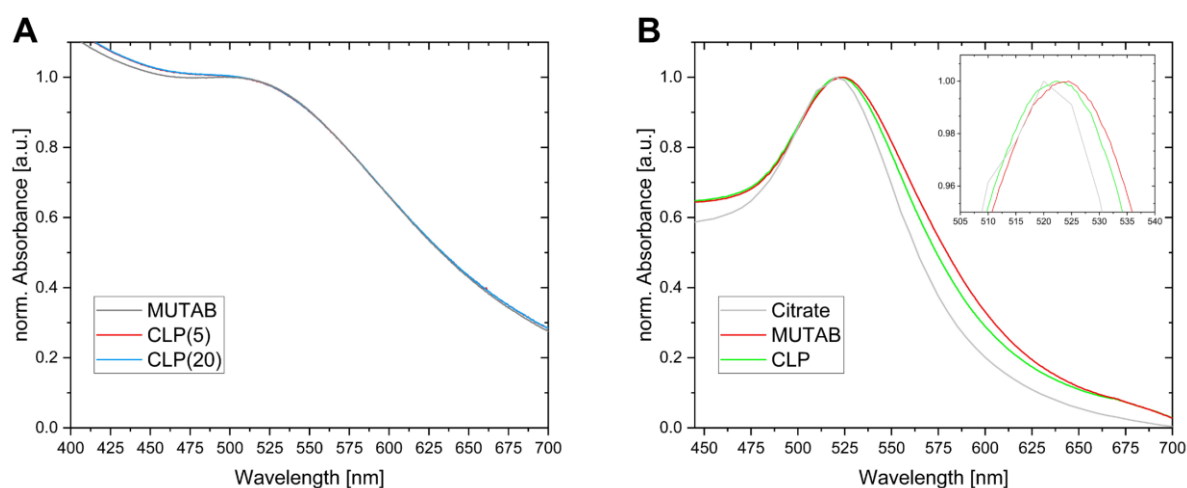


Figure 5.15: UV-Vis comparison between AuNPs of different sizes with different ligand shell composition. (A) Data of 3.5 nm AuNPs with MUTAB and different amounts of CLP molecules (5 and 20) on the NP surface. (B) Data of 13 nm AuNPs stabilized with citrate, MUTAB and mixed MUTAB-CLP (CLP) ligand shells. Inset: Magnification of plasmon resonance maximum shift.

The change from citrate to MUTAB for 13 nm large AuNPs goes along with a shift from 520 nm to 524 nm. AuNPs of 3.5 nm with MUTAB ligand shell feature a maximum at 504 nm. After CLP functionalization, a shift of the plasmon resonance is observed. AuNPs with 3.5 nm size and a mixed MUTAB-CLP ligand shell feature a maximum at 506 nm. Longer ligands than the CLP cause a red shift based on the increased polarizability compared to short ligands.^[296] For 13 nm large AuNPs a different behavior is observed. The maximum decreases from 524 nm to 522 nm. In this case, the polarizability based on the ligand length cannot only play a role because for both NP sizes the same ligands are applied. The major difference is the AuNP size. Larger AuNPs feature a stronger plasmon resonance than smaller ones. Therefore, it is assumed that the addition of the CLP influences the plasmon resonance and shifts to lower wavelengths. In previously published experiments, an observed shift from 520 nm to 522 nm for MUTAB to CLP addition is observed.^[10] In this and in previous work, AuNPs with the mixed

MUTAB-CLP ligand shell feature a maximum at 522 nm. On the other hand, this time the maximum for only MUTAB stabilized particles is at 524 nm instead of previously reported 520 nm. Nanoparticle aggregation could lead to a shift of the plasmon resonance to longer wavelength, but the determined PDI of the AuNPs used in this work is quite low and aggregation less likely (Table 5.10). The concentration of the AuNP sample also influences the plasmon resonance maximum. A sample with higher concentration usually features a shift towards longer wavelengths in comparison to a strongly diluted sample. In the end, it is not definitely clear why there is such a difference in the position of the plasmon resonance maximum of MUTAB stabilized particles.

In addition to the UV-Vis measurements, further characterization was carried out by DLS (Figure 8.16). A summary is listed in Table 5.10. AuNPs with a size of 3.5 nm and functionalized with MUTAB resulted in a very large D_{DLS} value with almost 61 nm. Thus, small AuNPs with MUTAB seem to be less stable and tend to agglomerate. For AuNPs of similar size with smaller ligands, lower diameters were reported.^[13] However, after CLP functionalization with either 5 or 20 CLP molecules per NP surface, the diameter drops significantly. There, the hydrodynamic diameter is closer to the diameter of 3.5 nm, determined via TEM. Still, for each of the three samples a high PDI value is observed. In TEM images it was shown that the size distribution is narrow, but DLS data indicate that the particles partially tend to agglomerate or residual agglomerates from purification steps are left. For further comparison, data of AuNPs of the same size but functionalized with shorter alkyl ligands are listed (Table 5.10, C2mix). There, the chain length is two carbon atoms and significantly shorter than MUTAB (11 carbon atoms). For the C2mix ligand shell, a lower PDI is observed. This comparison indicates either more stable particles or the particles from literature were synthesized with a narrower size distribution. On the other hand, the D_{DLS} value is almost 2 nm larger than for CLP functionalized AuNPs.

Table 5.10: DLS data for AuNPs of different sizes with altered ligand shell composition. Sample marked with an asterisk is listed for further comparison and derived from literature. C2mix equals a ligand shell composed of 2-(dimethylamino)ethanethiol and (2-mercaptoethyl)-*N,N,N*-trimethylammonium.^[13]

	Sample	D_{DLS} [nm]	PDI
3.5 nm	MUTAB	60.91	0.42
	CLP(5)	5.88	0.68
	CLP(20)	6.84	0.44
	C2mix*	8.62	0.22
13 nm	citrate	17.55	0.54
	MUTAB	17.94	0.13
	MUTAB+CLP	20.29	0.30

On the other hand, the ligand exchange from citrate to MUTAB for 13 nm AuNPs led to a small increase of hydrodynamic diameter and decrease of PDI to around 21 nm and 0.13, respectively. Changes in both values indicate the high stability of the larger AuNPs in comparison to smaller AuNPs with MUTAB. With CLP functionalization, the hydrodynamic diameter is increased. Since the CLP is longer than MUTAB, an increase in diameter is expected.

Next, ζ -potential measurements on water soluble AuNPs were carried out. In Figure 5.16A, 3.5 nm large AuNPs with different ligand shell compositions are shown. MUTAB stabilized 3.5 nm AuNPs feature a ζ -potential of 46.7 mV. The functionalization with CLP leads to a decrease in ζ -potential. AuNPs with mixed ligand shells with MUTAB and either 5 or 20 CLPs show 37.4 mV and 28.6 mV, respectively. With 20 CLPs per NP surface, the decrease in ζ -potential is higher, indicating more positively charged MUTAB is removed and exchanged with CLP molecules. In conclusion, the addition of more CLP molecules indeed led to more CLP molecules on the NP surface.

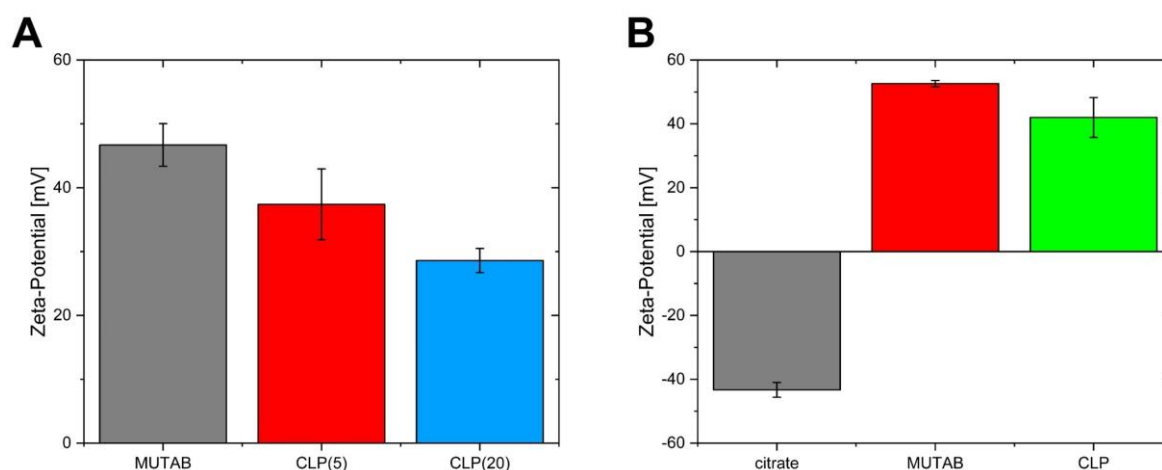


Figure 5.16: ζ -potential measurements of AuNPs. 3.5 nm (A) and 13 nm (B) large AuNPs with different ligand shell compositions.

Larger AuNPs of 13 nm are synthesized in water and are naturally stabilized with citrate molecules. In this case, the ζ -potential is negative (Figure 5.16B). The ligand exchange to MUTAB results in a change from -43.3 mV to 52.6 mV. In this case, the addition of CLP molecules to the ligand shell also causes a drop from 52.6 mV to 42.0 mV. Due to the exchange of MUTAB with CLP molecules on the NP surface a drop in ζ -potential is found.

In previous work, it is discussed that one negative charge of the CLP is likely screened by the positive charge of surrounding MUTAB ligands.^[10] In this case, the leftover charge of the CLP would be +1 (Figure 5.17; $\text{Asp}^{-1} + \text{Arg}^{+1} + \text{Lys}^{+1} = \text{CLP}^{+1}$). Therefore, it is expected that CLP molecules on the NP surface increase the amount of positive charge and leading to an increase in ζ -potential. In this work, the presented data indicates a different trend: The addition of CLP

decreases the ζ -potential. A loss of charge indicates that the screening of the glutamic acid is not occurring. Then, the overall charge of the CLP is assumed to be neutral ($\text{Glu}^{-1} + \text{Asp}^{-1} + \text{Arg}^{+1} + \text{Lys}^{+1} = \text{CLP}^0$). The exchange of a positively charged ligand with a neutral ligand could explain the observed decrease in ζ -potential.

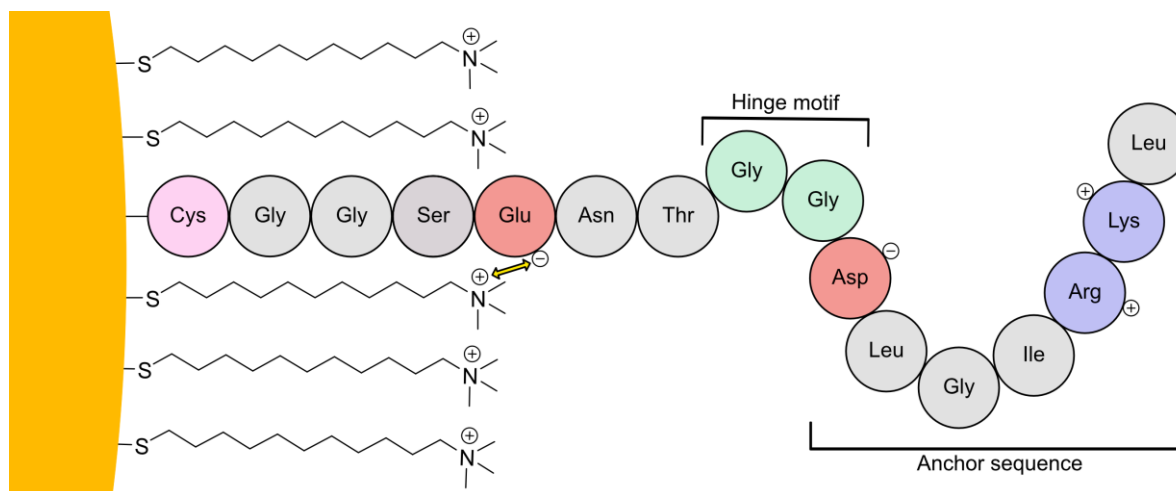


Figure 5.17: Idealized cartoon representation of a MUTAB and CLP functionalized gold nanoparticle surface.

The 16 amino acid long cargo-loading peptide (CLP) can be divided into three parts: N-terminal anchoring group, based on a cysteine residue (pink) for covalent binding to the gold nanoparticle surface; Flexible hinge motif containing two glycine residues (green); C-terminal anchor sequence (from Asp to Leu) that binds to the inner encapsulin surface. Possible interactions between the negatively charged glutamic acid and the positive charge of the MUTAB ligand are indicated by a yellow arrow. Charged residues are highlighted either in red (negative) or blue (positive). Figure adapted from KÜNZLE *et. al.*^[10]

Finally, AuNPs of two sizes were functionalized with a mixed ligand shell composed of MUTAB and CLP molecules. The addition of CLP to the MUTAB ligand shell influenced hydrodynamic diameters and ζ -potentials. However, the AuNPs were stable and ready for encapsulation experiments.

5.2.2.3 Scale-up of AuNP encapsulation

Originally, a few micro grams of protein were used to establish the encapsulation of AuNPs.^[10] To construct a three-dimensional material, a higher sample amount is needed. Therefore, the encapsulation process was carried out with milligrams of protein. The protocol is described in detail in chapter 7.7.4. In general, a protein solution with a high concentration was prepared. The desired amount of protein was diluted ten times with 10 mM phosphate buffer pH 1.0 and incubated for 1 h at 4 °C. Afterwards the protein sample is added to the reassembly buffer. The reassembly buffer for AuNP encapsulation is a 20 mM phosphate buffer pH 7.0 containing NaCl. The AuNP solution is added dropwise to the reassembly solution and gently swirled. Finally, the encapsulation experiment is incubated overnight at room temperature (Figure 5.18). The next day, the sample is concentrated and prepared for purification (chapter 5.2.2.5).

The salt concentration in the solution during the reassembly process plays a crucial role. In a previous work, it was shown that with a NaCl concentration of 350 mM an encapsulation efficiency of over 99 % of AuNPs with CLP into $\text{Enc}^{(\text{wt})}$ was achieved.^[10] For this work, the concentration of NaCl was screened to determine the highest encapsulation efficiency into $\text{Enc}^{(\text{neg})}$ and $\text{Enc}^{(\text{pos})}$. High salt concentrations will shield the charges of AuNP and protein cavity, decrease AuNP stability and no encapsulation will take place. On the other hand, a low salt concentration will increase non-specific interaction between AuNP and protein and lead to precipitation of both. The encapsulation efficiency is determined from negatively stained TEM images featuring loaded or empty protein containers. The aim is to find an optimal NaCl concentration that maximizes the encapsulation efficiency (above 90 %). Moreover, $\text{Enc}^{(\text{pos})}$ is oppositely surface charged, thus the amount of salt for efficient encapsulation may differ between protein variants.

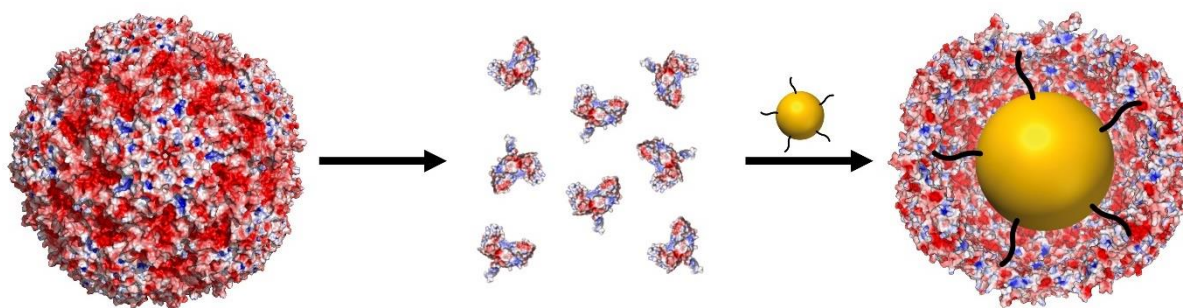


Figure 5.18: Schematic illustration of the encapsulation of AuNPs. At acidic pH, the protein is disassembled into its subunits. The reassembly is triggered by dilution and pH change to neutral. During reassembly, the CLP-functionalized AuNPs are added and finally encapsulated.

The NaCl concentration for the encapsulation of 13 nm large AuNPs was screened in a range from 200 mM to 500 mM in 50 mM steps. After each experiment, a negative stained TEM sample was prepared without further treatment (Figure 8.18). The summary of the encapsulation screening is shown in the following (Table 5.11).

Table 5.11: Schematic overview of NaCl concentration screening for the encapsulation 13 nm large AuNPs. Color and symbol coding to highlight the efficiency. High encapsulation (>90 %): blue/++; medium encapsulation (<90 %): green/+; low encapsulation (<20 %) and aggregation: yellow/~; no encapsulation or mostly aggregates: red/x.

		c(NaCl)						
		200 mM	250 mM	300 mM	350 mM	400 mM	450 mM	500 mM
sample	$\text{Enc}^{(\text{neg})}$	x	~	+	++	++	+	+
	$\text{Enc}^{(\text{pos})}$	x	~	+	++	++	+	+

Interestingly, in this screening the optimal NaCl concentration for both encapsulin variants is determined to be between 350 mM to 400 mM. Despite the change of surface charge, the

encapsulation of AuNPs with CLP into Enc^(pos) was as efficient as in Enc^(neg) (Figure 5.19). The inner surface was not mutated, therefore the interactions between particles and inner surface should not differ. At 300 mM and above 450 mM NaCl, encapsulation is still observed but less efficient. Moreover, at 250 mM NaCl more empty containers and aggregates are visible. At 200 mM, only aggregation or empty containers are observed.

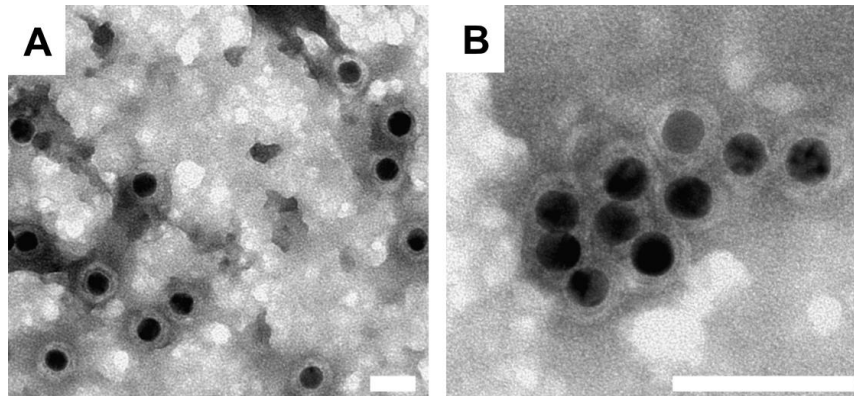


Figure 5.19: Negatively stained TEM images of AuNP-loaded Enc^(pos). Encapsulation experiments were carried out with either 350 mM NaCl (A) or 400 mM NaCl (B). Scale bars are 50 nm.

In conclusion, a certain concentration of NaCl is necessary to stabilize AuNPs, but too much salt might screen the electrostatic or weaken the CLP interaction with the Enc cavity. In both supercharged Enc variants CLP functionalized AuNPs of around 13 nm can be encapsulated. These reactions were carried out on the milligram-scale with respect to protein use.

5.2.2.4 Encapsulation of small AuNPs

Until now, only AuNPs with sizes of 11 nm and 13 nm have been encapsulated into Enc^(wt).^[10] In the previous chapter, 13 nm large AuNPs were encapsulated into Enc^(neg) and Enc^(pos). Since these AuNPs almost completely fill the cavity, experiments were carried out to encapsulate smaller AuNPs into Enc to investigate the possibility to encapsulate more than one nanoparticle per container. In detail, 3.5 nm large AuNPs functionalized with CLP were used in encapsulation experiments. Enc^(neg) and Enc^(pos) were chosen as target proteins. In general, the encapsulation procedure was carried out as described for 13 nm large AuNPs, but the NaCl concentration is lowered. In encapsulation experiments with AuNPs of around 3 nm into supercharged Ftn variants, the highest encapsulation rate was achieved at 200 mM NaCl. With higher NaCl concentrations the encapsulation efficiency decreased due to shielding of the charges.^[13] Therefore, the salt concentration of the reassembly buffer is adapted and adjusted from 350 mM NaCl to 200 mM NaCl. After the encapsulation experiments, TEM images were prepared of untreated samples to investigate possible encapsulation.

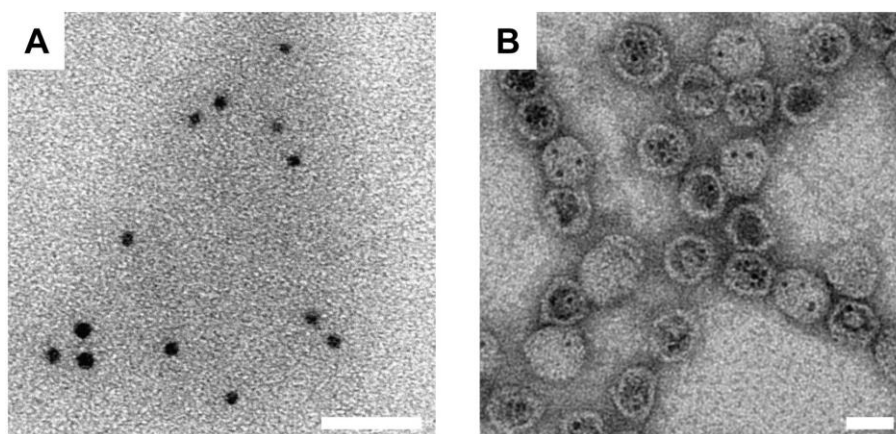


Figure 5.20: AuNP encapsulation experiment with $\text{Enc}^{(\text{pos})}$ visualized via TEM. Unstained (A) and negative stained (B) TEM image of $\text{Enc}^{(\text{pos})}$ encapsulation experiment prior further purification. Scale bars are 20 nm.

First, TEM images of the encapsulation experiment of smaller AuNPs functionalized with CLP into $\text{Enc}^{(\text{pos})}$ are shown. In detail, 3.5 nm large AuNPs with 5 CLPs per NP were used. In Figure 5.20A, pairs of two or three AuNPs are found, while also single AuNPs are present. All pairs are arranged within less than 24 nm, which indicates multiple AuNPs in a single $\text{Enc}^{(\text{pos})}$ container. Negative stained TEM images verify this assumption. One, two, three and even four AuNPs can be found within one protein container (Figure 5.20B). On all available TEM images, no free AuNPs, but also empty protein containers are observed in negative stained TEM images. This observation can be explained, because the ratio of AuNPs to $\text{Enc}^{(\text{pos})}$ for this encapsulation experiment was equal and multiple AuNPs are found within one container.

One additional experiment was carried out with 3.5 nm large AuNPs functionalized with 20 CLPs per NP to test if the higher number of CLPs on the NP surface affects the encapsulation. In this case, $\text{Enc}^{(\text{pos})}$ and $\text{Enc}^{(\text{neg})}$ were chosen for the encapsulation experiments. After complete reassembly, negative stained TEM images were prepared (Figure 5.21). In both experiments, the ratio of AuNPs to protein container was equal.

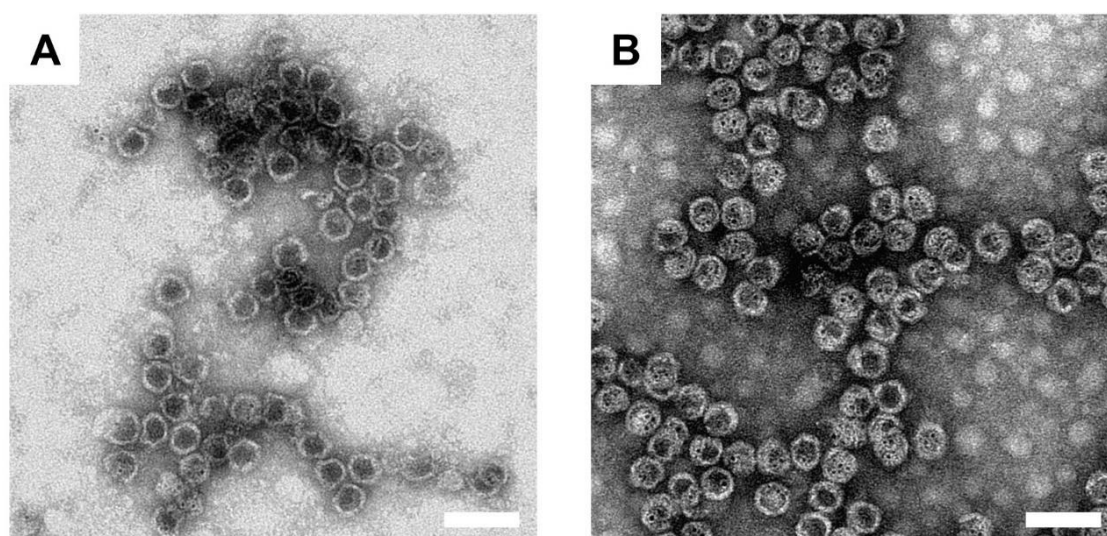


Figure 5.21: AuNP encapsulation experiment with $\text{Enc}^{(\text{neg})}$ and $\text{Enc}^{(\text{pos})}$ visualized via TEM. Negative stained TEM image of $\text{Enc}^{(\text{neg})}$ (A) and $\text{Enc}^{(\text{pos})}$ (B) encapsulation experiment. Scale bars are 50 nm.

In direct comparison, the encapsulation efficiency under the same reaction condition is significantly better for Enc^(pos) than Enc^(neg). Multiple AuNPs are found within most of the Enc^(pos) containers. Only a few containers that feature no cargo and no free AuNPs are observed. A few Enc^(neg) containers are filled, but even then, only with one or two AuNPs. All reaction parameters are the same, but the protein is different. The different behavior indicates that the AuNP-protein interaction differs between both protein variants. The AuNP ligand shell is positively charged due to the MUTAB ligand, while the outer surface of Enc^(neg) is completely negative. Electrostatic interactions between AuNP and Enc^(neg) are conceivable. Moreover, the outer surface of Enc^(pos) is completely positive and does not enable electrostatic interactions with the positive AuNPs. Only the negative cavity is available for electrostatic interactions and would explain the very efficient encapsulation. Also, AuNPs functionalized with MUTAB and CLP are supposed to interact with the inner protein surface, not the altered outer surface. The positive surface of Enc^(pos) prevents the interaction of the AuNPs with the outer surface. On the other hand, this phenomenon is not observed for 13 nm large AuNPs. There, the encapsulation into both containers seems to be equally efficient. There, the larger AuNP can act as a template and possibly enhance the reassembly process. The protein subunits interact with the CLP and reassemble around the large AuNPs. Therefore, interactions with the outer surface of Enc^(neg) are less favored. With smaller AuNPs like here, this is not plausible. In the end, it is assumed that the interaction between smaller AuNPs and the outer surface of Enc^(neg) is the reason for the low encapsulation efficiency. Increasing the NaCl concentration might improve the encapsulation into Enc^(neg) due to screening the interactions between particles and protein.

Furthermore, via TEM images no clear difference is observed in using AuNPs with 5 or 20 CLPs per NP for encapsulation into Enc^(pos). A future experiment could focus on increasing the AuNP-protein ratio to achieve loading of all available protein containers with multiple NPs. Based on experiments done by the DRAGNEA group, 12 FePt NPs of a size of 4.6 nm were encapsulated into a 28 nm large virus-like particle (VLP).^[297] Based on their report, a similar amount of AuNPs (3.5 nm) are feasible to be encapsulated into Enc (24 nm).

In conclusion, the encapsulation of small AuNPs into the encapsulin cavity was established. While the encapsulation into Enc^(neg) was not very efficient, Enc^(pos) was shown to be accessible for efficient encapsulation and even enables the uptake of multiple AuNPs.

5.2.2.5 Purification of AuNP-loaded Encapsulin

After the encapsulation experiments, the AuNP-loaded protein sample is purified via chromatographic methods. First, IEC is carried out to separate free AuNPs from protein. By using an anion exchange column, free AuNPs with positive ligand shells will not bind and run through to the column. The protein still binds to the column and is eluted with a salt gradient.

Afterwards, SEC is applied to remove aggregates from single protein containers. The cargo does not significantly affect the protein elution, because the protein size stays the same. In the purification steps, all buffers and columns are the same as for the empty protein containers (chapter 7.7.2).

In Figure 5.22A, an ion-exchange chromatogram for AuNP-loaded Enc^(neg) is shown. In detail, 13 nm large AuNPs were encapsulated into Enc^(neg) (AuEnc^(neg)) and purified. Only one peak at the expected conductivity range is observed. Due to the simultaneous absorbance at 280 nm, 260 nm and 520 nm the peak can be attributed to AuEnc^(neg), because free AuNPs do not bind to the column. After IEC, the eluted sample is concentrated and taken for SEC (Figure 5.22B). In SEC, AuEnc^(neg) elutes at the expected range at around 12.7 mL. A high absorbance at 520 nm indicates a high number of encapsulated AuNPs. Nevertheless, some AuNP containing protein aggregates are observed at around 8 mL to 12 mL and removed via SEC. Additional UV-Vis measurement is carried out to analyze the purified AuEnc^(neg) sample (Figure 8.19). Additionally to the high absorbance in the region of 260 nm to 280 nm, the protein sample features a strong absorbance at 522 nm.

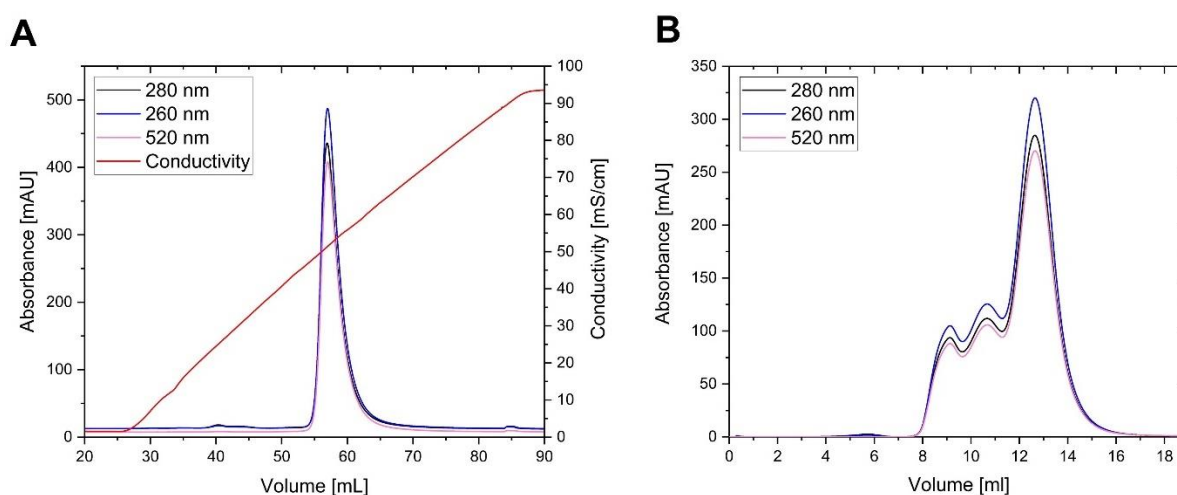


Figure 5.22: Ion-exchange and size-exclusion chromatograms for negatively surface charged encapsulin loaded with AuNPs. (A) IEC chromatogram for AuEnc^(neg). Protein elution at 52 mS/cm. (B) SEC chromatogram for AuEnc^(neg). Absorbance was monitored at 280 nm (black), 260 nm (blue) and 520 nm (pink). Conductivity is shown in red.

As shown in the previous chapter, the encapsulation of 13 nm large AuNPs into Enc^(pos) was established within this work. First, IEC is carried out to separate free AuNPs from protein sample. In this case, a cation exchange column is used. Free AuNPs bind to the column, instead of passing the column. A conductivity over 100 mS/cm is necessary to elute the AuNPs (Figure 8.20). Therefore, in the region below 100 mS/cm only protein with encapsulated AuNPs is supposed to elute. After IEC, less AuNP-loaded protein is recovered (Figure 5.23) than empty Enc^(neg) in the same purification step (Figure 5.22). In both experiments, the same

amount of protein and AuNPs were used under the same encapsulation conditions. Typically, Enc^(pos) is stored in a buffer containing 1.0 M NaCl, but for encapsulation only 0.35 M NaCl is used. The encapsulation might still occur, but the reassembled protein might be less stable in this condition. One possibility to improve protein stability is to directly add additional NaCl after complete reassembly. Another experiment would be to dialyze against a buffer with a high concentration of salt while the encapsulation process takes place. With this procedure, the NaCl concentration would slightly increase within the encapsulation sample. Nevertheless, the peak with high absorbance at 280 nm and 520 nm at the expected conductivity of around 72 mS/cm for Enc^(pos) indicates the desired protein loaded with AuNPs.

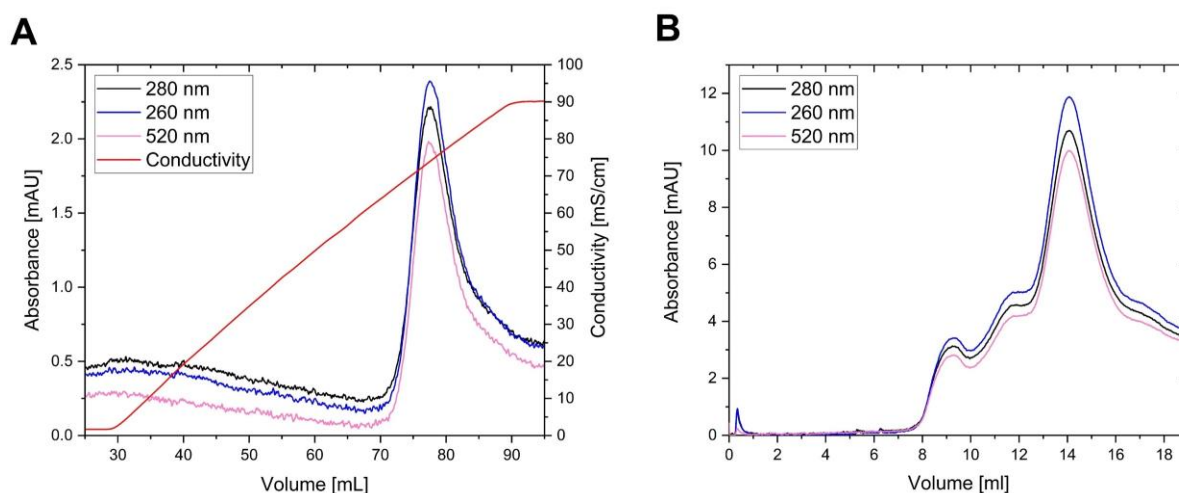


Figure 5.23: Ion-exchange and size-exclusion chromatograms for positively surface charged encapsulin loaded with AuNPs. (A) IEC chromatogram for AuEnc^(pos). Protein elution at 52 mS/cm. (B) SEC chromatogram for AuEnc^(pos). Absorbance was monitored at 280 nm (black), 260 nm (blue) and 520 nm (pink). Conductivity is shown in red.

All protein fractions derived from IEC were combined and prepared for SEC. Also for AuEnc^(pos) aggregates are observed in the region from 8 mL to 12 mL. Notably, the peak with high intensity at 280 nm, 260 nm and 520 nm is shifted to a higher elution volume of 14 mL. Typically, Enc^(pos) is expected to elute at around 13 mL. Moreover, a broad shoulder towards larger elution volume is observed. A larger elution volume indicates that smaller objects elute. Due to the observed low recovery of protein and broad elution peak in SEC, the overall protein stability seems to be decreased after AuNP encapsulation. The shoulder at around 17 mL might indicate partially reassembled Enc^(pos) around AuNPs since there is still absorption at 520 nm next to 280 nm and 260 nm. In addition, the purification of smaller AuNPs into Enc^(pos) was carried out. In detail, 3.5 nm large AuNPs with either 5 or 20 CLP molecules per NP surface were used. Also, for the smaller AuNPs, low Enc^(pos) recovery is achieved. There, the NaCl is even less with 0.2 M NaCl and might affect protein stability.

In the end, the purification of supercharged protein variants with differently sized AuNPs was established. In the future, the encapsulation for Enc^(pos) needs further improvement to increase the protein stability and therefore a higher AuNP loaded protein yield.

5.2.3 Quantum dot encapsulation

Since the overall aim is to create a binary superlattice composed of two oppositely supercharged protein containers with QDs and AuNPs inside, the encapsulation of QDs had to be established. All giant core/shell quantum dots (gQDs) used in this work were kindly provided by SONJA KROHN (*Fraunhofer CAN*, Hamburg). In detail, spherical CdSe/CdZnS gQDs with a diameter of 12.9 nm were chosen for encapsulation (Figure 5.24). Since these gQDs are synthesized in an organic solvent and stabilized with hydrophobic ligands, a ligand exchange must be carried out to achieve water solubility.

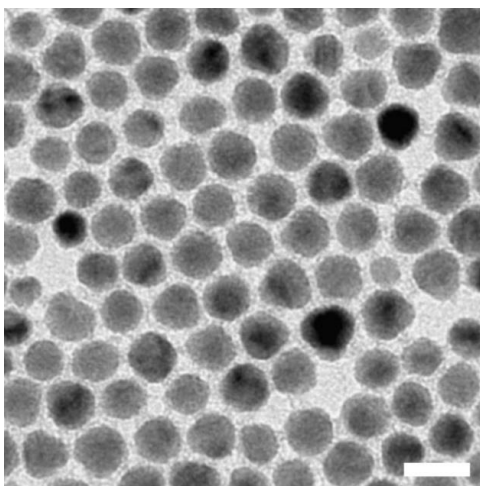


Figure 5.24: TEM image of gQDs with native ligand shell. Scale bar is 20 nm.

First, the hydrophobic ligands oleic acid and oleyl amine had to be removed. A selection of ligands to provide water solubility are shown in Figure 5.25. The anchoring group is a thiol group with strong affinity to the semiconductor surface, while different head group were tested. Moreover, the aim is to achieve a positive surface charge, since the protein cavity is negatively charged, and electrostatic interactions are beneficial towards encapsulation. Nevertheless, alternative ligands were tested to establish water soluble particles. In a second step, a CLP functionalization is planned to have gQDs for high efficiency encapsulation.

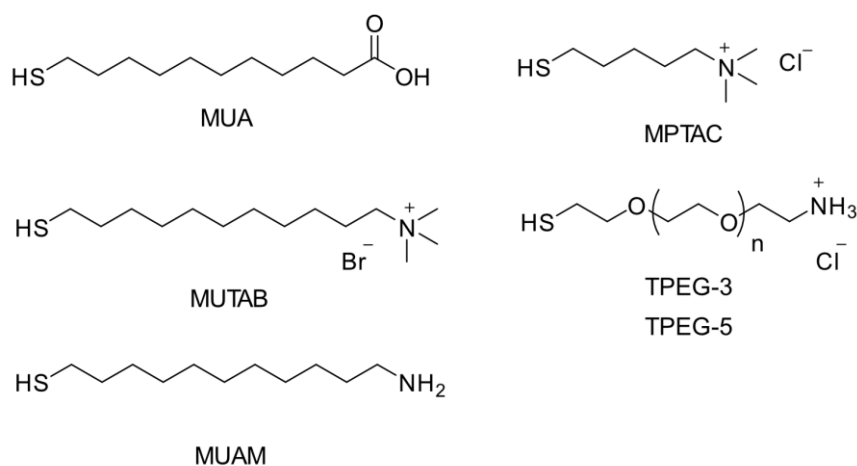


Figure 5.25: Chemical structures of ligands used to functionalize gQDs. Short names for each ligand are written below the chemical structure. For TPEG two molecules with different molecular weights (3 kDa and 5 kDa) are used.

5.2.3.1 Encapsulation of gQDs functionalized with small organic ligands

The ligand exchange reactions for MUTAB, 11-mercaptoundecanoic acid (MUA), 11-amino-1-undecanethiol hydrochloride (MUAM) and (5-mercaptopentyl)-*N,N,N*-trimethylammonium chloride (MPTAC) are performed as described in chapter 7.6.3. In general, the ligand exchange was based on a biphasic system consisting of aqueous KOH and organic chloroform phase, containing gQDs and ligands (Figure 5.25). The progress was tracked visually by the phase transition of gQDs. After visible phase transition, the aqueous phase is separated and washed with ultrapure water. Only for MUAM no phase transition was observed. Aqueous dispersions with MPTAC and a 1:1 mixture of MUTAB and MUAM ligands seemed to be very unstable since no resuspension was possible. A failure to exchange the ligands fully or partially may cause agglomeration. Moreover, the alkaline condition combined with the ligands might be unsuitable. The ligand exchange was carried out at room temperature. Increasing the temperature might have accelerated the phase transfer by increasing the motion of gQDs and ligand molecules in solution. On the other hand, heating the reaction mixture could also decrease the stability as well as the optical properties of the gQDs.^[298] Furthermore, the amount of ligands plays a significant role. In each experiment, the same amount of ligands was applied, which might have been too much or too less. To distinguish the exact ligand composition, a removal of the ligand shell followed by NMR investigations would be needed.

Promising results were obtained with MUA and MUTAB. Although MUA is a negatively charged ligand and ultimately maybe not ideal for encapsulation, it was already shown that MUA can be applied to quantum dot/rods.^[168] Moreover, water soluble particles with MUTAB were only partially soluble after washing steps. The sample stability was a few hours until visible precipitation of the particles occurred. After successful ligand exchange to MUA, the effect on

the fluorescence of the gQDs is investigated by fluorescence spectra (Figure 5.26). Only MUA-stabilized particles could be studied, since MUTAB stabilized particles do not exhibit long-term stability.

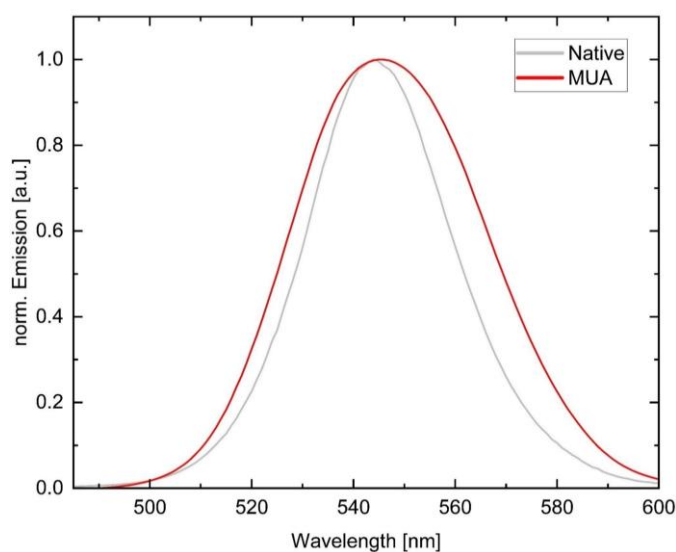


Figure 5.26: Normalized emission spectra of gQDs. Particles with native ligand shell in hexane (grey) and stabilized with MUA in water (red). Excitation wavelength: 350 nm.

Figure 5.26 visualizes the normalized emission spectra of gQDs with two different ligand shells. Particles with their native ligand shell (oleic acid and oleyl amine) feature an emission at 544 nm. For MUA-stabilized gQDs, the emission maximum is shifted towards 545 nm. The shift may be caused by the ligand exchange and the resulting transfer from an organic to an aqueous medium or it might be a consequence of measurement inaccuracy. Nevertheless, a broadening of the emission distribution is observed. The change of the ligand and an increase in polydispersity may affect the emission broadening.^[299]

Since only MUA functionalized gQDs showed a high long-term stability, the ligand exchange protocol was modified (chapter 7.6.3). In detail, 20 or 200 CLP molecules per NP were added to the reaction mixture. Here, it is also assumed that only half of the CLP molecules bind to the NP surface. Therefore, 10 or 100 CLPs are estimated to bind to the gQD surface after ligand exchange. NPs with native, MUTAB, MUA and mixed MUA-CLP ligand shell were characterized via DLS (Figure 8.22). The fluorescence of the gQDs may play a significant role in the measurement method. The wavelength of the laser used as light source inside the *Zetasizer* is close to the range of the excitation wavelength of the gQDs. In conclusion, the detected light might correspond not only to scattered light by the NPs but also light emitted by the gQDs themselves. An attempt was made by adding copper(II) chloride to the NP solution to quench the fluorescence and avoid possible interference. However, no change was detected (data not shown), which might be attributed to the stabilizing ligand shell or insufficient excitation of the gQDs. The final measurements were carried out without any quencher. All results are summarized in Table 5.12.

Table 5.12: Summary of DLS measurements on gQDs with different ligand shell composition.

Sample	D _{DLS} [nm]	PDI
Native	20.64	0.20
MUTAB	26.27	0.50
MUA	24.65	0.42
MUA-CLP(10)	26.10	0.31
MUA-CLP(100)	35.44	0.43

The hydrodynamic diameter of gQDs with a native ligand shell composed of oleic acid and oleyl amine in hexane is 20.64 nm. Moreover, a PDI of 0.20 is observed. After phase transfer and ligand exchange, an increase in D_{DLS} and PDI is observed. An increase in hydrodynamic diameter is caused by water molecules arranged around the ligand shell. For MUTAB-stabilized particles, a PDI of 0.50 is observed. A higher PDI may be caused by agglomeration or broader distribution of particles. Since the observed PDI is higher in comparison to particles with native ligand shell, the functionalized particles seem to be less stable. The argument for a lower stability is in accordance with the observed low long-term stability of these particles. MUA-stabilized particles feature a larger PDI than gQDs with a native ligand shell, indicating a more disperse sample and supporting the observation of broadening the emission distribution. From MUA only, to MUA with 10 CLPs to MUA with 100 CLP molecules per NP surface, a significant increase in hydrodynamic diameter is observed. The PDI drops from MUA only to mixed shell with 10 CLPs. The CLP can improve NP stability and could lead to more separated particles. The PDI of 0.31 for gQDs with a mixed shell composed of MUA and 10 CLP molecules is also the closest one to 0.20 (original value for native particles), found for gQDs with a native ligand shell. With 100 CLPs, the PDI increases again. Here, an increased PDI indicates more agglomeration.

Since a CLP functionalized cargo is desired for highly efficient encapsulation into Enc, further characterization is carried out on CLP-functionalized gQDs. TEM images of gQDs with mixed MUA CLP ligand shells are shown in Figure 5.27. Particles with either 10 or 100 CLP molecules per NP surface are in both cases well separated. Available TEM images offer limited information about some aggregates (Figure 5.27), which is indicated with higher PDI values in DLS measurements (Table 5.12). However, in Figure 5.27B some darker background is localized around the particles. Either some sort of imaging artifact or residual contamination might cause this shadowing.

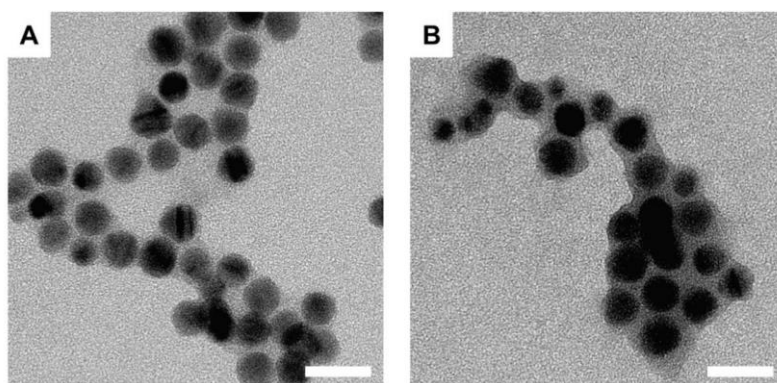


Figure 5.27: TEM image of water soluble gQDs with MUA and CLP functionalization. Particles are functionalized with MUA and either 10 (A) or 100 (B) CLP molecules per NP surface. Scale bars are 25 nm.

For further characterization, the ζ -potential of water soluble gQDs is determined (Figure 5.28). Due to the low stability of MUTAB stabilized gQDs, it was not possible to measure any ζ -potential. After ligand exchange to MUA, the ζ -potential is -62.3 mV. The addition of 10 CLP molecules on the NP surface leads to a less negative value of -42.6 mV. The change indicates that less MUA is bound, but CLP is present on the NP surface after an exchange of the negative charge. For MUTAB-functionalized AuNPs, a loss of charge is also observed, due to the exchange of CLP molecules (Figure 5.16). However, the functionalization with 100 CLPs per NP leads to an increase to -53.9 mV, instead of further decreasing the ζ -potential to lower negative numbers. For smaller AuNPs, 20 CLPs on the NP surface led to an additional loss of charge in comparison to 5 CLPs (Figure 5.16A). An oversaturation of CLP in the reaction solution could lead to a decreased efficiency of functionalization, due to formed disulfide bridges between CLPs. The difference in ζ -potential for both ligand shell compositions implies that only a certain amount of CLP can be added to the NP surface until saturation is achieved. As discussed in a previous chapter (chapter 5.2.2.2), the addition of CLP ligands to the NP surface leads to removal of charged ligands and therefore a decrease in ζ -potential. Though, for no other experiment that many CLPs were aimed to be on the NP surface and therefore no other source for comparison is available.

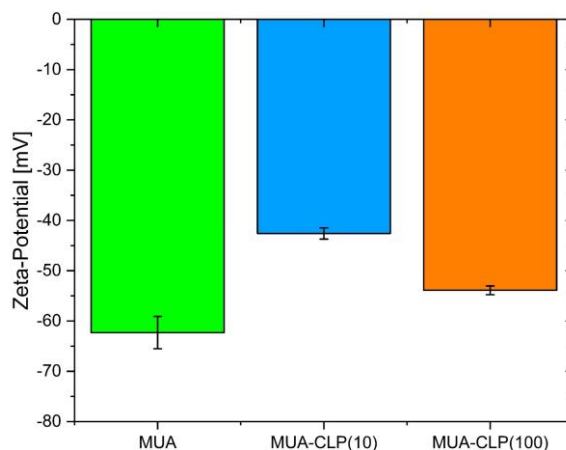


Figure 5.28: ζ -potential measurements of gQDs with different ligand shell composition. Ligand shell compositions based on MUA (green) or MUA mixed with CLP (blue, orange) feature negative ζ -potentials.

Due to the availability of two differently ligand shell systems, first MUA and CLP functionalized gQDs will be discussed. For effective disassembly, the protein is disassembled at pH 1.0. In comparison, for CLP-functionalized AuNPs of similar size, the best reassembly condition for encapsulation into Enc variants is a 20 mM phosphate buffer at pH 7.0 with 350 mM NaCl. As an initial test, this condition was tested with gQDs with 10 and 100 CLPs per NP. Negative stained TEM images of the reassembled samples are presented in Figure 5.29.

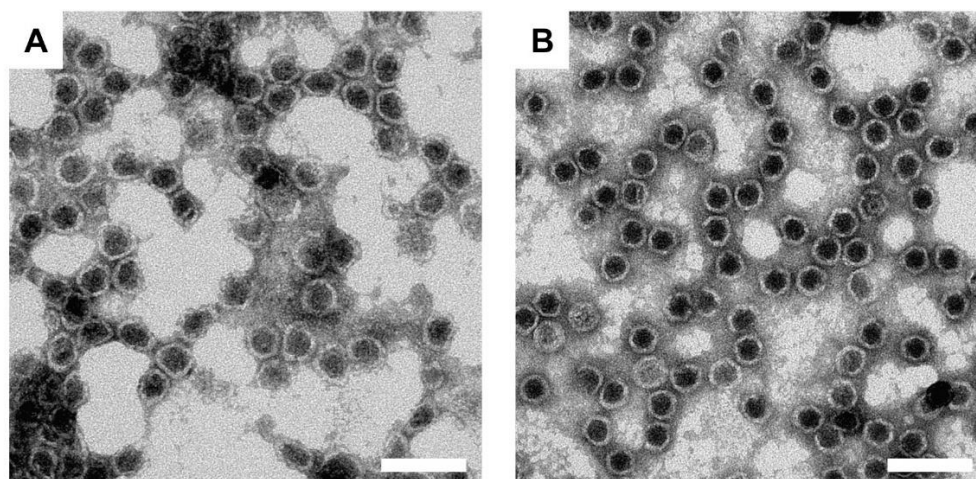


Figure 5.29: Negative stained TEM images of initial gQD encapsulation test. The encapsulation was aimed for gQDs functionalized with MUA and 10 (A) or 100 (B) CLP molecules on the NP surface. Scale bars are 50 nm.

Based on the TEM images in Figure 5.29, it is not possible to evaluate the success of the encapsulation. Despite the uneven staining, the spherical protein container shape and hexagonal morphology is especially apparent in Figure 5.29B. On the other hand, in Figure 5.29A, the protein shape is less preserved. In both images, no free gQDs are observed. Moreover, the container cavity is mostly quite darkish, in comparison to some single containers with a more grayish appearing contrast. QDs give less contrast in TEM due to their lower electron density compared to Au. Therefore, it is not possible to clearly determine if gQDs are encapsulated or not using the stained TEM images. The darker contrast inside the protein cavity and no visible free gQDs may indicate a successful encapsulation. To distinguish if CdSe/CdZnS particles are present inside the container cavity, energy dispersive X-ray spectroscopy (EDX) measurements could be carried out. Moreover, unstained TEM images of the same sample could give details as to whether any gQDs are present. Unfortunately, it was not possible to further investigate both TEM samples due to rapid grid ageing. A leftover sample was further processed and characterized. Along these lines, UV-Vis spectra were recorded (Figure 5.30). For comparison, gQDs with a mixed MUA-CLP ligand shell and Enc^(neg) are shown. Water soluble gQDs absorb over the complete shown range, while Enc^(neg) does not show any significant absorption for higher wavelengths. On the other side, the sample with possibly encapsulated gQDs in Enc^(neg) (gQDEnc^(neg)) does show absorption over the complete range. The absorption at wavelengths above 400 nm is caused by the co-existence of gQDs

and $\text{Enc}^{(\text{neg})}$ in solution and does not give direct information about whether the particles are encapsulated or not. Fluorescence emission spectra would result in the same conclusion. Therefore, protein purification will be carried out to remove residual gQDs and protein.

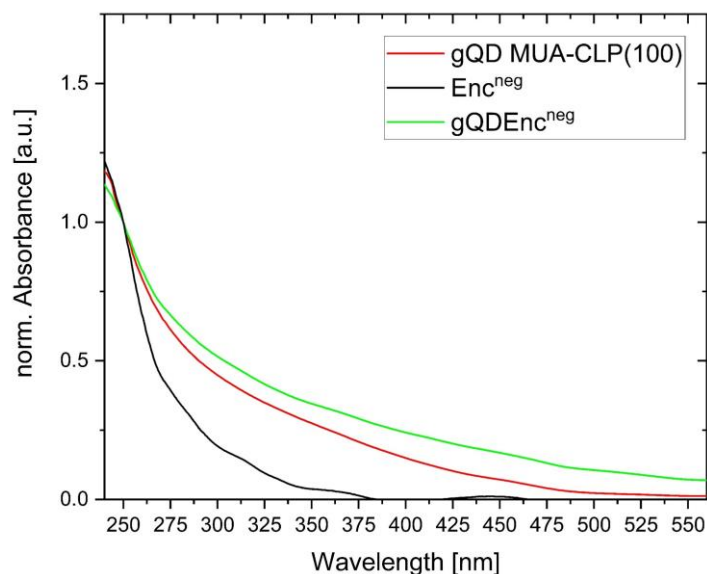


Figure 5.30: Normalized UV-Vis spectra of encapsulation test with gQDs into $\text{Enc}^{(\text{neg})}$ prior to any protein purification.

Typically, after nanoparticle reassembly the solution is concentrated towards a few milliliters and applied to IEC. Due to visible aggregation in sample concentration, IEC was not performed to avoid further loss and SEC was carried out immediately. The loss of samples is also observable in SEC (Figure 5.31A). At the elution volume for $\text{Enc}^{(\text{neg})}$ at around 12.7 mL, low values in absorbance are detected. For $\text{AuEnc}^{(\text{neg})}$ with the same protein amount used for encapsulation, values in a higher region are observed (Figure 5.22). Both observations indicate a less efficient encapsulation and decreased sample stability. The cargo should not affect the protein stability. Therefore the reassembly process might not yet be optimized for this kind of cargo with ligand shells. Charge repulsion between negatively charged particles and protein might decrease protein reassembly efficiency or stability during reassembly. Especially the absorbance at 380 nm and 400 nm is not intense. Weak absorbance might further indicate very inefficient encapsulation. Since the protein does not absorb at 380 nm and 400 nm, a higher peak at the same elution volume as the protein is expected for high encapsulation efficiency. Non-encapsulated gQDs would either elute later due to their smaller size or strongly interact with the column and bind.

Nevertheless, the protein fractions were collected, and the emission spectra were recorded (Figure 5.31B). For reference, the non-encapsulated particles and empty $\text{Enc}^{(\text{neg})}$ are also shown in the normalized emission spectra. All three measurements were carried out with the same settings.

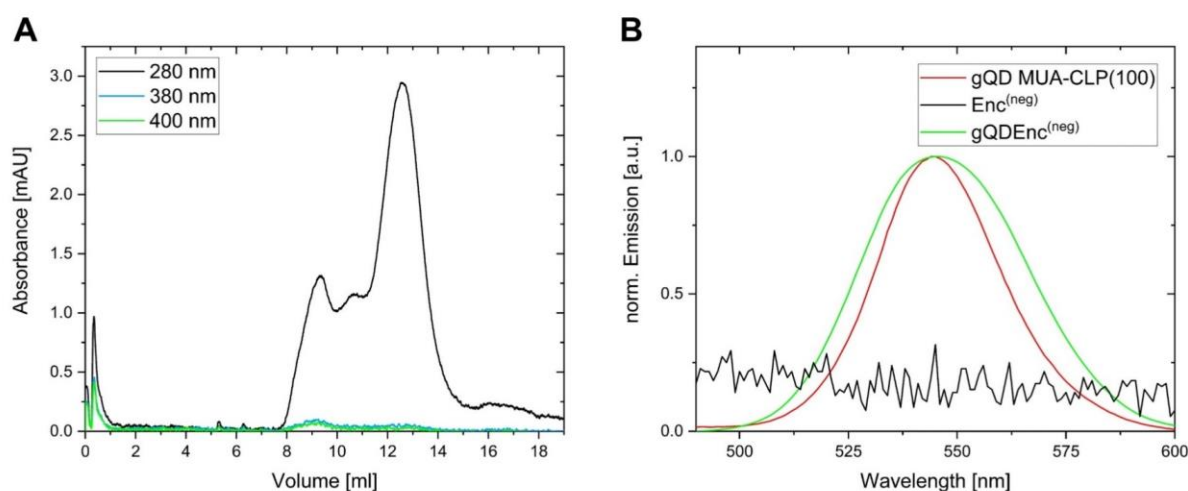


Figure 5.31: Purification and characterization of gQDEnc^(neg). Absorbance at 280 nm, 380 nm and 400 nm is tracked for the SEC of gQDEnc^(neg) (A). Normalized emission spectra of the purified sample and references. (B) Excitation wavelength: 350 nm.

The empty protein container does not emit light in the region from 500 nm to 600 nm. Fluorescence is only observed for non-encapsulated gQDs and the gQDEnc^(neg) sample. A small shift from 545 nm to 546 nm is observed after NP encapsulation. The width of the emission peak for gQDEnc^(neg) is significantly broader than for the non-encapsulated gQDs. The protein container itself may act as an additional ligand shell, causing the broadening. A broadening effect was also observed for the initial ligand shell functionalization of gQDs (Figure 5.26). The ligand shell strongly influences the optical properties of the semi-conductor material.^[300,301] Based on the emission of the sample eluted at around 12.7 mL in SEC, a successful encapsulation of gQDs is likely.

In addition, stained and unstained TEM images of gQDEnc^(neg) were prepared (Figure 5.32). In unstained TEM images, gQDs are found. Since the sample from SEC is imaged without any staining, no protein can be observed, only particles that feature enough contrast like gQDs. For both samples, aggregates are observed. Separated objects but also clusters appear. The particles and containers show the same visible features in the TEM images. The presence of gQDs in unstained images prove the encapsulation into Enc^(neg).

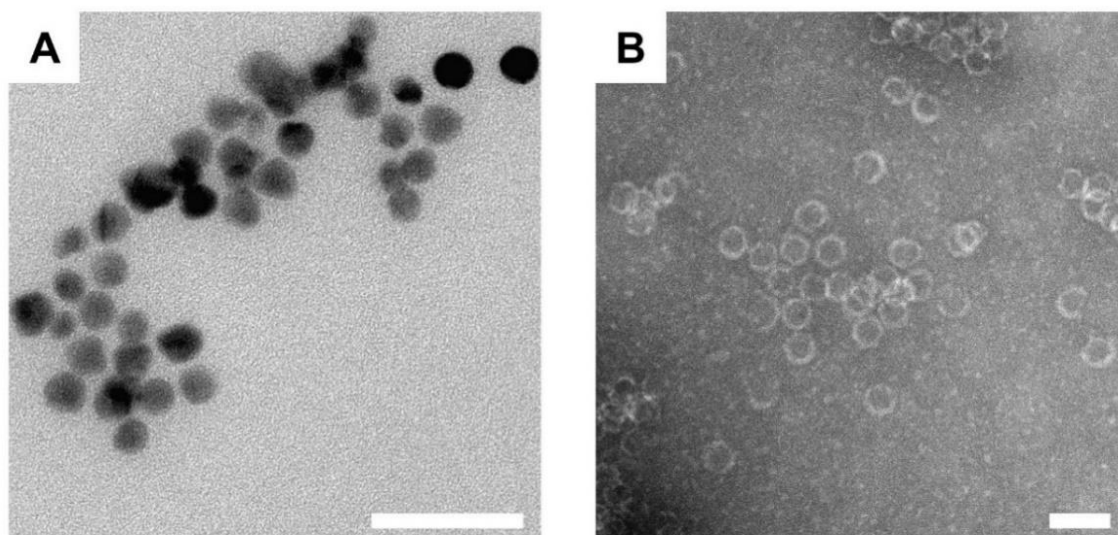


Figure 5.32: TEM images of gQDEnc^(neg) after SEC. Unstained (A) and stained (B) TEM images of gQDEnc^(neg). Scale bars are 50 nm.

To a certain extent, initial tests to encapsulate gQDs into negatively surface charged Enc^(neg) were successful. Characterization via emission spectra and TEM images of the protein fraction collected after SEC strengthen the hypothesis that gQDs were successfully encapsulated. Still, the encapsulation efficiency is low and high sample loss is observed. Additional characterization such as EDX mapping of the TEM grids would give further insight into the protein container interior.

5.2.3.2 Encapsulation of gQDs functionalized with PEG ligands

The previously shown approach to achieve water soluble gQDs was based on a biphasic system with small organic ligands. Another approach is based on mixing particles and PEG ligands suspended in chloroform and incubation over night at 65 °C (chapter 7.6.3). Afterwards, the solvent is removed with a rotary evaporator. Particles are resuspended in a 1:1 mixture of ultrapure water and ethanol. Finally, the suspension is centrifuged at a higher speed and only the optically clear supernatant is used. DRAGNEA and co-workers applied this procedure to functionalize QDs with PEG ligands, which were later incorporated into viral particles.^[204,302] Here, the approach is applied on gQDs using PEG ligands with thiol anchoring groups and amine functionalization (Figure 5.25). The suitability of PEG ligands to provide water solubility and biocompatibility for metal and semi-conductor nanoparticles has already been shown.^[303,304] Here, two PEG ligands with different PEG-MWs are used. Based on the MW of 3 kDa and 5 kDa the number (n) of repeating ethylene glycol units are estimated to be approximately 68 and 114, respectively. Therefore, TPEG-3 and TPEG-5 differ in their chain length and are significantly longer than previously applied ligands. In the end, the PEG chain does not end up as a straight chain. Instead, randomly coiled structures are expected.^[305,306]

Moreover, PEG ligands with amine functionalization were chosen, since a negative charge may decrease the encapsulation efficiency and a system with negatively charged MUA ligands is already established.

Purified gQDs functionalized with TPEG-3 and TPEG-5 are analyzed via DLS measurements (Figure 8.23). The results are summarized in Table 5.13. Particles with the native ligand shell are listed as a reference.

Table 5.13: Summary of DLS measurements on gQDs with different PEG ligands.

Sample	D _{DLS} [nm]	PDI
Native	20.64	0.20
TPEG-3	40.65	0.40
TPEG-5	56.40	0.52

Functionalized gQDs with PEG ligands result in larger hydrodynamic diameters than with shorter ligands such as MUA or MUTAB. Particles functionalized with TPEG-5 ligand exhibit further increased hydrodynamic diameters compared to TPEG-3 functionalized particles due to the longer ligand. Generally, with PEG ligands an increased PDI does not exclusively indicate larger size distribution or inhomogeneity of the sample. Due to the randomly arranged coiled chains, an increase of PDI is also expected. Therefore, a clear statement as to whether the particles tend to agglomerate or not cannot be made. By visual inspection, the particles show long-term stability for at least several days. Still, the hydrodynamic diameters indicate that these particles with ligand shell are quite large. To further evaluate the success of the ligand exchange, TEM samples were prepared (Figure 5.33). For each sample, well separated gQDs are observed. In both samples, some agglomeration also occurred. Based on available TEM images, most of the gQDs seem to be well stabilized. Further purification steps might decrease residual agglomerates. The current protocol focuses on centrifugation steps, which could be carried out at an even higher speed or for longer times. Additional treatment with small pore filters might increase sample homogeneity and remove larger aggregates.

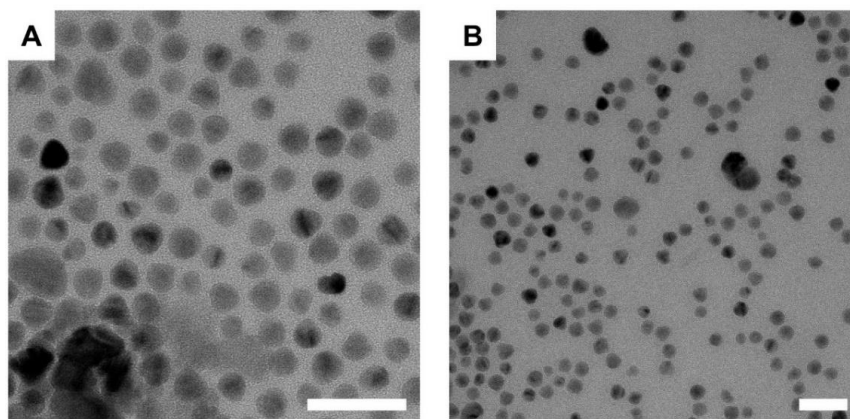


Figure 5.33: TEM images of gQDs functionalized with PEG ligands after ligand exchange. TPEG-3 (A) and TPEG-5 (B) stabilized gQDs. Scale bars are 50 nm.

In addition, the ζ -potential of water soluble TPEG-3 and TPEG-5 functionalized gQDs is shown in Figure 5.34. In general, small positive values are observed. In published works by the WELLER and PELLEGRINO groups, QDs are encapsulated in PEG-functionalized polymers. Depending on the end group, small ζ -potentials can be observed in deionized water.^[307,308] Particles with TPEG-3 feature an almost three times higher positive ζ -potential than those functionalized with TPEG-5. Due to the longer chain length, a considerable amount of charge might be covered by ethylene glycol units or arranged water molecules around the ligand shell. Since a positive ζ -potential is beneficial for encapsulation experiments, gQDs with TPEG-3 seem to be more suitable for encapsulation into Enc. Due to time restrictions, no CLP-functionalization was carried. However, it is unclear if the CLP-functionalization can be achieved with the described procedure. The ligand exchange takes place at 65 °C and the stability of the CLP at this temperature is not yet known. In addition, the CLP might be too short in comparison to TPEG ligands. Moreover, a protocol to add the CLP after the functionalization with TPEG ligands is not yet established. For first tests the established protocol for the AuNP CLP functionalization of already water soluble AuNPs is considerable and could be adapted.

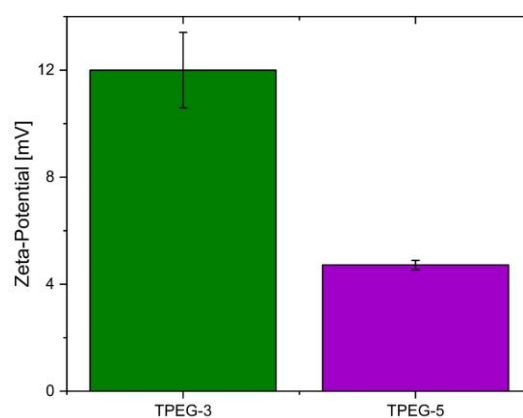


Figure 5.34: ζ -potential measurements of gQDs with PEG ligands. Particles are functionalized with two PEG ligands with different chain length.

In the end, it was possible to achieve water soluble gQDs with two ligand shell systems. One ligand shell system is based on negatively charged MUA with additional CLPs. For that particle system, the loading and yield of loaded protein after encapsulation seems low. Therefore, another ligand system based on PEG ligands was established. TPEG-stabilized particles feature positive ζ -potentials and show promising properties for encapsulation.

So far, the encapsulation was carried out with a reassembly buffer consisting of 20 mM phosphate, a pH of 7.0 and a defined amount of NaCl. Prior to encapsulation, particle stability and compatibility towards different buffers were tested. In detail, TPEG-stabilized gQDs show high stability in HEPES pH 6.0, phosphate pH 7.0, Tris pH 7.5 and Tris pH 9.0. After incubation for 1 h and centrifugation at 14000 g for 10 min, an extremely small pellet is observed for each buffer. A longer incubation time and repeated centrifugation did not result in more agglomeration. Agglomerates were most likely less stable, precipitated and were pelleted. However, a phosphate buffer at pH 7.0 was chosen since this buffer system was already well established. Changing the buffer might also decrease the reassembly efficiency. Buffers at pH 9.0 or 6.0 are not yet tested, but should also work, since the reassembly is triggered by dilution and pH change from very acidic condition towards neutral.^[9] Both kind of TPEG-stabilized particles showed stability in the same buffer used for the encapsulation of 13 nm large AuNPs (20 mM phosphate buffer at pH 7.0 with 0.35 M NaCl).

The encapsulation of gQDs stabilized with TPEG-3 or TPEG-5 is carried out according to an established protocol (chapter 7.7.4). After reassembly of Enc^(neg), protein purification is performed. For the encapsulation of TPEG-3 no protein peak at a conductivity of 52 mS/cm is observed in IEC (Figure 5.35A). On the other hand, the encapsulation with TPEG-5 stabilized particles feature a protein peak at 52 mS/cm (Figure 5.35B). Nevertheless, the fractions of the peaks eluted at around 45 mS/cm were collected. Each peak at 45 and 52 mS/cm was investigated via SEC (Figure 8.24; Figure 5.35C). The species mostly contains aggregated protein (8.5 mL) and only a small amount of pure protein containers. However, the protein species eluted at 52 mS/cm derived from IEC show less aggregates, but significantly more pure protein (Figure 5.35D).

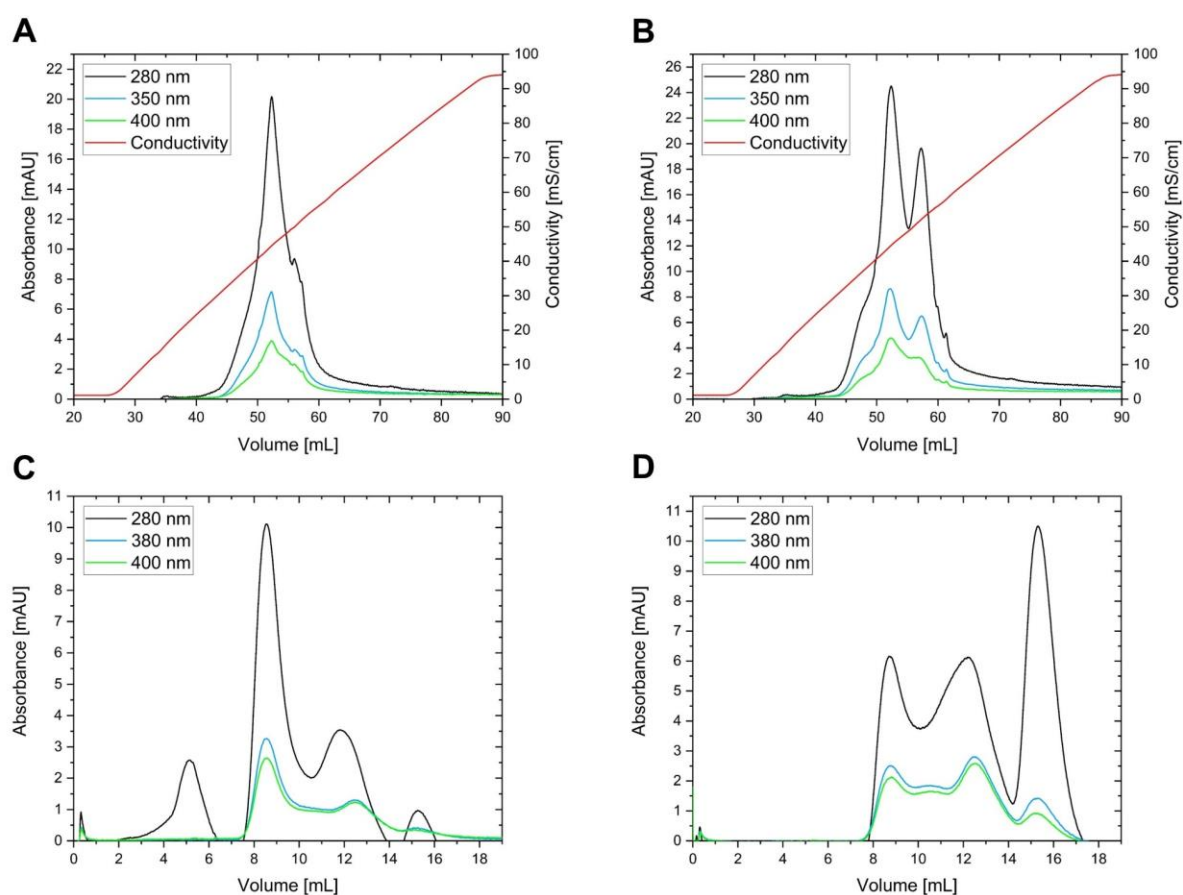


Figure 5.35: Purification of $\text{Enc}^{(\text{neg})}$ gQDs encapsulation tests. IEC for TPEG-3 (A) and TPEG-5 (B) stabilized gQDs used for encapsulation into $\text{Enc}^{(\text{neg})}$. $\text{Enc}^{(\text{neg})}$ elutes at 52 mS/cm. The first (C) and second (D) eluted species from IEC (B) were separately purified via SEC.

Typically, three peaks can be observed in SEC purification of $\text{Enc}^{(\text{neg})}$: Larger aggregates elute at 8.6 mL, while dimeric protein containers elute at 10.5 mL and monomeric protein containers at 12.6 mL. For each SEC, there is no maximum absorbance for 280 nm at 12.6 mL. Instead, a shift to smaller volumes (12 mL) is observed (Figure 5.35). In previous SEC experiments, no peak between 10.5 mL and 12.6 mL was observed. Especially in Figure 5.35C, no shoulder or clear second peak is detected at 12.6 mL for 280 nm. The maximum at 280 nm shifts from 11.8 mL in Figure 5.35C to 12.2 mL in Figure 5.35D. The absolute value of 280 nm is 3.5 and 6.1 mAU, respectively. With an almost doubled absorbance, the elution volume is shifted towards 12.6 mL. Due to the low absorbance, the shift in elution volume might also be attributed to inaccuracies in the measurements. On the other hand, the absorbance at 380 nm and 400 nm is located at 12.6 mL with even lower numbers in absorbance. It is not yet clear what exactly causes the shift in absorption. Maybe a mix of protein containers with gQDs and a larger protein species formed. Not correctly reassembled protein containers, that are slightly larger and may cause the shift towards 12 mL.

To evaluate the relative success of all shown gQD encapsulation experiments, the absorbance ratios at 380/280 and 400/280 are compared (Table 5.14). Due to the assumption that the

absorbance at 280 nm is shifted towards smaller volumes, the maximum is recognized to be at 12.6 mL and compared with the maxima at 380 nm and 400 nm at 12.6 mL.

Table 5.14: Comparison of absorbance ratios to evaluate encapsulation of gQD into Enc^(neg).

protein	gQD ligand	A380/280	A400/280	SEC
Enc ^(neg)	MUA-CLP	0.01	0.01	Figure 5.31A
	TPEG-3	0.23	0.10	Figure 8.24
	TPEG-5	0.45	0.42	Figure 5.35D

In conclusion, the encapsulation of negatively charged gQDs with CLP into Enc^(neg) was not very efficient. A high ratio indicates the presence of many gQDs. For this sample, the ratios are both very low. On the other side, encapsulation of gQDs with positive ligand shell even without CLP already results in higher absorption ratios. Especially for TPEG-5-functionalized gQDs ratios of 0.45 and 0.42 for A380/280 and A400/280, respectively are the highest observed. Due to the low amount of protein used in these initial experiments, it was not possible to prepare negatively stained TEM images to evaluate, if both gQDs and completely reassembled protein containers are visible. Despite featuring the highest D_{DLS} and lowest positive ζ -potential, gQDs with TPEG-5 yielded the purest gQD loaded Enc^(neg) sample to this point. The question about the encapsulation efficiency is not addressed and a suitable technique or combination of methods is not yet applied. As mentioned earlier, EDX mapping of negatively stained TEM samples might resolve the question. Filled protein containers should feature spherically distributed metals such as Cd and Zn. Both metals do not appear in the native protein. Moreover, high-resolution TEM might be applied to investigate the protein container cavity in more detail than with conventional TEM. With conventional TEM, the contrast is not sufficient to observe any cargo inside the protein cavity. The cavity might be imaged with higher resolution thus visualizing the gQDs. The particles are periodically ordered matter, the protein container is not. Therefore, in TEM images a filled protein container with a periodically ordered material should contain a gQD. With both TEM-based approaches (EDX mapping and HR-TEM), the encapsulation efficiency could be determined by counting the number of loaded and empty containers.

Particles functionalized with PEG ligands feature a positive ζ -potential and were used in encapsulation experiments. Apparently, the encapsulation does not seem to be successful due to the indication of uncomplete reassembly of protein containers observed in SEC experiments. TEM samples before and after SEC might give further inside if protein containers formed or not. Still, it would not be possible to see if the protein containers are partially or completely reassembled.

5.2.4 Protein functionalization

5.2.4.1 Integration of fluorophores into positively charged ferritin

In previous chapters the encapsulation of inorganic cargo into the protein container was discussed. Another approach to generate a new protein building block with novel properties is the incorporation of fluorophores. Previously, the loading of ferritin with fluorophores was established. In detail, the loading was mainly carried out by either diffusion or statistic encapsulation.^[12] A new approach was pioneered within the BECK group by MADE BUDIARTA and HENDRIK BÖHLER. The thiol-maleimide reaction (chapter 2.2.1.1) is applied to label non-native cysteine residues in ferritin with maleimide fluorophores. In a recent publication, the labeling of the Ftn^(neg)-Cys cavity with fluorophores is shown.^[12] The characterization of Ftn^(pos)-Cys is shown in a previous chapter (5.1.4).

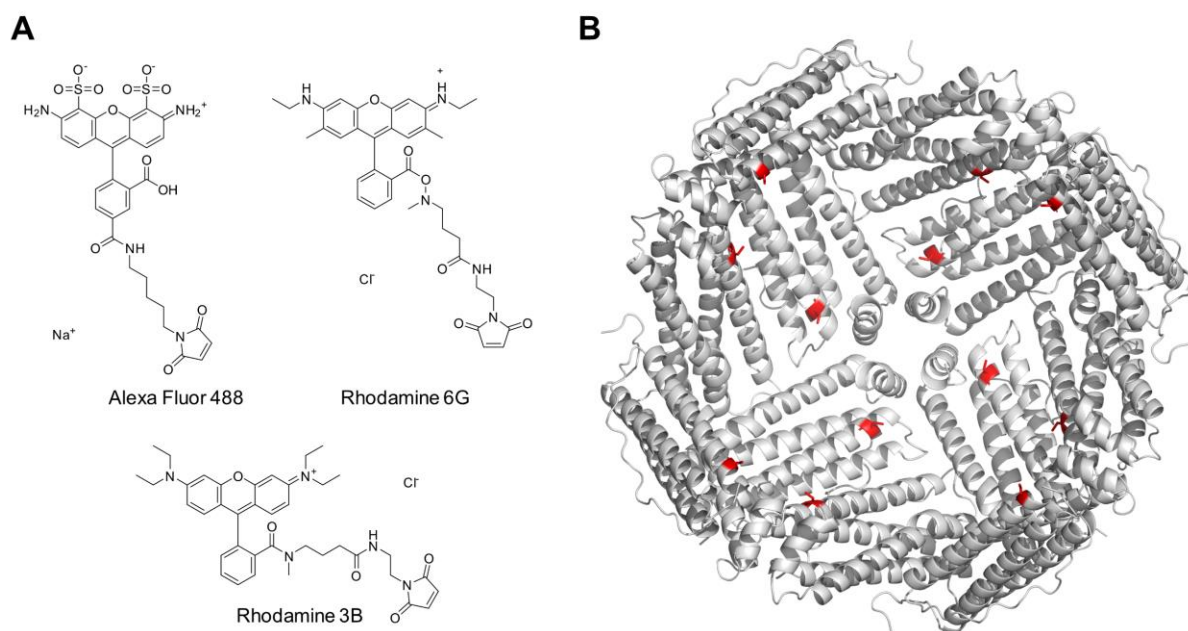


Figure 5.36: Overview of fluorophores used to label Ftn^(pos)-Cys via thiol-maleimide reaction. Maleimide-functionalized fluorophores (A): Alexa Fluor 488, rhodamine 3B and rhodamine 6G. Cutout of Ftn^(pos)-Cys container (B). Cysteine at position 53 is highlighted in red. The shortest distance between C- α atoms is 2.6 nm.

An overview of the chosen maleimide-functionalized fluorophores is given in Figure 5.36A. In later applications it is planned to achieve strong interactions between the fluorophore's dipole and the AuNPs plasmonic properties. Therefore, three fluorophores with different optical properties were chosen. Each of the three fluorophores cover a different absorbance and emission range (Figure 8.25 and Figure 8.27). Later, it is planned to investigate properties between for example fluorophore and AuNP, where the fluorophore emission overlaps with the plasmon resonance of the AuNP. Via thiol-maleimide reaction, the fluorophores will label Ftn^(pos)-Cys at the introduced Cys at position 53. The maximum amount of covalently bound fluorophores is 24 per container because the ferritin container is constructed out of 24 subunits

and only one Cys per subunit is present (Figure 5.36B). A full labeling of Ftn^(pos)-Cys would increase the number of fluorophores in positively charged Ftn from around 2 molecules to 24. Moreover, the labeling will enable fixed positions and distances between the fluorophores to yield defined optical properties in three dimensional assemblies. In detail, Alexa Fluor 488 (AF488), rhodamine 6G (Rh6G) and rhodamine 3B (Rh3B) are coupled with the ferritin container.

To label the inner protein surface, the protein container must be disassembled (Figure 5.37). The ferritin disassembly can be triggered by either pH or chaotropic conditions (chapter 7.7.5). Ftn^(pos)-Cys is incubated in either a buffered solution at pH 2.0 or in at least 7 M Gua. The disassembly via pH 2.0 or 7 M Gua might influence the efficiency of the labeling. For the disassembly triggered by acidic pH, most of the protein container is strongly charged and separated into its subunits. High concentrations of chaotropic agents such as Gua destroy non-covalent forces in the protein assembly and lead to disassembly due to unfolding. Moreover, the protein refolding might be affected with chaotropic agents and yield less protein. Therefore, the choice of disassembly may affect the labeling with fluorophores. After incubation for 4 h at RT, the coupling of fluorophore to protein takes place. The disassembly solution is diluted with a buffer of neutral pH and containing 1 M NaCl. Then two equivalents of fluorophore are added. The coupling and reassembly occur during incubation overnight at RT. The next day, the sample is washed to remove excess fluorophore.

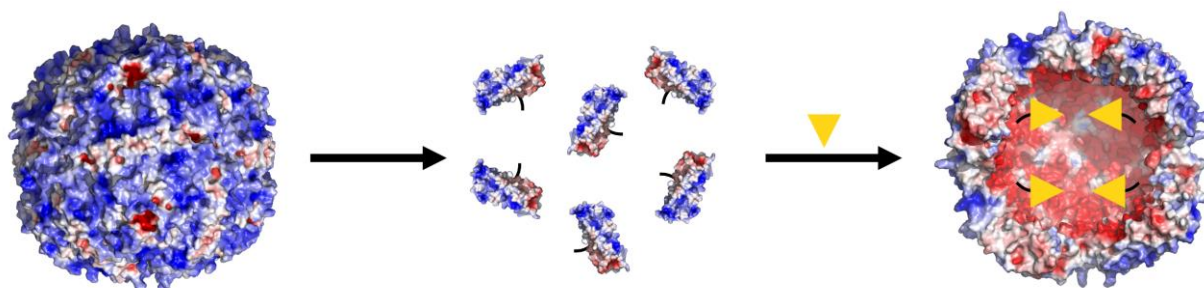


Figure 5.37: Schematic illustration of Ftn^(pos)-Cys fluorophore labeling. The ferritin container is first disassembled into its subunits by pH or chaotropic conditions. Fluorophores (yellow) are added to the disassembled Ftn^(pos)-Cys for protein labeling. After reassembly, the inner cavity of the protein container is labeled with fluorophores. Cysteine residues are outlined in black.

5.2.4.2 Purification of fluorophore-loaded positively charged ferritin

As a first experiment, Ftn^(pos)-Cys labeled with Rh3B after disassembly with pH 2.0 and 7 M Gua is purified (Figure 5.38). Both samples were treated the same way, only differing in their disassembly. In size-exclusion chromatography, Ftn^(pos)-Cys is supposed to elute at around 58 mL, which is also the case for the labeled protein. The typical absorbance at 534 nm and 568 nm for Rh3B (Figure 8.25) is well pronounced at the elution volume of the protein,

indicating successful labeling. Uncoupled fluorophore would elute at a higher elution volume, due to its smaller size. The protocol seems to be very suitable due to the absence of larger aggregates at around 52 mL and only pure containers being present. In direct comparison, the overall absorbance is lower for the Gua disassembled sample (Figure 5.38B). Moreover, the absorption ratios $A_{534}/280$ and $A_{568}/280$ between both experiments are compared (Table 8.7). Both ratios are slightly higher for the sample disassembled by acidic pH. Therefore, later coupling reactions are based on the acidic approach to yield more protein with a potentially higher labeling efficiency.

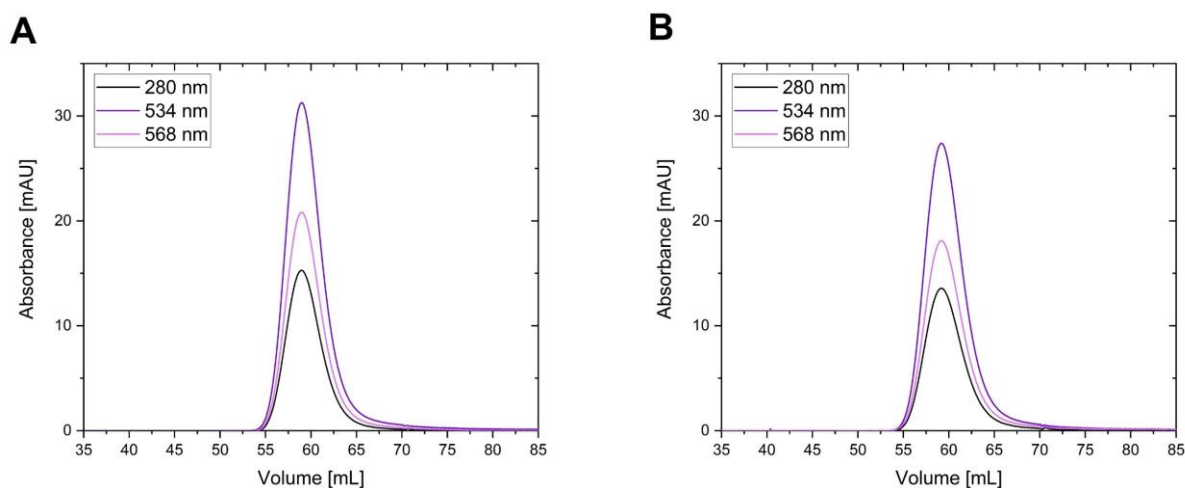


Figure 5.38: Comparison of two SECs of Rh3BFtn^(POS)-Cys. Prior the coupling, the protein was either disassembled at pH 2.0 (A) or with 7 M Gua (B).

After establishing the coupling protocol and purification of Rh3B labeled Ftn^(POS)-Cys, further labeling was carried out. In detail, Rh6GFtn^(POS)-Cys and AF488Ftn^(POS)-Cys were also purified via SEC (Figure 5.39). Each labeled protein features a significant absorption at the fluorophore-specific maximum and elutes at the proper volume, expected for the full-size container.

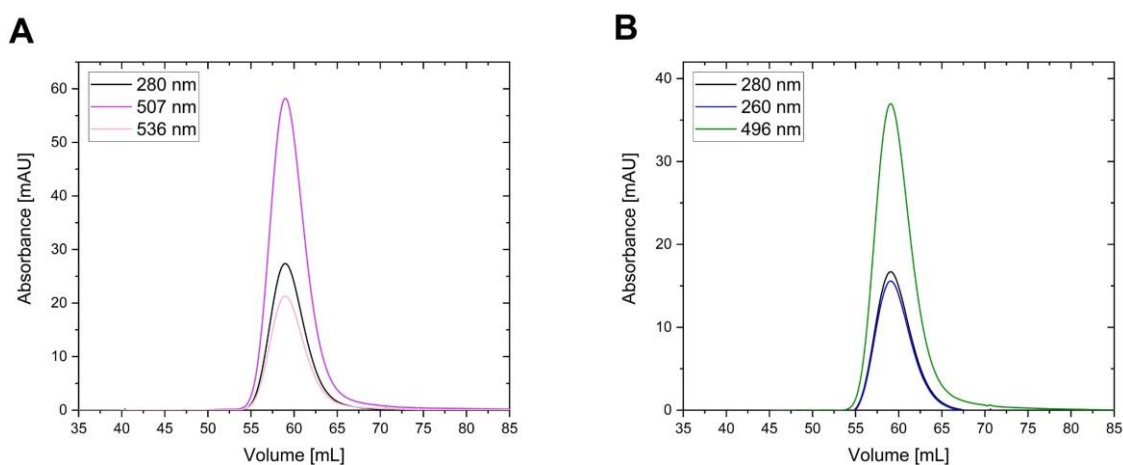


Figure 5.39: SECs of fluorophore-labeled-Ftn^(POS)-Cys. Ftn^(POS)-Cys is either labeled with Rh6G (A) or AF488 (B).

After purification of fluorophore-labeled Ftn^(POS)-Cys, the emission spectra were recorded (Figure 8.27). The absorbance and emission maxima are summarized in the following Table

5.15, with each labeled protein featuring the characteristic absorbance and fluorescence of the individual fluorophore. Three novel fluorescent protein variants are now available.

Table 5.15: Summary of absorbance and emission maxima for fluorophore-labeled Ftn^(pos)-Cys.

Sample	Absorbance [nm]	Emission [nm]	Spectra
AF488Ftn ^(pos) -Cys	496	519	Figure 8.27A
Rh3BFtn ^(pos) -Cys	534 / 568	612	Figure 8.27B
Rh6GFtn ^(pos) -Cys	507 / 536	559	Figure 8.27C

In conclusion, Ftn^(pos)-Cys protein containers were successfully labeled and purified. Prior protein crystallization, additional characterization is carried out and discussed in the next chapter.

5.2.4.3 Determination of degree of fluorophore labeling

The degree of fluorophore labeling is not yet addressed. Each commercial (*ThermoFisher Scientific; ATTO-TEC*) fluorophores supplier proposes different approaches to determine if a full or partial labeling is achieved. In detail, each method is based on UV-Vis measurements, but these methods cannot be applied to this system here. First, these methods are based on the protein concentration after labeling. Some fluorophore-labeled protein is lost due to centrifugation steps to concentrate the reassembly solution. Small amounts of colored precipitate are observed. Due to protein loss, the degree of labeling would be incorrect. Second, for both rhodamine-based fluorophores the degree of labeling is proposed to be determined on the absorption maximum of the fluorophore. Due to the coupling, the maxima is not only shifted but the second maximum also increases in intensity. Therefore, a measurement based on the absorbance maximum is not possible. A third possibility is to determine the concentration of the uncoupled dye. Due to the concentration step, uncoupled dye passes through the filter, and the concentration could be determined. Besides, aggregated colored protein is observed. Whether or not the protein is aggregated throughout stronger interactions with the dye is not clarified. Therefore, additional fluorophores might be extracted from the solution. The final concentration of uncoupled fluorophore might be lower than measured and would result in a higher degree of labeling. Additionally, the protein container is dis- and reassembled. The possibility of randomly encapsulated fluorophore molecules must be considered since this might lead to incorrect results. In conclusion, a more suitable approach was desired.

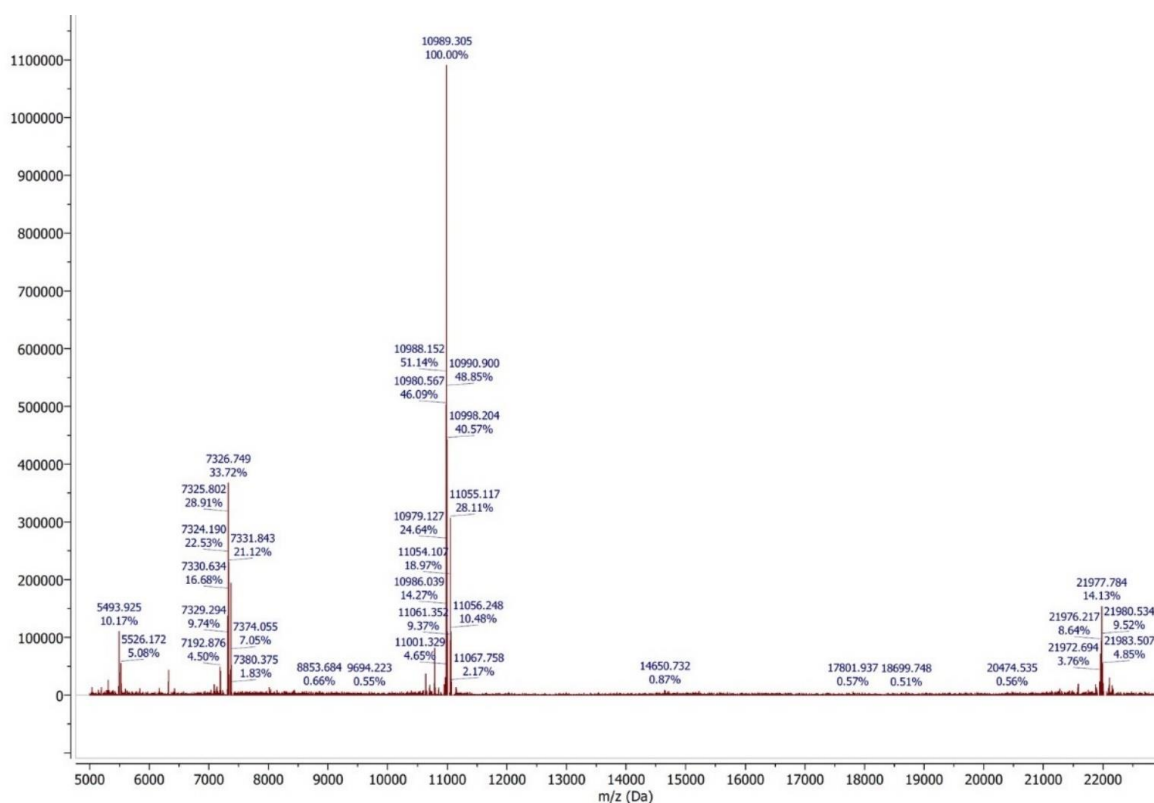


Figure 5.40: MALDI-TOF MS spectrum of AF488Ftn^(pos)-Cys.

A method to determine if every protein subunit of the container is labeled or not can be achieved via mass spectroscopy. Labeled and unlabeled protein significantly differ in molecular weight. If labeled and unlabeled protein are present, two species would be expected. Since ESI MS turned out to be very suitable to determine protein masses, fluorophore-labeled samples were submitted for ESI MS. Surprisingly, it was not possible to determine any protein mass via ESI MS. In detail, no protein was detected at all (data not shown). In a recent publication by DRAGNEA and co-workers, the ionization of fluorophore-labeled macromolecule was not possible. No protein mass was accessed via ESI, only via MALDI-TOF MS.^[289,309] Therefore, MALDI-TOF was also applied to determine the mass of fluorophore-labeled Ftn^(pos)-Cys. MS spectra for AF488 labeled Ftn^(pos)-Cys is shown in Figure 5.40. Rhodamine-labeled protein MS spectra are found in Figure 8.26. Via MALDI-TOF, it was possible to access the molecular mass of the fluorophore-labeled protein. For example, in Figure 5.40 positively charged protein molecules $[M]^+$, $[M]^{2+}$, $[M]^{3+}$ and $[M]^{4+}$ for AF488Ftn^(pos)-Cys are observed. Moreover, no single or multiple charged molecules corresponding to the unlabeled protein appear. In Table 5.16 the observed and calculated m/z values for AF488Ftn^(pos)-Cys are listed. Additionally, calculated m/z values for Ftn^(pos)-Cys are shown.

Table 5.16: Comparison of unlabeled and AF488 labeled Ftn^(pos)-Cys charged ions in MALDI-TOF. Values for Ftn^(pos)-Cys are calculated based on the prior determined [M]⁺ in chapter 5.1.4.

Molecular masses [g/mol]	[M]⁺	[M]²⁺	[M]³⁺	[M]⁴⁺
Ftn ^(pos) -Cys	21273.9	10702.6	7135.0	5351.3
AF488Ftn ^(pos) -Cys	21977.8	10989.3	7326.7	5493.9

None of the expected charged molecules for the unlabeled protein Ftn^(pos)-Cys appear in MS spectra. Also, MS spectra for protein labeled with Rh3B or Rh6G do not feature any charged proteins corresponding to the unlabeled Ftn^(pos)-Cys (Figure 8.26). Due to the absence of unlabeled protein in MALDI-TOF, a labeling degree of 100 % is achieved for every fluorophore-protein combination. For the sake of completeness, the calculated molecular masses are compared with the measured masses (Table 8.8). For every labeled fluorophore-protein combination, the mass was determined showing a small deviation within a feasible error range from the calculated mass.

Finally, the degree of labeling was determined via MALDI-TOF. Complete protein labeling was achieved. Moreover, the novel building block for the assembly of binary protein lattices is completely characterized, purified and available for crystallization.

5.3 Protein crystallization towards binary superlattices

The upcoming chapter is about the crystallization of protein containers to achieve three dimensional assemblies. To find a suitable condition for protein crystallization empty proteins were used to screen commercially available conditions. Via robotic screening a high throughput is achieved. Various conditions with different buffers, pH values and precipitants were screened. In some cases, the protein concentration was varied as well.

In general, vapor diffusion was used as the crystallization method. For this technique, a drop containing protein and reservoir solution is prepared and either placed above (hanging drop) or next to (sitting drop) the reservoir solution. Due to a difference in concentration in the drop and reservoir solution, water diffuses until both solutions have reached an equilibrium. Crystals will grow during this process (Figure 5.41).^[310]

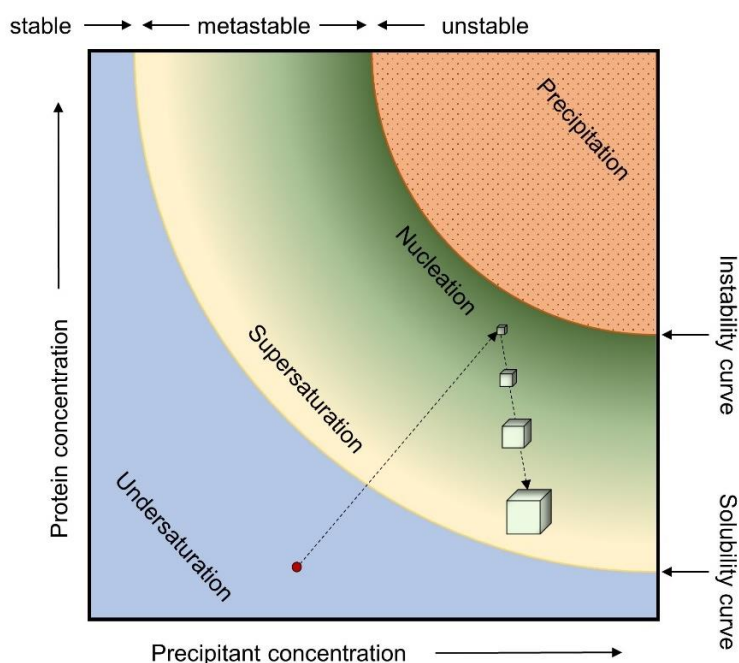


Figure 5.41: Schematic illustration of a protein crystallization phase diagram. The vapor diffusion crystallization route starts at the red dot. Figure adapted from RUPP.^[311]

First, the drop containing protein and reservoir solution starts in the undersaturated phase. Yet, no interactions between protein containers occur because the solution is too dilute. Diffusion of water out of the drop leads to an increase in protein and precipitant concentration and the drop reaches the nucleation zone. Nuclei formation and crystal growth happen simultaneously. Protein concentration decreases and only crystal growth occurs, without forming new nuclei.^[311]

The approach turned out to be very effective. Unitary and binary crystallization conditions for supercharged ferritin variants have been found by the BECK group (PDB: 5JJK, 5JKL, 5JKM, 6H6T, 6H6U). In the protein data bank (PDB), several hundred crystallization conditions for several ferritin variants from different organisms are reported from various research groups.

On the other hand, only two crystallization conditions for encapsulin are deposited. In detail, one of them is for the *T. maritima* Enc^(wt) (PDB: 3DKT). A cubic lattice with the space group $F4_132$ and $a = 669.04 \text{ \AA}$ was published by SUTTER *et. al.* The crystallization was carried out at 292 K in a vapor diffusion sitting drop experiment.^[217] The published condition could not be reproduced. Therefore, crystallization conditions for unitary negative and positive Enc, but also binary Enc conditions were aimed for (chapter 5.3.1).

In addition, hetero binary crystalline assemblies were investigated. MARCEL LACH initialized the screening of hetero binary crystals containing Ftn and Enc. His initial results were extended to assembling oppositely charged protein containers of different sizes loaded with nanoparticles or fluorophores towards novel biohybrid nanomaterials in this work (chapter 5.3.4).

Moreover, the stabilization of protein crystals was analyzed. In previous work, only glutaraldehyde was used to fixate protein crystals.^[13] Glutaraldehyde is easy to use but features two major drawbacks: To avoid glutaraldehyde's self-polymerization and fluorescence, the suitability of other cross-linkers is investigated (chapter 5.3.5).

5.3.1 Crystallization of negatively charged encapsulin

For the crystallization of charged Enc^(neg) and Enc^(pos), both proteins were stored in their respective storage buffers (20 mM Tris pH 7.5, 0.3 M NaCl for Enc^(neg) and 20 mM MES pH 6.0, 1.0 M NaCl for Enc^(pos)). The screening for unitary crystallization condition was carried out at 6 mg/mL protein, while binary conditions were additionally screened at 4 mg/mL. To identify suitable crystallization conditions, a robotic setup with sitting drop vapor diffusion was used. For unitary screening, 100 nL protein solution were added to 100 nL crystallization condition. In addition, binary screening was performed with 100 nL protein Enc^(pos) and 100 nL protein Enc^(neg) added to 200 nL crystallization condition. About 1,000 conditions were screened and over 30 drops yielded crystals with various morphologies such as rods, needles, plates as well as octahedral, cubic and rhombic. Conditions with crystals in robotic screening were chosen for further optimization in manual plates in a hanging drop setup. The main difference between robotic screening and manual plates is the increased size of the drops (10 times larger). To crystallize only one protein variant in a unitary setup, 1 μL protein is added to 1 μL crystallization condition with a final volume of 2 μL . In binary setups, 1 μL Enc^(pos) and 1 μL Enc^(neg) are added to 2 μL resulting in a 4 μL drop. In general, not every condition from robotic screening could be reproduced or yielded into crystalline material of high quality.

The structure of single crystals was determined by X-ray crystallography using synchrotron radiation. High resolution could not be achieved with Enc crystals of any type. The highest resolution achieved was 4.94 \AA for Enc^(neg) crystal derived from the CaOAc condition (Table

8.9). In general, the introduced mutations were not resolved due to low resolution and absence of electron density at the side chain coordinates. Nevertheless, the resolution was sufficient to determine lattice type and unit cell parameters for all conditions. For most cases molecular replacement was possible and gave insights into the protein containers position and orientation. Crystallographic data and refinement details can be found in the appendix (Table 8.9, Table 8.10 and Table 8.11).

First, unitary conditions are discussed within this chapter. Even if binary conditions were aimed for, identifying unitary conditions is beneficial. A possible hit in binary screening may be excluded because it is already known that one of the proteins already crystallizes in this specific condition. Moreover, unitary crystallization conditions give information about the contacts between protein containers in a crystal. The protein-protein interfaces play a crucial role in crystallization and its modification may even lead to different structures.

Crystallization conditions containing crystals in manual plates for Enc^(neg) are listed in Table 5.17. Three conditions were found to yield crystals with high reproducibility (Figure 5.42). Crystals grow up to 100 μm with well-defined shape.

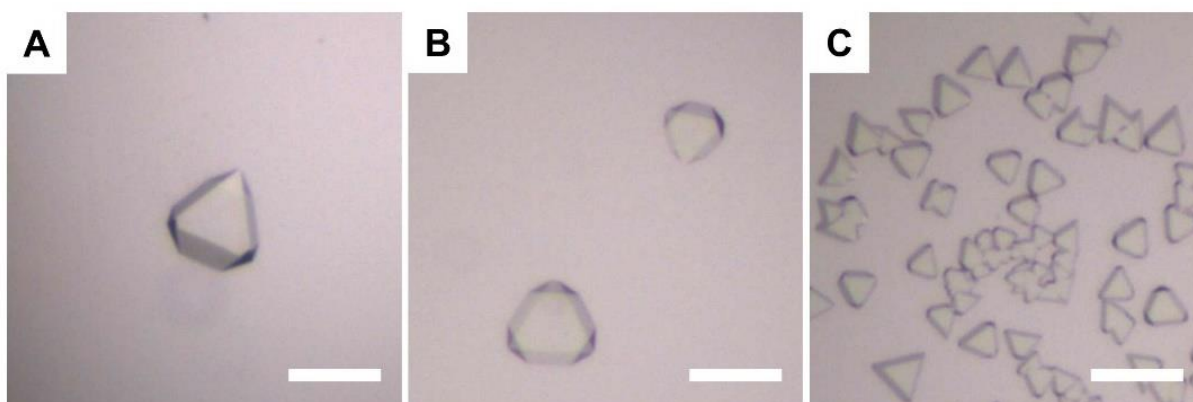


Figure 5.42: Protein crystals with different morphologies based on Enc^(neg). Crystal conditions from left to right: CaOAc (A), Li₂SO₄ (B) and NaCl (C). Scale bars are 100 μm .

For the calcium acetate (CaOAc) and lithium sulfate (Li₂SO₄) conditions the same space group with unit cell parameters were found in X-ray data analysis (Table 5.17.). A small deviation for the cell length is observed, due to low resolution data but still not significant. Here, a cubic $F4_132$ lattice with a unit cell length of 669 \AA is reported for Enc^(neg), similar to what was published for Enc^(wt). Both proteins differ only in one mutation (W90E), which is not surface exposed and does not play a role in protein-protein interfaces (Figure 8.30). Moreover, for the NaCl condition a yet unknown smaller cubic lattice is found.

Table 5.17: Crystallization conditions for Enc^(neg).

		Enc ^(neg)		
Acronym		CaOAc	Li ₂ SO ₄	NaCl
Condition		0.2 M Calcium acetate 0.1 M MES pH 6.0 4 % (v/v) Isopropanol	0.17 M Lithium sulfate 0.1 M MES pH 6.0 26 % (v/v) MPD	0.2 M NaCl 0.1 M HEPES pH 7.5 35 % (v/v) MPD
Lattice		Cubic	Cubic	Cubic
Space group		<i>F</i> 4 ₁ 32	<i>F</i> 4 ₁ 32	<i>P</i> 4 ₂ 32
Unit cell parameters	Length [Å]	669.36 / 669.36 / 669.36	668.57 / 668.57 / 668.57	334.73 / 334.73 / 334.73
	Angle [°]	90.0 / 90.0 / 90.0	90.0 / 90.0 / 90.0	90.0 / 90.0 / 90.0

In direct comparison, the Li₂SO₄ and NaCl conditions are similar. Thus, the attempt to convert one condition to the other by changing the concentration of 2-Methyl-2,4-pentanediol (MPD) was carried out. The idea behind was to see if the crystal morphology changes, thus indicating a phase transition. The MPD concentration is higher in the Li₂SO₄ condition. Increasing the MPD concentration in the Li₂SO₄ condition from 26 % (v/v) towards 35 % (v/v) significantly influences the crystal formation. Till 28 % (v/v) MPD crystals get smaller until crystal growth is terminated above 28 % (v/v). Moreover, the addition of NaCl to the protein buffer does not support crystal formation. A decrease in MPD for the NaCl below 35 % (v/v) yielded in no crystals. For the NaCl condition, the pH is at 7.5 and NaCl is used as salt, instead of pH 6.0 and Li₂SO₄ as for the other condition. Therefore, the pH and the bivalent ions seem to be crucial for the larger cell. Changing the pH and swapping the salt source was not further investigated.

To further investigate the interfaces between the proteins in the cubic lattice, the corresponding interfaces are visualized. First, the larger cubic lattice (condition CaOAc and Li₂SO₄) is discussed and visualized in Figure 5.43.

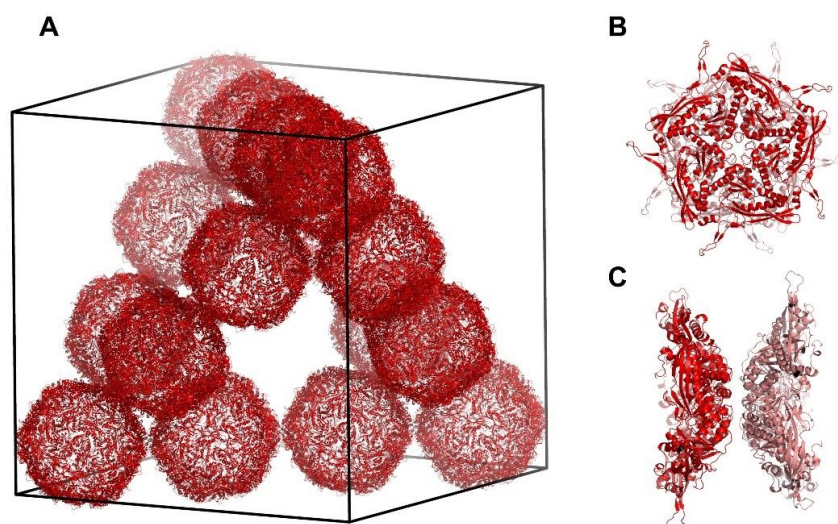


Figure 5.43: Crystal lattice and protein interfaces in $Enc^{(neg)}$ conditions. Cubic protein lattice (A) based on 16 $Enc^{(neg)}$ containers within one unit cell. Protein interface along the fivefold axis (B) and from the side (C).

The crystal lattice is face-centered. The space filling of the cell is around 39 % and in comparison, to face-centered cubic close packing, where around 74 % are achieved, quite low. In a single unit cell, the 16 containers form a tetrahedra with hollow space. In 3D, the crystal has large channels due to the periodically arranged hollow tetrahedra. In terms of later applications, such a lattice might be beneficial for transport of small molecules or ions, because diffusion into or through the crystal might be easier than in a densely packed crystal without larger channels. Moreover, the hollow tetrahedra could act as a cage and host larger guest molecules. The only interface between the protein containers is the interface along the fivefold axis. Two pentamers are facing each other (Figure 5.43B+C). The same interface and container orientation are observed for the published structure by SUTTER *et. al.*^[217]

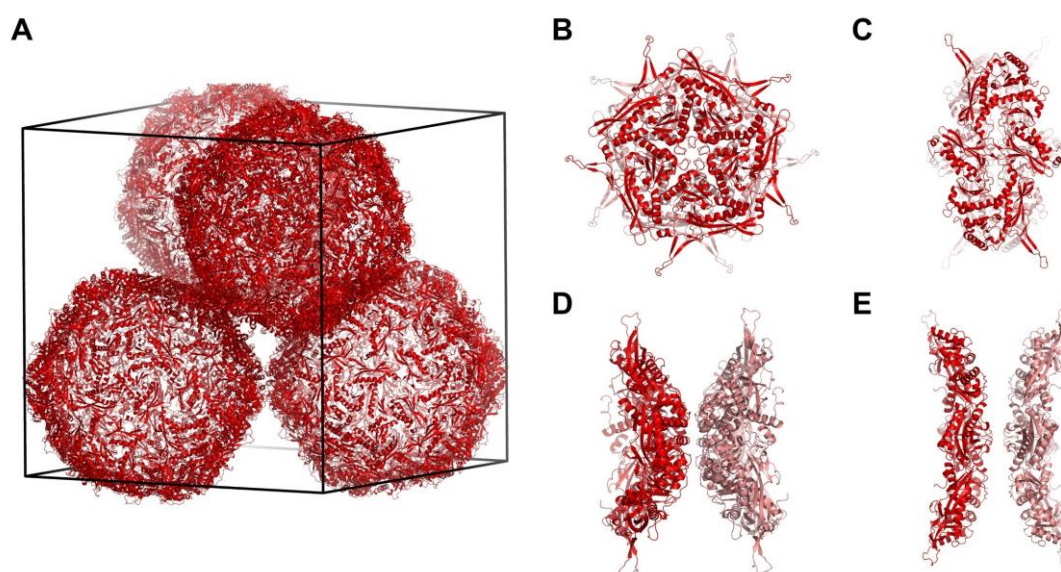


Figure 5.44: Visualization of crystal lattice and protein interfaces in NaCl conditions. Cubic protein lattice (A) based on four $Enc^{(neg)}$ containers. Protein interface along the fivefold axis (B) and from the side (C). Second interface along the twofold axis (C) is also shown by side (E).

On the other hand, the smaller cubic lattice found in the from the NaCl condition features a second interface between Enc^(neg) along the twofold axis (Figure 5.44C+E). The protein containers are oriented the same way as in Figure 5.43 since the pentameric interface features the same orientation (Figure 5.44B).

The new interface at the twofold axis is not present in the other Enc^(neg) conditions. In both conditions the pH is at 6.0. The published structure was crystallized at pH 5.1, but in this case the pH is at 7.5. With decreasing the pH towards 14, the surface charge of the protein container gets more negative. In direct comparison between the pH 6.0 and pH 7.5 of the twofold interface only a small change in surface charge towards more negative is observed (Figure 5.45). The change might not be strong, but still possible that at the right salt concentration at pH 7.5 the proteins are attracted to each other at the twofold interface.

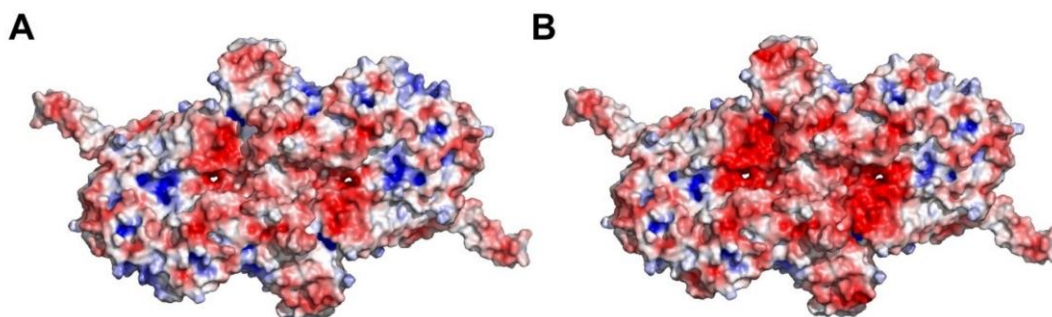


Figure 5.45: Electrostatic surface potential of one partially built protein container at the twofold interface in the NaCl condition of Enc^(neg). Surface potential is calculated at pH 6.0 (A) and pH 7.5 (B). Colors are from red (-5 kT/e) to blue (+5 kT/e).

Every crystallization condition contains a buffer to keep the pH fix, but the pH of the crystallization drop can still be influenced by temperature. Molecular vibrations in the solution rise with rising temperature resulting in the ionization and formation of H⁺ ions. Moreover, with an increased temperature, the ion product of water increases and causing an increase of H⁺ ions. Additional H⁺ ions lead to a more acidic solution. Therefore, the pH decreases with increasing temperature. Typically, the pipetting process is carried out at RT, but the crystallization plates stored at 20 °C. Crystallization solutions are also stored at RT. At a certain point, a temperature influence on the crystallization process for the CaOAc condition was observed. Storing all crystallization solutions and performing the crystallization experiment at higher temperatures resulted in a change in crystal morphology. To investigate this behavior, three buffers were prepared at 22.5 °C. Each buffer was incubated for at least 2 h at either 15.0 °C or 30.0 °C prior pH determination (Figure 5.46). At every temperature, a range of around 0.2 in pH is covered. Afterwards, a crystallization experiment is carried out with solutions incubated and manual plates stored at 15.0 °C, 22.5 °C or 30.0 °C.

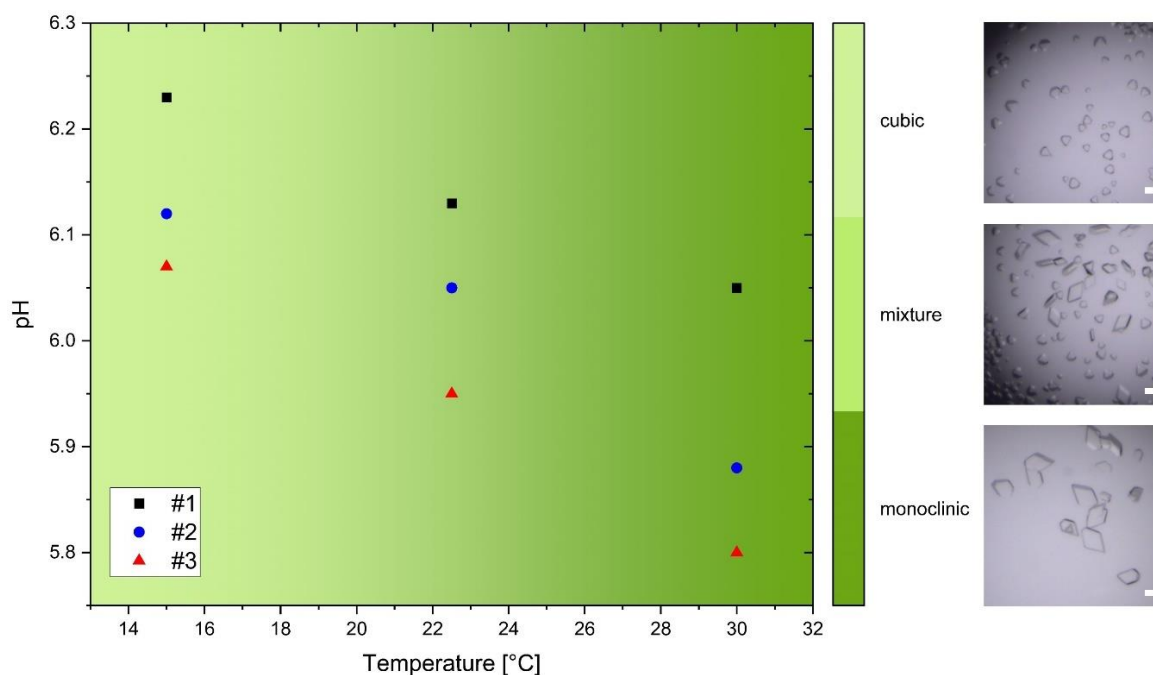


Figure 5.46: Crystallization screening with different buffers at different temperatures. For each screening condition, the composition was identical, but differed in the pH of the buffer. The pH meter calibration was carried out at 22.5 °C. Bright green: crystals with cubic lattice; medium green: mixture of two crystal morphologies; dark green: crystals with monoclinic lattice. Scale bars are 100 μm .

At 15 °C, for the pH range from 6.08 or 6.23 only the previous observed crystal morphology is found. In previous X-ray data analysis, a cubic lattice was determined. Increasing the temperature to 22.5 °C, a pH range from 5.95 to 6.15 is covered. At each data point two crystal morphologies are present in crystallization drops. Further increasing the temperature leads to a further decrease in pH range from 5.80 to 6.05. At 30 °C, only rhombic shaped crystals are found. From X-ray data analysis also a change of the crystal lattice is observed (Table 8.10). Rhombic shaped crystals in the CaOAc condition at 30 °C are based on a monoclinic crystal system. Due to the change of the crystal system, also the unit cell parameters change, and a dense packing is achieved (Figure 5.47). Again, residues at the fivefold and twofold axis are involved in protein-protein interfaces. However, the interface is not along the fivefold axis, but slightly shifted. In comparison to the previous interface along the twofold axis, the protein containers are rotated to each other.

As discussed above, a change in crystal morphology and lattice is observed between 15 °C and 30 °C at different pH values. Increasing temperature results in adding additional energy to the crystallization process. Thus, the cubic might be the kinetically and the monoclinic the thermodynamically stable lattice type. The temperature influence on the crystallization is only observed for the CaOAc condition but not for the other two. The major difference is the precipitant. While MPD is used for Li_2SO_4 and NaCl conditions, isopropanol is used in CaOAc condition. MPD is more viscous than water and results in a larger drop than using isopropanol.

On the other hand, isopropanol evaporates faster than MPD. Isopropanol causes a spreading of the drop on the cover slide due to the loss of surface tension. A different drop shape influences the evaporation process.^[312] Faster or slower evaporation based on additive, temperature and drop shape could result in faster or slower crystallization process and therefore different crystal phases.

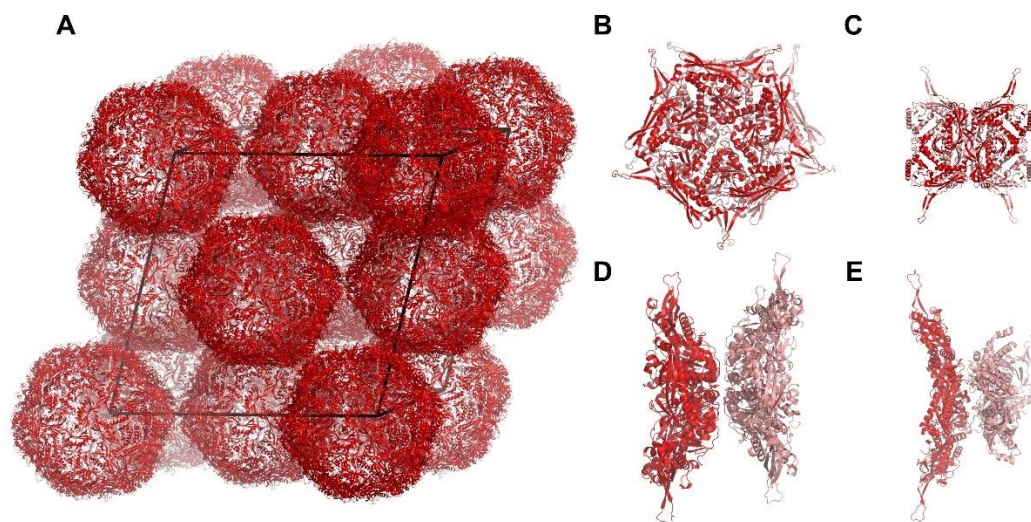


Figure 5.47: Visualization of crystal lattice and protein interfaces in CaOAc condition at higher temperatures. Monoclinic protein lattice (A) based on Enc^(neg) containers. Protein interface along the fivefold axis (B) and from the side (C). Second interface along the twofold axis (D) is also shown by side (E).

5.3.1.1 AuNP-loaded Enc^(neg) crystals

In previous chapters, the encapsulation of 13 nm large AuNPs and the crystallization of empty protein containers was discussed. The next step is the crystallization of NP-loaded protein containers towards highly ordered superlattices. In detail, AuEnc^(neg) was crystallized in the CaOAc condition at higher temperatures, since this condition leads to a densely packed assembly (Figure 5.48).

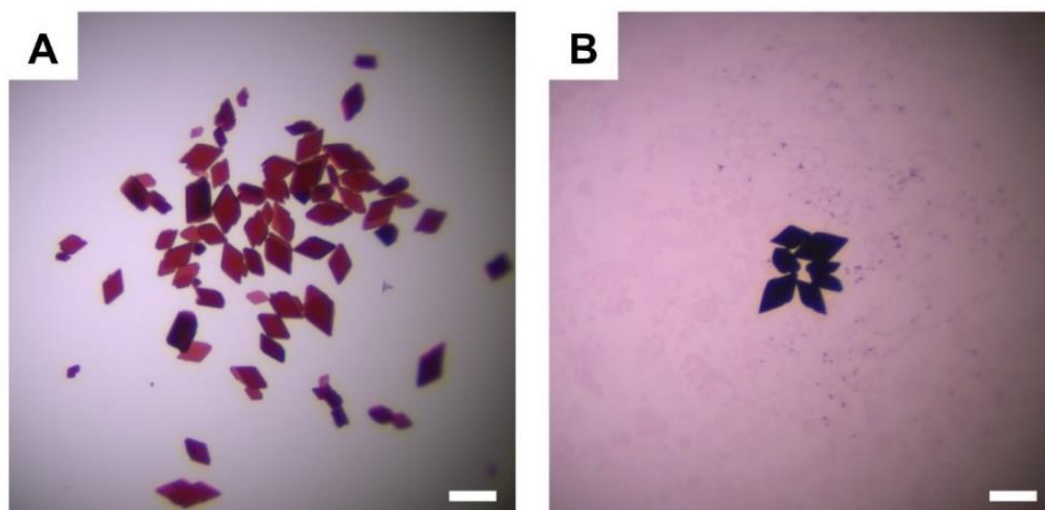


Figure 5.48: AuNP-loaded Enc^(neg) crystals. AuNP loading is either 50 % (A) or 100 % (B). Scale bars are 200 μ m.

First, empty Enc^(neg) was mixed 1:1 with AuEnc^(neg) to test the suitability of the CaOAc condition. Bright to dark red rhombic crystals are observed (Figure 5.48A). Pure AuEnc^(neg) crystals are completely black, due to the high loading of AuNPs (Figure 5.48B). The crystallization condition showed high reproducibility with AuEnc^(neg). In this case, a cross-linked AuEnc^(neg) crystal was dried on a Si-wafer and further characterized via SEM (Figure 5.49). The EDX mapping of the crystal highlights the homogenous distribution of AuNP in the crystal. Moreover, it is even possible to visualize the Enc^(neg) containers on the crystal surface via SEM and investigate the visible (100) orientation. (Figure 8.33).

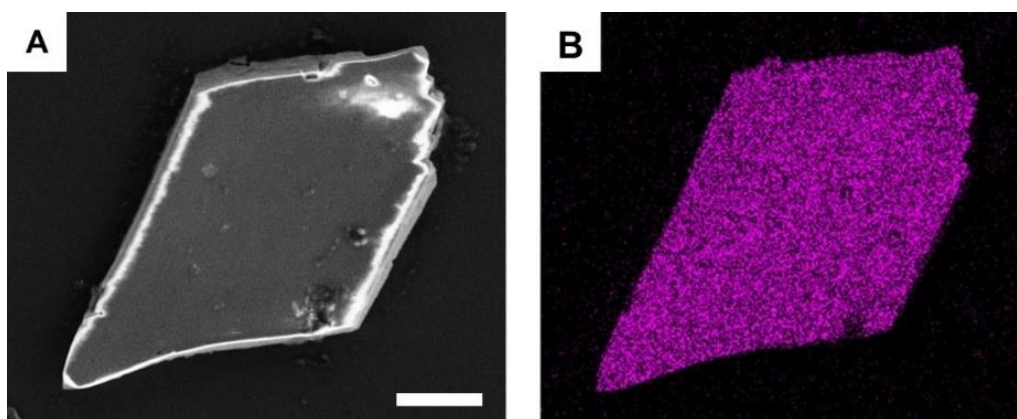


Figure 5.49: SEM measurement of AuEnc^(neg) crystal and EDX mapping. SEM image of AuEnc^(neg) crystal (A) and EDX mapping of Au M α_1 (B). Scale bar is 10 μm .

To further characterize the superlattice, experiments were carried out at the beamline P14 at EMBL Hamburg. The applied approach enables to further characterize protein crystals loaded with NPs. Usually, small-angle X-ray scattering is carried out to determine the NP lattice.^[15] The major disadvantage of a typical SAXS experiment, is the requirement of a large number of crystals in a capillary. The procedure consumes high amounts of NP-loaded protein, which might be difficult to achieve due to low yields. Moreover, the transfer process of crystals from protein drop to capillary leads to a loss of crystals. Measuring in such an experiment as presented here, requires single crystals. Beamline P14 is one of several at DESY, that features a robotic sample changer and high sample throughput. Measuring a dataset as discussed here takes a few minutes. Moreover, P14 beamline features an experimental setup to move the detector several meters away from the sample and to observe diffraction at lower angles.

In such samples, the AuNP lattice is equal to the protein lattice, due to AuNPs encapsulated in the protein containers, which are responsible for the assembly. Since the crystal is loaded with AuNPs, the intensity of the diffraction spots will be stronger than for a usual protein crystal. Due to the interaction of the X-ray beam with the AuNPs, the beam is stronger scattered through the higher number of electrons. In general, the scattering factor increases with the number of electrons. In detail, the crystals were prepared as usual in a macromolecular X-ray experiment, but the detector distance was set to 2 m. The protein crystal itself does not diffract

very well, therefore the diffraction pattern of the AuNP lattice was of interest. One X-ray absorption edge for Au is at 11.9 keV and for this experiment, the energy was set to 12.7 keV. First, to have high absorption without damaging the crystal too much and secondly, to achieve intense diffraction. Still, the chosen energy led to stronger radiation damage than measuring below the absorption edge. Nevertheless, it was possible to characterize the AuNP lattice in a AuEnc^(neg) crystals (Table 8.12). In detail, the unit cell parameters were determined (Table 5.18). For the AuNP-loaded protein crystal, the cell length is slightly enlarged in every dimension. The deviation is likely caused by radiation damage, due to the strong absorption of the AuNP protein crystal.

Table 5.18: Comparison of lattice parameters of empty and AuNP loaded Enc^(neg) crystal.

Crystal	Length [Å]	Angles [°]
eEnc ^(neg)	410.90 / 224.80 / 389.36	90.0 / 108.7 / 90.0
AuEnc ^(neg)	417.18 / 228.12 / 403.32	90.0 / 108.1 / 90.0

At this point, other NP loaded Enc crystals were not available yet, due to the low encapsulation or protein yield after purification. Nevertheless, the unitary AuEnc^(neg) crystals with sizes above 100 μm might be interesting for applications such as SERS. The AuNPs are highly ordered, and hot spots should form between the AuNPs. To verify if 13 nm large AuNPs encapsulated in a 24 nm large protein container still form hot spots, a first simulation with the software *Lumerical* was carried out (Figure 8.32). The distance between the AuNPs is 24 nm, therefore exactly the size of one protein container and close to the distance between particles in a crystal derived from the CaOAc crystallization condition. The strongest interactions between the AuNPs are observed at 556 nm. Further simulations could focus on constructing several layers of AuNPs based on an Enc crystal structure and carry out simulations as done for AuNP lattices in work by MUELLER *et. al* to estimate the field enhancement for a future application as biocompatible SERS substrate.^[25,111,245] In the end, additional simulations are required to discuss collective properties of the AuNPs (Au absorption, plasmon coupling) in AuEnc^(neg) crystals.

5.3.2 Crystallization of positively charged encapsulin

In a second step, the crystallization of unitary Enc^(pos) was carried out. The protein container Enc^(pos) was established within this work and so far, no other positive Enc variant or any other crystal structures have been reported. In this work, three conditions were found to yield crystals with defined shapes and high reproducibility. Crystals with different morphologies than observed for Enc^(neg) are shown in Figure 5.50. In detail, three conditions namely Na citrate, citrate-HEPES (4-(2-hydroxyethyl)-1-piperazineethanesulfonic acid) and Phosphate are found

for Enc^(pos) (Table 5.19). In addition to previously reported cubic and monoclinic lattices, orthorhombic and tetragonal lattices were found (Table 8.10). Comparing the three conditions, it is striking that not only MPD, but also citrate is found in every condition. Due to the positive surface charge of the positive Enc container, the citrate anion may play a crucial role in stabilization and crystallization.

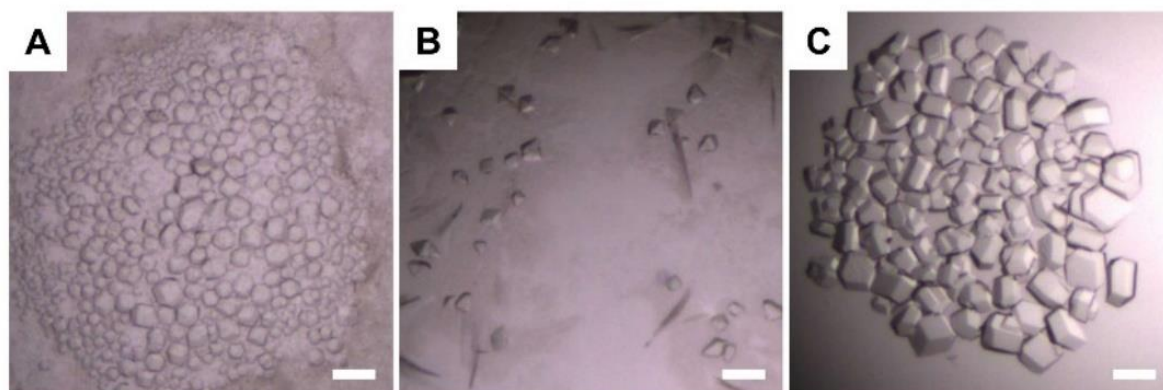


Figure 5.50: Protein crystals with different morphologies based on Enc^(pos). Crystal conditions from left to right: CaOAc (A), Li₂SO₄ (B) and NaCl (C). Scale bars are 100 μ m.

Moreover, the pH of each condition is different. The pH of the Na citrate condition is 8.4, while the phosphate condition is more acidic with pH 4.2. The pH of the citrate-HEPES condition is determined by the mixture of HEPES pH 7.5 and the sodium citrate, resulting in a final pH of 7.8. At pH 4.2 the protein surface is mainly positive. A change in pH towards 7.8 and 8.4 results in less positively charged Enc^(pos) containers (Figure 8.31). Despite the minor difference in pH between citrate-HEPES and Na citrate condition, two different crystal systems are observed.

Table 5.19: Crystallization conditions for Enc^(pos).

		Enc ^(pos)		
Acronym		Na citrate	Citrate-HEPES	Phosphate-citrate
Condition		0.1 M Trisodium citrate	0.2 M Trisodium citrate	0.1 M Phosphate-citrate
		pH 5.5	0.1 M HEPES pH 7.5	pH 4.2
		22 % (v/v) MPD	30 % (v/v) MPD	40 % (v/v) MPD
Lattice		Orthorhombic	Monoclinic	Tetragonal
Space group		<i>P</i> 2 ₁ 2 ₁ 2 ₁	<i>C</i> 2	<i>P</i> 4 ₂ 2 ₁ 2
Unit cell parameters	Length [Å]	260.08 / 367.14 / 368.27	384.15 / 236.52 / 407.72	464.23 / 464.23 / 311.15
	Angle [°]	90.0 / 90.0 / 90.0	90.0 / 108.7 / 90.0	90.0 / 90.0 / 90.0

To further understand the assembly, protein-protein interfaces are compared. First, the interfaces in the citrate condition between Enc^(pos) containers are discussed (Figure 5.51). Here, the first protein interface is along the threefold axis (Figure 5.51B+D). A second interface

between containers is found close to the other one, but the containers are shifted to each other (Figure 5.51C+E). Strikingly, no interface at the fivefold or twofold axis is observed as before. The introduction of new residues on the outer surface towards positive charge and the acidic pH mainly causes these new interfaces.

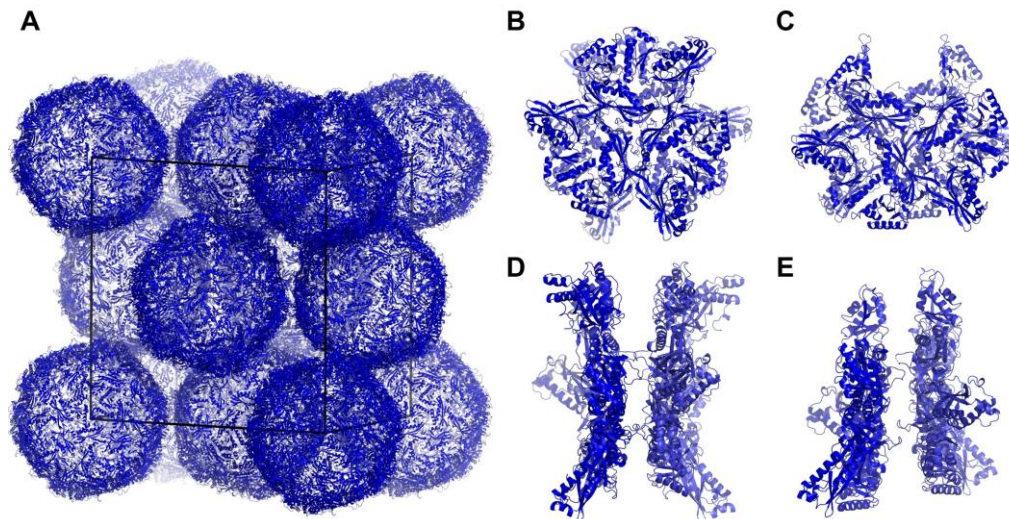


Figure 5.51: Visualization of crystal lattice and protein interfaces of Enc^(pos) in Na citrate condition. Orthorhombic protein lattice (A) based on four Enc^(pos) containers visualized with 14 full containers. Protein interface along the threefold axis (B) and from the side (D). Second interface shown in (C) and (E) from the side.

In addition, the interfaces of the citrate-HEPES and phosphate structures are visualized (Figure 8.28 and Figure 8.29). Also, for these new structures, no interface at the fivefold axis is observed. Mainly residues at the threefold axis are involved in protein-protein interfaces. Moreover, the positive Enc variant seem to be more flexible in terms of possible crystal systems. While for Enc^(neg) mainly cubic systems are reported, Enc^(pos) also features orthorhombic or tetragonal crystals systems. Either way, the introduced mutations seemingly influence the assembly of the protein containers. The lack of the protein-protein interface at the fivefold axis for Enc^(pos) is significant. Due to low resolution, it is not resolved which amino acids are involved in forming the interfaces, but at the fivefold axis two residues were mutated (E143K, E186K). Both times, glutamic acid is mutated in Enc^(neg) to lysine in Enc^(pos). Possibly the glutamic acids produce dimers connected through a linking metal ion. The mutation to lysine removes the possibility of forming this metal ion coordination. Thus, the interface along the fivefold axis remains apparently less favorable for Enc^(pos). A future experiment to resolve this question could include a Enc^(pos) variant that features the native amino acids at position 143 and 186. Since these amino acids are part of the fivefold interface, it is questionable if the Enc^(neg) conditions that lead to cubic crystal systems can also be applied on that variant.

5.3.3 Crystallization of negatively and positively charged encapsulin variants

Since the overall aim was to achieve a binary lattice composed of $\text{Enc}^{(\text{neg})}$ and $\text{Enc}^{(\text{pos})}$, a screening with both proteins was carried out. The crystallization of both containers turned out to be difficult. In robotic screening, mostly already known unitary conditions contained crystals. In some cases, crystalline precipitation or not well-defined morphologies were observed. These conditions were taken and further investigated in manual plates. Crystallization experiments in manual plates led to four conditions that seem to yield binary assemblies. Control experiments were carried out to exclude unitary crystals. Instead of adding protein stored in buffer to the crystallization drop only the storage buffer is added to the drop containing crystallization condition and the second protein. If a drop containing only one of two proteins stays clear, but the drop containing both proteins feature a crystal, then this one is likely binary. Based on this approach the conditions listed in Table 5.20 were further investigated.

Table 5.20: Promising conditions for binary Enc crystals.

$\text{Enc}^{(\text{pos})} + \text{Enc}^{(\text{neg})}$				
Acronym	EtOH	HEPES	MgCl ₂	Mg formate
Condition	0.1 M Tris pH 7.0 2 % (v/v) Ethanol	0.1 M HEPES pH 6.5 2 % (v/v) MPD	0.1 M MgCl ₂ 0.1 M Imidazole pH 8.0 8 % (v/v) Ethanol	0.25 M Magnesium formate

Every condition was optimized in terms of pH, salt and precipitant concentrations as well as protein concentration. In the MgCl₂ and Mg formate conditions both proteins form objects that do not appear as a well-shaped crystal (Figure 5.52C+D). On the other hand, the EtOH and HEPES conditions lead to very small objects (Figure 5.52A+B).

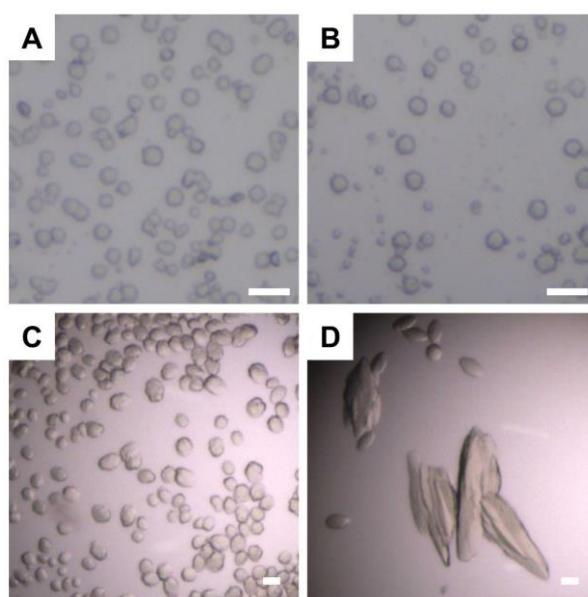


Figure 5.52: Overview of crystallization conditions containing $\text{Enc}^{(\text{neg})}$ and $\text{Enc}^{(\text{pos})}$. Conditions shown are EtOH (A), HEPES (B), MgCl₂ (C) and Mg formate (D). Scale bars are 50 μm .

Due to their small size and limited resolution of the setup, it is not definitely safe if the objects in Figure 5.52A+B have a defined morphology or not. To this point, it was not possible to increase the size of the objects. Further investigation is needed to verify if these objects indeed are binary crystals. Even if the control experiments were negative for unitary crystals, there is still the possibility that the first protein act as a precipitant that is needed for the second protein to crystallize. Since the resolution of Enc crystals is not high, other methods need to be applied to solve the structure. Labeling one protein variant with e.g. fluorophores on the inner cavity and crystallize it with unlabeled protein could give further insight into the composition of these objects. Nevertheless, the pH of both conditions is close with 6.5 and 7.0 and might indicate a suitable pH range for both containers to interact. To improve the crystallization further mutations could be carried out. As mentioned for Enc^(pos), modifications at the pore along the fivefold axis might lead to stronger interactions between protein containers. Moreover, aromatic residues might also be implemented in interfaces to induce π - π stacking.^[313]

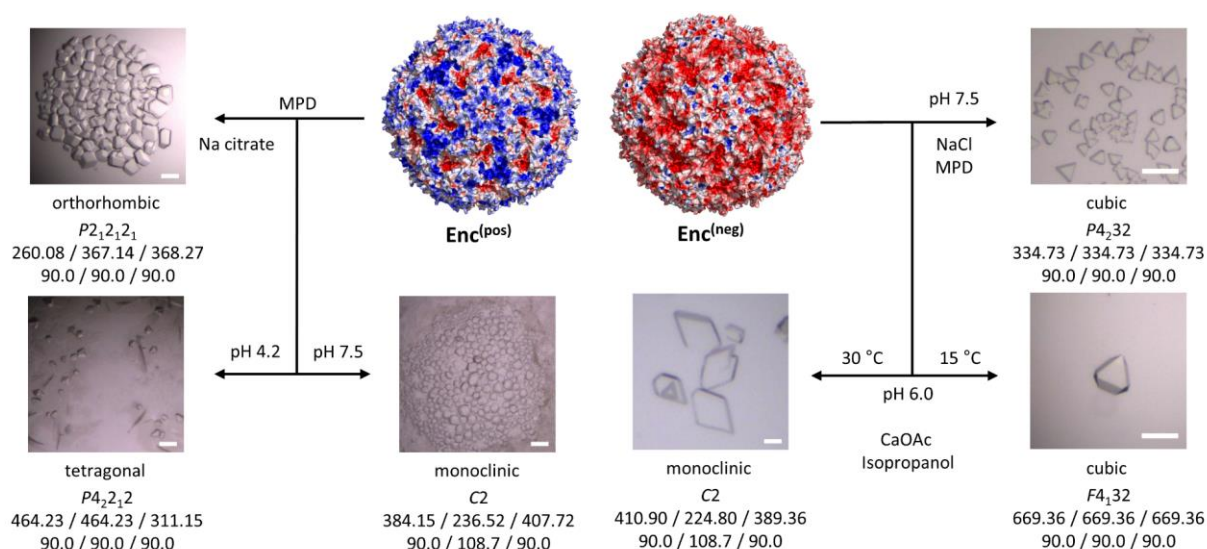


Figure 5.53: Schematic overview of available unitary crystal systems. Scale bars are 100 nm.

In summary, all prior listed crystal systems based on two unique Enc variants highlight the suitability of protein containers as a basic building block. Depending on the crystallization condition, different systems are possible (Figure 5.53). The positive Enc can be crystallized with MPD and Na citrate in an orthorhombic lattice. Adjusting the pH towards pH 4.2 or 7.5 leads to either a tetragonal or monoclinic lattice. For the negative Enc, a larger monoclinic crystal system is reported. Decreasing the temperature needed for the monoclinic structure, a cubic crystal system is achieved. In addition, a novel smaller cubic crystal system is reported for Enc^(neg). For certain applications, such as efficient plasmon coupling short distances between nanoparticles are desired. Therefore, a crystal system that features a densely packed unit cell is beneficial in comparison to a unit cell with a low space filling. A densely packed unit cell features more neighbors in close contact, than with a lower space filling (Figure 5.43 vs.

Figure 5.47) All these crystal systems are a selection giving a choice to choose the suitable system depending on the application. Despite the low resolution some insights into the protein-protein interfaces were gained. The knowledge gained by unitary protein-protein interfaces may be used to design novel Enc variants that are more likely to interact with each other and form binary crystals of high quality.

5.3.4 Negatively charged encapsulin and positively charged ferritin

The lack of a binary encapsulin crystallization condition was overcome by changing the positive container from Enc^(pos) to Ftn^(pos). The Ftn container is only half the size of Enc, namely 12 nm in diameter. Originally, MARCEL LACH screened crystallization conditions between Enc^(wt) and Ftn^(pos) and found crystals with hetero-binary composition, which is not yet published.

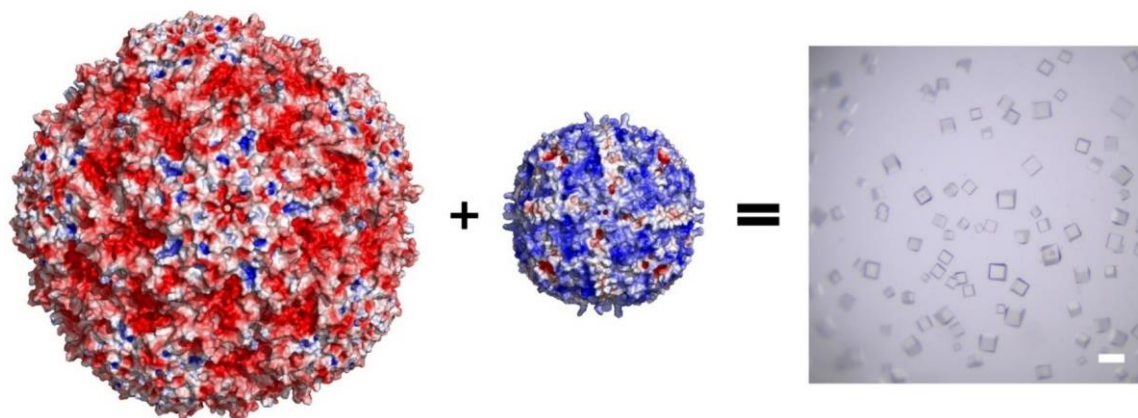


Figure 5.54: Schematic illustration for the assembly of hetero binary crystals. Colors are from red (-5 kT/e) to blue (+5 kT/e). Scale bar is 200 μm .

A crystallization condition containing ammonium sulfate $(\text{NH}_4)_2\text{SO}_4$ yielded crystals with cubic morphology. The crystallization condition was successfully applied on flavin-free Enc^(neg) with Ftn^(pos) (Figure 5.54). Initial X-ray data analysis revealed that the resolution was not sufficient to determine the molecular structure. Despite low resolution, the crystal system and unit cell parameters were determined. A cubic lattice *P*432 with $a = 242.6 \text{ \AA}$ was reported (Table 8.13).

5.3.4.1 NP-loaded hetero binary crystals

In a next step, nanoparticle-loaded protein containers were crystallized (Figure 5.55). Purified Ftn^(pos) loaded with either magnetic iron oxide (FeO_x) or cerium oxide (CeO_2) was kindly provided by MARCEL LACH. The NP core is up to 5 nm and 6 nm large for FeO_x and CeO_2 NPs, respectively.^[15] Together with AuEnc^(neg), different combinations of binary systems could be obtained.

At times, the nanoparticle cargo affected the crystallization of the protein containers. Ftn loaded with FeO_x NPs and empty $\text{Enc}^{(\text{neg})}$ yielded crystals up to $80\ \mu\text{m}$, but with CeO_2 loaded Ftn the size drops significantly towards $40\ \mu\text{m}$. $\text{AuEnc}^{(\text{neg})}$ with empty $\text{Ftn}^{(\text{pos})}$ yielded smaller crystals, up to $20\ \mu\text{m}$. Hetero binary crystals loaded with two kinds of nanoparticles resulted in crystals of same size. The small size of crystals complicates the handling and manipulation of these crystals. The incorporation of nanoparticles in one protein variant and the resulting color change of the crystal verify that the crystals are indeed a hetero binary assembly. $\text{AuEnc}^{(\text{neg})}/\text{eFtn}^{(\text{pos})}$ crystals are black, based on the densely packed AuNPs. Crystals based on empty $\text{Enc}^{(\text{neg})}$ and $\text{FeFtn}^{(\text{pos})}$ feature a typical color observed for iron oxide nanoparticles (Figure 5.55). These NP-loaded protein crystals were further characterized. Since the resolution of empty crystals was not sufficient to solve the structure, other methods had been applied to verify the crystal system and unit cell parameters.

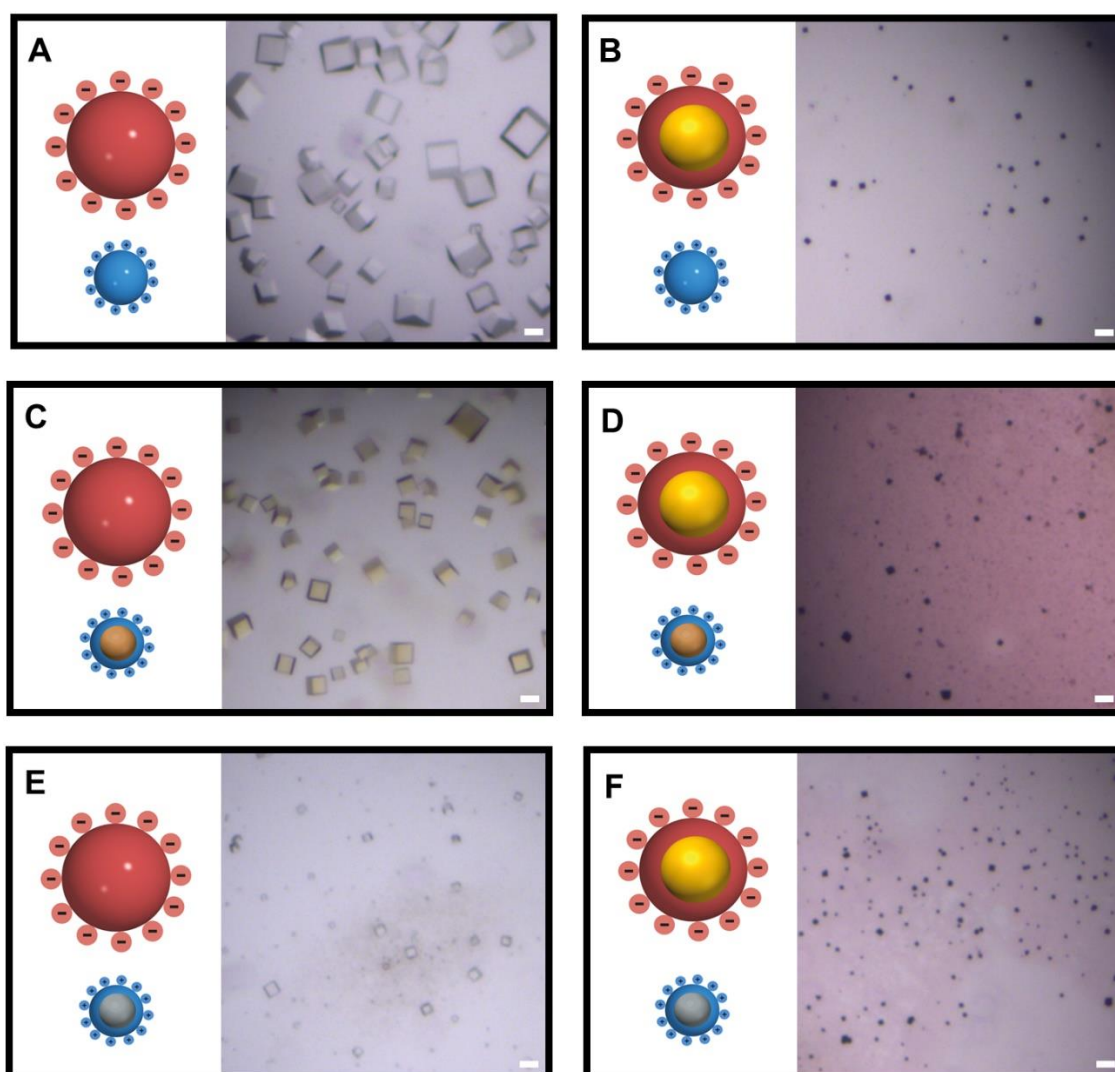


Figure 5.55: Optical microscopy images of protein crystals with different nanoparticle cargo. Empty protein containers crystallized (A). Only one container loaded with either Au (B), FeO_x (C) or CeO_2 (E) nanoparticles. Combination of metal oxide NP and AuNP (D+F). Scale bars are $50\ \mu\text{m}$.

First, SEM measurements were carried out with a hetero binary $\text{AuEnc}^{(\text{neg})}/\text{eFtn}^{(\text{pos})}$ crystal to visually verify the cubic arrangement of the protein containers. (Figure 5.56). In detailed analysis, spherical objects of one size are observed. The spherical objects are 24 nm large, indicating that only $\text{AuEnc}^{(\text{neg})}$ is visualized. Due to the AuNP loading the Enc container gives stronger contrast than $\text{eFtn}^{(\text{pos})}$. The cubic lattice of the crystal clearly sticks out. Very bright objects are on the top layer. Having less intensity, containers of lower levels appear greyish. The surface features darker spots, which are holes indicating a missing container in one layer. Also, empty protein containers would result in less intense or even not visible spots. The distance between the containers is around 24 nm and fits very well to the previous determined unit cell parameter of 24.6 nm. Moreover, in AFM measurements the AuNP-loaded protein containers are visible in phase imaging and roughly 24 nm apart from each other (Figure 8.34). Since the smaller $\text{eFtn}^{(\text{pos})}$ is not observed, the AuNP-loaded Enc container seems to get more rigid, causing a stronger phase shift and is well pronounced in both SEM and AFM imaging.

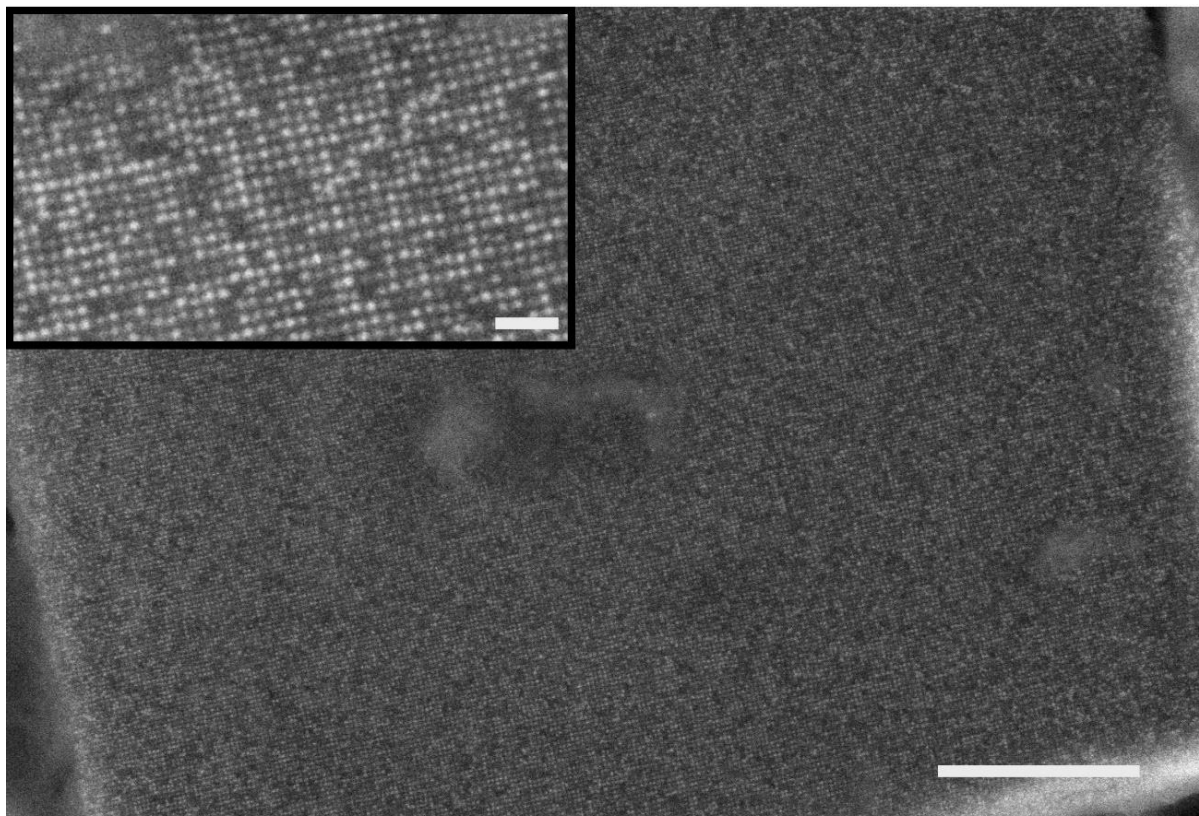


Figure 5.56: SEM image of a hetero binary $\text{AuEnc}^{(\text{neg})}/\text{eFtn}^{(\text{pos})}$ crystal. The protein crystal is several microns large. Scale bar is 1 μm . Further zoom is shown in the inset. Bright spots are $\text{AuEnc}^{(\text{neg})}$ containers on top layer. Having less intensity, containers of lower levels are visible. Inset scale bar is 100 nm.

In TEM measurements, a hetero binary $\text{AuEnc}^{(\text{neg})}/\text{eFtn}^{(\text{pos})}$ crystal is analyzed (Figure 5.57). Due to the low electron density, the protein container is not visible in TEM without further staining and only AuNPs encapsulated in $\text{Enc}^{(\text{neg})}$ are visible. There are also free AuNPs particles visible, distributed around the crystal. The free AuNPs derive from $\text{AuEnc}^{(\text{neg})}$, but the

protein shell is not visible due to the unstained TEM image. The cubic crystal is a few microns large, therefore too thick to look through the crystal. Milling the crystal with a focused ion beam into thin lamellas would simplify the investigation. Nevertheless, thinner parts of the crystal seemed suitable for imaging. In detail, one projection on the crystal is further analyzed. Well-ordered AuNPs of a periodic lattice are observed. Distances between AuNPs can be attributed to the (101) plane of a cubic crystal system. The determined distances of the AuNPs in TEM further strengthen and verify the presence of a cubic crystal system.

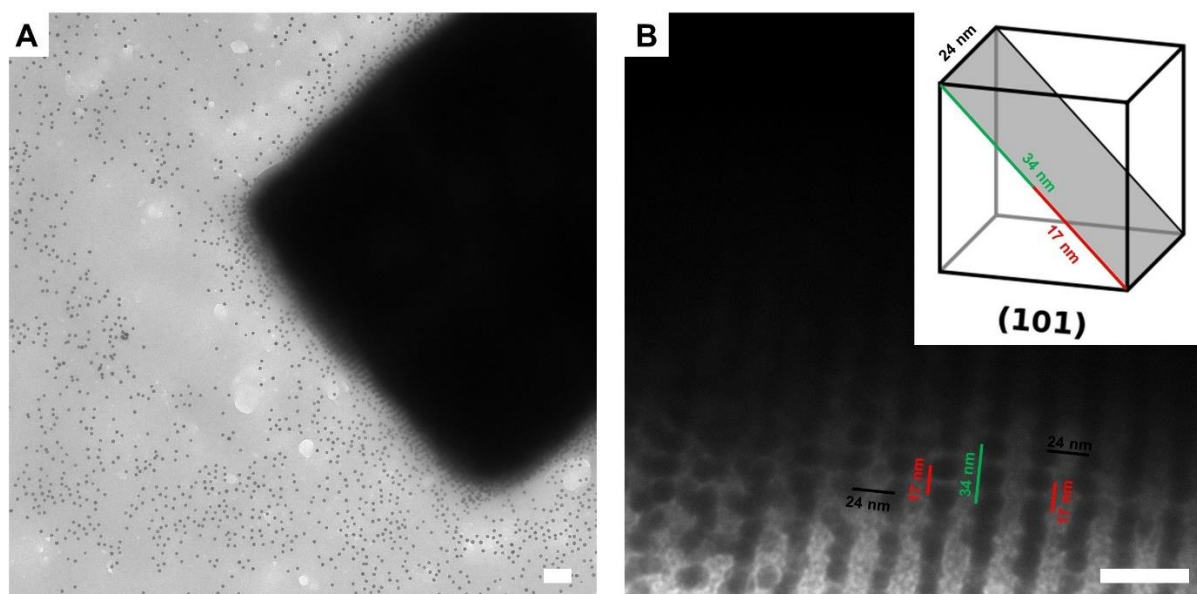


Figure 5.57: TEM images of a cubic AuEnc^(neg)/eFtn^(pos) crystal. Single AuNP and highly ordered AuNPs are visible. Inset: schematic visualization of different lengths in (101) plane. Scale bar is either 100 nm (A) or 50 nm (B).

For every experimental setup, hetero binary crystals with empty Enc and loaded Ftn were prepared. Each time, the protein surface was either uneven or no NP lattice was observed (data not shown). Due to the lack of information of the Ftn arrangement, single crystal diffraction experiments with NP loaded protein crystals were carried out (Table 5.21). The same experimental setup as for unitary AuEnc^(neg) crystal was applied.

Table 5.21: Comparison of single crystal X-ray data of empty and nanoparticle loaded protein crystals.

Crystal	Length [Å]	Angles [°]
eEnc ^(neg) /eFtn ^(pos)	242.57 / 242.57 / 242.57	90.0 / 90.0 / 90.0
AuEnc ^(neg) /eFtn ^(pos)	244.48 / 244.48 / 244.48	90.0 / 90.0 / 90.0
eEnc ^(neg) /CeFtn ^(pos)	244.00 / 244.00 / 244.00	90.0 / 90.0 / 90.0

In comparison to the protein lattice of the empty protein crystal, the lattice of different NP loaded protein crystals did not result into strong deviations. Even for the Ftn loaded crystal, a cubic lattice with lengths in the expected region is found. In the end, sufficient data is gathered

and implies a cubic lattice for the hetero binary crystals (Table 8.12). The position of the encapsulins is fixed, but still the positions of the ferritin cannot be elucidated with the current methods. Also, the information about the container orientations is currently not accessible. Due to residual space inside a unit cell, a possible unit cell contains one $\text{Enc}^{(\text{neg})}$ and four $\text{Ftn}^{(\text{pos})}$ containers (Figure 5.58). Unit cells containing only one kind of protein container are also visualized. The $\text{Ftn}^{(\text{pos})}$ containers are centered in the middle and on the faces of the unit cell, while the $\text{Enc}^{(\text{neg})}$ containers form a primitive cubic lattice. The reported results will be carried on in further research within the BECK group to completely reveal protein container positioning and orientation.

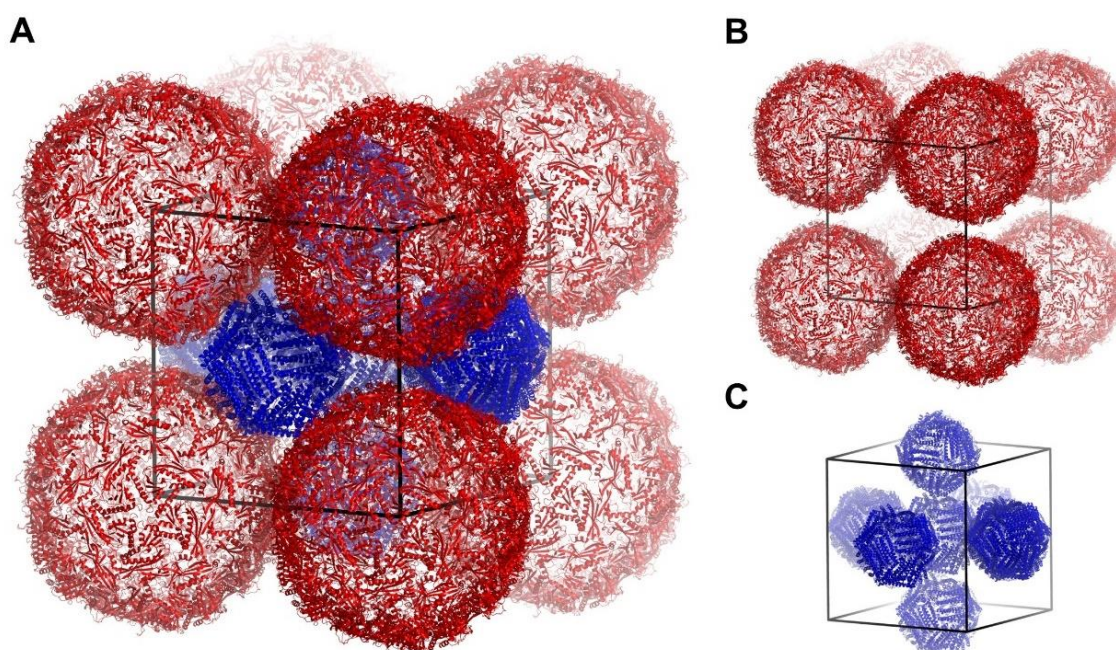


Figure 5.58: Hetero binary unit cell composed of $\text{Enc}^{(\text{neg})}$ and $\text{Ftn}^{(\text{pos})}$. Either both supercharged containers (A) or only $\text{Enc}^{(\text{neg})}$ (B) or $\text{Ftn}^{(\text{pos})}$ (C) containers are featured in a unit cell. Red: $\text{Enc}^{(\text{neg})}$; blue: $\text{Ftn}^{(\text{pos})}$.

Nevertheless, hetero binary crystals composed of $\text{Enc}^{(\text{neg})}$ and $\text{Ftn}^{(\text{pos})}$ loaded with several NP combinations are presented. These binary superlattices containing AuNPs in Enc containers might be interesting for catalysis and SERS detection. In detail, iron or cerium oxide nanoparticles are suitable for oxidase- and peroxidase-like catalysis.^[205] Moreover, plasmonic AuNP superlattices are suitable for SERS.^[118] Combining both kinds of NPs would enable to track the catalytic conversion of a substance while detecting SERS signals.^[314] On the other hand, magnetic FeO_x NPs in $\text{Ftn}^{(\text{pos})}$ combined with AuNPs Enc^(neg) in a protein crystal result in a magneto-plasmonic superlattice. An external magnetic field can modify the properties of a surface plasmon and combined influence light through magneto-optical effects such as the FARADAY and KERR effect.^[315-317] Such a magneto-plasmonic crystal might be applied in telecommunications, magnetic field sensing or optical magnetic data storage.^[318]

5.3.4.2 AuNP and fluorophore-loaded hetero binary crystals

The efficient labeling of a $\text{Ftn}^{(\text{pos})}$ variant with additional cysteine on the inner surface $\text{Ftn}^{(\text{pos})}$ -Cys was discussed in chapter 5.2.4. As shown in the last chapter, $\text{Enc}^{(\text{neg})}$ and $\text{Ftn}^{(\text{pos})}$ can be crystallized yielding cubic crystals.

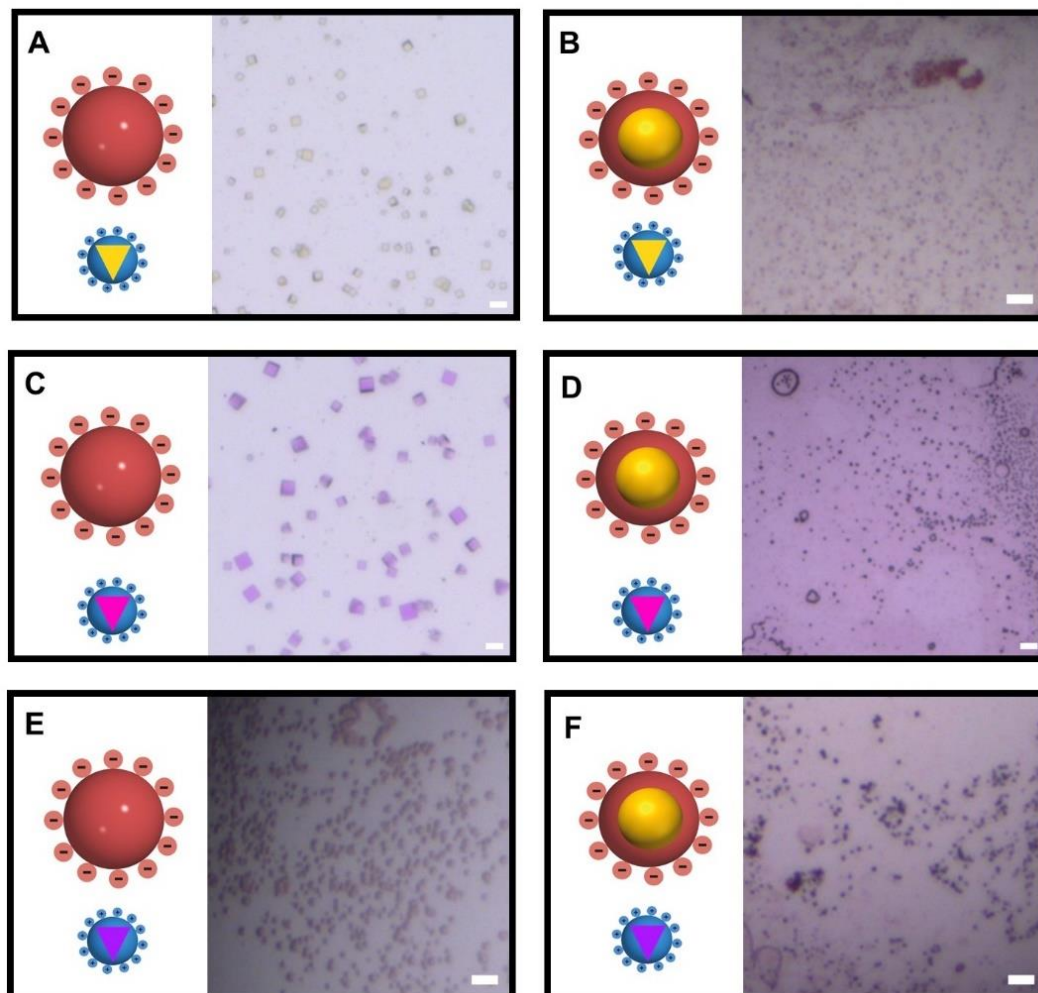


Figure 5.59: Optical microscopy images of protein crystals with fluorophore labeling and AuNP cargo. Only one container loaded with either AF488 (A), Rh3B (C) or Rh6G (E) nanoparticles. Combination of AuNP and fluorophore (B+D+F). Scale bars are 50 μm.

The new variant $\text{Ftn}^{(\text{pos})}$ -Cys (without functionalization yet) forms crystals with $\text{Ftn}^{(\text{neg})}$ and with $\text{Enc}^{(\text{neg})}$ since no residue was mutated at the outer surface. Moreover, in an initial test, the Rh3B-labeled $\text{Ftn}^{(\text{pos})}$ -Cys still crystallizes with $\text{Ftn}^{(\text{neg})}$ (Figure 8.35). Therefore, the crystallization of fluorophore-labeled $\text{Ftn}^{(\text{pos})}$ -Cys samples together with $\text{AuEnc}^{(\text{neg})}$ was carried out (Figure 5.59). Depending on the fluorophore, the crystal color differs. Moreover, the protein labeling affected the crystal size. Cubic crystal composed of fluorophore-labeled $\text{Ftn}^{(\text{pos})}$ -Cys and empty $\text{Enc}^{(\text{neg})}$ grew up to 50 μm, while completely unmodified proteins grow double the size. Fluorophore-labeled $\text{Ftn}^{(\text{pos})}$ -Cys and AuNP loaded $\text{Enc}^{(\text{neg})}$ yielded in even smaller crystals with sizes below 10 μm. The handling of such small crystals is extraordinarily difficult. Transferring such a small object with usual crystallographic tools needs high precision.

Moreover, washing a crystal prior further analysis in water mainly causes losing the crystal either in the drop or to the crystallographic transfer tool. Besides, with currently available optical microscopes it is difficult to distinguish if an object of that small size really is a protein crystal, aggregated protein or contamination. Nevertheless, it was possible to characterize these crystals further.

Optical microscopy and fluorescence images of the crystals loaded either only with fluorophore or combined with AuNPs are shown in Figure 5.60. However, optical properties of binary fluorophore-AuNP crystals are discussed in detail in a following chapter 5.3.6., see below.

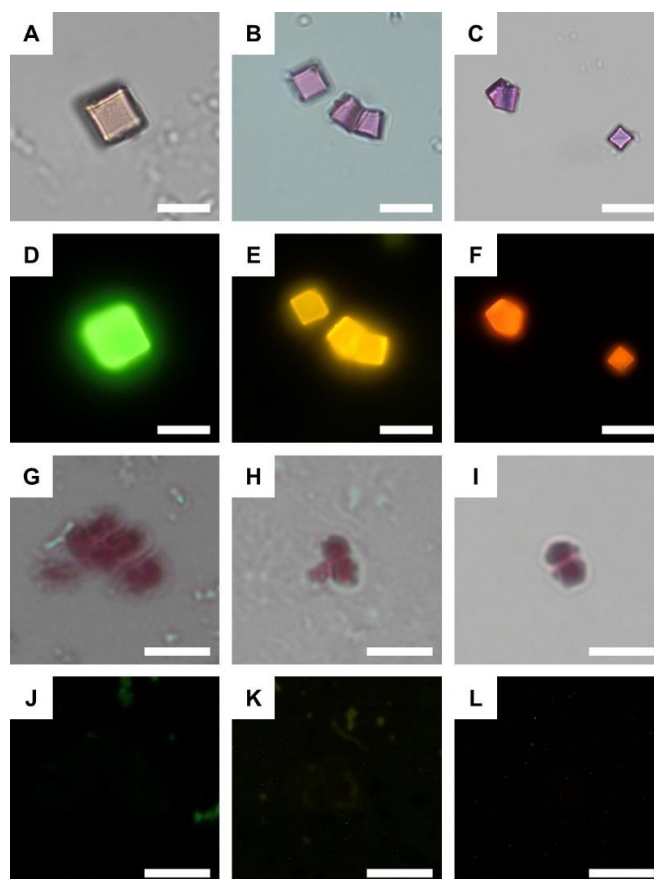


Figure 5.60: Optical microscopy images of fluorophore and fluorophore-AuNP loaded crystals. Bright field images of crystals with only fluorophore (A), (B) and (C) or AuNP and fluorophore (G), (H) and (I). Fluorescence microscopy images of crystals with only fluorophore (D), (E) and (F) or AuNP plus fluorophore (J), (K) and (L). Left to right column: AF488, Rh3B and Rh6G. Scale bar is either 10 μm in (A) to (F) or 5 μm in (G) and (L).

For each fluorophore loaded hetero binary crystal either green (AF488), yellow (Rh6G) or orange (Rh3B) fluorescence is observed (Figure 5.60D, E and F). The incorporation of AuNPs into the hetero binary superlattice results in quenched fluorescence (Figure 5.60J, K and L). In fact, all pictures were taken at the same settings. The power of the lamp was at the lowest level. Increasing the illumination power mainly increased background luminescence.

However, fluorophore-labeled protein crystal without AuNPs may even be of interest. Recently, the group of DRAGNEA reported a fluorophore-labeled brome mosaic virus (BMV) container in

solution with radiation brightening at room temperature. First, increasing the number of fluorophores towards 150 molecules per BMV container led to quenching. With additional labeling, the quenching was suppressed and fluorescence was restored. The BMV container was labeled with up to 300 fluorophores and properties such as superradiance and superfluorescence are under discussion. Due to the labeling, the labeled BMV features properties that isolated single fluorophores do not have. Based on fixed positions and orientations the fluorophore dipoles are expected to interact even stronger with each other.^[11] The current Ftn^(pos)-Cys container only features up to 24 fluorophores per container but can be upgraded with additional labeling sites on the inner cavity. Moreover, the inner encapsulin surface can also act as a template for fluorophore labeling. There, one additional cysteine per subunit already makes it possible to covalently link 60 fluorophores per container and can even be increased. Investigating the properties in solution and in crystal towards superfluorescence or superradiance might be of interest, since not many systems report both phenomenon at room temperature. Moreover, these characteristics occur in a biocompatible system and might overcome limitations of inorganic probes.

5.3.5 Protein cross-linkers and their influence on crystal properties

A protein crystal either loaded with AuNPs or empty needs to be stabilized by a suitable cross-linker for manipulations and characterizations outside the crystallization drop. Protein crystals are fragile and tend to break under mechanical stress. For stabilization, the cross-linking agent is added to the reservoir solution. Through evaporation glutaraldehyde slowly diffuses into the drop and gently cross-links the protein crystal. In detail, the glutaraldehyde is a dialdehyde that cross-links lysine residues of the protein container. After cross-linking the protein crystal can easily be manipulated without destruction. Usually, the protein crystal is washed with pure water to remove residual glutaraldehyde. One crucial drawback of using glutaraldehyde is the formation of polymeric glutaraldehyde species in solution. Moreover, the polymerization may start in solution forming a protein film from residual protein in solution. Or it can form a polymeric film and attach to the protein crystal. For AFM or SEM characterization, such a thin film is not desired. In addition, glutaraldehyde is expected to show green fluorescence at around 560 nm.^[267] Since fluorophore-labeled and AuNP loaded protein crystals will be investigated, additional fluorescence should be avoided. Ideally the samples feature neither an attached polymeric film nor fluorescence at any wavelength.

To overcome the problems associated with glutaraldehyde, three protein cross-linkers of different length were investigated (Figure 8.36). In detail, sulfosuccinimidyl-4-(N-maleimidomethyl)cyclohexan-1-carboxylate (sulfo-SMCC), bis(sulfo-succinimidyl)suberate (BS3) and PEGylated bis(sulfosuccinimidyl)suberate (BS(PEG)₅) were applied to stabilize

protein crystals. Both, BS3 and BS(PEG)₅ are homofunctional cross-linkers and react with primary amines. On the other side, sulfo-SMCC is a heterofunctional cross-linker and links thiols with primary amines. The maleimide functionality is also reported to react with amines,^[319] resulting in a mixture of lysine and cysteine residues reacting with sulfo-SMCC.

Adding the cross-linker dissolved in water directly to the crystallization drop might lead to disintegration of the crystal due to destabilizing effects by the significant concentration decrease of salt and precipitant. Therefore, the cross-linker is dissolved in water and then mixed 1:1 with the crystallization condition. The protein cross-linker is added to the crystallization drop. After incubation for at least 16 h, no polymeric or protein skin is observed. It should be noted that the protein buffer is Tris, which features one primary amine. Tris molecules in the crystallization drop might also react in the cross-linking, but would not result in larger contamination and only consume cross-linker. The crystal is transferred from the crystallization drop into a water drop, to check the stability. Protein crystals cross-linked with either sulfo-SMCC, BS3 or BS(PEG)₅ showed high stability in water. Afterwards, the cross-linked protein crystals were transferred on a glass substrate, illuminated and imaged via optical microscopy (Figure 5.61).

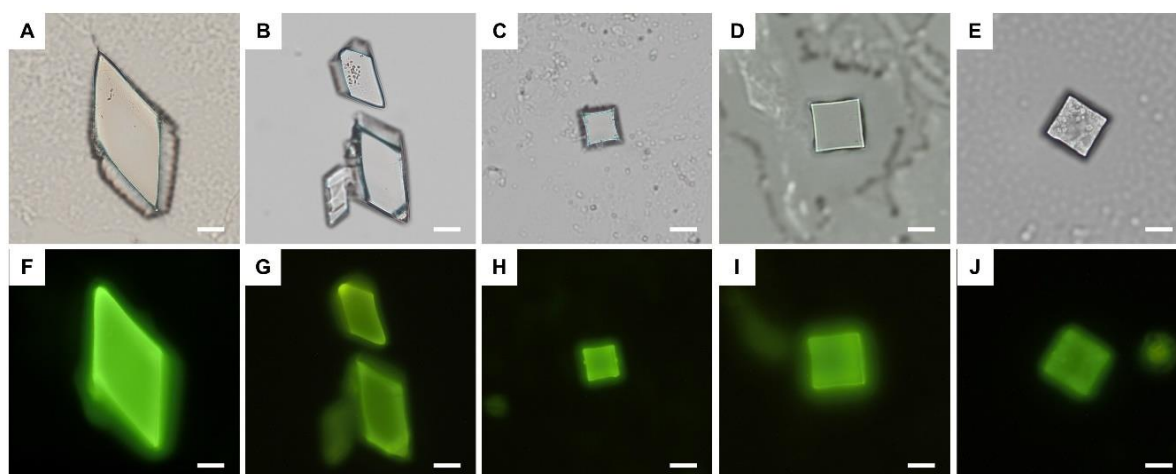


Figure 5.61: Optical microscopy images of cross-linked protein crystals. Unitary Enc^(neg) cross-linked with glutaraldehyde (A, F) or Sulfo-SMCC (B, G). Hetero binary crystals composed of Enc^(pos) and Enc^(neg) cross-linked with either Sulfo-SMCC (C, H), BS3 (D, I) or BS(PEG)₅ (E, J). Scale bar in (A), (B), (F) and (G) is 20 μm , the rest 10 μm .

The unitary Enc^(neg) crystal features green fluorescence for both glutaraldehyde and sulfo-SMCC. Aromatic amino acids are known to feature fluorescence in the ultraviolet (< 400 nm), but not in the green.^[320,321] As expected, the Enc protein in solution does not feature any emission in the green (> 495 nm) (Figure 8.37). Hetero binary crystals cross-linked with sulfo-SMCC, BS3 and BS(PEG)₅ also show green fluorescence. Despite using no glutaraldehyde, crystals are still fluorescent. The observation is contradictory to previous assumptions, that the green fluorescence is caused by the glutaraldehyde.^[13] The presence of the green

fluorescence may be caused by cross-linking agents in general. Due to the reaction of the cross-linker with two amino acids the local electronic structure could change and might lead to green fluorescence. On the other hand, novel properties may emerge with forming the protein crystal. Short hydrogen bonds are discussed to enhance fluorescence of non-aromatic amino acids in protein fibrils.^[322] Moreover, self-assembled peptide nanostructures were reported to feature intrinsic semi-conductive properties.^[323] In protein crystals, hydrogen bonding occurs not only intraproteic but also interproteic. Protein structures with a high content of hydrogen bonds may lead to proton transfer across hydrogen bonds which can lower electron excitation energies.^[324]

Nevertheless, three commercially available cross-linkers for protein crystal stabilization were established within this work. The cross-linking process was optimized towards the absence of protein or polymeric films in the crystallization drop. The origin of the fluorescence of protein crystals remains unsettled. Still, the fluorescence of sulfo-SMCC, BS3 and BS(PEG)₅ cross-linked protein crystals seem to be less intense (Figure 5.61).

5.3.6 Optical properties of nanoparticle – fluorophore loaded protein crystals

Hetero binary Enc^(neg)/Ftn^(pos)-Cys crystals cross-linked with sulfo-SMCC were chosen for optical characterization. In this work, crystals without cargo, loaded with AuNPs or labeled with fluorophore have already been shown (chapter 5.3.4.2). To achieve a large overlap and study the influence of the overlap between plasmon band of the AuNPs with the fluorophore emission, AF488, Rh6G and Rh3B were chosen. In Figure 5.62, the overlap of the absorbance and emission of the corresponding fluorophore-labeled protein is shown relative to the plasmon band of the encapsulated AuNPs in solution.

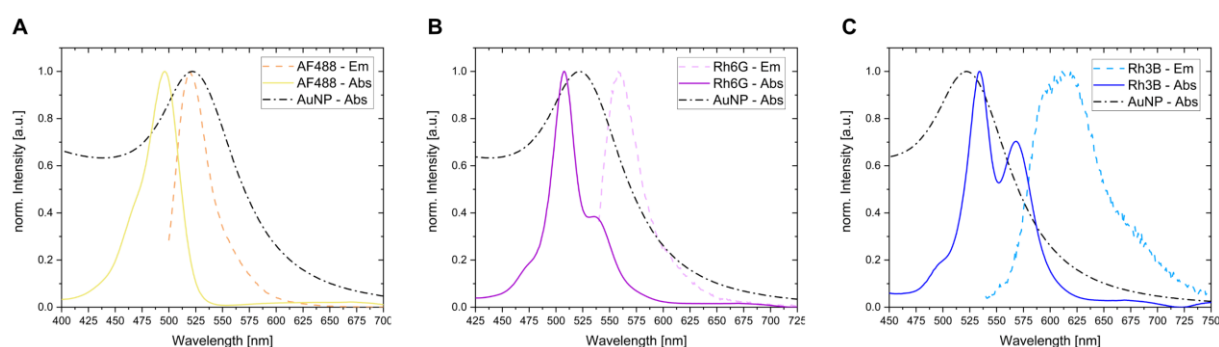


Figure 5.62: Comparison between absorbance of AuEnc^(neg) and emission and absorbance spectra of fluorophore-labeled Ftn^(pos)-Cys. Spectra for AF488 (A), Rh6G (B) or Rh3B (C) labeled Ftn^(pos)-Cys with AuEnc^(neg) as reference.

The coupling between fluorophores and AuNPs inside the binary crystal lattice were studied via fluorescence imaging. First, the loading of Enc^(neg) is addressed, then the Ftn^(pos)-Cys loading. Empty crystals (e/e), crystals filled with one component (e/AF488, e/Rh6G, e/Rh3B,

Au/e) and binary crystals (Au/AF488, Au/Rh6G, AuRh3B) were investigated with a confocal microscope at an excitation wavelength of 440 nm (Figure 5.63). Interference bands from the diode laser were filtered using a short path filter (450 nm). In addition, a long path filter (473 nm) is implemented to block the laser and pass light with wavelengths above 473 nm.

On closer inspection, empty protein crystals (Figure 5.63, green line) do not feature the previous observed fluorescence at 560 nm caused by glutaraldehyde (Figure 2.19).^[13] Here, an emission at 490 nm is observed. Emission at wavelengths below 473 nm are not recorded, due to the long path filter at 473 nm. The origin of the fluorescence of empty protein crystals remains unsettled, as discussed in previous chapter 5.3.5.

For Au/e crystals, the maximum at 490 nm is no longer clearly visible in emission spectra (Figure 5.63, blue line). A broad emission with two maxima at 525 nm and 625 nm is observed. The origin of the fluorescence is not unequivocal clear but can be attributed to the protein containers and AuNPs, respectively. Depending on the AuNP size, differently pronounced processes are reported.^[325] In size-independent systems, the emission is mainly influenced by the local binding geometry of AuNP ligands.^[326] In a previously published report by the BECK group, Au/e crystals composed of smaller AuNPs showed a different optical behavior. With an excitation wavelength at 405 nm, an emission maximum at around 480 nm is found (Figure 2.19).^[13] Above 500 nm, no maximum is visible. Most likely, most of the fluorescence is quenched due to absorption of the AuNPs and leftover fluorescence is caused by the protein content. Therefore, at this point the emission spectrum of Au/e crystals (Figure 5.63, blue line) is not clarified. FDTD simulations with the *Lumerical* software could assist in clarifying the properties of the AuNP lattice.

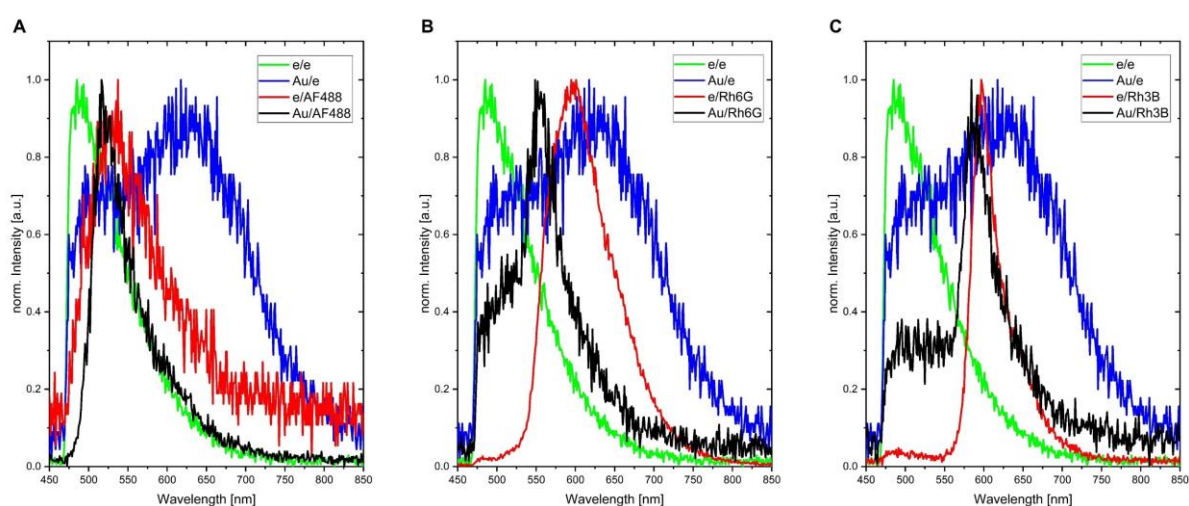


Figure 5.63: Emission spectra of hetero binary $Enc^{(neg)}/Ftn^{(pos)}$ -Cys crystals with AuNPs and fluorophores. Fluorescence spectra of AF488 (A), Rh6G (B) and Rh3B (C) hetero binary crystals either empty or with AuNPs. Excitation wavelength: 440 nm.

For a clearer presentation and direct comparison, the emission spectra of empty/fluorophore and AuNP/fluorophore crystals are extracted to Figure 5.64. Discussed emission maxima are also summarized in Table 5.22.

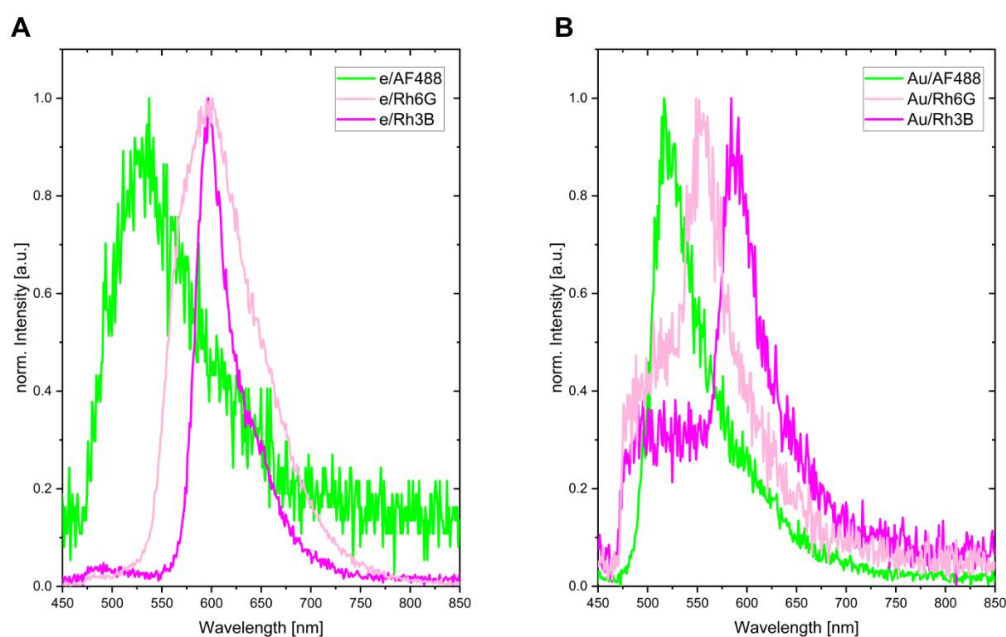


Figure 5.64: Emission spectra of empty/fluorophore and AuNP/fluorophore protein crystals. For direct comparison, the presented data is extracted from Figure 5.63.

The emission spectrum for e/AF488 crystals appears quite noisy, due to fluorescence of low intensity (Figure 5.64A, green line). Moreover, the emission peak with a maximum at 530 nm is broad in comparison to other emission spectra. The broad peak may be caused by an overlay of protein fluorescence and AF488 fluorescence. In solution, an emission maximum at 519 nm is shown (Figure 5.62). For the e/AF488 crystal, a shift of 11 nm towards longer wavelength (530 nm) occurs. For e/Rh6G and e/Rh3B crystals, fluorescence below 500 nm is observed, which is most likely present due to the protein or cross-linker content (Figure 5.64A, pink and magenta line, respectively). Also in other experiments within the BECK group, fluorescence in the region below 500 nm is found, that is probably caused by the protein content and not as strong as the fluorophore emission.^[13] Both e/Rh6G and e/Rh3B crystals have an emission maximum at 597 nm, while the peak of e/Rh6G is quite broad. In comparison between emission maxima in crystal and solution (Figure 5.62), shifts towards longer wavelength for Rh6G and shift towards smaller wavelengths for Rh3B are detected. Transitions from solution to solid state are known to cause shifts of emission. In solution, particles are free to move and rotate, but have fixed positions and orientations in a crystal lattice.^[327,328] The distance between fluorophores from one labeled container to another is shorter than in solution. Plus, the control over placement and orientation of fluorophores results in a molecular fluorophore superlattice. Most likely fluorophore-fluorophore interactions inside the lattice or collective coupling are causing the shifts.

In Figure 5.64B, emission spectra of hetero binary crystals composed of AuNPs and fluorophores are shown. In direct comparison between both green lines (Figure 5.64A and B), a shift from 530 nm towards 516 nm is found. The introduction of AuNPs into protein crystals containing AF488 seem to cause this shift. The protein crystals Au/Rh3B also feature a small shift towards smaller wavelengths (from 597 nm to 586 nm). Moreover, a significant shift of emission maxima is observed for the system Au/Rh6G. The protein crystal containing AuNPs and Rh6G features a maximum at 555 nm, while without AuNPs a maximum at 597 nm is found (Figure 5.64, pink line). The strong shift might indicate strong exciton-plasmon interactions. Additionally, only Au/Rh6G and Au/Rh3B feature a clearly visible second maximum at around 520 nm. It can be assumed that this fluorescence derives from the protein matrix, since the fluorescence was also found in crystal containing only AuNPs (Figure 5.63, blue line, Au/e). The measured fluorescence is quite weak, indicated by the high signal-to-noise ratio. In conclusion, the AuNPs do not completely quench the fluorescence, but absorb most of the energy.

Table 5.22: Summary of observed emission maxima of protein crystals composed of fluorophores and AuNPs.

Crystal composition	AF488Ftn ^(pos) -Cys	Rh6GFtn ^(pos) -Cys	Rh3BFtn ^(pos) -Cys
eEnc ^(neg)	530 nm	597 nm	597 nm
AuEnc ^(neg)	516 nm	555 nm	586 nm

In comparison to a previously published system containing smaller AuNPs and less fluorophores per protein container (more detailed description found in chapter 2.5.3), e/RhB crystals feature a maximum at 580 nm, while Au/RhB crystals at 575 nm. The implementation of AuNPs leads to a shift of 5 nm towards smaller wavelength.^[13] In this work, a shift of 11 nm is observed (Table 5.22). Larger AuNPs and a higher number of fluorophore molecules are expected to cause stronger exciton-plasmon interactions, indicated by a stronger shift in emission.

AF488 and Rh6G have the largest spectral overlap with the absorption spectra of the plasmonic AuNPs, while Rh3B the lowest (Figure 5.62). Therefore, interactions in Au/AF488 and Au/Rh6G crystals are expected to be the strongest. Based on the shifts in emission maxima, this trend is not visible in current data. Au/AF488 and Au/Rh3B spectra feature shifts of similar dimensions, while the largest shift is found for Au/Rh6G. The emission maximum for Rh6G functionalized Ftn^(pos)-Cys is slightly shifted towards longer wavelengths in relation to the maximal absorption of the plasmonic AuNPs. It seems like a larger spectral overlap in terms of absorption between AuNP and fluorophore and a smaller spectral overlap between AuNP absorption and fluorophore emission lead to strong interactions. Possibly, each spectral

overlap is not allowed to be either too large or too small. Further FDTD simulations are required to investigate and verify this observation. Moreover, expanding the library of fluorophores to further screen different spectral overlaps might help to understand the requirements for strong interactions and the observations described in this work.

In addition, fluorescence decay curves of the three systems were recorded (Figure 5.65). Empty crystals (e/e) feature the longest lifetime, while Au/e crystals by far the shortest lifetime.

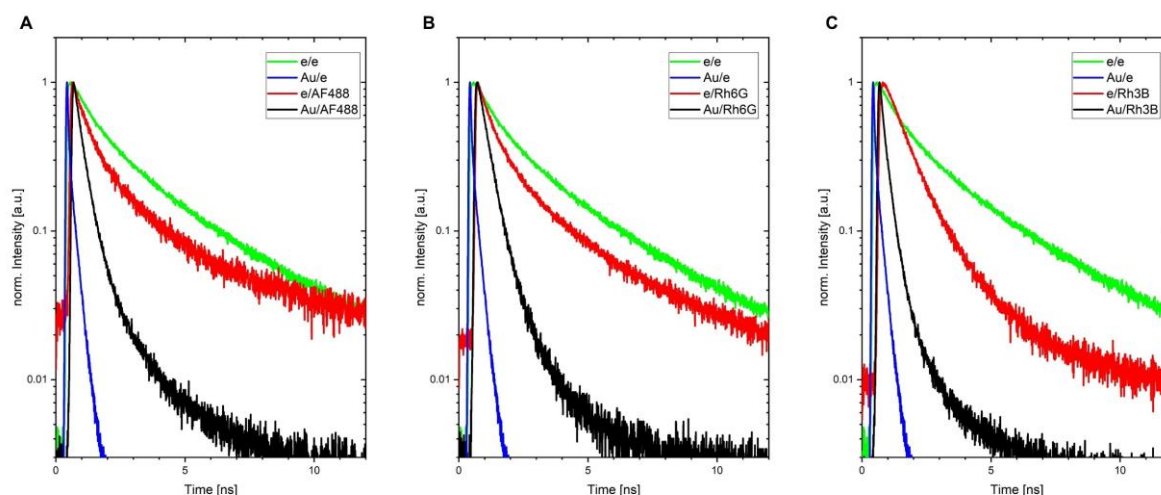


Figure 5.65: Lifetime curves for fluorophore and fluorophore-AuNP loaded protein crystals determined in confocal microscopy. Lifetimes curves of AF488 (A), Rh6G (B) and Rh3B (C) hetero binary crystals either empty or with AuNPs.

As shown in Figure 5.65, the coupling between fluorophores and AuNPs seem to be stronger as in previous work (Figure 2.19), due to strong exciton-plasmon coupling. Lifetimes of $\text{AuFtn}^{(\text{pos})}/\text{RhBFtn}^{(\text{neg})}$ crystals were significantly longer, indicating weaker coupling. In this work, both the AuNP size and the number of fluorophores increased significantly: From 3 to 13 nm large AuNPs and from 2 to 24 fluorophores per container.^[13] As discussed in previous chapters, AuNPs of a size of 3 nm are not expected to show as strong plasmonic properties as 13 nm large particles. Also, decay curves for $\text{eFtn}^{(\text{pos})}/\text{RhBFtn}^{(\text{neg})}$ crystals (Figure 2.19) feature longer lifetimes than observed for $\text{eEnc}^{(\text{neg})}/\text{Rh3BFtn}^{(\text{pos})}$ -Cys crystals (Figure 5.65C). This indicates, that not only coupling with gold nanoparticles but also the collective interactions between the increased number of fluorophores with fixed positions and orientations are stronger.

The lifetime curves for empty/fluorophore and AuNP/fluorophore crystals are extracted into Figure 5.66 to directly compare each of the novel systems in more detail. Lifetime curves for e/AF488 and e/Rh6G are quite similar. Besides, the curve for e/Rh3B indicates a slightly longer lifetime. In general, the addition of AuNPs to the fluorophore-loaded protein crystals lead to a significant decrease in fluorescence lifetimes. Such a strong decrease is based on energy transfers between fluorophores and gold plasmons via exciton-plasmon coupling. Also, the

decay curves for Au/AF488 and Au/Rh6G are very similar. For Au/Rh3B crystals, the lifetime is slightly shorter. Interestingly, the spectral overlap of Rh3B and AuNP was the lowest, but feature the shortest lifetime. Usually, a shorter lifetime caused by strong coupling effects. Based on the large shift of emission maxima, the strongest coupling is determined to occur in the Au/Rh6G system. On the other hand, the fluorescence lifetime curves indicate that the strongest coupling is found in the Au/Rh3B and not Au/Rh6G crystal. Therefore, the shift of emission might not be the perfect property to evaluate a strong or weak coupling. The investigation of fluorescence lifetimes might be more suitable for evaluation.

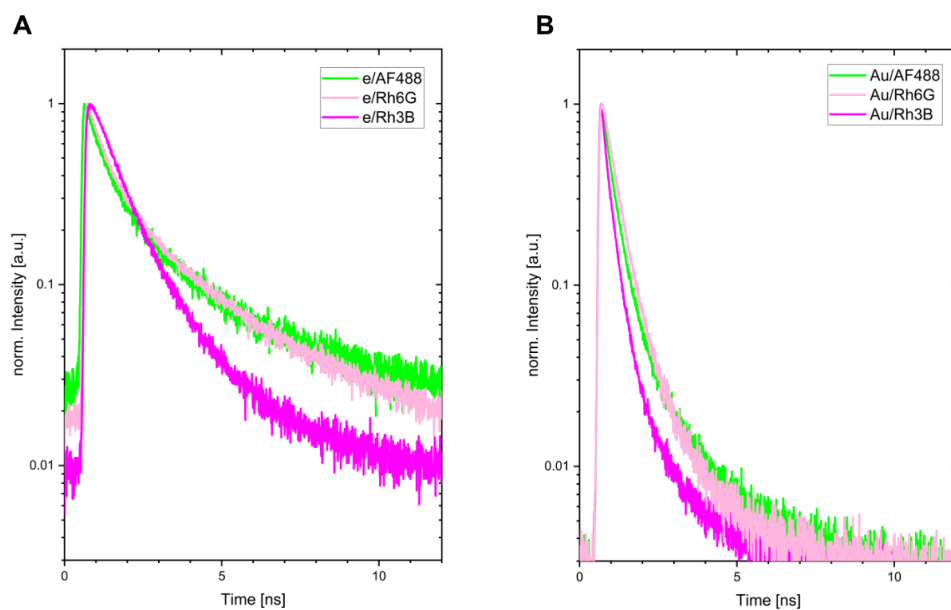


Figure 5.66: Lifetimes curves for empty/fluorophore and AuNP/fluorophore protein crystals. For direct comparison, the presented data is extracted from Figure 5.65.

To further understand the system, additional modelling is needed. The distance between AuNP and fluorophore plays a significant role in the type and strength of interaction. Based on the crystal structure model (Figure 5.58), the distance between AuNPs is estimated to be 24.4 nm. The closest distance calculated on the C- α atom distance between C53 residues within a Ftn^(pos)-Cys container is 2.6 nm. The longest distance is across the container cavity with 8.3 nm. Between two Ftn^(pos)-Cys containers, the shortest distance of two C- α atoms is 4.2 nm. The distance between AuNP surface to the closest C- α atom of a C53 residue is assumed to be between 7 nm to 8 nm. From AuNP core to C53 residue the distance is roughly 14.2 nm. Future FDTD simulations could make it possible to simulate the plasmonic properties of the AuNP lattice, but also add dipoles as emitters into the simulation and calculate the coupling. Due to the crystal structure, a fluorophore-labeled Ftn^(pos)-Cys container is located between four AuNP loaded Enc^(neg) containers. Between the AuNPs hot spots are expected to occur and the location of the fluorophores at the hot spot region might be beneficial for effective coupling.

In the end, measurements were carried out to investigate the properties of binary superlattices composed of fluorophores and AuNPs. The incorporation of AuNPs led to a significant decrease in fluorescence lifetime, indicating strong interactions between AuNPs and fluorophores. Moreover, emission spectra of AuNP and fluorophore-loaded protein crystals feature properties their single components have. Even assemblies with AuNPs show characteristic emission spectra. In the end, detailed comparisons between previously published and the here reported novel hetero binary system were conducted. Still, further simulations are required to understand and explain the described results.

6 Summary and perspective

In conclusion, protein containers were organized into highly ordered nanomaterials with unique properties. For this purpose, supercharged protein containers based on encapsulin and ferritin were produced and purified. Subsequently, the protein containers were either loaded with nanoparticles or labeled with fluorophores and assembled in a crystalline lattice.

The first part is about the generation of novel building blocks for the assembly of binary superlattices. The supercharging and removal of the flavin binding-site of the *T. maritima* encapsulin was carried out by mutagenesis. Both Enc^(neg) and Enc^(pos) were produced, purified and characterized by ESI MS, TEM, DLS and ζ -potential. In addition, a positively supercharged ferritin with additional cysteine on the inner surface was produced, purified and characterized.

The second part is about the incorporation of nanoparticles and fluorophores in protein containers. To encapsulate nanoparticles into encapsulin, the dis- and reassembly process was investigated with TEM. In previous works, the disassembly at pH 2.0 was possible, but had to be adjusted to a pH value of 1.0 to achieve complete disassembly. Subsequently, gold nanoparticles of a size of 13 nm were encapsulated in both supercharged Enc variants. To achieve high encapsulation efficiencies, the salt concentration was screened and adjusted. Then, the encapsulation was upscaled to milligrams of protein because larger amounts are needed for crystallization. Moreover, the synthesis of smaller gold nanoparticles was carried out. After CLP functionalization and characterization via TEM, DLS and ζ -potential, the encapsulation in supercharged Enc containers was shown. Encapsulation experiments were evaluated with TEM. Protein containers featured multiple small gold nanoparticles inside their cavity. The ability to encapsulate multiple smaller objects highlights that the cargo can also be significantly smaller and opens the possibility of incorporating multiple particles. To further exploit the encapsulation on other spherical particles, semiconductor particles were chosen. Two ligand systems based on small organic molecules and longer PEGylated ligands were applied on giant core/shell quantum dots. First characterization via TEM and emission spectra indicates successful encapsulation, but further optimization is needed. The encapsulation of another type of cargo highlights the universal approach of the encapsulation of nanoparticles into protein containers. Since it was shown that multiple smaller gold nanoparticles can be encapsulated, the option to encapsulate single or multiple quantum dots into the encapsulin cavity is opened. Also, the encapsulation of anisotropic particles may be possible. Moreover, the inner ferritin container surface was functionalized with fluorophores. In detail, three different fluorophores were integrated into the ferritin container. Mass spectroscopy verified full labeling for each fluorophore-labeled protein, indicating the high efficiency of the thiol-maleimide coupling. Here, it is possible to incorporate more fluorophores into the ferritin cavity by increasing the number of cysteines per subunit. Moreover, the inner encapsulin container

surface can also be altered with additional cysteines for fluorophore labeling. Based on the larger size of the encapsulin container, even more fluorophores can be incorporated. Protein containers act as a template for fluorophore labeling and enable the control of position and orientation of fluorophores. Optical properties such as superradiance or superfluorescence might be enabled with such systems.

The last part is about the crystallization of novel protein containers towards binary superlattices. First, oppositely charged encapsulin variants were screened in a robotic screening setup. Several unitary crystallization conditions were found, but no binary encapsulin structure. X-ray diffraction experiments were carried out at DESY and EMLB in Hamburg to collect data and solve structures of unitary protein crystals. Despite the low resolution, it was possible to determine unit cell parameters and position the containers. Detailed analysis of all crystal structures revealed which protein container surface areas are involved in protein-protein interfaces. Based on these results, further design could be carried out on encapsulin containers to enable binary encapsulin crystals. The introduction of aromatic residues in interfaces may enable π - π stacking between oppositely charged protein containers. In addition, introduced mutations along the fivefold axis in positively supercharged encapsulin could be removed. No interface was observed for positive encapsulin, while negatively charged encapsulin possess interfaces along the fivefold axis. The *Rosetta* software suite features modules to analyze protein-protein interfaces and may give further hints towards feasible protein design for binary protein crystals. Binary encapsulin crystals could combine gold nanoparticles and quantum dots towards binary superlattices with properties such as energy transfer.

Moreover, gold nanoparticle-loaded protein crystals were achieved with high reproducibility and characterized with SEM and EDX. Protein crystal surfaces were imaged and highlight the high order of the protein crystals. In addition, gold nanoparticle-loaded encapsulin crystals were characterized by X-ray diffraction at beamline P14 (EMBL, Hamburg) to study the nanoparticle lattice. Such a gold nanoparticle-loaded protein crystal might act as a biocompatible SERS substrate. Moreover, gold nanoparticle-loaded protein containers may also be deposited on surfaces to achieve thin layers. Analytes might not be able to diffuse into thick protein crystals, therefore several layers of gold nanoparticles might be sufficient. Further knowledge of the suitability of protein-based SERS substrates is needed. FDTD simulations should be performed to calculate enhancement factors of possible assemblies. Different crystallization conditions with different densely packed crystal systems were established. Some systems feature larger channels between protein containers, while others are tightly packed. Moreover, protein crystals based on protein containers loaded with 13 nm or 3.5 nm gold nanoparticles may exhibit varying degrees of catalytic activity.

Since no binary encapsulin crystals were obtained, an alternative route was taken using encapsulin and positively charged ferritin. Ferritin combined with encapsulin enabled binary superlattices based on two differently sized protein containers. In conclusion, the aim of establishing binary protein crystals composed of two oppositely charged protein containers was successful. Despite the low resolution, a cubic crystal system was determined. Crystallization of both protein containers with different cargo verified that these crystals are indeed binary. Binary superlattices based on gold nanoparticles in encapsulin with magnetic iron oxide or cerium oxide nanoparticles in ferritin were characterized by TEM, AFM and SEM. Additionally, single crystals were characterized by X-ray diffraction at beamline P14 (EMBL, Hamburg). It was possible to determine cubic crystal systems in nanoparticle loaded hetero binary protein crystals. Based on these methods, it was possible to verify the cubic crystal system.

Binary protein crystals loaded with gold and cerium oxide nanoparticles may be a suitable platform to track catalyzed reactions directly via SERS. Cerium oxide nanoparticles were shown to be applied in e.g. peroxidase, while gold nanoparticles are suitable for SERS. In addition, the combination of plasmonic and magnetic nanoparticles may result in a protein crystal with unique properties. Such a material could feature magneto-optical properties not yet reported for any protein-based assembly. Since the iron oxide nanoparticles synthesized inside the ferritin container does not feature strong magnetic properties, larger magnetic nanoparticles could be encapsulated in encapsulin. The CLP-mediated encapsulation seems to be very promising for the encapsulation of nanoparticles.

Moreover, binary protein superlattices composed of gold nanoparticles and fluorophores were prepared. Despite their small size, crystals composed of fluorophores and combined with gold nanoparticles were characterized by confocal microscopy. Interactions between plasmonic particles and fluorophores were observed. In presence of gold nanoparticles, fluorescence lifetimes are significantly decreased. Emission spectra of gold nanoparticle and rhodamine-based crystals look like a combination of their single components. To further understand the kind of interactions, additional FDTD simulations are required. The encapsulins are densely packed and should enable plasmon coupling between the encapsulated gold nanoparticles. Ideally, hot spots form between the gold nanoparticles. Since each encapsulin is also surrounded by fluorophore-labeled ferritins, interactions between gold nanoparticles and fluorophores are very likely. In addition, protein crystals only composed of fluorophore-labeled proteins might be of interest. The incorporation of even more fluorophores per protein container in a protein crystal might result in a superfluorescent crystalline material. Such a material might gain interest in optical applications.

7 Experimental part

7.1 General

All syntheses, buffer preparations, labeling and crystallization experiments were carried out with ultrapure water. Ultrapure water was prepared with a *Purelab Flex 2* system (resistivity 18.2 M Ω cm) manufactured by *ELGA LabWater*. Glassware and magnetic stir bars used for gold nanoparticle synthesis were cleaned with aqua regia and rinsed with ultrapure water to remove residual adsorbents. Prepared buffers were filtered with a 0.22 μ m membrane filter (*Carl Roth*). For general sample storage or labeling experiments, 15 mL and 50 mL polystyrene tubes (*Carl Roth*) or 1.5 mL and 2.0 mL reaction tubes (*Carl Roth*) were used. The centrifugation of larger polystyrene tubes (15 mL and 50 mL) was performed with an *Eppendorf 5810R* centrifuge, while smaller tubes (1.5 mL and 2.0 mL) were centrifugated in a *Heraeus Fresco 21* microcentrifuge from *Thermo Scientific*. Volumes above 50 mL were centrifugated in a *Multifuge X4R Pro* manufactured by *Thermo Scientific*. Experiments that require sterile conditions were performed under a biosafety cabinet *Maxisafe 2030i* from *Thermo Scientific*. Cryo-cultures and competent cells were stored at -80 °C. Protein containing cell pellets were stored at -20 °C. Purified protein solutions and solutions with loaded or labeled protein containers were stored at 4 °C. Crystal plates were stored at 20 °C unless stated otherwise. Protein concentrations were determined with a *NanoDrop One C* spectrophotometer manufactured by *Thermo Scientific*. Centrifugal filter units *Vivaspin[®] Turbo 15* from *Sartorius* and *Amicon[®] Ultra-0.5* from *Merck* with molecular weight cut-offs (MWCO) of either 30 kDa or 100 kDa were used for dialysis (including concentration, washing and buffer exchange).

7.2 *E. coli* strains

Table 7.1: List of used *E. coli* strains.

Strain	Genotype	Supplier
DH5 α	F- Φ 80lacZ Δ M15 Δ (lacZYA-argF) U169 recA1 endA1 hsdR17(rk-, mk+) phoA supE44 thi-1 gyrA96 relA1 λ -	Invitrogen
BL21(DE3)	<i>E. coli</i> B F- dcm ompT hsdS(rB- mB-) gal λ (DE3)	Agilent
C43(DE3)	F- ompT hsdSB (rB- mB-) gal dcm (DE3)	NEB

7.3 Chemicals

All chemicals were purchased from commercial suppliers and used without further purification (chapter 13).

7.4 Analytical methods

7.4.1 Transmission electron microscopy

In general, carbon-coated copper grids with 400 mesh size (*Ted Pella*, 01814-F-X) were used for transmission electron microscopy (TEM) measurements. Protein or nanoparticle containing samples were investigated by *Stefan Werner* (University of Hamburg, Germany) on a *JEOL JEM 1011* operated at 100 kV. Unstained samples were prepared by drying 2 μL of the sample on the TEM grid. For uranyl acetate-stained samples, a 2 % solution is used. First, the grid is incubated 1 min on a droplet of 10 μL sample. Afterwards, the grid is washed three times in ultrapure water, followed by one wash and one incubation step (60 s) on a 2 % uranyl acetate droplet. Residual solution is blotted and the grid dried. Protein crystals were investigated on a *Tecnai G2 Spirit TWIN* at 120 kV. 10 μL ultrapure water are placed on a TEM grid and the crystal transferred into the drop, prior removal of the drop.

Images were analyzed with the *ImageJ* software.^[329] The size of AuNPs was determined by converting the images into binary images (black/white) with the threshold function and to enable automatic counting and area determination. At least 200 NPs were considered for size determination. Protein containers were measured manually by analyzing 100 particles per sample. Around the whole protein container, a circle was drawn to determine the size.

7.4.2 Scanning electron microscopy

Scanning electron microscopy (SEM) measurements of unitary $\text{Enc}^{(\text{neg})}$ crystals were carried out by *Robert Schön* (University of Hamburg, Germany) on a *Zeiss Leo1550* scanning electron microscope and operated at 2.0 kV. Energy-dispersive electron X-ray (EDX) spectroscopy was performed with an EDX detector (SDD 100 mm^2). Hetero binary $\text{Enc}^{(\text{neg})}/\text{Ftn}^{(\text{pos})}$ crystals were investigated on a *FEI (Thermo Fisher) Nova NanoSEM 450* operated by *Dr. Thomas F. Keller* (DESY, Hamburg, Germany) at 10.0 kV. Protein crystals were washed with ultrapure water, transferred into a drop of ultrapure water on a silicon wafer and dried under air.

7.4.3 Electrospray ionization mass spectrometry

Protein samples were rebuffed to ultrapure water with a centrifugal filter. The sample is filled up with ultrapure water to a maximum volume and concentrated until dead volume is reached.

The process is repeated five times. Protein concentrations is set to be around 2 mg/mL. Molecular masses of proteins are determined with electrospray ionization (ESI) time of flight mass spectrometry (*Agilent 6224 ESI-TOF*). Measurements were carried out by the *MS Service* (University of Hamburg, Germany) in positive mode with a tracked mass range of m/z values between 110 and 3200 with a rate of 1.03 spectra per second. The instruments source temperature was set to 325 °C, the gas flow at 10 L/min and nebulizer pressure at 15 psig. The capillary voltage was set to 4 kV.

Data interpretation was carried out with the software *MestreNova*.^[330] Each signal observed in MS spectra can be attributed to an ion with a specific charge z and mass m . Based on the mass to charge ratio (m/z) of two neighboring signals and the mass of a proton (m_H) the charge z can be calculated as shown in equation (1).

$$z = \frac{\frac{m_2}{z_2} - m_H}{\frac{m_1}{z_1} - \frac{m_2}{z_2}} \quad (1)$$

The molecular mass of the protein can be calculated for one signal and its specific mass to charge ratio (m/z) if the charge is known (equation 2).

$$M_{protein} = z_1 \left(\frac{m_1}{z_1} - m_H \right) \quad (2)$$

7.4.4 Matrix-assisted laser desorption/ionization mass spectrometry

The protein sample preparation was carried out as for ESI. For the measurement setup, either dihydroxybenzoic acid (DHB) or 2',5'-Dihydroxyacetophenon (DHAP) were used as a matrix. DHB was dissolved in an acetonitrile water mixture (3:7) supplemented with 0.1 % trifluoroacetic acid to a final concentration of 20.0 mg/mL. DHAP was dissolved in an ethanol di-ammonium citrate (18.0 mg/mL) mixture in a ratio of 3:1 with a final DHAP concentration of 15.2 mg/mL. For each DHB and sample 0.7 μ l were mixed and crystallized. DHAP, sample and 2 % trifluoroacetic acid were mixed in equal volumes (2.0 μ L) and 1 μ L of the mixture applied and crystallized. The MALDI measurements were carried out by the *MS Service* (University of Hamburg, Germany) on an *ultrafleXtreme* manufactured by *Bruker* in positive reflection mode. Data interpretation and evaluation was done as described in chapter 7.4.4.

7.4.5 SDS-Page and native PAGE

For SDS-PAGE, protein samples were denaturated for 10 min at 95 °C in a 1:1 mixture with SDS loading buffer (50 mM Tris pH 6.8, 10 % (v/v) glycerol, 0.1 % (w/v) bromophenol blue, 2 % (w/v) SDS and 250 mM DTT). The samples were then loaded on the gel and electrophoresis was carried out at 200 V using 1x Tris-Glycine SDS buffer (25 mM Tris,

250 mM Glycine, 0.1 % (w/v) SDS). Precast Tris-Glycine (4 % - 20 %) gels were purchased at *Biotrend*.

For native PAGE gels, SDS was omitted for all buffers. The native dye solution (20 % (v/v) 1.5 M Tris pH 8.8, 60 % (v/v) glycerol and 0.6 % (w/v) bromophenol blue) is added in a 5:1 ratio to the sample. The electrophoresis was carried out at constant voltage of 150 V using 1x Tris-Glycine buffer. Samples were separated with 4 % native gels. The native gel was prepared as described in Table 7.2.

Table 7.2: Native-PAGE gel composition.

4 % Native gel	
Chemical	Volume [mL]
Ultrapure water	6.1
1.5 M Tris pH 8.8	2.5
30 % Acrylamide / 3.3 % Bisacrylamide	1.3
10 % (w/v) APS	0.1
TEMED	0.01

After electrophoresis, gels were stained using Coomassie Brilliant Blue stain solution (40 % (v/v) methanol, 10 % (v/v) acetic acid, 0.2 % (w/v) Coomassie Brilliant Blue R250) overnight. Excess stained was removed by a destain solution consisting of 20 % (v/v) isopropyl alcohol and 10 % (v/v) acetic acid.

7.4.6 UV-Vis spectroscopy

Absorbance spectra were recorded on a *Cary 60 UV-Vis* spectrophotometer manufactured by *Agilent*. Disposable UV microcuvettes (*Brand*) with 1 cm path length were used. As reference either ultrapure water or respective buffer acted as reference.

Emission spectra were recorded on a *Fluoromax 4000* by *Horiba Jobin Yvon*. Disposable UV microcuvettes (*Brand*) with 1 cm path length were used. As reference either ultrapure water or respective buffer acted as reference.

7.4.7 Dynamic light scattering

Dynamic light scattering (DLS) measurements were carried out on a *Zetasizer Nano S* from *Malvern Instrument*. The device is equipped with HeNe laser (633 nm). All measurements were performed at a backscattering angle of 173 ° and at a temperature of 25 °C. Protein container samples were stored in the respective storage buffer. The protein concentration was 1 mg/mL.

Nanoparticles were measured in ultrapure water. The nanoparticle solution was diluted until the plasmonic peak intensity was below 0.1 AU. Aqueous solutions were measured in disposable cuvettes (*Brandt*) and organic solvents in quartz cuvettes. First, the samples were equilibrated for 120 s and then measured. At least three runs were performed and averaged.

7.4.8 Zeta potential

Zeta potential measurements were performed on a *Zetasizer Nano S* from *Malvern Instrument* furnished with HeNe laser (633 nm). Measurements were conducted at 25 °C in micro zeta disposable capillary cells (DTS1070, *Malvern Instrument*). Protein and nanoparticles samples were prepared as described in chapter 7.4.7. The samples were equilibrated for 120 s and at least three measurements were performed and averaged. For data analysis, the SMOLUCHOWSKI approximation is applied to convert the electrophoretic mobility to the zeta potential.

7.4.9 Atomic absorption spectroscopy

Atomic absorption spectroscopy (AAS) measurements to determine Au concentrations were performed by *Zentrale Element-Analytik Service* (University of Hamburg, Germany) on a *AAAnalyst 600* manufactured by *Perkin Elmer*. Prior the measurement, the samples were treated with aqua regia. Each sample was measured three times.

7.4.10 Optical microscopy

Imaging of crystals were performed with three different setups. For imaging of empty or nanoparticle crystals, either a *Leica S9D* equipped with a *Flexacam C1* or a *CrysCam™ Digital Microscope* (*Dunn Labortechnik*) was used. The scale bar is based on a microscope calibration millimeter. To investigate the fluorescence of protein crystals a *BX51 fluorescence microscope* from *Olympus* equipped with a *X-Cite 120PC Q* illumination system is used.

7.4.11 Confocal imaging

Emission spectra and fluorescence decay curve measurements on protein crystals were performed by *Dr. Christian Strelow* (University of Hamburg, Germany) on a home-built confocal microscope.

7.5 Gold nanoparticle synthesis

For the synthesis of AuNPs, two different syntheses were performed to obtain AuNPs of the desired size. After synthesis, native ligands were removed via ligand exchange reaction. All samples were analyzed by TEM, DLS, zeta-potential and UV-Vis.

7.5.1 Improved TURKEVICH synthesis

AuNPs were synthesized by the protocol of SCHULZ *et. al.*^[41] Trisodium citrate dihydrate (121.0 mg) and citric acid (29.0 mg) were dissolved in 150 mL ultrapure water. The citrate buffer was stirred (3 cm stir bar, 300 rpm) and heated until boiling. The flask was covered with a small beaker to prevent excessive evaporation. The gold precursor tetrachloroauric(III) acid trihydrate (16.0 mg) was dissolved in 50 mL ultrapure water and heated at 80 °C. After boiling the citrate buffer for 14 min, EDTA (1.5 mg) was dissolved in 0.1 mL ultrapure water and added to the solution. After one additional minute, the hot gold precursor solution was quickly added to the reaction mixture. After color change from colorless to wine-red the mixture was continuously stirred and heated for additional 20 minutes. In the end, the reaction mixture was cooled at room temperature until the lukewarm solution is stored at 4 °C until further treatment.

7.5.2 PENG synthesis

Smaller gold nanoparticles were synthesized by a protocol published by PENG *et. al.*^[294] A precursor solution containing 2 mL tetralin (1.94 g), 2 mL oleylamine (1.63 g) and 20 mg tetrachloroauric(III) acid trihydrate were prepared in a SCHLENK flask. Under nitrogen atmosphere, the solution was stirred for 2 min followed by 30 min heating at 30 °C. Subsequently, a reducing solution containing tetralin (0.2 mL), oleylamine (0.2 mL) and tert-butylamine borane complex (32.2 mg) was added under nitrogen stream. The color of the solution immediately changes from orange to dark red. The reaction mixture was stirred for an additional hour at 30 °C. Afterwards, 40 mL acetone were added terminate the reaction. The black precipitate was centrifugated (6000 g, 8 min), washed with 9 mL acetone and one additional time repeated. The pellet was resuspended in dichlormethane (10 mL).

7.5.3 Calculation of gold nanoparticle concentration

The AuNP concentration is required to calculate the number of ligands to be used for the ligand exchange. The gold concentration $c(Au)$ was determined by AAS. Subsequently, the AuNP concentration $c(AuNP)$ can be calculated by using the number of atoms per NP $N_{Atom/NP}$ (equation 3).

$$c(\text{AuNP}) = c(\text{Au})/N_{\text{Atom/NP}} \quad (3)$$

The number of atoms per NP can be calculated according to equation (4). The density of gold ρ_{Au} (19.32 g/cm³), volume of a spherical AuNP V_{AuNP} in cm³ determined by TEM, the molar mass of Au M_{Au} (196.97 g/mol) and the Avogadro constant N_A ($6.022 \cdot 10^{23}$ mol⁻¹) are required.

$$N_{\text{Atom/NP}} = \frac{\rho_{\text{Au}} V_{\text{AuNP}} N_A}{M_{\text{Au}}} \quad (4)$$

7.6 Ligand exchange

7.6.1 Citrate stabilized AuNPs

Citrate stabilized AuNPs based on the TURKEVICH method were first used for ligand exchange. The ligand exchange was performed as described elsewhere.^[10] For the ligand exchange from citrate to 11-(Mercaptoundecyl)-N,N,N-trimethyl ammonium bromide (MUTAB), the latter one is dissolved as a 100-fold excess as referred to the maximum number of ligands on the nanoparticle surface in a 2 M HCl solution. The MUTAB containing HCl solution is added to the NP solution resulting in a HCl concentration of 0.1 M HCl. The sample was incubated at room temperature for 48 h. Excess MUTAB and exchanged citrate were removed via centrifugal concentration steps. First, the sample is washed five times with 0.1 M HCl, followed by five washing steps with ultrapure water. Finally, the sample is concentrated to a volume of 1 mL.

Prior CLP functionalization, a CLP stock solution (0.5 mg/mL in DMF) is prepared. MUTAB-stabilized AuNPs are diluted 1:10 with DMF. Subsequently, an amount of CLP corresponding to 20 peptides per NP were added to the NP solution. After 16 h incubation at room temperature, the NP solution was diluted 1:10 with water. In the end, the solution is concentrated and washed five times with water using a centrifugal filter and concentrated to a volume of 1 mL.

7.6.2 Oleyl amine stabilized AuNPs

Oleyl amine stabilized AuNPs based on the PENG synthesis were rigorously mixed with a MUTAB containing solution of ultrapure water in equal volumes. MUTAB is added in a 100-fold excess. The ligand exchange reaction is incubated at room temperature for 16 h. Then, the aqueous solution is extracted and five times washed with water with a centrifugal filter. The sample is concentrated to a final volume of 1 mL.

For CLP functionalization, a CLP stock solution (0.5 mg/mL in DMF) was used. MUTAB stabilized AuNPs were diluted 1:10 with DMF. Either 5 or 10 CLPs per NP were added to the ligand exchange. After incubation for 16 h at room temperature, the sample was diluted 1:10

with water and washed five times with water. In the end, the sample was concentrated to a final volume of 1 mL.

7.6.3 Giant core/shell QDs

The ligand exchange for short organic molecules was based on a biphasic system containing chloroform and water. First, 1.5 mg gQDs were taken and the solvent hexane was removed under reduced pressure. Subsequently, 10 mL of the ligand solution (0.5 mg/mL) in chloroform was added to the yellow solid. In a 1:2 ratio aqueous potassium hydroxide (KOH, 89 mM) is added to the reaction mixture. The biphasic system was stirred gently for 16 h at room temperature. The organic phase was separated and washed with 2 mL of an 89 mM KOH solution. Both aqueous phases were combined and precipitated with methanol at 12000 g for 10 min. Methanol was removed and the resulting yellow solid resuspended in 2 mL ultrapure water.

For CLP functionalization, a CLP stock solution (0.5 mg/mL in chloroform) was used. The protocol was carried out as described above. Either 10 or 100 CLP molecules per nanoparticle were added to the MUA ligand solution.

PEG based ligands were applied in a direct approach.^[204] A solution containing 1 mg of gQDs was taken and the solvent hexane was removed under reduced pressure. 10 mg of PEG ligand were dissolved in 1 mL chloroform and added to the dried gQDs. The solution was heated overnight at 65 °C. On the next day, the solvent was removed under reduced pressure. The residue was suspended in 2 mL of a 1:1 mixture of ultrapure water and ethanol. After centrifugation at 12000 g for 10 min, the supernatant is taken for further experiments and the pellet discarded.

7.7 Protein related protocols

7.7.1 QuikChange™ site-directed mutagenesis

The protein supercharging was performed by multiple cycles of QuikChange™ site-directed mutagenesis using a two-step polymerase chain reaction (PCR).^[279] Primers designed for the different mutations are shown in Table 8.4 and ordered at *Eurofins Genomics*.

First, a mixture was prepared by combining 2.9 µL pET-22b(+) plasmid (7 ng/µL) containing the gene of interest, 1 µL 10 mM dNTP mix, 5 µL buffer (200 mM Tris-HCl pH 8.8, 100 mM ammonium sulfate, 100 mM KCl, 1 % (v/v) Triton X-100, 1 mg/mL BSA), 1 µL Pfu DNA polymerase (2.5 U/µL) and 38.1 µL ultrapure water. Then, the mixture is split equally in two microtubes. In each tube 1 µL of either forward or reverse primer (100 pmol/µL) is added.

Subsequently, the PCR (*Eppendorf Mastercycler Nexus PCR Cycler*) is performed with the following parameters (Table 7.3). After segment 2 (“Hold”), both mixtures containing forward and reverse primers were combined.

Table 7.3: Two-step PCR cycling protocol.

Segment	Cycles	Temperature [°C]	Time	Total time
1	1x	95	30 s	23.5 min
		95	30 s	
2	3x	58	1 min	23.5 min
		68	6 min	
Hold	-	4	∞	-
		95	30 s	
3	16x	58	1 min	120 min
		68	6 min	
4	-	68	10 min	10 min
Storage	-	4	∞	-

The finished PCR is followed by a digestion of parental plasmid by adding 1 µL DpnI (10 U/µL) and incubation overnight at 37 °C. The next day, DpnI is deactivated by 20 min heating at 80 °C and purified by using *NucleoSpin™ Gel and PCR Clean-up Kit (Macherey-Nagel™)* according to the manual protocol. Next, 100 µL competent cells were mixed with 200 ng of the plasmid and incubated for 30 min on ice, followed by a heat shock for 45 s at 42 °C. After two minutes on ice, the competent cells were added to 0.9 mL super optimal broth (SOB) media and incubated for 1 h at 37 °C, shaking at 250 rpm. Afterwards the cells were gently pelleted by centrifugation at 1000 g for 1 min. The cells were resuspended in 100 µL media, plated onto LB agar plates with ampicillin (150 µg/mL) and incubated for 16 h at 37 °C. The next day, a single colony was picked and incubated at 37 °C and 250 rpm in 5 mL sterile LB medium supplemented with 150 µg/mL ampicillin. After 16 h incubation, the plasmids were extracted by *NucleoSpin™ Plasmid Miniprep Kit (Macherey-Nagel™)*.

DNA sequencing was carried out at *Eurofins Genomics*. 500 ng Plasmid were mixed with 25 pmol T7 forward or reverse primer in a 10 µL solution. The results were analyzed by *CLC Sequence Viewer (QIAGEN Bioinformatics)*. Plasmids containing the desired mutations were chosen as parental plasmids for further mutations, until all mutations were present.

7.7.2 Protein production and purification

Either an *ÄKTA pure 25 M* or *ÄKTA go* fast protein liquid chromatography (FPLC) system by *Cytiva* were used for purification and analysis of empty, loaded and labeled protein samples. All buffers were prepared with ultrapure water, filtered and degassed for at least 30 min.

7.7.2.1 Negatively charged Enc

The production of Enc^(neg) was slightly changed in comparison to previously published production of Enc^(wt).^[10]

First, 100 µL calcium competent *E. coli* C43 cells were thawed on ice for 10 min. Then 200 ng plasmid was added to the cells and incubated on ice. After 30 min incubation, a heat shock was done at 42 °C for 45 s, followed by additional 2 min incubation on ice. Cells were then suspended in 0.9 mL SOB media and incubated for 1 h at 37 °C. The cells were pelleted at 1000 g at 1 min and 0.9 mL of the mixture was removed. The pellet is then resuspended in 100 µL media and plated on a LB agar plate containing ampicillin (150 µg/mL). After incubation at 37 °C for 16 h, a preculture is prepared by incubation of single colonies in 5 mL sterile LB medium supplemented with ampicillin (150 µg/mL) at 37 °C and 250 rpm overnight. The next day, 4 mL of the preculture are added to 400 mL terrific broth (TB) containing ampicillin (150 µg/mL). The cells were grown at 37 °C and 250 rpm to an OD₆₀₀ of 0.7. Protein overexpression was induced by isopropyl-β-D-1-thiogalactopyranoside (IPTG) at a final concentration of 0.5 mM. After 24 h expression at 37 °C, cells were harvested via centrifugation at 4000 g. Pellets were stored at -20 °C until further use.

For protein purification, cell pellets were resuspended in 20 mL buffer (50 mM Tris pH 9.0, 0.3 M NaCl) supplemented with 30 mg RNase A and 15 mg DNase I. Cell lysis was achieved by 15 times sonication at 60 % amplitude for 1 min on ice with 1 min breaks between each sonication step with a *Vibra-Cell VCX-130 Ultrasonic Processor (Sonics)*. The lysed suspension was centrifuged at 14000 g for 20 min. The pelleted cell debris is discarded and the supernatant supplemented with MgCl₂ (2.5 mM) and CaCl₂ (0.5 mM) prior incubation for at least 4 h at 37 °C. Subsequently, the solution was cleared by centrifugation at 14000 g for 15 min. Residual *E. coli* proteins were denatured by heating the solution for 15 min at 65 °C in a water bath and removed by subsequent centrifugation at 14000 g for 15 min. Proteins left in solution were precipitated with ammonium sulfate at a final concentration of 70 % of its saturation. After centrifugation at 14000 g for 20 min, the pellet was redissolved in 10 mL buffer (50 mM Tris pH 9.0) and a second ammonium sulfate precipitation step carried out. The resulting protein pellet was dissolved in 50 mL buffer (50 mM Tris pH 9.0) and purified by ion-exchange chromatography using a 5 mL *HiTrap™ Q HP* anion exchange column (*Cytiva*). A linear gradient from 0 M to 1 M NaCl is used. Both Enc^(neg) and nanoparticle loaded Enc^(neg)

samples were collected and concentrated with a centrifugal filter unit to a final volume of 1.5 mL. Further purification was performed on a *Superose 6 Increase 10/300 GL* gel filtration column (*Cytiva*) in SEC buffer (20 mM Tris pH 7.5, 0.3 M NaCl). For crystallization, three runs were performed in total on a sample to achieve high purity.

7.7.2.2 Positively charged Enc

The production of Enc^(pos) was similar to previously described production of Enc^(neg). The preculture was produced as described above. After the cells were grown at 37 °C to an OD₆₀₀ of 0.7 in 400 mL TB containing ampicillin (150 µg/mL), protein overexpression was induced with IPTG (0.5 mM). Cell cultures were incubated at 250 rpm and 18 °C for 48 h.

The purification protocol was similar to Enc^(neg) with minor changes. The cell pellet was resuspended in 20 mL buffer (50 mM MES pH 6.0, 1.5 M NaCl) and supplemented only with 30 mg RNase A. The subsequent steps were carried out as for Enc^(neg), but protein pellets were resuspended with 10 mL buffer of different pH and salt concentration (50 mM MES pH 6.0, 0.5 M NaCl).

The IEC was performed with a linear gradient from 0 M to 1 M NaCl, but a 50 mM MES pH 6.0 buffer was used on a 5 mL *HiTrap™ SP HP* cation exchange column (*Cytiva*). Enc^(pos) and nanoparticle loaded Enc^(pos) samples were collected and concentrated with a centrifugal filter unit to a final volume of 1.5 mL. Further purification via SEC were carried out on a *Superose 6 Increase 10/300 GL* gel filtration column (*Cytiva*) with another SEC buffer (20 mM MES pH 6.0, 1.0 M NaCl). For crystallization experiments, the protein sample was two additional times purified via SEC.

7.7.2.3 Positively charged Ftn with additional cysteine

Positively charged Ftn^(pos)-Cys was produced and purified as reported for Ftn^(pos).^[15] Transformation was performed as described above, but *E. coli* BL21 cells were used for Ftn. Single colonies were incubated in 5 mL LB medium supplemented with ampicillin (150 µg/mL) at 37 °C and 250 rpm for 16 h. Subsequently, 400 mL LB medium were supplemented with 4 mL preculture and ampicillin (150 µg/mL) and incubated at 37 °C and 250 rpm. Cell cultures were grown to and OD₆₀₀ of 0.2. Protein overexpression was induced with IPTG (0.25 mM). After 5 h incubation at 37 °C, cells were harvested by centrifugation at 4000 g for 20 min. Cell pellets were stored at -20°C until further use.

For purification, a cell pellet was resuspended in 20 mL buffer (50 mM Tris pH 7.5, 1.0 M NaCl). The suspension was sonicated six times for 1 min (60 % amplitude) with 1 min break in

between with a *Vibra-Cell VCX-130 Ultrasonic Processor (Sonics)*. Then, the lysed suspension was centrifuged for 15 min at 14000 g. The supernatant was incubated with 25 mg RNase A at 37 °C for 3.5 h. After digestion, the solution was centrifuged at 14000 g for 15 min. Subsequently, the supernatant was heated at 65 °C in a water bath for 10 min and centrifuged at 14000 g for 15 min. Saturated ammonium sulfate was added until 70 % of its saturation was reached. The solution was centrifuged at 14000 g for 20 minutes. The pellet was redissolved in 10 mL buffer (50 mM MES pH 6.0, 0.5 M NaCl) and again precipitated with saturated ammonium sulfate. Finally, the pellet was resuspended in 50 mL buffer (50 mM MES pH 6.0, 0.5 M NaCl).

Unlabeled and labeled protein samples were taken for further purification. For IEC the sample was purified on a 5 mL *HiTrap™ SP HP* cation exchange column (*Cytiva*) with a linear gradient from 0.5 M to 1.5 M NaCl based on 50 mM MES pH 6.0 buffers. The Ftn^(pos)-Cys containing fractions were collected and concentrated to a final volume of 2 mL. The sample was further purified via SEC on a *Hiload 16/600 Superdex 200 PG* gel filtration column (*Cytiva*) with buffer (50 mM Tris pH 7.5, 1.0 M NaCl). Two additional SEC runs were performed for protein crystallization.

7.7.3 Encapsulin dis- and reassembly

Encapsulin disassembly was achieved by acidic pH. In detail, 1.0 mg Enc (52.2 µL, 19.2 mg/mL stock solution) in storage buffer (20 mM Tris pH 7.5, 0.3 M NaCl) was diluted ten times with 10 mM phosphate pH 1.0 for 1 h at 4 °C. Reassembly was initiated by diluting the sample 100-fold with reassembly buffer (20 mM phosphate pH 7.0) and incubation at room temperature overnight. After complete reassembly, the sample was concentrated using a centrifugal filter unit.

7.7.4 Nanoparticle encapsulation

For nanoparticle encapsulation 1.0 mg Enc was disassembled as described above, if not stated otherwise. While initiating protein container reassembly, the NP solution is added dropwise and gently swirled. After incubation at room temperature overnight, the sample was concentrated using a centrifugal filter unit. Either further purification via FLPC or characterization was carried out. Depending on the NP cargo, different wavelengths were detected simultaneously in FPLC purification.

7.7.5 Fluorophore functionalization

Positively supercharged Ftn with additional cysteine on the inner surface was disassembled either at pH 2.0 or in 7 M Gua. In detail, 1.0 mg Ftn^(pos)-Cys (43.4 μ L, 23.05 mg/mL stock solution) was incubated in 1.5 mL 10 mM phosphate pH 2.0, 20 mM NaCl for 4 h at room temperature. Subsequently, 30 mL reassembly buffer (50 mM Tris pH 7.6, 1 M NaCl) was added to trigger Ftn reassembly. For functionalization, two equivalents of fluorophore were added per cysteine residue. After overnight incubation at room temperature in the dark, the sample is concentrated and washed with 15 mL SEC buffer (50 mM Tris pH 7.5, 1.0 M NaCl). Either further purification via FLPC or characterization was carried out. Depending on the fluorophore, different wavelengths were detected simultaneously in FPLC purification.

7.7.6 Determination of flavin content

The concentration of riboflavin was determined from the absorption at $\lambda = 450$ nm. The protein concentration was determined from the absorption at 280 nm after subtracting the absorption of riboflavin at 280 nm. Here, it is assumed that the absorption ratio of 280/450 is constant at any concentration. For both, protein and riboflavin standard calibration curves were prepared in the range of 2 μ M to 100 μ M. In the end the riboflavin concentration is the ratio of riboflavin concentration to protein concentration.

7.8 Protein crystallography

7.8.1 Hanging drop vapor diffusion

For the crystallization of proteins, the hanging drop vapor diffusion method was applied in pre-greased 4 x 6 well *CrystalClear* plates (*Jena Bioscience*). The protein concentration was 6 mg/mL, if not stated otherwise. The reservoir was filled with 500 μ L crystallization condition. The crystallization drop was placed on a siliconized cover slide. For unitary crystals, the volume of the crystallization drop was set through 1 μ L crystallization condition and 1 μ L protein solution was. For binary crystals, 2 μ L crystallization condition were mixed with 1 μ L Ftn and 1 μ L Enc. In the end, the cover slide was flipped over and used to close the reservoir well. The crystallization plate was stored at 20 °C, if not stated otherwise.

7.8.2 Stabilization of protein crystals

7.8.2.1 Glutaraldehyde

For the stabilization of protein crystals, the cover slide with the drop containing crystals was briefly removed to add 10 μ L of 25 % glutaraldehyde to the reservoir solution. After mixing the

cross-linker and crystallization condition, the cover slide was placed back to seal the well. Cross-linking was carried out for 16 h at 20 °C. In the end, the glutaraldehyde containing reservoir is exchanged with water.

7.8.2.2 Alternative cross-linkers

Alternative cross-linkers such as sulfosuccinimidyl-4-(N-maleimidomethyl)cyclohexan-1-carboxylate (Sulfo-SMCC), bis(sulfo-succinimidyl)suberate (BS3) and PEGylated bis(sulfo-succinimidyl)suberate (BS(PEG)₅) were used for crystal stabilization. Fresh stock solutions of Sulfo-SMCC (4.8 mg/mL), BS3 and BS(PEG)₅ (both 10 mg/mL) were prepared with ultrapure water. The cover slide was briefly removed and 100 µL of the stock solution are added to the crystallization condition and mixed. Depending on the crystal drop size, half the volume of drop is taken from the mixed reservoir and added for crystal cross-linking. The well is sealed with the cover slide and crystals were cross-linked for 16 h at 20 °C.

7.8.2.3 Structure determination and refinement

Protein crystals were soaked for 30 s in a solution containing 2 µL 50 % (v/v) MPD (unitary Enc) or glycerol (binary/NP loaded) and 2 µL of the respective reservoir solution, prior vitrification in liquid nitrogen.

Diffraction data were collected at 100 K on the P11 (DESY) or P14 (EMBL) beamline in Hamburg, Germany. Data were processed and scaled with *XDS*.^[331] Molecular replacement was done with *Phaser*^[332] using a modified structure model based on the PDB 3DKT. In detail, CLP and water molecules were removed. Subsequent refinement was carried out with *Refmac*^[333] within the *CCP4* suite.^[334] Mutations were introduced with *Coot*.^[335] Manual rebuilding of mutated residues, placing of water molecules and metal ions and subsequent iterations of refinements were not possible due to low resolution.

Data collection statistics and results are shown in the appendix (Table 8.9, Table 8.10, Table 8.11, Table 8.12, Table 8.13).

Figures of single protein containers and crystals were prepared with *PyMOL* (*DeLano Scientific LLC*). Electrostatic surface potential of protein containers were visualized with the APBS plugin.^[336]

8 Appendix

Table 8.1: Weights used for the protein redesign in *Rosetta*.

Run	Aspartic acid (D)	Glutamic acid (E)	Arginine (R)	Lysine (L)
01	-0.25	-0.30	-0.30	-0.15
02	-0.33	-0.40	-0.40	-0.27
03	-0.41	-0.50	-0.50	-0.33
04	-0.50	-0.60	-0.60	-0.40
05	-0.58	-0.70	-0.70	-0.46
06	-0.66	-0.80	-0.80	-0.53
07	-0.74	-0.90	-0.90	-0.60
08	-0.83	-1.00	-1.00	-0.66
09	-0.91	-1.10	-1.10	-0.73
10	-0.99	-1.20	-1.20	-0.80
11	-1.08	-1.30	-1.30	-0.86
12	-1.16	-1.40	-1.40	-0.93
13	-1.24	-1.50	-1.50	-0.99

	20	40	60	80	100						
run01	MEFLKRSFAP	LTEKQWQE ID	NRARE I FK TQ	LYGRKFVDVE	GPYGW EYAAH	PLG E V E V L S D	ENEVVKWGLR	KSLPL I E L R A	TFTLDLWELD	NLERGKPNVD	100
run02	100
run03	100
run04	100
run05	100
run06	100
run07	100
run08	100
run09	100
run10	100
run11	100
run12	100
run13	100
	120	140	160	180	200						
run01	LSSLEETVRK	VAE FE D E V I F	RGCEKSGVKG	LLSFEERKIE	CGSTPKD L L E	AI VRALS I F S	KDG I E G P Y T L	V I N T D R W I N F	L K E E A G H Y P L	E K R V E E C L R G	200
run02	200
run03	200
run04	200
run05	200
run06	200
run07	200
run08	200
run09	200
run10	200
run11	200
run12	200
run13	200
	220	240	260								
run01	GK I I T T P R I E	DALVVSERGG	DFKL I L G Q D L	S I G Y E D R E K D	AVR L F I T E T F	TFQV V N P E A L	I L L K	264			
run02	264			
run03	264			
run04	264			
run05	264			
run06	264			
run07	264			
run08	264			
run09	264			
run10	264			
run11	264			
run12	264			
run13	264			

Figure 8.1: Supercharging of *T. maritima* Encapsulin towards positive charge based on a run with chain j.

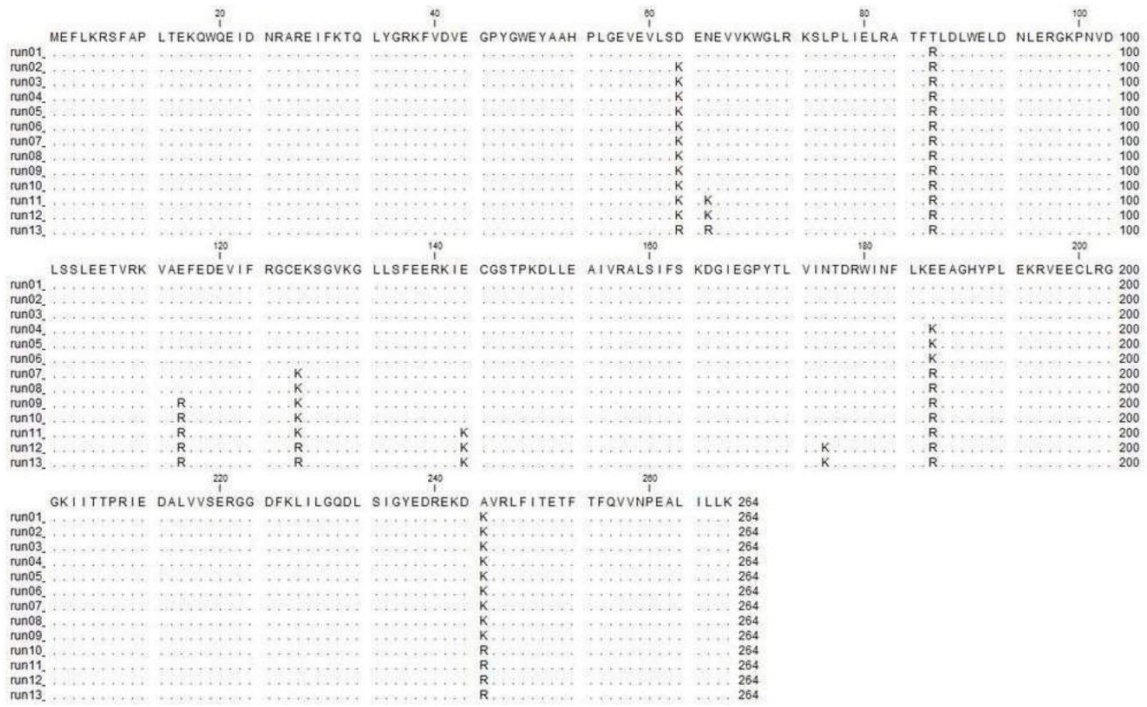


Figure 8.2: Supercharging of *T. maritima* Encapsulin towards positive charge based on a run with chain i.

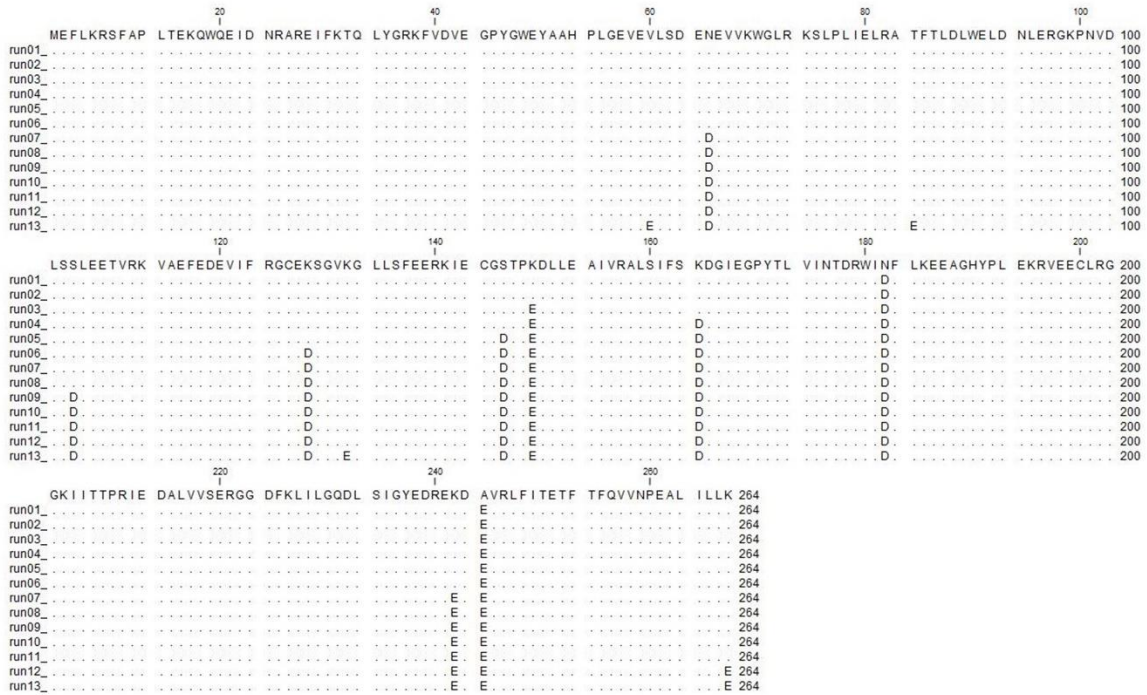


Figure 8.3: Supercharging of *T. maritima* Encapsulin towards negative charge based on a run with chain j.

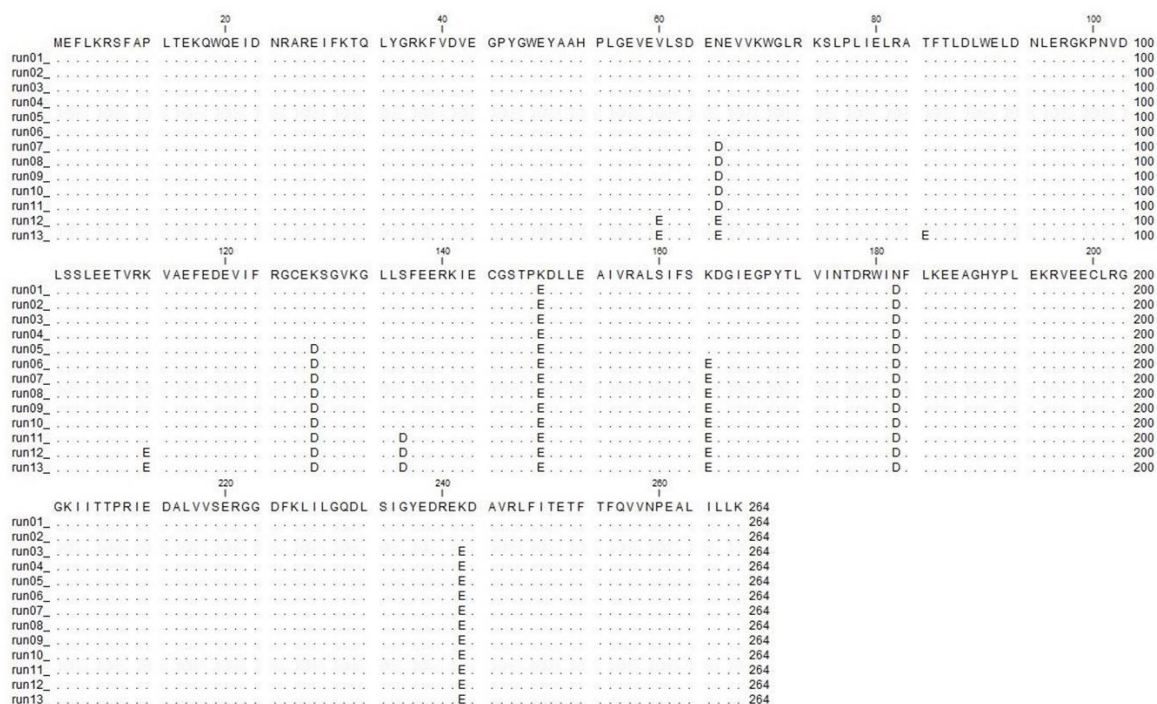


Figure 8.4: Supercharging of *T. maritima* Encapsulin towards negative charge based on a run with chain i.

Table 8.2: Feasible positions for the supercharging of the encapsulin container based on *Rosetta* calculations. Considered positions for a final design of a positively charged encapsulin variant are colored in blue.

Position	Native amino acid	Mutation – positive	Mutation – negative
60	V	R	E
63	D	K	-
65	N	K	D
84	T	-	E
86	T	R	-
106	S	-	D
113	K	-	E
116	E	R	-
127	E	K	-
128	K	-	D
132	K	-	E
136	S	K	D
143	E	K	-
146	S	-	D
164	K	-	D
176	N	K	-
178	D	R	-

182	N	R	D
186	E	R	-
241	E	R	-
242	K	-	E
243	D	R	-
244	A	K	E
267	K	-	E

Table 8.3: Sequence of primers used for the mutagenesis of Ftn^(pos).

Mutation	Forward primer
K53C	5'-GATGTTGCTCTGAAGAAGCTTTGCGTGCTACTTTCTGCATCAGTCTCATGAA-3'
C130A	5'-AGAACGATCCGCATCTCGCCGACTTCATCGAAACCC-3'

Table 8.4: Sequence of all primers used for the supercharging of *T. maritima* wild type encapsulin. Asterix marked mutations refer to Enc^(pos).

Mutation	Forward primer
W90A	CGTTCACACTCGACTTGGCGGAGTTGGACAATCTCG
W90E	CGTTCACACTCGACTTGGAGGAGTTGGACAATCTCG
W90A*	CGTTCAGACTCGACTTGGCGGAGTTGGACAATCTCG
W90R*	CGTTCAGACTCGACTTGGAGGAGTTGGACAATCTCG
D63K	CGAGGTGTTAAGCAAGGAAAACGAGGTTGTGAAATGGGG
T86R	GCGTGCGACGTTTCAGACTCGACTTGTGGGAGTTGG
E116R	CGGTTGCAAGGTTGCCAGATTTGAAGATGAAGTG
E127K	CTTTCGTGGATGTAAGAAAAGTGGCGTCAAAGGCC
E143K	CCTTTGAAGAACGCAAGATTAATGCGGCTCTACCCCG
E186K	GGATCAACTTTCTGAAAAAGGAAGCAGGCCACTATCCGC
E241R	CGTTACGAAGATCGCAGGAAAGATGCTGTACGGC

Table 8.5: Protein sequences for protein variants of this work.

Protein variant	Protein sequence
Enc ^(wt)	MVNMEFLKRSFAPLTEKQWQEIDNRAREIFKTQLYGRKFVDVEGPYGWEYAAHPLGEVEVL SDENEVVKWGLRKSPLIELRATFTLDLWELDNLERGKPNVDLSSLEETVRKVAEFEDIVFR GCEKSGVKGLLSFEERKIECGSTPKDLLEAIVRALSIFSCKDIEGPTYLVINTDRWINFLKKEAG HYPLEKRVEECLRGGKIITTPRIEDALVVSERGGDFKLILGQDLSIGYEDREKDAVRLFITETFT FQVVNPEALILLKF
Enc ^(neg)	MVNMEFLKRSFAPLTEKQWQEIDNRAREIFKTQLYGRKFVDVEGPYGWEYAAHPLGEVEVL SDENEVVKWGLRKSPLIELRATFTLDLEELDNLERGKPNVDLSSLEETVRKVAEFEDIVFR GCEKSGVKGLLSFEERKIECGSTPKDLLEAIVRALSIFSCKDIEGPTYLVINTDRWINFLKKEAG HYPLEKRVEECLRGGKIITTPRIEDALVVSERGGDFKLILGQDLSIGYEDREKDAVRLFITETFT FQVVNPEALILLKF
Enc ^(neg) -Ala	MVNMEFLKRSFAPLTEKQWQEIDNRAREIFKTQLYGRKFVDVEGPYGWEYAAHPLGEVEVL SDENEVVKWGLRKSPLIELRATFTDLAELDNLERGKPNVDLSSLEETVRKVAEFEDIVFR GCEKSGVKGLLSFEERKIECGSTPKDLLEAIVRALSIFSCKDIEGPTYLVINTDRWINFLKKEAG HYPLEKRVEECLRGGKIITTPRIEDALVVSERGGDFKLILGQDLSIGYEDREKDAVRLFITETFT FQVVNPEALILLKF
Enc ^(pos) -Fla	MVNMEFLKRSFAPLTEKQWQEIDNRAREIFKTQLYGRKFVDVEGPYGWEYAAHPLGEVEVL SKENEVVKWGLRKSPLIELRATFRLDLWELDNLERGKPNVDLSSLEETVRKVARFEDIVFR GCKKSGVKGLLSFEERKIKCGSTPKDLLEAIVRALSIFSCKDIEGPTYLVINTDRWINFLKKEAG HYPLEKRVEECLRGGKIITTPRIEDALVVSERGGDFKLILGQDLSIGYEDRRKDAVRLFITETFT FQVVNPEALILLKF
Enc ^(pos) -Ala	MVNMEFLKRSFAPLTEKQWQEIDNRAREIFKTQLYGRKFVDVEGPYGWEYAAHPLGEVEVL SKENEVVKWGLRKSPLIELRATFRLDLAELDNLERGKPNVDLSSLEETVRKVARFEDIVFR GCKKSGVKGLLSFEERKIKCGSTPKDLLEAIVRALSIFSCKDIEGPTYLVINTDRWINFLKKEAG HYPLEKRVEECLRGGKIITTPRIEDALVVSERGGDFKLILGQDLSIGYEDRRKDAVRLFITETFT FQVVNPEALILLKF
Enc ^(pos)	MVNMEFLKRSFAPLTEKQWQEIDNRAREIFKTQLYGRKFVDVEGPYGWEYAAHPLGEVEVL SKENEVVKWGLRKSPLIELRATFRLDLRELDNERGKPNVDLSSLEETVRKVARFEDIVFR GCKKSGVKGLLSFEERKIKCGSTPKDLLEAIVRALSIFSCKDIEGPTYLVINTDRWINFLKKEAG HYPLEKRVEECLRGGKIITTPRIEDALVVSERGGDFKLILGQDLSIGYEDRRKDAVRLFITETFT FQVVNPEALILLKF
Ftn ^(pos)	MTTASTSQVRQNYHQDSEKAINRQIRLELYASYVYLSMSYYFDRDDVALKNFAKYFLHQSHE EREHAEKLMKLNQRGGRIFLQDIQPKDDWESGLRAMEKALKLEKKVNQSLLELHKLATK KNDPHLCDFIETHYLNEQVKAIKELGDHVTNLRKMGAPRSGLAEYLFDKHTLGDSDNES
Ftn ^(pos) -Cys	MTTASTSQVRQNYHQDSEKAINRQIRLELYASYVYLSMSYYFDRDDVALKNFACYFLHQSHE EREHAEKLMKLNQRGGRIFLQDIQPKDDWESGLRAMEKALKLEKKVNQSLLELHKLATK KNDPHLADFIETHYLNEQVKAIKELGDHVTNLRKMGAPRSGLAEYLFDKHTLGDSDNES

Table 8.6: DNA sequences for protein variants of this work.

Protein variant	DNA sequence
Enc ^(wt)	<p>ATGGTGAACATGGAATTTCTGAAACGCTCTTTTGCGCCACTGACCGAGAAGCAATGGCAGGAAATCG ACAATCGTGCTCGCGAAATTTCAAGACACAGCTGTATGGCCGCAAATTTGTCGACGTAGAAGGTCC ATACGGGTGGGAGTATGCCGCACATCCGTTAGGCCGAAGTCGAGGTGTTAAGCGATGAAAACGAGGT TGTGAAATGGGGTCTGCGCAAATCACTTCCGCTGATTGAACTGCGTGCGACGTTACACTCGACTTG TGGGAGTTGGACAATCTCGAACCGGGAAACCGAATGTCGACCTGTCTCGCTGGAAGAAACGGTT CGCAAAGTTGCCGAATTTGAAGATGAAGTGATCTTTCGTGGATGTGAGAAAAGTGGCGTCAAAGGCC TTCTGTCCCTTTGAAGAACGCAAGATTGAATGCGGGCTCTACCCCGAAAGACCTCTTGAAGCGATTGT TCGTGCGCTTAGCATCTTCAGCAAAGATGGCATTGAAGGACCTTACACCCTCGTGATCAACACGGAT CGCTGGATCAACTTTCTGAAAGAGGAAGCAGGCCACTATCCGCTGAAAAAGCGTGTTGAAGAGTGC TTACGTGGTGGGAAAATTATTACACTCCTCGGATTGAGGATGCACTGGTGGTATCGGAACGTGGTG GCGATTTCAAACCTGATTCTGGGTCAAGATCTGTCAATCGGTTACGAAGATCGCGAGAAAGATGCTGT ACGGCTGTTTATTACCGAGACTTTTACCTTTCAGGTGGTGAATCCCGAAGCCTTAATCCTGTTGAAAT TCTAA</p>
Enc ^(neg)	<p>ATGGTGAACATGGAATTTCTGAAACGCTCTTTTGCGCCACTGACCGAGAAGCAATGGCAGGAAATCG ACAATCGTGCTCGCGAAATTTCAAGACACAGCTGTATGGCCGCAAATTTGTCGACGTAGAAGGTCC ATACGGGTGGGAGTATGCCGCACATCCGTTAGGCCGAAGTCGAGGTGTTAAGCGATGAAAACGAGGT TGTGAAATGGGGTCTGCGCAAATCACTTCCGCTGATTGAACTGCGTGCGACGTTACACTCGACTTG GAGGAGTTGGACAATCTCGAACCGGGAAACCGAATGTCGACCTGTCTCGCTGGAAGAAACGGTT CGCAAAGTTGCCGAATTTGAAGATGAAGTGATCTTTCGTGGATGTGAGAAAAGTGGCGTCAAAGGCC TTCTGTCCCTTTGAAGAACGCAAGATTGAATGCGGGCTCTACCCCGAAAGACCTCTTGAAGCGATTGT TCGTGCGCTTAGCATCTTCAGCAAAGATGGCATTGAAGGACCTTACACCCTCGTGATCAACACGGAT CGCTGGATCAACTTTCTGAAAGAGGAAGCAGGCCACTATCCGCTGAAAAAGCGTGTTGAAGAGTGC TTACGTGGTGGGAAAATTATTACACTCCTCGGATTGAGGATGCACTGGTGGTATCGGAACGTGGTG GCGATTTCAAACCTGATTCTGGGTCAAGATCTGTCAATCGGTTACGAAGATCGCGAGAAAGATGCTGT ACGGCTGTTTATTACCGAGACTTTTACCTTTCAGGTGGTGAATCCCGAAGCCTTAATCCTGTTGAAAT TCTAA</p>
Enc ^(neg) -Ala	<p>ATGGTGAACATGGAATTTCTGAAACGCTCTTTTGCGCCACTGACCGAGAAGCAATGGCAGGAAATCG ACAATCGTGCTCGCGAAATTTCAAGACACAGCTGTATGGCCGCAAATTTGTCGACGTAGAAGGTCC ATACGGGTGGGAGTATGCCGCACATCCGTTAGGCCGAAGTCGAGGTGTTAAGCGATGAAAACGAGGT TGTGAAATGGGGTCTGCGCAAATCACTTCCGCTGATTGAACTGCGTGCGACGTTACACTCGACTTG GCGGAGTTGGACAATCTCGAACCGGGAAACCGAATGTCGACCTGTCTCGCTGGAAGAAACGGTT CGCAAAGTTGCCGAATTTGAAGATGAAGTGATCTTTCGTGGATGTGAGAAAAGTGGCGTCAAAGGCC TTCTGTCCCTTTGAAGAACGCAAGATTGAATGCGGGCTCTACCCCGAAAGACCTCTTGAAGCGATTGT TCGTGCGCTTAGCATCTTCAGCAAAGATGGCATTGAAGGACCTTACACCCTCGTGATCAACACGGAT CGCTGGATCAACTTTCTGAAAGAGGAAGCAGGCCACTATCCGCTGAAAAAGCGTGTTGAAGAGTGC TTACGTGGTGGGAAAATTATTACACTCCTCGGATTGAGGATGCACTGGTGGTATCGGAACGTGGTG GCGATTTCAAACCTGATTCTGGGTCAAGATCTGTCAATCGGTTACGAAGATCGCGAGAAAGATGCTGT ACGGCTGTTTATTACCGAGACTTTTACCTTTCAGGTGGTGAATCCCGAAGCCTTAATCCTGTTGAAAT TCTAA</p>

ATGGTGAACATGGAATTTCTGAAACGCTCTTTTGCGCCACTGACCGAGAAGCAATGGCAGGAAATCG
ACAATCGTGCTCGCGAAATTTCAAGACACAGCTGTATGGCCGCAAATTTGTCGACGTAGAAGGTCC
ATACGGGTGGGAGTATGCCGCACATCCGTTAGGCCAAGTCGAGGTGTTAAGCAAGGAAAACGAGGT
TGTGAAATGGGGTCTGCGCAAATCACTTCCGCTGATTGAACTGCGTGCGACGTTTCAGACTCGACTTG
TGGGAGTTGGACAATCTCGAACCGGGAAACCGAATGTCGACCTGTCTCGCTGGAAGAAAACGTT
CGCAAAGTTGCCAGATTTGAAGATGAAGTATCTTTTCGTGGATGTAAGAAAAGTGGCGTCAAAGGCC
TTCTGTCCCTTTGAAGAACGCAAGATTAATGCGGGCTACCCCCGAAAGACCTCTTGAAGCGATTGTT
CGTGCGCTTAGCATCTTCAGCAAAGATGGCATTGAAGGACCTTACACCCTCGTGATCAACACGGATC
GCTGGATCAACTTTCTGAAAAAGGAAGCAGGCCACTATCCGCTGGAAGAGCGTGTTGAAGAGTGCTT
ACGTGGTGGGAAAATTATTACCACTCCTCGGATTGAGGATGCACTGGTGGTATCGGAACGTGGTGG
CGATTTCAAACGATTCTGGGTCAAGATCTGTCAATCGGTTACGAAGATCGCAGGAAAAGATGCTGTA
CGGCTGTTCAATTACCGAGACTTTTACCTTTACGGTGGTGAATCCCGAAGCCTTAATCCTGTTGAAATT
CTAA

ATGGTGAACATGGAATTTCTGAAACGCTCTTTTGCGCCACTGACCGAGAAGCAATGGCAGGAAATCG
ACAATCGTGCTCGCGAAATTTCAAGACACAGCTGTATGGCCGCAAATTTGTCGACGTAGAAGGTCC
ATACGGGTGGGAGTATGCCGCACATCCGTTAGGCCAAGTCGAGGTGTTAAGCAAGGAAAACGAGGT
TGTGAAATGGGGTCTGCGCAAATCACTTCCGCTGATTGAACTGCGTGCGACGTTTCAGACTCGACTTG
GCGGAGTTGGACAATCTCGAACCGGGAAACCGAATGTCGACCTGTCTCGCTGGAAGAAAACGTT
CGCAAAGTTGCCAGATTTGAAGATGAAGTATCTTTTCGTGGATGTAAGAAAAGTGGCGTCAAAGGCC
TTCTGTCCCTTTGAAGAACGCAAGATTAATGCGGGCTACCCCCGAAAGACCTCTTGAAGCGATTGTT
CGTGCGCTTAGCATCTTCAGCAAAGATGGCATTGAAGGACCTTACACCCTCGTGATCAACACGGATC
GCTGGATCAACTTTCTGAAAAAGGAAGCAGGCCACTATCCGCTGGAAGAGCGTGTTGAAGAGTGCTT
ACGTGGTGGGAAAATTATTACCACTCCTCGGATTGAGGATGCACTGGTGGTATCGGAACGTGGTGG
CGATTTCAAACGATTCTGGGTCAAGATCTGTCAATCGGTTACGAAGATCGCAGGAAAAGATGCTGTA
CGGCTGTTCAATTACCGAGACTTTTACCTTTACGGTGGTGAATCCCGAAGCCTTAATCCTGTTGAAATT
CTAA

ATGGTGAACATGGAATTTCTGAAACGCTCTTTTGCGCCACTGACCGAGAAGCAATGGCAGGAAATCG
ACAATCGTGCTCGCGAAATTTCAAGACACAGCTGTATGGCCGCAAATTTGTCGACGTAGAAGGTCC
ATACGGGTGGGAGTATGCCGCACATCCGTTAGGCCAAGTCGAGGTGTTAAGCAAGGAAAACGAGGT
TGTGAAATGGGGTCTGCGCAAATCACTTCCGCTGATTGAACTGCGTGCGACGTTTCAGACTCGACTTG
AGGGAGTTGGACAATCTCGAACCGGGAAACCGAATGTCGACCTGTCTCGCTGGAAGAAAACGTT
CGCAAAGTTGCCAGATTTGAAGATGAAGTATCTTTTCGTGGATGTAAGAAAAGTGGCGTCAAAGGCC
TTCTGTCCCTTTGAAGAACGCAAGATTAATGCGGGCTACCCCCGAAAGACCTCTTGAAGCGATTGTT
CGTGCGCTTAGCATCTTCAGCAAAGATGGCATTGAAGGACCTTACACCCTCGTGATCAACACGGATC
GCTGGATCAACTTTCTGAAAAAGGAAGCAGGCCACTATCCGCTGGAAGAGCGTGTTGAAGAGTGCTT
ACGTGGTGGGAAAATTATTACCACTCCTCGGATTGAGGATGCACTGGTGGTATCGGAACGTGGTGG
CGATTTCAAACGATTCTGGGTCAAGATCTGTCAATCGGTTACGAAGATCGCAGGAAAAGATGCTGTA
CGGCTGTTCAATTACCGAGACTTTTACCTTTACGGTGGTGAATCCCGAAGCCTTAATCCTGTTGAAATT
CTAA

ATGACCACAGCTAGTACGTCCCAAGTACGTCAGAACTATCACCAAGATAGCGAGAAAAGCCATTAATC
GCCAAATTCGCTTGGAACTGTATGCATCGTATGTCTACCTGTCAATGAGCTACTACTTTGATCGTGAT
GATGTTGCTCTGAAGAACTTTGCGAAATACTTTCTGCATCAGTCTCATGAAGAACGCGAACATGCCGA
GAACTGATGAACTGCAGAATCAGCGTGGTGGACGCATCTTCTTACAGGACATTCAGAAAACGGAT
AAAGACGATTGGGAAAAGCGGGTTGCGTGCGATGGAGAAAGCACTGAACTGGAAGAAAAGTGAAT
CAGTCTCTGCTGGAACCTCCACAAATTAGCGACGAAGAAGACGATCCGCATCTCTGCGACTTCATCG
AAACCCACTATTTAAACGAGCAAGTGAAGCGATCAAAGAACTTGGCGATCACGTTACCAACCTTCG
GAAAATGGGTGCACCACGCAGTGGCTTGGCCGAATATCTGTTCCGACAAAACATACTCTGGGCGATTCC
GACAATGAGTCGTAA

ATGACCACAGCTAGTACGTCCCAAGTACGTCAAGACTATCACCAAGATAGCGAGAAAGCCATTAATC
 GCCAAATTCGCTTGGAACTGTATGCATCGTATGTCTACCTGTCAATGAGCTACTACTTTGATCGTGAT
 GATGTTGCTCTGAAGAACTTTGCGAAATACTTTCTGCATCAGTCTCATGAAGAACGCGAACATGCCGA
 GAAACTGATGAAACTGCAGAATCAGCGTGGTGGACGCATCTTCTTACAGGACATTCAGAAACCGGAT
Ftn^(pos)-Cys AAAGACGATTGGGAAAGCGGGTTGCGTGCGATGGAGAAAGCACTGAAACTGGAAAAGAAAGTGAAT
 CAGTCTCTGCTGGAATCCACAAATTAGCGACGAAGAAGACGATCCGCATCTCGCCGACTTCATCG
 AAACCCACTATTTAAACGAGCAAGTAAAAGCGATCAAAGAACTTGGCGATCACGTTACCAACCTTCG
 GAAAATGGGTGCACCACGCAGTGGCTTGGCCGAATATCTGTTTCGACAAACATACTCTGGGCGATTCC
 GACAATGAGTCGTAA

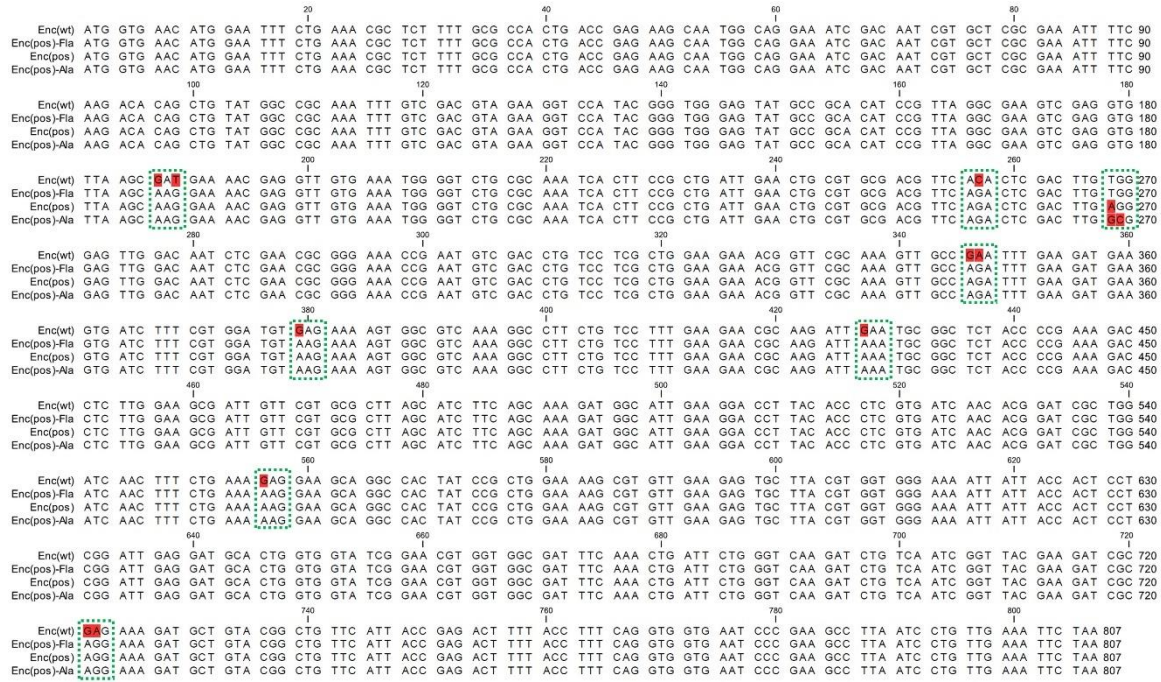


Figure 8.5: Aligned sequences of wild type encapsulin and positively supercharged encapsulin variants. Nucleobase triplets for planned mutations are marked green. Red highlighted letters indicate a variance of nucleobases at a specific position.

```

                20          40          60          80
Enc(wt)  ATG GTG AAC ATG GAA TTT CTG AAA CGC TCT TTT GCG CCA CTG ACC GAG AAG CAA TGG CAG GAA ATC GAC AAT CGT GCT CGC GAA ATT TTC 90
Enc(neg)-Ala  ATG GTG AAC ATG GAA TTT CTG AAA CGC TCT TTT GCG CCA CTG ACC GAG AAG CAA TGG CAG GAA ATC GAC AAT CGT GCT CGC GAA ATT TTC 90
Enc(neg)  ATG GTG AAC ATG GAA TTT CTG AAA CGC TCT TTT GCG CCA CTG ACC GAG AAG CAA TGG CAG GAA ATC GAC AAT CGT GCT CGC GAA ATT TTC 90

                100          120          140          160          180
Enc(wt)  AAG ACA CAG CTG TAT GGC CGC AAA TTT GTC GAC GTA GAA GGT CCA TAC GGG TGG GAG TAT GCC GCA CAT CCG TTA GGC GAA GTC GAG GTG 180
Enc(neg)-Ala  AAG ACA CAG CTG TAT GGC CGC AAA TTT GTC GAC GTA GAA GGT CCA TAC GGG TGG GAG TAT GCC GCA CAT CCG TTA GGC GAA GTC GAG GTG 180
Enc(neg)  AAG ACA CAG CTG TAT GGC CGC AAA TTT GTC GAC GTA GAA GGT CCA TAC GGG TGG GAG TAT GCC GCA CAT CCG TTA GGC GAA GTC GAG GTG 180

                200          220          240          260          270
Enc(wt)  TTA AGC GAT GAA AAC GAG GTT GTG AAA TGG GGT CTG CGC AAA TCA CTT CCG CTG ATT GAA CTG CGT GCG ACG TTC ACA CTC GAC TTG GCG 270
Enc(neg)-Ala  TTA AGC GAT GAA AAC GAG GTT GTG AAA TGG GGT CTG CGC AAA TCA CTT CCG CTG ATT GAA CTG CGT GCG ACG TTC ACA CTC GAC TTG GCG 270
Enc(neg)  TTA AGC GAT GAA AAC GAG GTT GTG AAA TGG GGT CTG CGC AAA TCA CTT CCG CTG ATT GAA CTG CGT GCG ACG TTC ACA CTC GAC TTG GCG 270

                280          300          320          340          350          360
Enc(wt)  GAG TTG GAC AAT CTC GAA CGC GGG AAA CCG AAT GTC GAC CTG TCC TCG CTG GAA GAA ACG GTT CGC AAA GTT GCC GAA TTT GAA GAT GAA 360
Enc(neg)-Ala  GAG TTG GAC AAT CTC GAA CGC GGG AAA CCG AAT GTC GAC CTG TCC TCG CTG GAA GAA ACG GTT CGC AAA GTT GCC GAA TTT GAA GAT GAA 360
Enc(neg)  GAG TTG GAC AAT CTC GAA CGC GGG AAA CCG AAT GTC GAC CTG TCC TCG CTG GAA GAA ACG GTT CGC AAA GTT GCC GAA TTT GAA GAT GAA 360

                380          400          420          440          450
Enc(wt)  GTG ATC TTT CGT GGA TGT GAG AAA AGT GGC GTC AAA GGC CTT CTG TCC TTT GAA GAA CGC AAG ATT GAA TGC GGC TCT ACC CCG AAA GAC 450
Enc(neg)-Ala  GTG ATC TTT CGT GGA TGT GAG AAA AGT GGC GTC AAA GGC CTT CTG TCC TTT GAA GAA CGC AAG ATT GAA TGC GGC TCT ACC CCG AAA GAC 450
Enc(neg)  GTG ATC TTT CGT GGA TGT GAG AAA AGT GGC GTC AAA GGC CTT CTG TCC TTT GAA GAA CGC AAG ATT GAA TGC GGC TCT ACC CCG AAA GAC 450

                460          480          500          520          540
Enc(wt)  CTC TTG GAA GCG ATT GTT CGT GCG CTT AGC ATC TTC AGC AAA GAT GGC ATT GAA GGA CCT TAC ACC CTC GTG ATC AAC ACG GAT CGC TGG 540
Enc(neg)-Ala  CTC TTG GAA GCG ATT GTT CGT GCG CTT AGC ATC TTC AGC AAA GAT GGC ATT GAA GGA CCT TAC ACC CTC GTG ATC AAC ACG GAT CGC TGG 540
Enc(neg)  CTC TTG GAA GCG ATT GTT CGT GCG CTT AGC ATC TTC AGC AAA GAT GGC ATT GAA GGA CCT TAC ACC CTC GTG ATC AAC ACG GAT CGC TGG 540

                560          580          600          620          630
Enc(wt)  ATC AAC TTT CTG AAA GAG GAA GCA GGC CAC TAT CCG CTG GAA AAG CGT GTT GAA GAG TGC TTA CGT GGT GGG AAA ATT ATT ACC ACT CCT 630
Enc(neg)-Ala  ATC AAC TTT CTG AAA GAG GAA GCA GGC CAC TAT CCG CTG GAA AAG CGT GTT GAA GAG TGC TTA CGT GGT GGG AAA ATT ATT ACC ACT CCT 630
Enc(neg)  ATC AAC TTT CTG AAA GAG GAA GCA GGC CAC TAT CCG CTG GAA AAG CGT GTT GAA GAG TGC TTA CGT GGT GGG AAA ATT ATT ACC ACT CCT 630

                640          660          680          700          720
Enc(wt)  CCG ATT GAG GAT GCA CTG GTG GTA TCG GAA CGT GGT GGC GAT TTC AAA CTG ATT CTG GGT CAA GAT CTG TCA ATC GGT TAC GAA GAT CGC 720
Enc(neg)-Ala  CCG ATT GAG GAT GCA CTG GTG GTA TCG GAA CGT GGT GGC GAT TTC AAA CTG ATT CTG GGT CAA GAT CTG TCA ATC GGT TAC GAA GAT CGC 720
Enc(neg)  CCG ATT GAG GAT GCA CTG GTG GTA TCG GAA CGT GGT GGC GAT TTC AAA CTG ATT CTG GGT CAA GAT CTG TCA ATC GGT TAC GAA GAT CGC 720

                740          760          780          800
Enc(wt)  GAG AAA GAT GCT GTA CCG CTG TTC ATT ACC GAG ACT TTT ACC TTT CAG GTG GTG AAT CCC GAA GCC TTA ATC CTG TTG AAA TTC TAA 807
Enc(neg)-Ala  GAG AAA GAT GCT GTA CCG CTG TTC ATT ACC GAG ACT TTT ACC TTT CAG GTG GTG AAT CCC GAA GCC TTA ATC CTG TTG AAA TTC TAA 807
Enc(neg)  GAG AAA GAT GCT GTA CCG CTG TTC ATT ACC GAG ACT TTT ACC TTT CAG GTG GTG AAT CCC GAA GCC TTA ATC CTG TTG AAA TTC TAA 807
    
```

Figure 8.6: Aligned sequences of wild type encapsulin and two encapsulin variants with a mutation at W90. Nucleobase triplets for planned mutations are marked green. Red highlighted letters indicate a variance of nucleobases at a specific position.

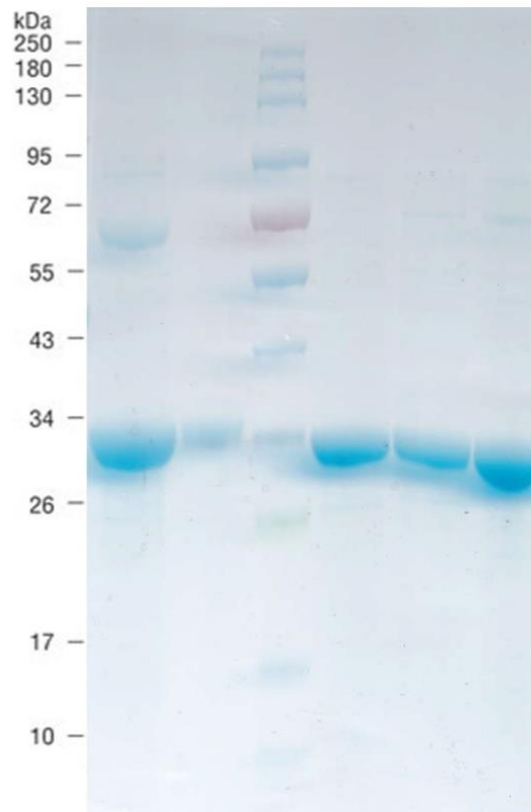


Figure 8.7: SDS gel of novel encapsulin variants. From left to right: Enc^(neg), Enc^(neg)-Ala, marker, Enc^(pos)-Fla, Enc^(pos), Enc^(pos)-Ala.

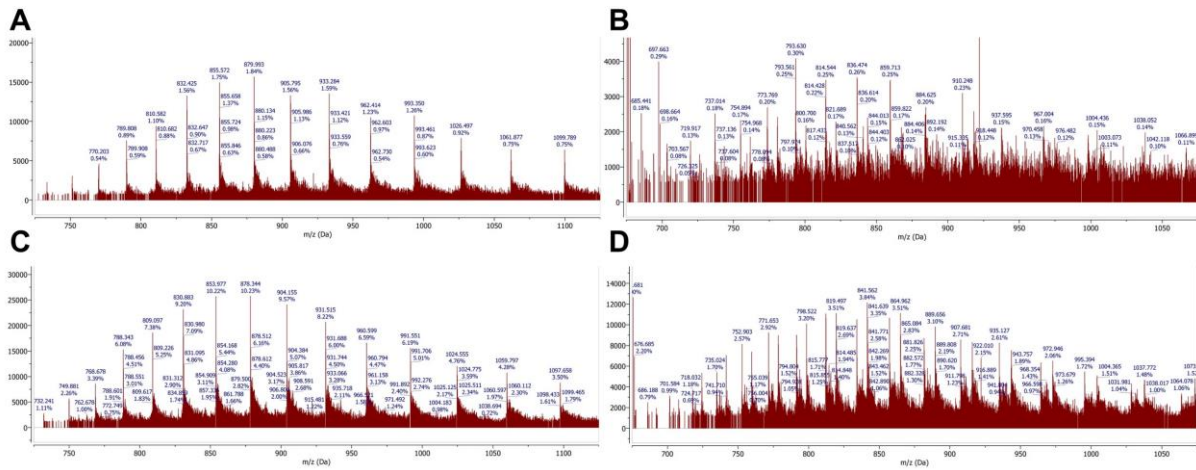


Figure 8.8: ESI MS spectra to characterize novel Enc variants. Enc^(neg) (A), Enc^(pos) (B), Enc^(neg)-Ala (C) and Enc^(pos)-Fla (D) ESI MS spectra.

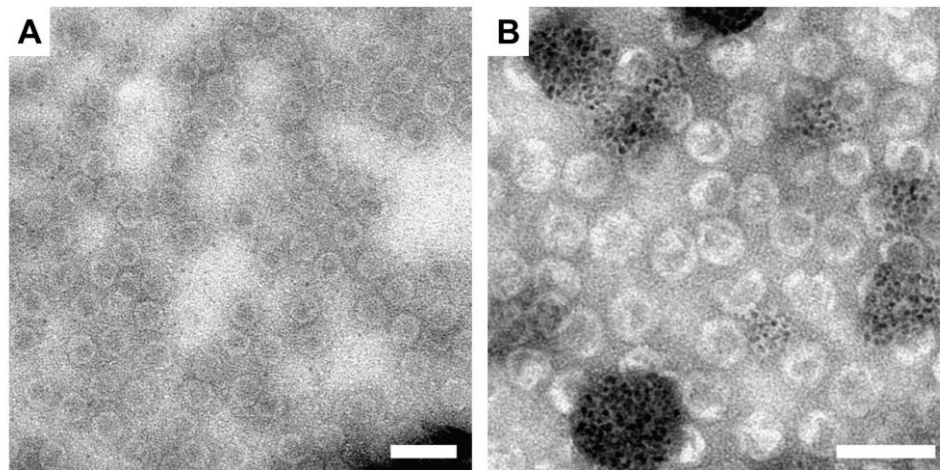


Figure 8.9: TEM images of novel Enc variants. Negative stained TEM images of Enc^(neg)-Ala (A) and Enc^(pos)-Ala (B). Visible contamination origin from aggregated staining material or contaminated tweezers. Scale bars are 50 nm.

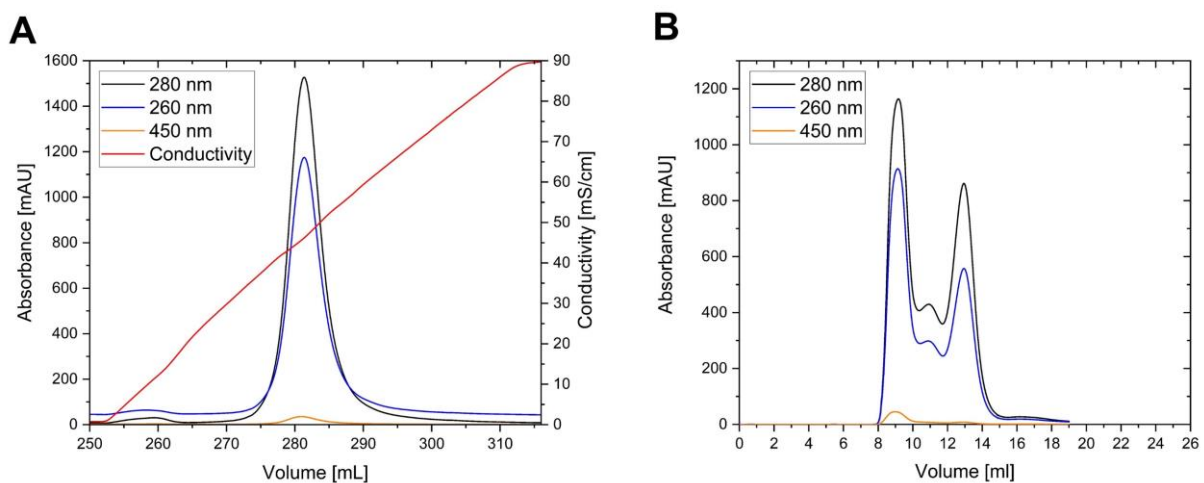


Figure 8.10: Ion-exchange and size-exclusion chromatograms for Enc^(neg)-Ala. (A) IEC chromatogram for Enc^(neg)-Ala. (B) SEC chromatogram for Enc^(neg)-Ala. Absorbance was monitored at 280 nm (black), 260 nm (blue) and 450 nm (orange). Conductivity is shown in red.

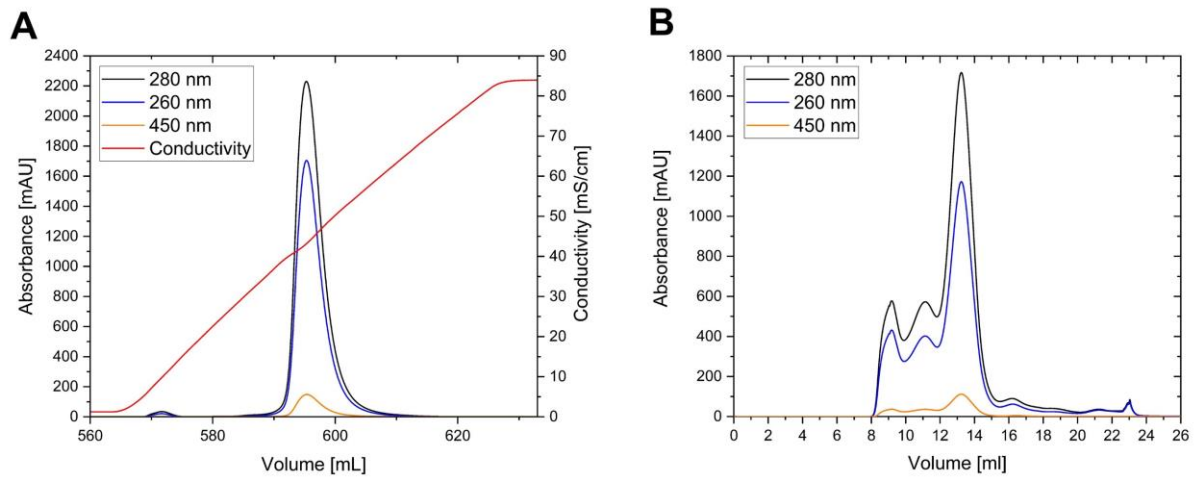


Figure 8.11: Ion-exchange and size-exclusion chromatograms for wild type encapsulin. (A) IEC chromatogram for Enc^(wt). (B) SEC chromatogram for Enc^(wt). Absorbance was monitored at 280 nm (black), 260 nm (blue) and 450 nm (orange). Conductivity is shown in red.

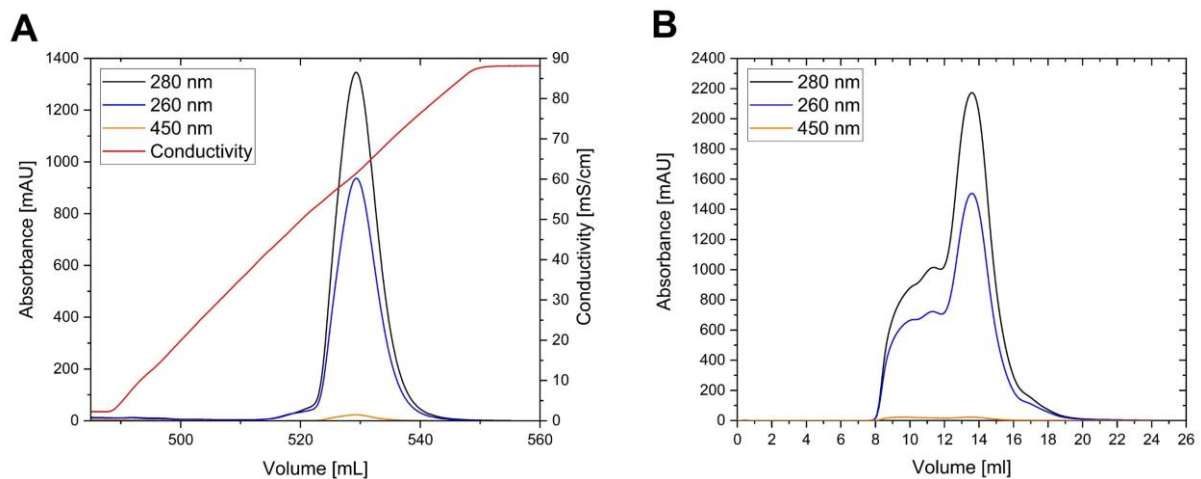


Figure 8.12: Ion-exchange and size-exclusion chromatograms for Enc^(pos)-Ala. (A) IEC chromatogram for Enc^(pos)-Ala. (B) SEC chromatogram for Enc^(pos)-Ala. Absorbance was monitored at 280 nm (black), 260 nm (blue) and 450 nm (orange). Conductivity is shown in red.

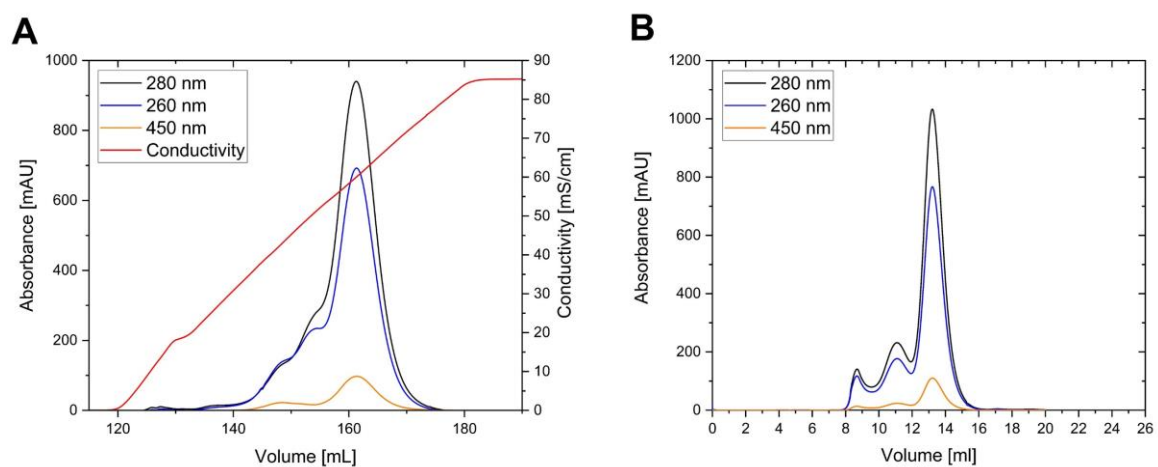


Figure 8.13: Ion-exchange and size-exclusion chromatograms for Enc^(pos)-Fla. (A) IEC chromatogram for Enc^(pos)-Fla. (B) SEC chromatogram for Enc^(pos)-Fla. Absorbance was monitored at 280 nm (black), 260 nm (blue) and 450 nm (orange). Conductivity is shown in red.

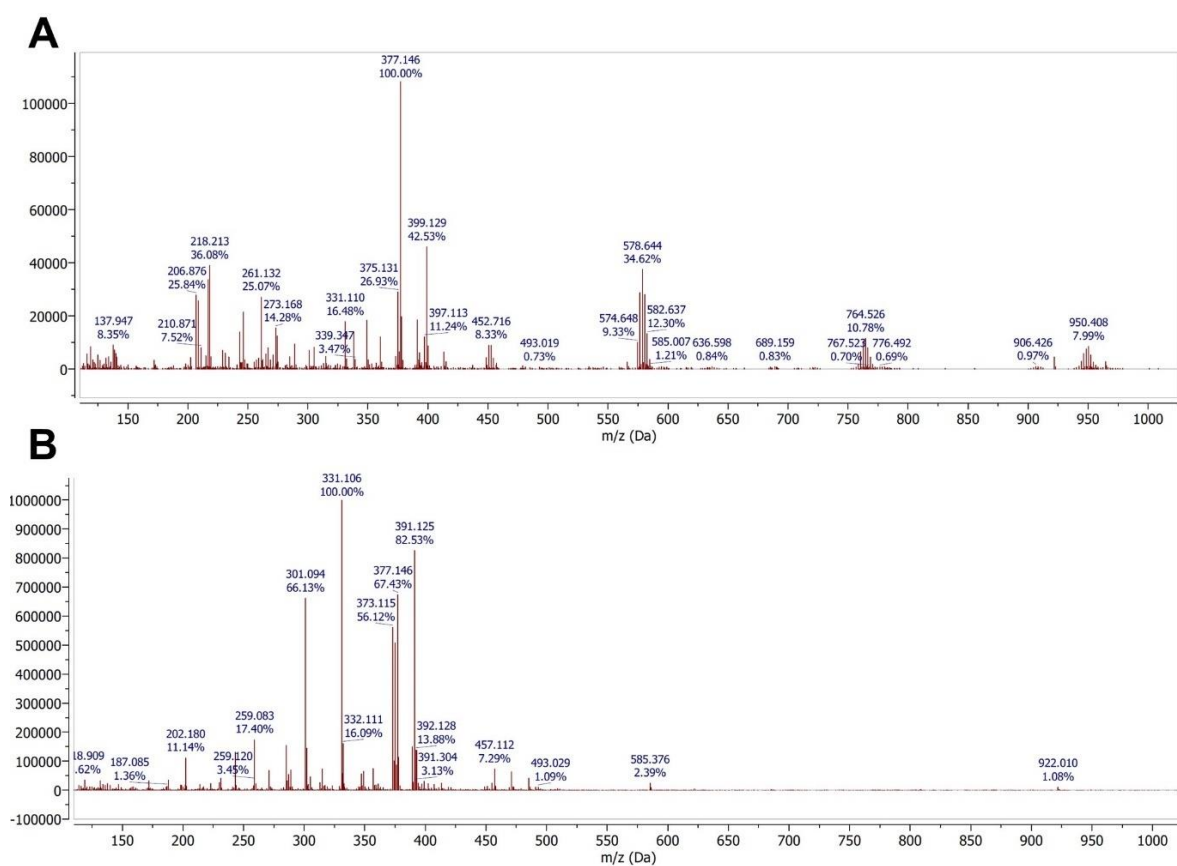


Figure 8.14: ESI MS spectra to distinguish which flavin is bound to encapsulin. Enc^(wt) with higher concentration (A) and Enc^(pos)-Fla (B). ESI MS spectra with m/z range from 110 Da to 1025 Da.

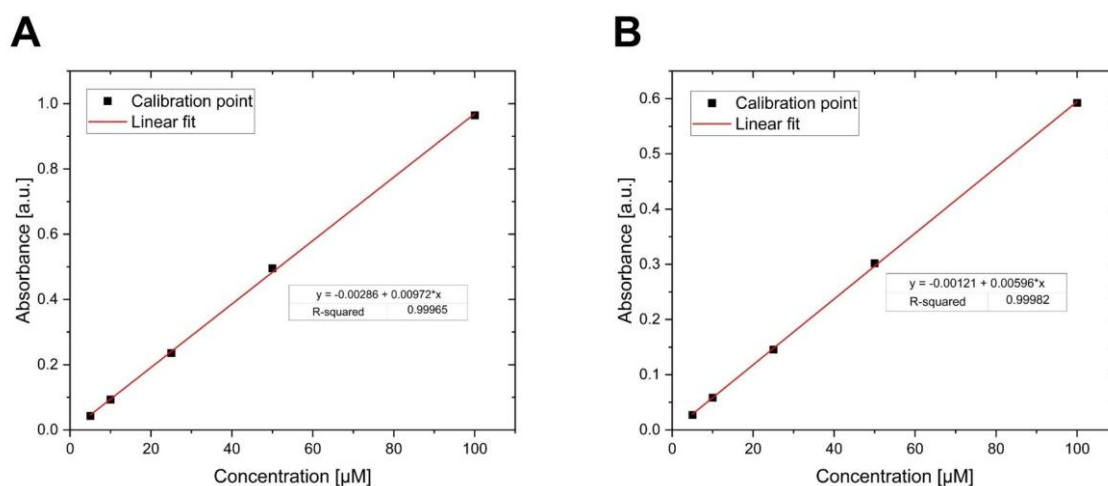


Figure 8.15: UV-Vis calibration curves and linear fits to estimate flavin concentration. Absorbance maxima measured at 280 nm (A) and 450 nm (B) for riboflavin at each calibration point.

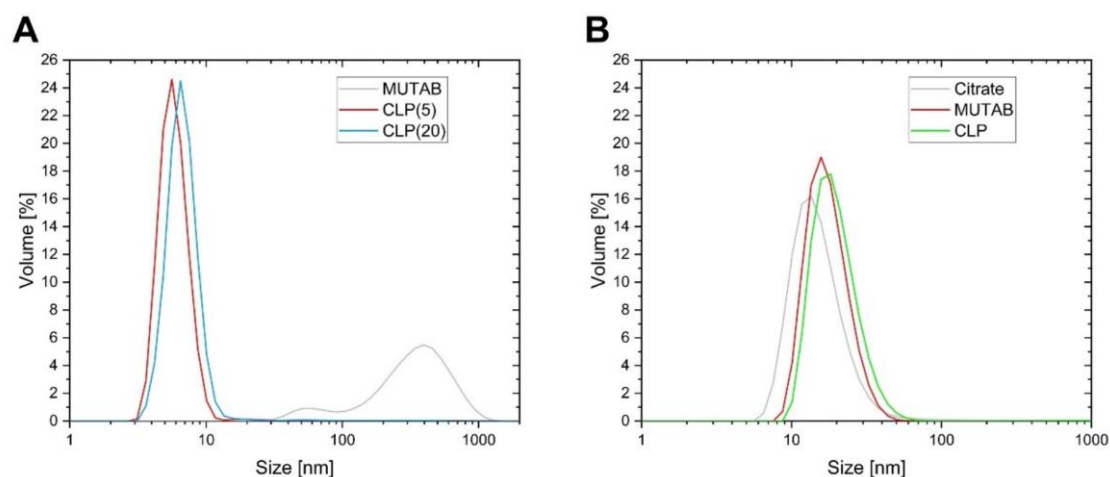


Figure 8.16: Volume-weighted hydrodynamic diameters determined by DLS for AuNPs. 3.5 nm (A) and 13 nm (B) large AuNPs with different ligand shell composition.



Figure 8.17: Native gel of $Enc^{(wt)}$ at different pH values to investigate disassembly behavior. From left to right: pH 1.0, pH 1.5 and pH 2.0. Protein subunits are smaller and found at the lower part of the gel, while complete protein container is large and found at the upper part of the gel.

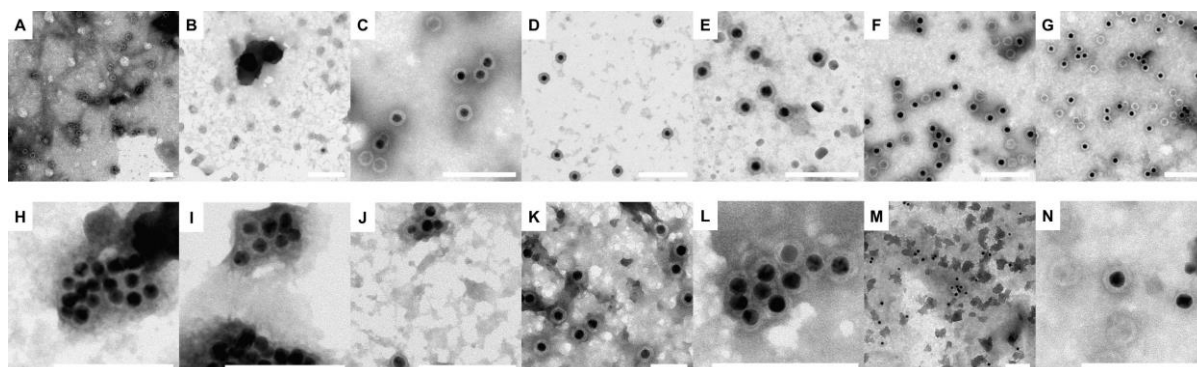


Figure 8.18: Salt screening for efficient AuNP encapsulation into supercharged Enc variants. From left to right: 200 mM to 500 mM NaCl in 50 mM steps. Screening of $Enc^{(neg)}$ (A) to (G) and $Enc^{(pos)}$ (H) to (N). Scale bar equals 100 nm.

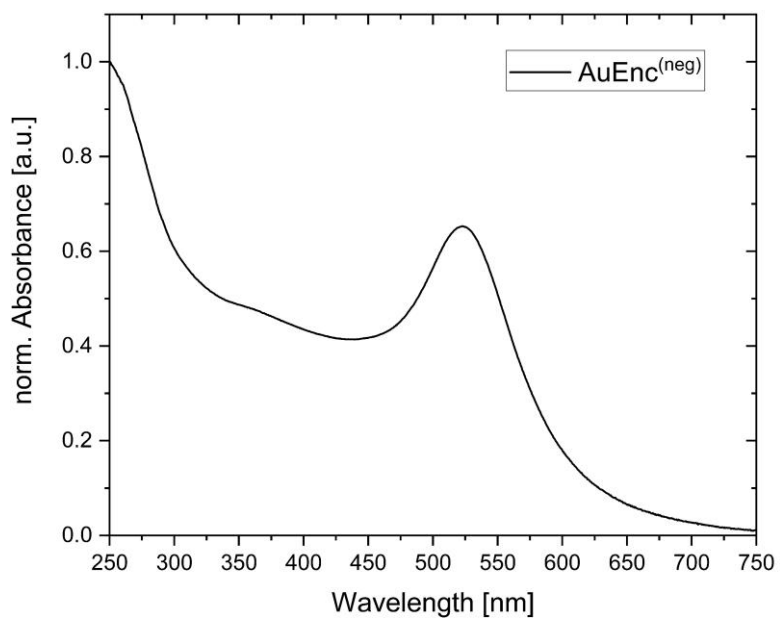


Figure 8.19: UV-Vis absorbance spectra of AuEnc^(neg) after SEC.

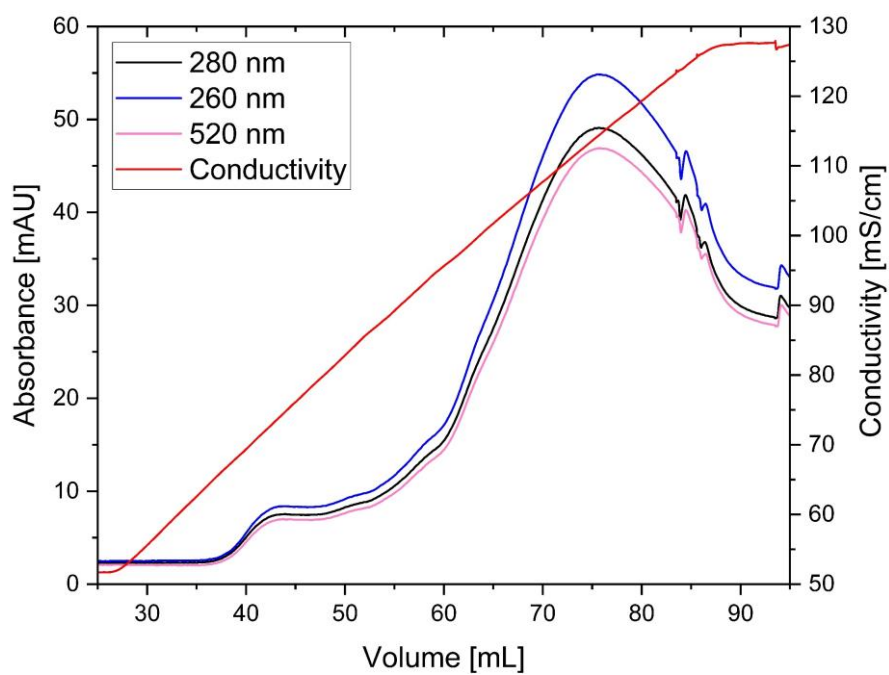


Figure 8.20: IEC with a higher salt gradient to elute AuNPs from cation exchange column.

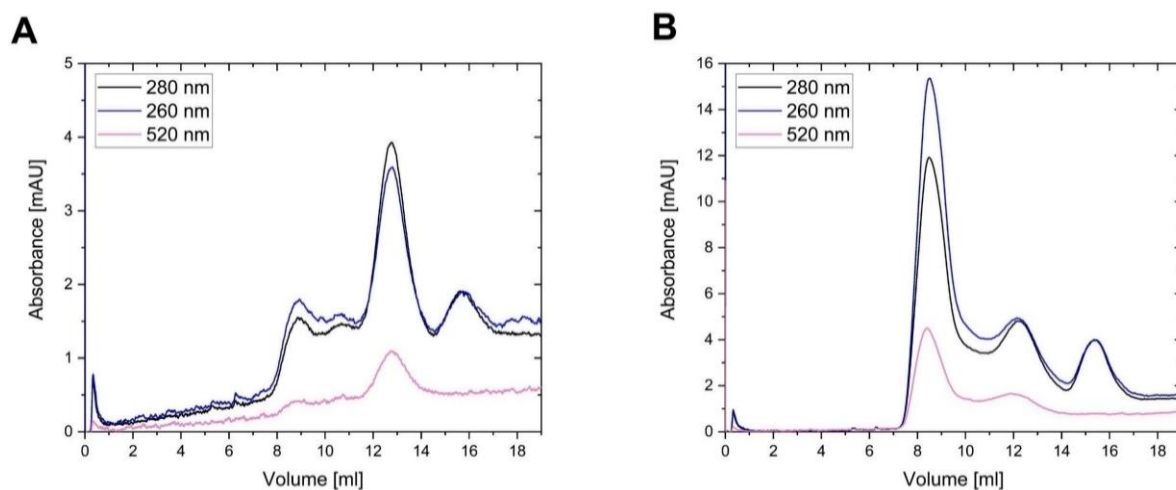


Figure 8.21: Size-exclusion chromatograms for positively surface charged encapsulin loaded with small AuNPs. SEC chromatograms for Enc^(pos) with encapsulated 3.5 nm large AuNPs with 5 (A) and 20 (B) CLP molecules per NP surface. Absorbance was monitored at 280 nm (black), 260 nm (blue) and 520 nm (pink).

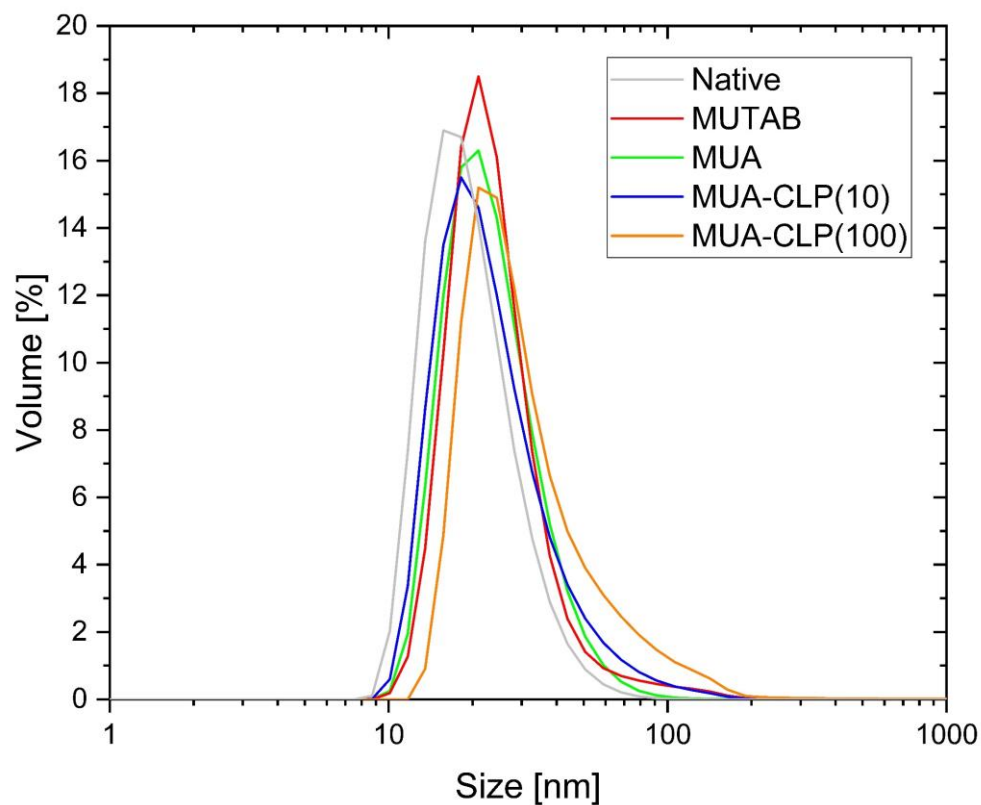


Figure 8.22: Volume-weighted hydrodynamic diameters determined by DLS for gQDs with different ligand shells.

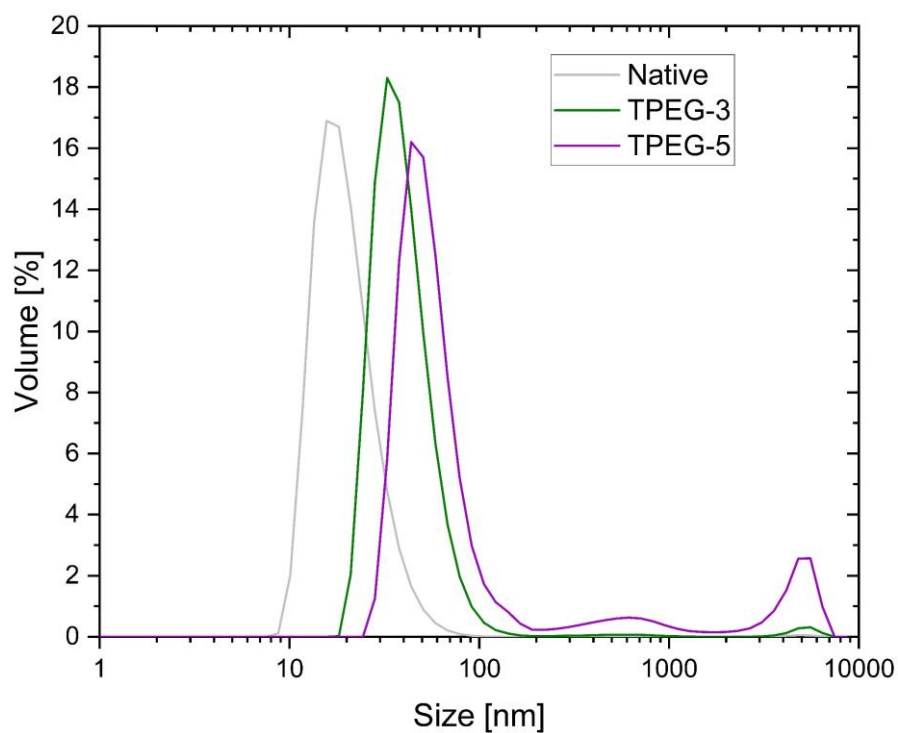


Figure 8.23: Volume-weighted hydrodynamic diameters determined by DLS for gQDs with different PEG ligands.

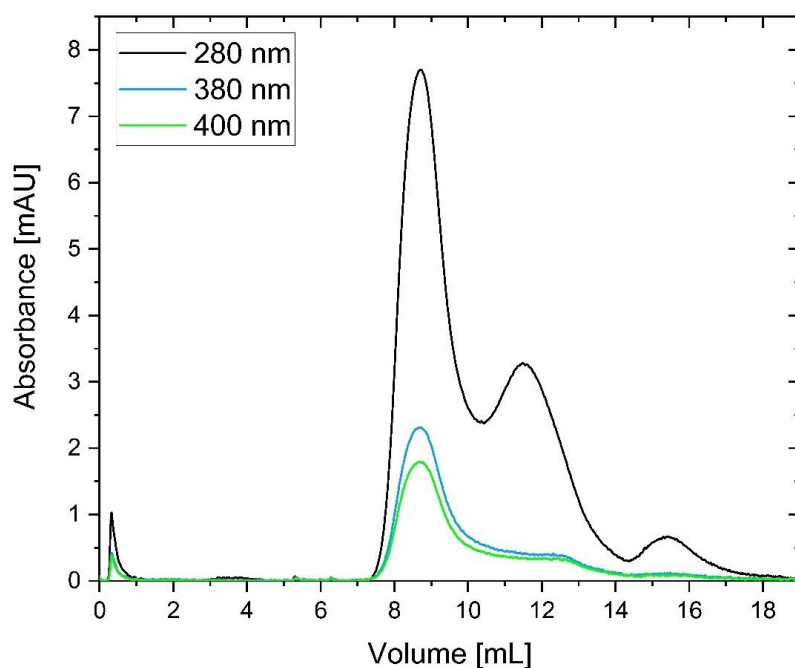


Figure 8.24: SEC of Enc^(neg) encapsulation test of gQDs functionalized TPEG-3 ligand. Absorbance at 280 nm, 380 nm and 400 nm is tracked.

Table 8.7: Absorption ratios for RhB3 labeled Ftn^(pos)-Cys in SEC.

disassembly	A534/280	A568/280	SEC
pH 2.0	2.05	1.36	Figure 5.38A
7 M Gua	2.02	1.33	Figure 5.38B

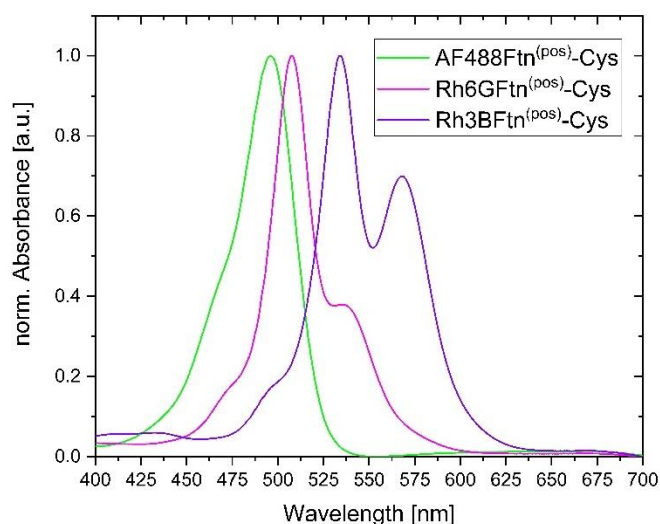


Figure 8.25: UV-Vis spectrum featuring the characteristic absorption features of maleimide fluorophores.

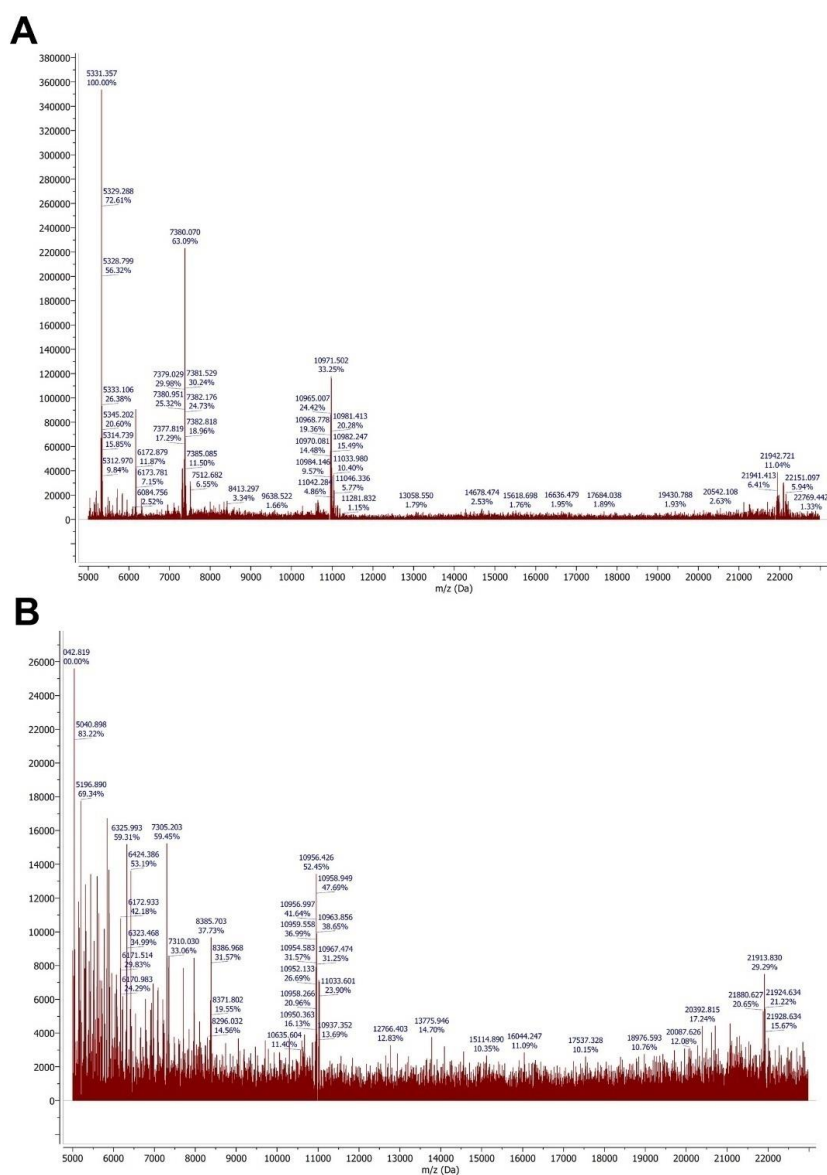


Figure 8.26: MALDI-TOF MS spectra of fluorophore-labeled Ftn^(POS)-Cys. MS spectra of labeled protein with Rh3B (A) and Rh6G (B)

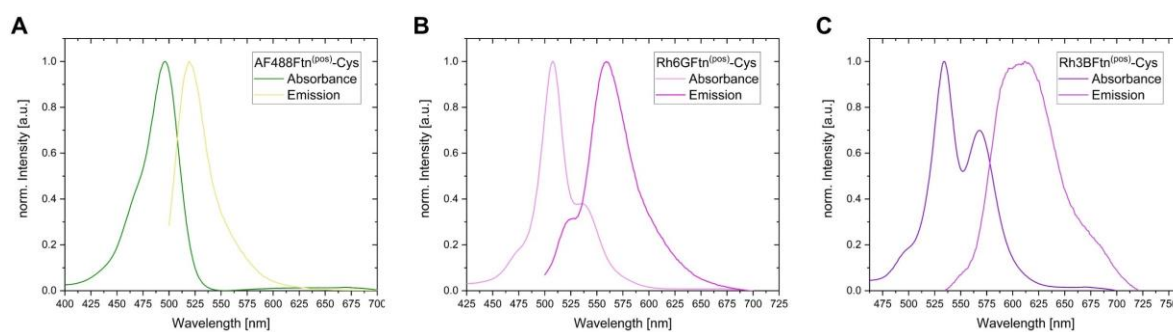


Figure 8.27: UV-Vis and emission spectra of purified fluorophore-labeled Ftn^(pos)-Cys. AF488 (A), Rh6G (B) and Rh3B (C) labeled Ftn^(pos)-Cys spectra.

Table 8.8: Summarized MS results for fluorophore-labeled Ftn^(pos)-Cys

Molecular masses [g/mol]	AF488Ftn ^(pos) -Cys	Rh3BFtn ^(pos) -Cys	Rh6GFtn ^(pos) -Cys
Calculated	21971.0	21938.7	21910.6
MALDI-TOF	21977.8	21942.7	21913.8

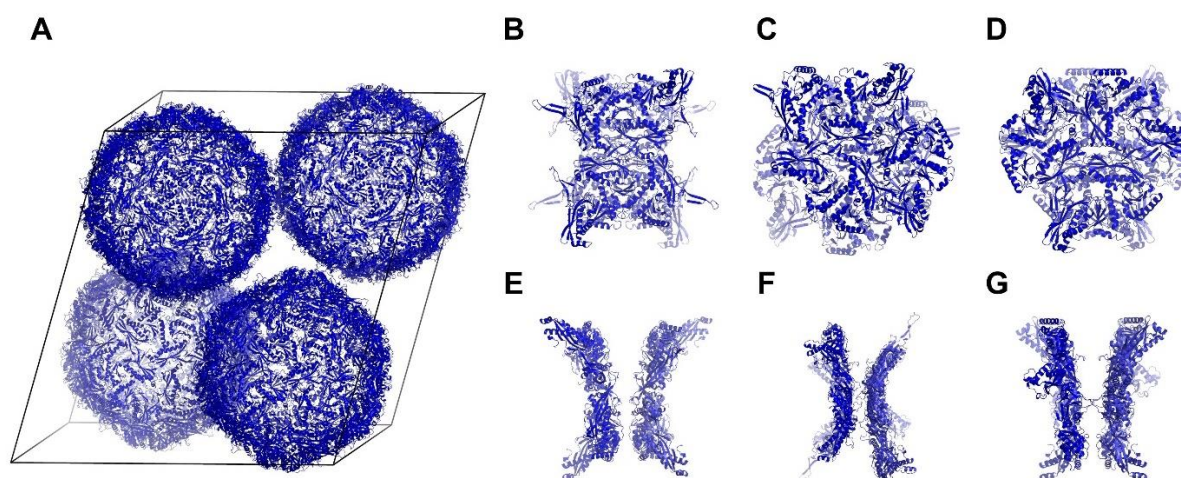


Figure 8.28: Visualization of crystal lattice and protein interfaces of Enc^(pos) in citrate-HEPES condition. Monoclinic protein lattice (A) based on four Enc^(pos) containers. Protein interface close to the twofold axis (B) and from the side (E). Other interfaces are close to the threefold axis but either shifted (C+F) or angled to each other (D+G).

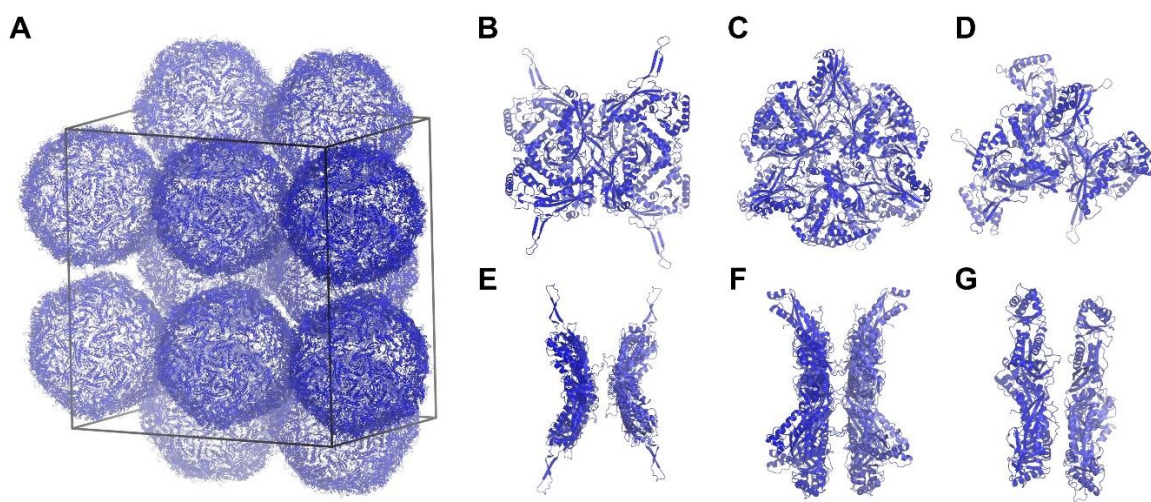


Figure 8.29: Visualization of crystal lattice and protein interfaces of *Enc*^(pos) in phosphate condition. Tetragonal protein lattice (A) based on eight *Enc*^(pos) containers depicted with 12 complete containers. Protein interface along the twofold axis (B) and from the side (E). Second interface is found along the threefold axis (C) and visualized from the side (F). Another interface is found close to threefold axis with containers shifted to each other.

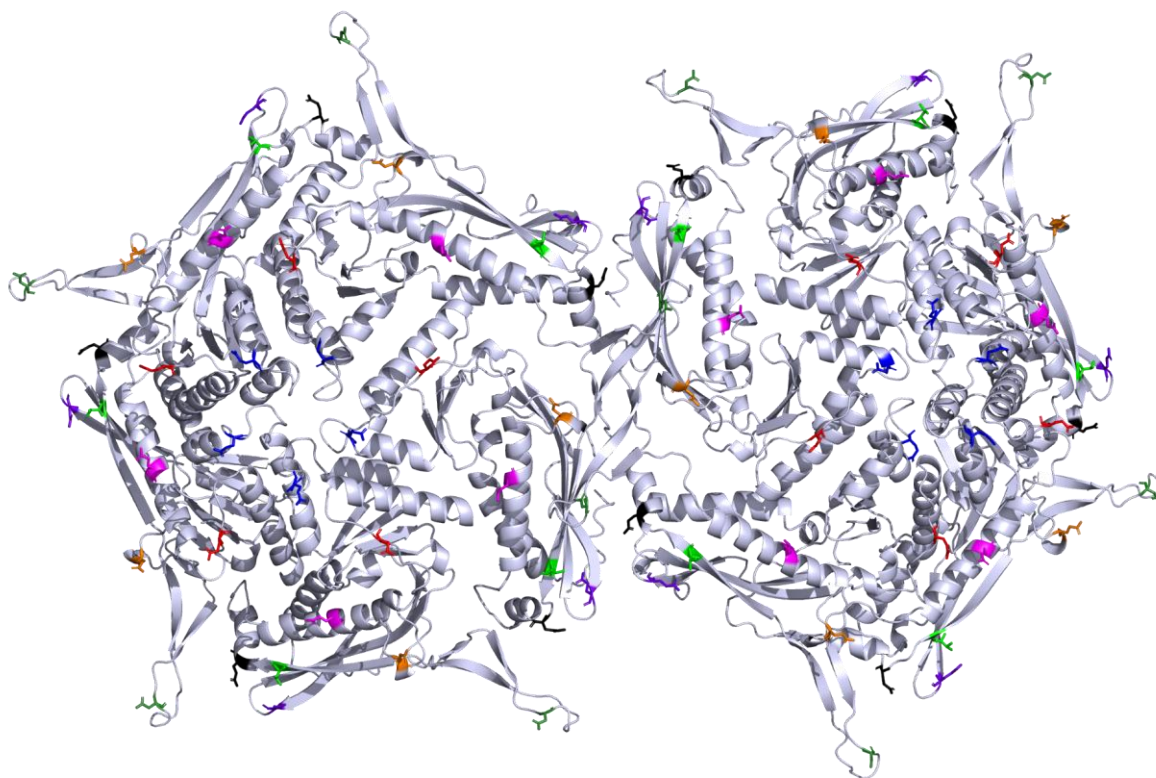


Figure 8.30: Overview of all introduced mutations in *Enc*. Two pentamers of *Enc*^(neg) are visualized. Every residue that was chosen for mutation is colored. Dark green: D63; bright green: T86; black: W90; magenta: E116; orange: E127; red: E143; blue: E186; purple: E241.

Table 8.9: Data statistics and refinement details for unitary Enc^(neg) crystals. (*) Value in parentheses indicates number of reflections used for R_{free} calculation.

	CaOAc	Li ₂ SO ₄	NaCl
Data collection			
Wavelength (Å)	1.033	1.033	1.033
Space group	<i>F</i> 4 ₁ 32	<i>F</i> 4 ₁ 32	<i>P</i> 4 ₂ 32
Unit cell dimensions (<i>a</i> , <i>b</i> , <i>c</i> [Å]; α, β, γ [°])	669.36 90	668.57 90	334.73 90
Resolution range (Å)	102.10 - 4.94	96.50 - 5.97	83.68 - 7.16
Highest resolution shell (Å)	5.12 - 4.94	6.18 - 5.97	7.42 - 7.16
No. of observed reflections	4645658	2645850	773587
No. of unique reflections*	57724 (5656)	33004 (3235)	9946 (963)
Multiplicity	80.5 (84.7)	80.2 (82.3)	77.8 (72.2)
Completeness (%)	99.86 (99.96)	99.71 (99.97)	99.50 (100.00)
<I/σI>	21.39 (2.59)	23.30 (1.95)	16.56 (2.02)
R _{merge} (%)	22.38 (256.7)	24.23 (346.8)	32.89 (273.8)
R _{meas} (%)	22.53 (258.2)	24.39 (348.9)	33.12 (275.8)
CC1/2	0.99 (0.83)	0.99 (0.71)	0.99 (0.75)
Wilson B-factor	258.6	335.69	337.53
Refinement			
R _{work} (%)	25.50	21.96	21.23
R _{free} (%)	28.84	22.15	23.54
No. atoms	21920	21970	21970
macromolecules	21920	21970	21970
ligands	0	0	0
solvent	0	0	0
<i>B</i> -factor (Å ²)	293.11	314.53	309.66
macromolecules	293.11	314.53	309.66
ligands	0	0	0
solvent	0	0	0
R.m.s. deviations			
bond lengths (Å)	0.016	0.014	0.013
bond angles (deg)	2.27	1.89	1.75
Ramachandran statistics (%)			
favored	93.5	98.2	98.3
outliers	6.5	1.8	1.7

Table 8.10: Data statistics and refinement details for unitary Enc^(neg) crystal in CaOAc condition at higher temperature. (*) Value in parentheses indicates number of reflections used for R_{free} calculation.

		CaOAc - 30°C
Data collection		
Wavelength (Å)		1.033
Space group		C2
Unit cell dimensions	410.90, 224.80, 389.36	
(<i>a</i> , <i>b</i> , <i>c</i> [Å]; α , β , γ [°])	90.0, 108.7, 90.0	
Resolution range (Å)		64.89 - 7.65
Highest resolution shell (Å)		7.92 - 7.65
No. of observed reflections		287247
No. of unique reflections*		40525 (4053)
Multiplicity		7.1 (7.4)
Completeness (%)		98.56 (99.63)
<1/ σ >		5.08 (0.78)
R _{merge} (%)		32.25 (261.8)
R _{meas} (%)		34.86 (281.5)
CC1/2		0.99 (0.30)
Wilson B-factor		399.98
Refinement		
R _{work} (%)		27.99
R _{free} (%)		34.69
No. atoms		128460
macromolecules		128460
ions / glycerol		0
water		0
<i>B</i> -factor (Å ²)		425.66
macromolecules		425.66
ions / glycerol		0
solvent		0
R.m.s. deviations		
bond lengths (Å)		0.013
bond angles (deg)		1.71
Ramachandran statistics (%)		
favored		98.9
outliers		1.1

Table 8.11: Data statistics and refinement details for unitary Enc^(pos) crystals. (*) Value in parentheses indicates number of reflections used for R_{free} calculation.

	Na citrate	Citrate-HEPES	Phosphate-citrate
Data collection			
Wavelength (Å)	1.033	1.033	1.033
Space group	<i>P2₁2₁2₁</i>	<i>C2</i>	<i>P4₂2₁2</i>
Unit cell dimensions (<i>a</i> , <i>b</i> , <i>c</i> [Å]; α, β, γ [°])	260.08, 367.14, 368.27 90.0, 90.0, 90.0	384.15, 236.52, 407.72 90.0, 108.7, 90.0	464.23, 464.23, 311.15 90.0, 90.0, 90.0
Resolution range (Å)	73.51 - 4.82	96.53 - 7.81	54.48 - 9.87
Highest resolution shell (Å)	4.99 - 4.82	8.09 - 7.81	10.22 - 9.87
No. of observed reflections	1157583	277652	494579
No. of unique reflections*	169758 (16797)	38988 (3740)	19538 (1927)
Multiplicity	6.8 (7.1)	7.1 (6.4)	25.3 (20.6)
Completeness (%)	99.85 (99.99)	98.73 (95.65)	98.77 (100.00)
<I/σI>	7.98 (1.65)	5.80 (1.76)	7.24 (1.92)
R _{merge} (%)	17.42 (110.3)	30.60 (103.5)	41.83 (246.6)
R _{meas} (%)	18.87 (119.0)	33.03 (112.5)	42.71 (252.9)
CC1/2	0.99 (0.73)	0.99 (0.60)	0.99 (0.66)
Wilson B-factor	211.43	194.04	280.37
Refinement			
R _{work} (%)	21.33	25.93	29.73
R _{free} (%)	25.81	27.95	32.76
No. atoms	128460	128820	128820
macromolecules	128460	128820	128820
ions / glycerol	0	0	0
water	0	0	0
B-factor (Å ²)	236.85	214.59	278.31
macromolecules	236.85	214.59	278.31
ions / glycerol	0	0	0
solvent	0	0	0
R.m.s. deviations			
bond lengths (Å)	0.017	0.013	0.014
bond angles (deg)	1.89	1.71	1.72
Ramachandran statistics (%)			
favored	98.5	98.9	99.0
outliers	1.5	1.1	1.0

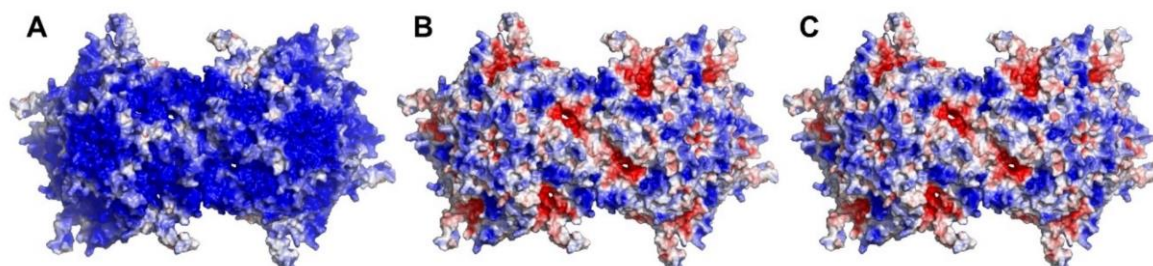


Figure 8.31: Surface charge of Enc^(pos) at different pH values. From left to right: pH 4.2 (A), 7.8 (B) and 8.4 (C). Colors are from red (-5 kT/e) to blue (+5 kT/e).

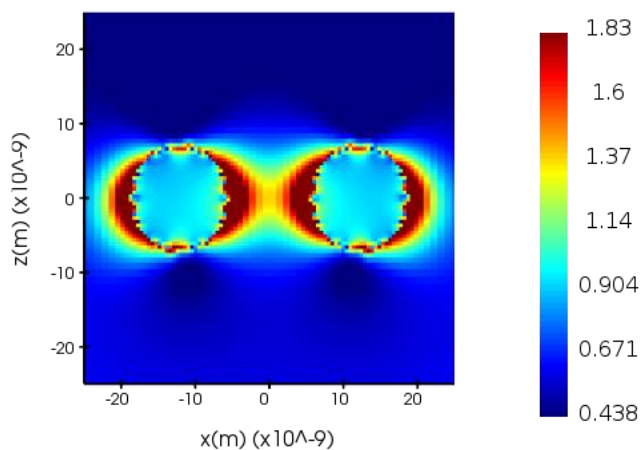


Figure 8.32: Initial simulation of plasmonic interactions between two AuNPs. The diameter of each AuNP is 13 nm. The distance between both AuNPs is 24 nm. The electric field distribution is shown from 1.830 V/m (red) to 0.438 V/m (blue). The calculation is based on a finite difference time domain (FDTD) simulation.

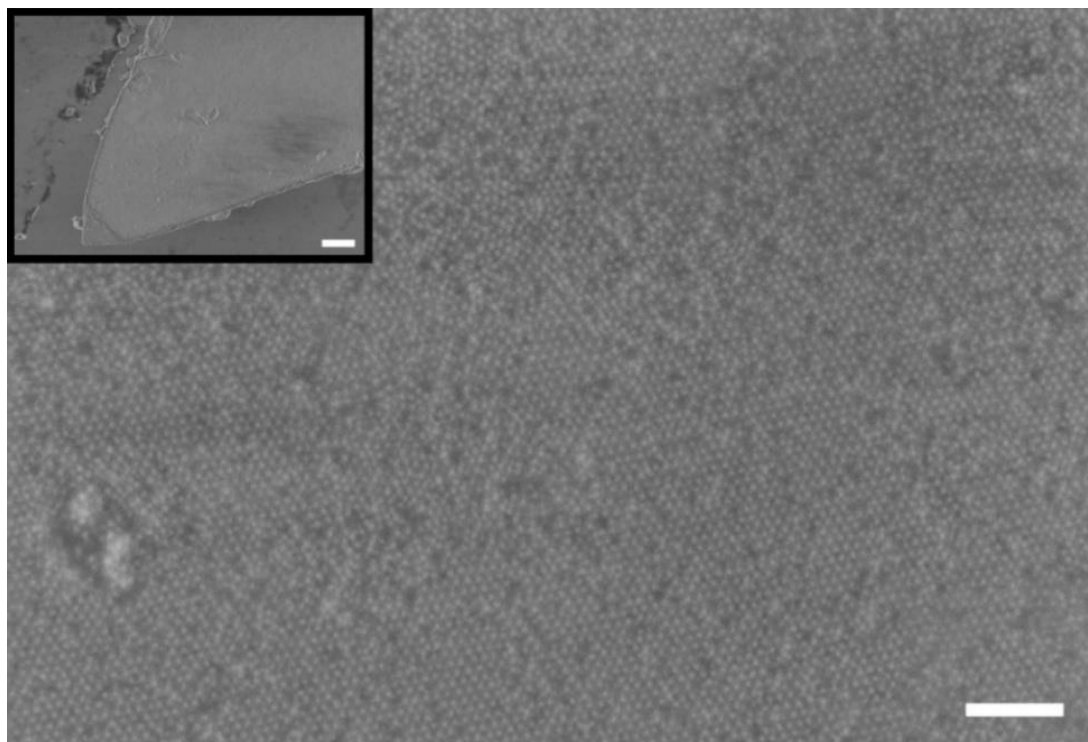


Figure 8.33: SEM image of AuEnc^(neg) crystal surface. View from above on the (100) orientation. Several levels of the protein surface are visible. Not every position seems to be filled and leaves a hole on the surface. Scale bar is 200 nm. Inset: Overview of protein crystal. Scale bar in inset is 2 μ m.

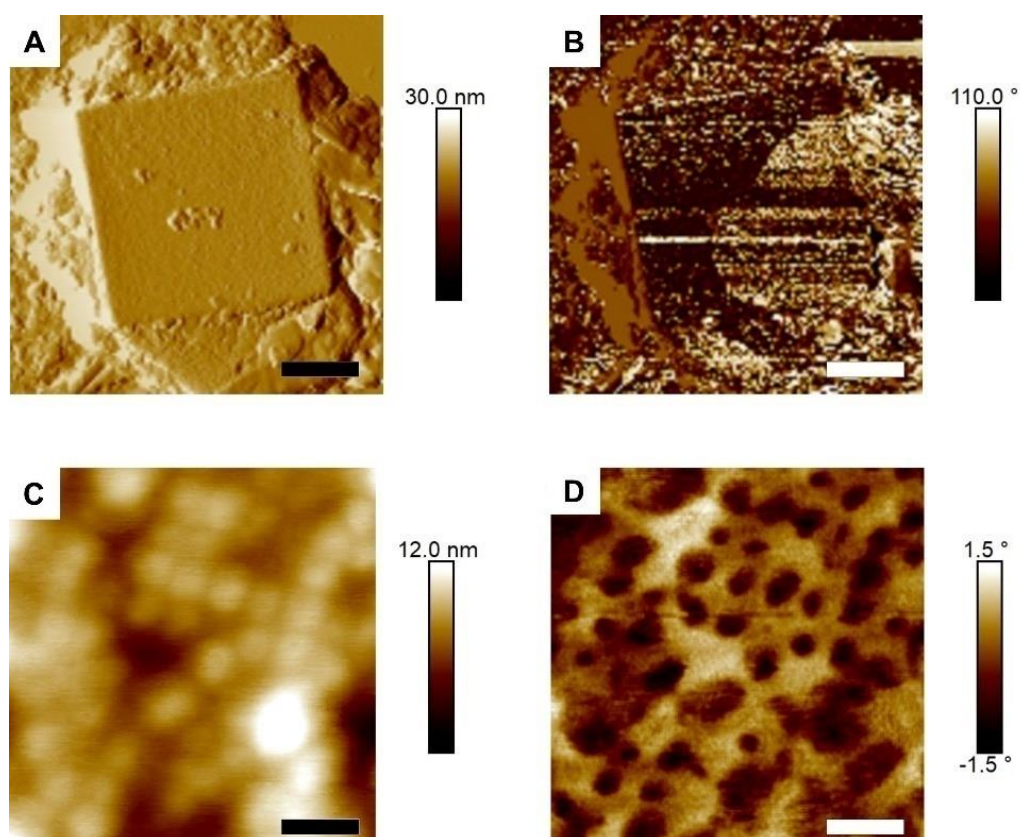


Figure 8.34: AFM images of a hetero binary crystal. Enc^(neg) is loaded with AuNPs, while Ftn^(pos) remains empty. AFM images based on either height (A+C) or phases (B+D). Bright (C) or dark spots (D) indicate AuEnc^(neg). Distance between spots is around 24 nm and fits very well to the unit cell ($a = 24.6$ nm). Scale bar in (A) and (B) is 2 μ m. Scale bar in (C) and (D) is 40 nm.

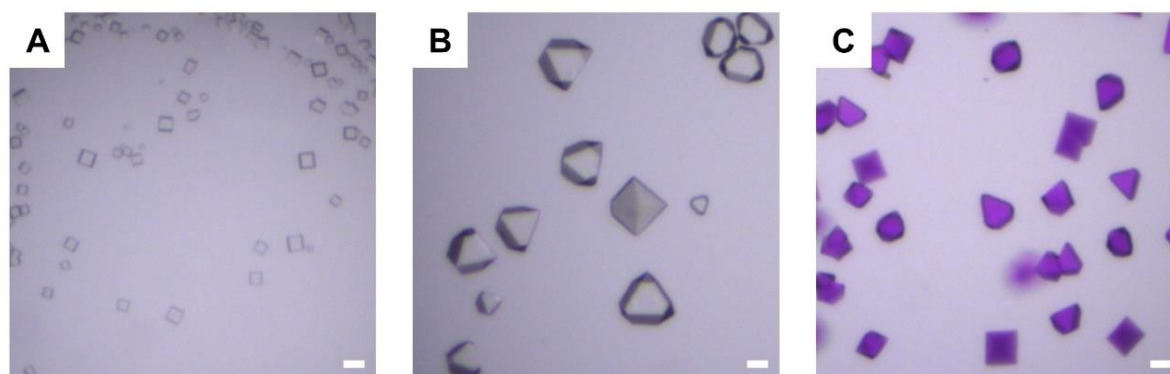


Figure 8.35: Optical microscopy images of protein crystals. Ftn^(pos)-Cys crystallized with either Enc^(neg) (A) or Ftn^(neg) (B). Rh3B labeled Ftn^(pos)-Cys protein crystallized with Ftn^(neg) (C). Scale bars are 50 μ m.

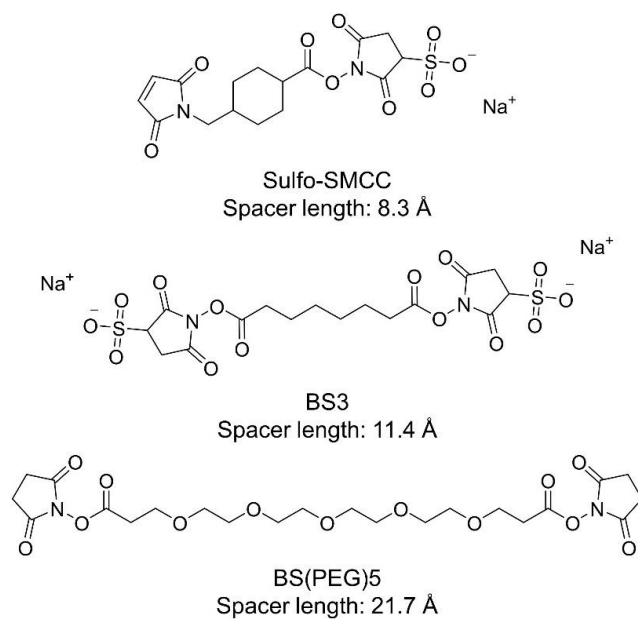


Figure 8.36: Overview of cross-linker and their length.

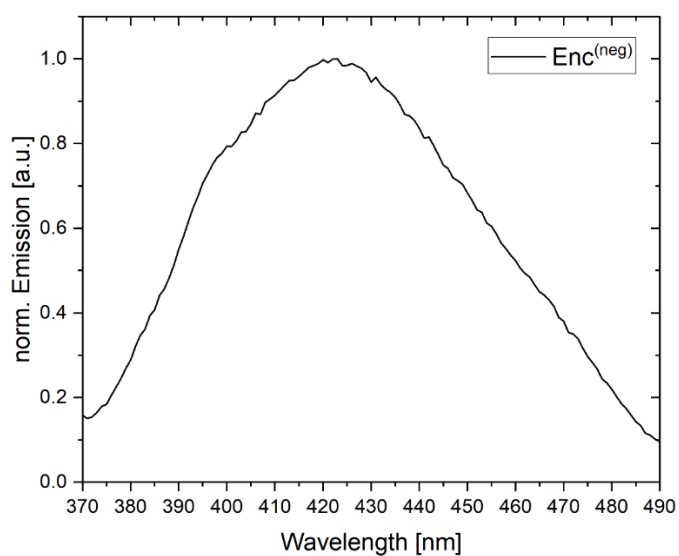


Figure 8.37: Normalized emission spectra of Enc^(neg).

Table 8.12: Data statistics for nanoparticle loaded protein crystals.

	AuEnc^(neg)	AuEnc^(neg)/eFtn^(pos)	eEnc^(neg)/CeFtn^(pos)
Data collection			
Wavelength (Å)	0.984	0.984	0.984
Space group	<i>C2</i>	<i>P432</i>	<i>P432</i>
Unit cell dimensions (<i>a</i> , <i>b</i> , <i>c</i> [Å]; α , β , γ [°])	417.18, 228.12, 403.32 90.0, 108.1, 90.0	244.48, 244.48, 244.48 90.0, 90.0, 90.0	244.00, 244.00, 244.00 90.0, 90.0, 90.0
Resolution range (Å)	383.28 - 18.00	109.33 - 30.09	244.00 - 18.09
Highest resolution shell (Å)	18.23 - 18.00	30.32 - 30.09	18.18 - 18.09
No. of observed reflections	20673	3563	18177
No. of unique reflections	3366	123	510
Multiplicity	6.1	28.97	35.64
Completeness (%)	97.0	96.9	99.4
$\langle I/\sigma \rangle$	12.54	10.31	8.61
R _{merge} (%)	5.94	37.30	4.45

Table 8.13: Data statistics for hetero binary protein crystals

	eEnc^(neg)/eFtn^(pos)
Data collection	
Wavelength (Å)	1.033
Space group	<i>P432</i>
Unit cell dimensions (<i>a</i> , <i>b</i> , <i>c</i> [Å]; α , β , γ [°])	242.57, 242.57, 242.57 90.0, 90.0, 90.0
Resolution range (Å)	49.51 - 10.00
Highest resolution shell (Å)	11.18 - 10.00
No. of observed reflections	52052
No. of unique reflections	1515
Multiplicity	34.36
Completeness (%)	98.1
$\langle I/\sigma \rangle$	3.51
R _{merge} (%)	53.15

9 Bibliography

- [1] A. Heuer-Jungemann, *et al.*, *Chem. Rev.* **2019**, *119*, 4819-4880.
- [2] E. Petryayeva, W. R. Algar, I. L. Medintz, *Appl. Spectrosc.* **2013**, *67*, 215-252.
- [3] M. C. Daniel, D. Astruc, *Chem. Rev.* **2004**, *104*, 293-346.
- [4] K. A. Kang, J. Wang, J. B. Jasinski, S. Achilefu, *J. Nanobiotechnology* **2011**, *9*, 16.
- [5] S. Laurent, D. Forge, M. Port, A. Roch, C. Robic, L. Vander Elst, R. N. Muller, *Chem. Rev.* **2008**, *108*, 2064-2110.
- [6] C. Yun, A. Javier, T. Jennings, M. Fisher, S. Hira, S. Peterson, B. Hopkins, N. Reich, G. Strouse, *J. Am. Chem. Soc.* **2005**, *127*, 3115-3119.
- [7] T. W. Giessen, *Annu. Rev. Biochem.* **2022**, *91*, 353-380.
- [8] S. C. Andrews, *Biochim Biophys Acta* **2010**, *1800*, 691-705.
- [9] C. Cassidy-Amstutz, L. Oltrogge, C. C. Going, A. Lee, P. Teng, D. Quintanilla, A. East-Seletsky, E. R. Williams, D. F. Savage, *Biochemistry* **2016**, *55*, 3461-3468.
- [10] M. Künzle, J. Mangler, M. Lach, T. Beck, *Nanoscale* **2018**, *10*, 22917-22926.
- [11] J. Holmes, A. A. Sushma, I. B. Tsvetkova, W. L. Schaich, R. D. Schaller, B. Dragnea, *J. Phys. Chem. Lett.* **2022**, *13*, 3237-3243.
- [12] M. Budiarta, W. Xu, L. Schubert, M. Meledina, A. Meledin, D. Wöll, A. Pich, T. Beck, *J. Colloid Interface Sci.* **2021**, *591*, 451-462.
- [13] M. Lach, C. Strelow, A. Meyer, A. Mews, T. Beck, *ACS Appl. Mater. Interfaces* **2022**, *14*, 10656-10668.
- [14] L. Zhang, J. B. Bailey, R. H. Subramanian, A. Groisman, F. A. Tezcan, *Nature* **2018**, *557*, 86-91.
- [15] M. Künzle, T. Eckert, T. Beck, *J. Am. Chem. Soc.* **2016**, *138*, 12731-12734.
- [16] H. Goesmann, C. Feldmann, *Angew. Chem.* **2010**, *122*, 1402-1437.
- [17] M. Auffan, J. Rose, J. Y. Bottero, G. V. Lowry, J. P. Jolivet, M. R. Wiesner, *Nat. Nanotechnol.* **2009**, *4*, 634-641.
- [18] W. G. Kreyling, M. Semmler-Behnke, Q. Chaudhry, *Nano Today* **2010**, *5*, 165-168.
- [19] W. J. Parak, L. Manna, T. Nann, *Nanotechnology. Volume 1: Principles and Fundamentals, Vol. 1*, **2008**.
- [20] P. P. Edwards, J. M. Thomas, *Angew. Chem., Int. Ed.* **2007**, *46*, 5480-5486.
- [21] M. Comotti, C. Della Pina, R. Matarrese, M. Rossi, *Angew. Chem., Int. Ed.* **2004**, *43*, 5812-5815.
- [22] M. Auffan, *et al.*, *Langmuir* **2008**, *24*, 3215-3222.
- [23] P. Hoyer, H. Weller, *Chem. Phys. Lett.* **1994**, *221*, 379-384.
- [24] J. Piella, N. G. Bastús, V. Puntès, *Chem. Mater.* **2016**, *28*, 1066-1075.
- [25] N. S. Mueller, E. Pfitzner, Y. Okamura, G. Gordeev, P. Kusch, H. Lange, J. Heberle, F. Schulz, S. Reich, *ACS Nano* **2021**, *15*, 5523-5533.

- [26] Q. Ding, J. Wang, X. Chen, H. Liu, Q. Li, Y. Wang, S. Yang, *Nano Lett.* **2020**, *20*, 7304-7312.
- [27] G. Bodelon, *et al.*, *Nat. Mat.* **2016**, *15*, 1203-1211.
- [28] J. Yin, H. Zheng, A. Li, J. Zhang, L. Tian, F. Zhao, Y. Shao, *Nanotechnology* **2021**, *32*.
- [29] J. Aaron, K. Travis, N. Harrison, K. Sokolov, *Nano Lett.* **2009**, *9*, 3612-3618.
- [30] I. H. El-Sayed, X. Huang, M. A. El-Sayed, *Nano Lett.* **2005**, *5*, 829-834.
- [31] G. Li, C. Cherqui, N. W. Bigelow, G. Duscher, P. J. Straney, J. E. Millstone, D. J. Masiello, J. P. Camden, *Nano Lett.* **2015**, *15*, 3465-3471.
- [32] S. Bhowmick, S. Saini, V. B. Shenoy, B. Bagchi, *J. Chem. Phys.* **2006**, *125*, 181102.
- [33] V. Faessler, C. Hrelescu, A. A. Lutich, L. Osinkina, S. Mayilo, F. Jäckel, J. Feldmann, *Chem. Phys. Lett.* **2011**, *508*, 67-70.
- [34] T. Sojinrin, J. Conde, K. Liu, J. Curtin, H. J. Byrne, D. Cui, F. Tian, *Anal. Bioanal. Chem.* **2017**, *409*, 4647-4658.
- [35] T. Dang-Bao, I. Favier, M. Gómez, *Metal Nanoparticles in Polyols: Bottom-up and Top-down Syntheses and Catalytic Applications*, **2021**.
- [36] R. Janot, D. Guerard, *Prog. Mater. Sci* **2005**, *50*, 1-92.
- [37] T. Prasad Yadav, R. Manohar Yadav, D. Pratap Singh, *Nanosci Nanotechnol Lett* **2012**, *2*, 22-48.
- [38] N. R. Jana, X. Peng, *J. Am. Chem. Soc.* **2003**, *125*, 14280-14281.
- [39] W. Leng, P. Pati, P. J. Vikesland, *Environ. Sci. Nano* **2015**, *2*, 440-453.
- [40] X. Ji, X. Song, J. Li, Y. Bai, W. Yang, X. Peng, *J. Am. Chem. Soc.* **2007**, *129*, 13939-13948.
- [41] F. Schulz, T. Homolka, N. G. Bastus, V. Puentes, H. Weller, T. Vossmeier, *Langmuir* **2014**, *30*, 10779-10784.
- [42] S. Mourdikoudis, L. M. Liz-Marzán, *Chem. Mater.* **2013**, *25*, 1465-1476.
- [43] V. K. LaMer, R. H. Dinegar, *J. Am. Chem. Soc.* **1950**, *72*, 4847-4854.
- [44] E. C. Vreeland, *et al.*, *Chem. Mater.* **2015**, *27*, 6059-6066.
- [45] N. T. Thanh, N. Maclean, S. Mahiddine, *Chem. Rev.* **2014**, *114*, 7610-7630.
- [46] B. Streszewski, W. Jaworski, K. Paclawski, E. Csapó, I. Dékány, K. Fitzner, *Colloids and Surfaces A: Physicochemical and Engineering Aspects* **2012**, *397*, 63-72.
- [47] W. Ostwald, *Zeitschrift für Physikalische Chemie* **1900**, *34U*, 495-503.
- [48] S. T. Gentry, S. F. Kendra, M. W. Bezpalko, *J. Phys. Chem. C* **2011**, *115*, 12736-12741.
- [49] A. Kraynov, T. E. Müller, *Concepts for the Stabilization of Metal Nanoparticles in Ionic Liquids, Vol. 7*, **2012**.
- [50] J. Hierrezuelo, A. Sadeghpour, I. Szilagyi, A. Vaccaro, M. Borkovec, *Langmuir* **2010**, *26*, 15109-15111.

- [51] S. A. Macpherson, G. B. Webber, R. Moreno-Atanasio, *Adv. Powder. Technol.* **2012**, 23, 478-484.
- [52] F. Loosli, P. Le Coustumer, S. Stoll, *Sci. Total Environ.* **2015**, 535, 28-34.
- [53] W. Yang, T. Wang, Z. Fan, *Energy & Fuels* **2017**, 31, 9016-9025.
- [54] T. Laaksonen, P. Ahonen, C. Johans, K. Kontturi, *ChemPhysChem* **2006**, 7, 2143-2149.
- [55] W. P. Wuelfing, S. M. Gross, D. T. Miles, R. W. Murray, *J. Am. Chem. Soc.* **1998**, 120, 12696-12697.
- [56] A. Housni, M. Ahmed, S. Liu, R. Narain, *J. Phys. Chem. C* **2008**, 112, 12282-12290.
- [57] M. B. Einarson, J. C. Berg, *J. Colloid Interface Sci.* **1993**, 155, 165-172.
- [58] P. Alexandridis, *Chem. Eng. Technol.* **2011**, 34, 15-28.
- [59] B. Svensson, U. Olsson, P. Alexandridis, *Langmuir* **2000**, 16, 6839-6846.
- [60] R. B. Grubbs, *Polym. Eng. Rev.* **2007**, 47, 197-215.
- [61] A. M. Alkilany, S. R. Abulateefeh, C. J. Murphy, *Part. Part. Syst. Charact.* **2018**, 36.
- [62] G. Yang, W. S. Chang, D. T. Hallinan, Jr., *J. Colloid. Interface Sci.* **2015**, 460, 164-172.
- [63] J. Manson, D. Kumar, B. J. Meenan, D. Dixon, *Gold Bull.* **2011**, 44, 99-105.
- [64] L. Li, S. Chakrabarty, J. Jiang, B. Zhang, C. Ober, E. P. Giannelis, *Nanoscale* **2016**, 8, 1338-1343.
- [65] C. Pan, K. Pelzer, K. Philippot, B. Chaudret, F. Dassenoy, P. Lecante, M. J. Casanove, *J. Am. Chem. Soc.* **2001**, 123, 7584-7593.
- [66] I. Larson, D. Y. C. Chan, C. J. Drummond, F. Grieser, *Langmuir* **1997**, 13, 2429-2431.
- [67] J. Cure, Y. Coppel, T. Dammak, P. F. Fazzini, A. Mlayah, B. Chaudret, P. Fau, *Langmuir* **2015**, 31, 1362-1367.
- [68] R. G. Nuzzo, L. H. Dubois, D. L. Allara, *J. Am. Chem. Soc.* **1990**, 112, 558-569.
- [69] R. G. Nuzzo, F. A. Fusco, D. L. Allara, *J. Am. Chem. Soc.* **1987**, 109, 2358-2368.
- [70] J. Hassinen, V. Liljestrom, M. A. Kostianen, R. H. Ras, *Angew. Chem., Int. Ed.* **2015**, 54, 7990-7993.
- [71] M. Grzelczak, J. Perez-Juste, P. Mulvaney, L. M. Liz-Marzan, *Chem. Soc. Rev.* **2008**, 37, 1783-1791.
- [72] C. Noguez, *J. Phys. Chem. C* **2007**, 111, 3806-3819.
- [73] K. L. Kelly, E. Coronado, L. L. Zhao, G. C. Schatz, *J. Phys. Chem. B* **2002**, 107, 668-677.
- [74] Y. Sun, Y. Xia, *Science* **2002**, 298, 2176-2179.
- [75] B. Wiley, Y. Sun, B. Mayers, Y. Xia, *Chemistry* **2005**, 11, 454-463.
- [76] T. S. Ahmadi, Z. L. Wang, T. C. Green, A. Henglein, M. A. El-Sayed, *Science* **1996**, 272, 1924-1926.

- [77] J. Turkevich, P. C. Stevenson, J. Hillier, *Discussions of the Faraday Society* **1951**, *11*, 55-75.
- [78] H. Yagyu, M. Hamamoto, Y. Wang, *Microfluid. Nanofluidics* **2022**, *26*.
- [79] M. Faraday, *The London, Edinburgh The London, Edinburgh, and Dublin Philosophical Magazine and Journal of Science* **1857**, *14*, 512-539.
- [80] A. Syafiuddin, Salmiati, M. R. Salim, A. Beng Hong Kueh, T. Hadibarata, H. Nur, *J. Chin. Chem. Soc.* **2017**, *64*, 732-756.
- [81] J. Kimling, M. Maier, B. Okenve, V. Kotaidis, H. Ballot, A. Plech, *J. Phys. Chem. B* **2006**, *110*, 15700-15707.
- [82] P. Zhao, N. Li, D. Astruc, *Coord. Chem. Rev.* **2013**, *257*, 638-665.
- [83] R. Dinkel, B. Braunschweig, W. Peukert, *J. Phys. Chem. C* **2016**, *120*, 1673-1682.
- [84] E. Z. Jahromi, J. Gailer, *Dalton Trans.* **2010**, *39*, 329-336.
- [85] J. Hühn, *et al.*, *Chem. Mater.* **2016**, *29*, 399-461.
- [86] A. H. Lu, E. L. Salabas, F. Schuth, *Angew. Chem., Int. Ed.* **2007**, *46*, 1222-1244.
- [87] T. Guo, *et al.*, *J. Nanomater.* **2018**, *2018*, 1-8.
- [88] F. Hussain, M. Hojjati, M. Okamoto, R. E. Gorga, *J. Compos. Mater.* **2006**, *40*, 1511-1575.
- [89] X. Li, M. Rui, J. Song, Z. Shen, H. Zeng, *Adv. Funct. Mater.* **2015**, *25*, 4929-4947.
- [90] O. Stranik, H. M. McEvoy, C. McDonagh, B. D. MacCraith, *Sens. Actuators B Chem.* **2005**, *107*, 148-153.
- [91] A. Puzder, A. J. Williamson, F. A. Reboredo, G. Galli, *Phys. Rev. Lett.* **2003**, *91*, 157405.
- [92] N. Xia, Q. Wang, L. Liu, *Sensors* **2014**, *15*, 499-514.
- [93] J. Li, J. Z. Zhang, *Coord. Chem. Rev.* **2009**, *253*, 3015-3041.
- [94] I. Freestone, N. Meeks, M. Sax, C. Higgitt, *Gold Bull.* **2007**, *40*, 270-277.
- [95] D. Schaming, H. Remita, *Found. Chem.* **2015**, *17*, 187-205.
- [96] K. A. Willets, R. P. Van Duyne, *Annu. Rev. Phys. Chem.* **2007**, *58*, 267-297.
- [97] A. J. Haes, C. L. Haynes, A. D. McFarland, G. C. Schatz, *Mater. Res. Bull.* **2005**, *30*, 368-375.
- [98] K. Hamamoto, R. Micheletto, M. Oyama, A. A. Umar, S. Kawai, Y. Kawakami, *J. Opt.* **2006**, *8*, 268-271.
- [99] J. Krajczewski, K. Kołataj, A. Kudelski, *RSC Advances* **2017**, *7*, 17559-17576.
- [100] N. G. Khlebtsov, L. A. Dykman, *J. Quant. Spectrosc. Radiat. Transf.* **2010**, *111*, 1-35.
- [101] J. H. Song, F. Kim, D. Kim, P. Yang, *Chemistry* **2005**, *11*, 910-916.
- [102] R. D. Near, S. C. Hayden, M. A. El-Sayed, *J. Phys. Chem. C* **2013**, *117*, 18653-18656.
- [103] G. Mie, *Annalen der Physik* **1908**, *330*, 377-445.

- [104] J. Zheng, X. Cheng, H. Zhang, X. Bai, R. Ai, L. Shao, J. Wang, *Chem. Rev.* **2021**, *121*, 13342-13453.
- [105] A. Agarwal, S. Huang, M. O'donnell, K. Day, M. Day, N. Kotov, S. Ashkenazi, *J. Appl. Phys.* **2007**, *102*, 064701.
- [106] M. Xu, L. V. Wang, *Rev. Sci. Instrum.* **2006**, *77*.
- [107] E. M. Donnelly, K. P. Kubelick, D. S. Dumani, S. Y. Emelianov, *Nano Lett.* **2018**, *18*, 6625-6632.
- [108] Y. Mantri, J. V. Jokerst, *ACS Nano* **2020**, *14*, 9408-9422.
- [109] A. M. Alkilany, C. J. Murphy, *J. Nanopart. Res.* **2010**, *12*, 2313-2333.
- [110] C. Kuttner, R. P. M. Holler, M. Quintanilla, M. J. Schnepf, M. Dulle, A. Fery, L. M. Liz-Marzan, *Nanoscale* **2019**, *11*, 17655-17663.
- [111] F. Schulz, O. Pavelka, F. Lehmkuhler, F. Westermeier, Y. Okamura, N. S. Mueller, S. Reich, H. Lange, *Nat. Commun.* **2020**, *11*, 3821.
- [112] N. S. Mueller, Y. Okamura, B. G. M. Vieira, S. Juergensen, H. Lange, E. B. Barros, F. Schulz, S. Reich, *Nature* **2020**, *583*, 780-784.
- [113] A. McLintock, N. Hunt, A. W. Wark, *Chem. Commun.* **2011**, *47*, 3757-3759.
- [114] H. Xu, J. Aizpurua, M. Käll, P. Apell, *Phys. Rev. E* **2000**, *62*, 4318.
- [115] J. Feng, X. Wu, W. Ma, H. Kuang, L. Xu, C. Xu, *Chem. Commun. (Cambridge)* **2015**, *51*, 14761-14763.
- [116] M. Blanco-Formoso, N. Pazos-Perez, R. A. Alvarez-Puebla, *Nanoscale* **2020**, *12*, 14948-14956.
- [117] P. P. Patra, R. Chikkaraddy, R. P. Tripathi, A. Dasgupta, G. Kumar, *Nat. Commun.* **2014**, *5*, 1-8.
- [118] C. Matricardi, C. Hanske, J. L. Garcia-Pomar, J. Langer, A. Mihi, L. M. Liz-Marzan, *ACS Nano* **2018**, *12*, 8531-8539.
- [119] H. Alaeian, J. A. Dionne, *Opt. Express* **2012**, *20*, 15781-15796.
- [120] C. Soennichsen, B. M. Reinhard, J. Liphardt, A. P. Alivisatos, *Nat. Biotechnol.* **2005**, *23*, 741-745.
- [121] P. C. Ray, G. K. Darbha, A. Ray, J. Walker, W. Hardy, *Plasmonics* **2007**, *2*, 173-183.
- [122] T. Zhao, T. Li, Y. Liu, *Nanoscale* **2017**, *9*, 9841-9847.
- [123] P. C. Ray, Z. Fan, R. A. Crouch, S. S. Sinha, A. Pramanik, *Chem. Soc. Rev.* **2014**, *43*, 6370-6404.
- [124] A. A. Ansari, V. K. Thakur, G. Chen, *Coord. Chem. Rev.* **2021**, *436*.
- [125] K. S. Kim, J. H. Kim, H. Kim, F. Laquai, E. Arifin, J. K. Lee, S. I. Yoo, B. H. Sohn, *ACS Nano* **2012**, *6*, 5051-5059.
- [126] N. Aissaoui, K. Moth-Poulsen, M. Kall, P. Johansson, L. M. Wilhelmsson, B. Albinsson, *Nanoscale* **2017**, *9*, 673-683.

- [127] S. L. Capehart, M. P. Coyle, J. E. Glasgow, M. B. Francis, *J. Am. Chem. Soc.* **2013**, *135*, 3011-3016.
- [128] L.-Y. Wei, K.-S. Huang, H.-H. Lin, Y.-P. Wu, K.-T. Tan, Y. Y. Lee, I. C. Chen, *J. Phys. Chem. C* **2018**, *122*, 28431-28438.
- [129] J. R. Lakowicz, *Principles of fluorescence spectroscopy*, Springer, **2006**.
- [130] A. Jablonski, *Nature* **1933**, *131*, 839-840.
- [131] P. Anger, P. Bharadwaj, L. Novotny, *Phys. Rev. Lett.* **2006**, *96*, 113002.
- [132] L. K. Fraiji, D. M. Hayes, T. Werner, *J. Chem. Educ.* **1992**, *69*, 424.
- [133] F. Liu, W. D. Kohn, J. P. Mayer, *J. Pept. Sci.* **2012**, *18*, 336-341.
- [134] K. H. Drexhage, *J. Res. Natl. Bur. Stand. A Phys. Chem.* **1976**, *80A*.
- [135] J. Demasa, G. Crosby, *J. Chem. Phys* **1968**, *48*, 4726.
- [136] M. Bossi, J. Folling, V. N. Belov, V. P. Boyarskiy, R. Medda, A. Egner, C. Eggeling, A. Schonle, S. W. Hell, *Nano Lett.* **2008**, *8*, 2463-2468.
- [137] W. Liu, M. Howarth, A. B. Greytak, Y. Zheng, D. G. Nocera, A. Y. Ting, M. G. Bawendi, *J. Am. Chem. Soc.* **2008**, *130*, 1274-1284.
- [138] P. H. Chan, *et al.*, *J. Am. Chem. Soc.* **2008**, *130*, 6351-6361.
- [139] S. Vira, E. Mekhedov, G. Humphrey, P. S. Blank, *Anal. Biochem.* **2010**, *402*, 146-150.
- [140] S. F. Hedegaard, *et al.*, *Sci. Rep.* **2018**, *8*, 6327.
- [141] W. Nomura, Y. Tanabe, H. Tsutsumi, T. Tanaka, K. Ohba, N. Yamamoto, H. Tamamura, *Bioconjug. Chem.* **2008**, *19*, 1917-1920.
- [142] C. P. Toseland, *J. Chem. Biol.* **2013**, *6*, 85-95.
- [143] D. P. Nair, M. Podgorski, S. Chatani, T. Gong, W. Xi, C. R. Fenoli, C. N. Bowman, *Chem. Mat.* **2014**, *26*, 724-744.
- [144] A. Michael, *J. Am. Chem.* **1887**, *9*, 115.
- [145] P. McDaid, Y. Chen, L. Deng, *Angew. Chem., Int. Ed.* **2002**, *41*.
- [146] J. Yadav, B. Reddy, G. Baishya, *J. Org. Chem. Res.* **2003**, *68*, 7098-7100.
- [147] T. Miyadera, E. M. Kosower, *J. Med. Chem.* **1972**, *15*, 534-537.
- [148] M. E. Gindy, S. Ji, T. R. Hoye, A. Z. Panagiotopoulos, R. K. Prud'homme, *Biomacromolecules* **2008**, *9*, 2705-2711.
- [149] L. C. Radu, J. Yang, J. Kopecek, *Macromol. Biosci.* **2009**, *9*, 36-44.
- [150] B. H. Northrop, S. H. Frayne, U. Choudhary, *Polymer Chemistry* **2015**, *6*, 3415-3430.
- [151] Y. Sun, H. Liu, L. Cheng, S. Zhu, C. Cai, T. Yang, L. Yang, P. Ding, *Polymer International* **2018**, *67*, 25-31.
- [152] A. Sanchez, E. Pedroso, A. Grandas, *Chem. Commun. (Cambridge)* **2013**, *49*, 309-311.
- [153] P. W. Atkins, J. de Paula, J. J. Keeler, C. Hartmann, *Physikalische Chemie*, Wiley, **2021**.

- [154] R. Gross, A. Marx, *Festkörperphysik*, Oldenbourg Wissenschaftsverlag, **2012**.
- [155] H. Weller, *Angew. Chem. Int. Ed.* **1993**, *32*, 41-53.
- [156] S. Kargozar, S. J. Hoseini, P. B. Milan, S. Hooshmand, H. W. Kim, M. Mozafari, *Biotechnol. J.* **2020**, *15*, e2000117.
- [157] G. Weber, F. W. J. Teale, *J. Chem. Soc., Faraday Trans.* **1957**, *53*.
- [158] S. Fery-Forgues, D. Lavabre, *J. Chem. Educ.* **1999**, *76*.
- [159] M. Sun, X. Ma, X. Chen, Y. Sun, X. Cui, Y. Lin, *RSC Adv.* **2014**, *4*, 1120-1127.
- [160] C. B. Murray, D. J. Norris, M. G. Bawendi, *J. Am. Chem. Soc.* **1993**, *115*, 8706-8715.
- [161] X. Tong, Z. M. Wang, *Core/Shell Quantum Dots, Vol. 28*, Springer, **2020**.
- [162] Y. C. Cao, J. Wang, *J. Am. Chem. Soc.* **2004**, *126*, 14336-14337.
- [163] W. W. Yu, X. Peng, *Angew. Chem., Int. Ed.* **2002**, *41*, 2368-2371.
- [164] Z. Deng, L. Cao, F. Tang, B. Zou, *J. Phys. Chem. B* **2005**, *109*, 16671-16675.
- [165] R. Burke, N. M. B. Cogan, A. Oi, T. D. Krauss, *J. Phys. Chem. C* **2018**, *122*, 14099-14106.
- [166] J. Ostermann, *et al.*, *ACS Nano* **2013**, *7*, 9156-9167.
- [167] Z.-J. Li, X.-B. Li, J.-J. Wang, S. Yu, C.-B. Li, C.-H. Tung, L.-Z. Wu, *Energy Environ. Sci.* **2013**, *6*, 465-469.
- [168] K. P. Acharya, *et al.*, *Nano Lett.* **2011**, *11*, 2919-2926.
- [169] F. W. Eagle, N. Park, M. Cash, B. M. Cossairt, *ACS Energy Lett.* **2021**, *6*, 977-984.
- [170] M. Chern, T. T. Nguyen, A. H. Mahler, A. M. Dennis, *Nanoscale* **2017**, *9*, 16446-16458.
- [171] Y. U. Staechelin, M. Deffner, S. Krohn, C. Castillo Delgadillo, J. S. Niehaus, H. Lange, *J. Chem. Phys.* **2022**, *156*, 061102.
- [172] A. Hinsch, *et al.*, *J. Phys. Chem. C* **2019**, *123*, 24338-24346.
- [173] K. Boldt, N. Kirkwood, G. A. Beane, P. Mulvaney, *Chem. Mat.* **2013**, *25*, 4731-4738.
- [174] H. Shen, *et al.*, *Adv. Funct. Mater.* **2014**, *24*, 2367-2373.
- [175] J. S. Steckel, P. Snee, S. Coe-Sullivan, J. P. Zimmer, J. E. Halpert, P. Anikeeva, L. A. Kim, V. Bulovic, M. G. Bawendi, *Angew. Chem., Int. Ed.* **2006**, *45*, 5796-5799.
- [176] M. Protiere, P. Reiss, *Small* **2007**, *3*, 399-403.
- [177] Y. Chen, J. Vela, H. Htoon, J. L. Casson, D. J. Werder, D. A. Bussian, V. I. Klimov, J. A. Hollingsworth, *J. Am. Chem. Soc.* **2008**, *130*, 5026-5027.
- [178] S. Christodoulou, *et al.*, *J. Mater. Chem. C* **2014**, *2*.
- [179] K. Bourzac, *Nature* **2013**, *493*, 283.
- [180] R. Burke, K. L. Bren, T. D. Krauss, *J. Chem. Phys.* **2021**, *154*, 030901.
- [181] F. P. Garcia de Arquer, D. V. Talapin, V. I. Klimov, Y. Arakawa, M. Bayer, E. H. Sargent, *Science* **2021**, *373*.
- [182] H. Jung, N. Ahn, V. I. Klimov, *Nat. Photonics* **2021**, *15*, 643-655.
- [183] W. M. Aumiller, M. Uchida, T. Douglas, *Chem. Soc. Rev.* **2018**, *47*, 3433-3469.

- [184] T. G. W. Edwardson, M. D. Lévasseur, S. Tetter, A. Steinauer, M. Hori, D. Hilvert, *Chem. Rev.* **2022**, *122*, 9145-9197.
- [185] O. Daumke, G. R. Lewin, *Cell Res* **2022**, *32*, 117-118.
- [186] Keiichi Namba, P. Rekha, G. Stubbs, *J. Mol. Biol.* **1989**, *208*.
- [187] F. F. Miranda, K. Iwasaki, S. Akashi, K. Sumitomo, M. Kobayashi, I. Yamashita, J. R. Tame, J. G. Hedde, *Small* **2009**, *5*, 2077-2084.
- [188] A. Korpi, E. Anaya-Plaza, S. Valimaki, M. Kostianen, *WIREs Nanomed Nanobiotechnol.* **2020**, *12*, e1578.
- [189] M. Uchida, *et al.*, *Adv. Mater.* **2007**, *19*, 1025-1042.
- [190] F. H. Crick, J. D. Watson, *Nature* **1956**, *177*, 473-475.
- [191] K. Majsterkiewicz, *et al.*, *Nano Lett.* **2022**, *22*, 3187-3195.
- [192] T. Douglas, M. Young, *Science* **2006**, *312*, 873-875.
- [193] D. J. Huard, K. M. Kane, F. A. Tezcan, *Nat. Chem. Biol.* **2013**, *9*, 169-176.
- [194] W. J. Altenburg, N. Rollins, P. A. Silver, T. W. Giessen, *Sci. Rep.* **2021**, *11*, 4951.
- [195] T. Beck, S. Tetter, M. Kunzle, D. Hilvert, *Angew. Chem., Int. Ed.* **2015**, *54*, 937-940.
- [196] M. Khoshnejad, C. F. Greineder, K. W. Pulsipher, C. H. Villa, B. Altun, D. C. Pan, A. Tsourkas, I. J. Dmochowski, V. R. Muzykantov, *Bioconjug. Chem.* **2018**, *29*, 1209-1218.
- [197] T. N. Szyszka, E. N. Jenner, N. Tasneem, Y. H. Lau, *ChemSystemsChem* **2021**, *4*.
- [198] E. M. Williams, S. M. Jung, J. L. Coffman, S. Lutz, *ACS Synth. Biol.* **2018**, *7*, 2514-2517.
- [199] E. C. Theil, X. S. Liu, T. Tosha, *Inorg. Chim. Acta* **2008**, *361*, 868-874.
- [200] L. S. R. Adamson, *et al.*, *Sci. Adv.* **2022**, *8*, eabl7346.
- [201] T. Tosha, H. L. Ng, O. Bhattasali, T. Alber, E. C. Theil, *J. Am. Chem. Soc.* **2010**, *132*, 14562-14569.
- [202] C. Lv, S. Zhang, J. Zang, G. Zhao, C. Xu, *Biochemistry* **2014**, *53*, 2232-2241.
- [203] A. Liu, M. Verwegen, M. V. de Ruiter, S. J. Maassen, C. H. Traulsen, J. J. Cornelissen, *J. Phys. Chem. B* **2016**, *120*, 6352-6357.
- [204] S. K. Dixit, *et al.*, *Nano Lett.* **2006**, *6*, 1993-1999.
- [205] M. Lach, M. Kunzle, T. Beck, *Chemistry* **2017**, *23*, 17482-17486.
- [206] A. M. Wen, N. F. Steinmetz, *Chem. Soc. Rev.* **2016**, *45*, 4074-4126.
- [207] T. Douglas, E. Strable, D. Willits, A. Aitouchen, M. Libera, M. Young, *Adv. Mater.* **2002**, *14*, 415-418.
- [208] M. Allen, D. Willits, M. Young, T. Douglas, *Inorg. Chem.* **2003**, *42*, 6300-6305.
- [209] M. Allen, D. Willits, J. Mosolf, M. Young, T. Douglas, *Adv. Mater.* **2002**, *14*, 1562-1565.
- [210] N. Valdes-Stauber, S. Scherer, *Appl. Environ. Microbiol.* **1994**, *60*, 3809-3814.

- [211] W. F. Rurup, J. Snijder, M. S. Koay, A. J. Heck, J. J. Cornelissen, *J. Am. Chem. Soc.* **2014**, *136*, 3828-3832.
- [212] M. P. Andreas, T. W. Giessen, *Nat. Commun.* **2021**, *12*, 4748.
- [213] T. W. Giessen, P. A. Silver, *Nat. Microbiol.* **2017**, *2*, 17029.
- [214] R. J. Nichols, C. Cassidy-Amstutz, T. Chaijarasphong, D. F. Savage, *Crit. Rev. Biochem. Mol. Biol.* **2017**, *52*, 583-594.
- [215] J. A. Jones, T. W. Giessen, *Biotechnol. Bioeng.* **2021**, *118*, 491-505.
- [216] J. Heinemann, W. S. Maaty, G. H. Gauss, N. Akkaladevi, S. K. Brumfield, V. Rayaprolu, M. J. Young, C. M. Lawrence, B. Bothner, *Virology* **2011**, *417*, 362-368.
- [217] M. Sutter, D. Boehringer, S. Gutmann, S. Gunther, D. Prangishvili, M. J. Loessner, K. O. Stetter, E. Weber-Ban, N. Ban, *Nat. Struct. Mol. Biol.* **2008**, *15*, 939-947.
- [218] T. W. Giessen, B. J. Orlando, A. A. Verdegaal, M. G. Chambers, J. Gardener, D. C. Bell, G. Birrane, M. Liao, P. A. Silver, *Elife* **2019**, *8*.
- [219] B. J. LaFrance, C. Cassidy-Amstutz, R. J. Nichols, L. M. Oltrogge, E. Nogales, D. F. Savage, *Sci. Rep.* **2021**, *11*, 22810.
- [220] R. J. Nichols, B. LaFrance, N. R. Phillips, D. R. Radford, L. M. Oltrogge, L. E. Valentin-Alvarado, A. J. Bischoff, E. Nogales, D. F. Savage, *Elife* **2021**, *10*.
- [221] Y. Zhang, *et al.*, *Nat. Commun.* **2020**, *11*, 5421.
- [222] T. W. Giessen, P. A. Silver, *ACS Synth. Biol.* **2016**, *5*, 1497-1504.
- [223] R. E. Williams, N. C. Bruce, *Microbiology (Reading)* **2002**, *148*, 1607-1614.
- [224] T. Wiryaman, N. Toor, *IUCrJ* **2021**, *8*, 342-350.
- [225] I. Boyton, S. C. Goodchild, D. Diaz, A. Elbourne, L. E. Collins-Praino, A. Care, *ACS Omega* **2022**, *7*, 823-836.
- [226] N. D. Chasteen, P. M. Harrison, *J. Struct. Biol.* **1999**, *126*, 182-194.
- [227] R. R. Naik, S. J. Stringer, G. Agarwal, S. E. Jones, M. O. Stone, *Nat. Mater.* **2002**, *1*, 169-172.
- [228] R. M. Kramer, C. Li, D. C. Carter, M. O. Stone, R. R. Naik, *J. Am. Chem. Soc.* **2004**, *126*, 13282-13286.
- [229] E. V. Shevchenko, D. V. Talapin, N. A. Kotov, S. O'Brien, C. B. Murray, *Nature* **2006**, *439*, 55-59.
- [230] J. Zhu, *et al.*, *Adv. Mater.* **2020**, *32*, 1906600.
- [231] M. Künzle, T. Eckert, T. Beck, *Inorg. Chem.* **2018**, *57*, 13431-13436.
- [232] J. B. Bailey, L. Zhang, J. A. Chiong, S. Ahn, F. A. Tezcan, *J. Am. Chem. Soc.* **2017**, *139*, 8160-8166.
- [233] T. Kister, D. Monego, P. Mulvaney, A. Widmer-Cooper, T. Kraus, *ACS Nano* **2018**, *12*, 5969-5977.

- [234] M. Xu, K. H. Ku, Y. J. Lee, T. Kim, J. J. Shin, E. J. Kim, S.-H. Choi, H. Yun, B. J. Kim, *Macromolecules* **2021**, *54*, 3084-3092.
- [235] A. M. Kalsin, M. Fialkowski, M. Paszewski, S. K. Smoukov, K. J. Bishop, B. A. Grzybowski, *Science* **2006**, *312*, 420-424.
- [236] M. Grzelczak, J. Vermant, E. M. Furst, L. M. Liz-Marzán, *ACS Nano* **2010**, *4*, 3591-3605.
- [237] F. Schulz, I. Lokteva, W. J. Parak, F. Lehmkuhler, *Part. Part. Syst. Charact.* **2021**, *38*.
- [238] A. Michelson, B. Minevich, H. Emamy, X. Huang, Y. S. Chu, H. Yan, O. Gang, *Science* **2022**, *376*, 203-207.
- [239] J. M. Wessels, H. G. Nothofer, W. E. Ford, F. von Wrochem, F. Scholz, T. Vossmeier, A. Schroedter, H. Weller, A. Yasuda, *J. Am. Chem. Soc.* **2004**, *126*, 3349-3356.
- [240] F. Toderas, M. Baia, L. Baia, S. Astilean, *Nanotechnology* **2007**, *18*.
- [241] A. Dong, J. Chen, P. M. Vora, J. M. Kikkawa, C. B. Murray, *Nature* **2010**, *466*, 474-477.
- [242] F. Schulz, S. Tober, H. Lange, *Langmuir* **2017**, *33*, 14437-14444.
- [243] X. Ye, *et al.*, *Nat. Commun.* **2015**, *6*, 10052.
- [244] C. Hamon, S. M. Novikov, L. Scarabelli, D. M. Solis, T. Altantzis, S. Bals, J. M. Taboada, F. Obelleiro, L. M. Liz-Marzan, *ACS Photonics* **2015**, *2*, 1482-1488.
- [245] B. G. M. Vieira, N. S. Mueller, E. B. Barros, S. Reich, *J. Phys. Chem. C* **2019**, *123*, 17951-17960.
- [246] D. M. Solis, J. M. Taboada, F. Obelleiro, L. M. Liz-Marzan, F. J. Garcia de Abajo, *ACS Nano* **2014**, *8*, 7559-7570.
- [247] R. Bonifacio, L. Lugiato, *Phys. Rev. A* **1975**, *11*, 1507.
- [248] G. Raino, M. A. Becker, M. I. Bodnarchuk, R. F. Mahrt, M. V. Kovalenko, T. Stoferle, *Nature* **2018**, *563*, 671-675.
- [249] N. Skribanowitz, I. Herman, J. MacGillivray, M. Feld, *Phys. Rev. Lett.* **1973**, *30*, 309.
- [250] M. S. Malcuit, J. J. Maki, D. J. Simkin, R. W. Boyd, *Phys. Rev. Lett.* **1987**, *59*, 1189.
- [251] K. Miyajima, Y. Kagotani, S. Saito, M. Ashida, T. Itoh, *J. Phys.: Condens. Matter* **2009**, *21*, 195802.
- [252] D. Dai, A. Monkman, *Phys. Rev. B* **2011**, *84*, 115206.
- [253] G. Timothy Noe II, J.-H. Kim, J. Lee, Y. Wang, A. K. Wójcik, S. A. McGill, D. H. Reitze, A. A. Belyanin, J. Kono, *Nat. Phys.* **2012**, *8*, 219-224.
- [254] M. Biliroglu, *et al.*, *Nat. Photonics* **2022**, *16*, 324-329.
- [255] G. Findik, *et al.*, *Nat. Photonics* **2021**, *15*, 676-680.
- [256] Z. Cao, F. Hu, C. Zhang, S. Zhu, M. Xiao, X. Wang, *Adv. Photonics* **2020**, *2*.
- [257] M. A. Boles, M. Engel, D. V. Talapin, *Chem. Rev.* **2016**, *116*, 11220-11289.
- [258] C. B. Murray, C. R. Kagan, M. G. Bawendi, *Annu. Rev. Mater. Sci.* **2000**, *30*, 545-610.

- [259] S. Chakraborti, A. Korpi, M. Kumar, P. Stepien, M. A. Kostianen, J. G. Heddle, *Nano Lett.* **2019**, *19*, 3918-3924.
- [260] M. A. Kostianen, P. Hiekkataipale, A. Laiho, V. Lemieux, J. Seitsonen, J. Ruokolainen, P. Ceci, *Nat. Nanotechnol.* **2013**, *8*, 52-56.
- [261] V. Liljestrom, J. Mikkila, M. A. Kostianen, *Nat. Commun.* **2014**, *5*, 4445.
- [262] J. Zhu, *et al.*, *Chem. Rev.* **2021**, *121*, 13701-13796.
- [263] P. A. Sontz, J. B. Bailey, S. Ahn, F. A. Tezcan, *J. Am. Chem. Soc.* **2015**, *137*, 11598-11601.
- [264] A. Liu, M. V. de Ruiter, W. Zhu, S. J. Maassen, L. Yang, J. J. L. M. Cornelissen, *Adv. Funct. Mater.* **2018**, *28*.
- [265] B. J. M. Verduin, *J. Gen. Virol.* **1978**, *39*, 131-147.
- [266] C. A. Hommersom, B. Matt, A. van der Ham, J. J. Cornelissen, N. Katsonis, *Org. Biomol. Chem.* **2014**, *12*, 4065-4069.
- [267] J. S. Collins, T. H. Goldsmith, *J. Histochem. Cytochem.* **1981**, *29*, 411-414.
- [268] A. Leaver-Fay, *et al.*, *Meth. Enzymol.* **2011**, *487*, 545-574.
- [269] A. E. Miklos, *et al.*, *Biol. Chem.* **2012**, *19*, 449-455.
- [270] J. A. Batsis, *et al.*, *World acad. eng. technol.* **2019**, *13*, 340-348.
- [271] R. Fraczkiewicz, W. Braun, *J. Comput. Chem.* **1998**, *19*, 319-333.
- [272] H. Choi, S. Eom, H. U. Kim, Y. Bae, H. S. Jung, S. Kang, *Biomacromolecules* **2021**, *22*, 3028-3039.
- [273] T. K. Sau, A. Pal, T. Pal, *J. Phys. Chem. B* **2001**, *105*, 9266-9272.
- [274] E. Cohen-Hoshen, G. W. Bryant, I. Pinkas, J. Sperling, I. Bar-Joseph, *Nano Lett.* **2012**, *12*, 4260-4264.
- [275] D. Sun, O. Gang, *J. Am. Chem. Soc.* **2011**, *133*, 5252-5254.
- [276] T. Tigges, T. Heuser, R. Tiwari, A. Walther, *Nano Lett.* **2016**, *16*, 7870-7874.
- [277] Y. Hu, *et al.*, *Adv. Sci.* **2020**, *7*, 2000557.
- [278] M. Gross, S. Haroche, *Phys. Rep.* **1982**, *93*, 301-396.
- [279] W. Wang, B. A. Malcolm, *BioTechniques* **1999**, *26*, 680-682.
- [280] S. Silaban, S. Gaffar, M. Simorangkir, I. Maksum, T. Subroto, in *IOP Conference Series: Earth and Environmental Science, Vol. 217*, IOP Publishing, **2018**, p. 012039.
- [281] M. Gueroult, D. Picot, J. Abi-Ghanem, B. Hartmann, M. Baaden, *PLoS Comput. Biol.* **2010**, *6*, e1001000.
- [282] U. Blaszczyk, A. Duda-Chodak, *Rocz. Panstw. Zakl. Hig.* **2013**, *64*.
- [283] D. M. Francis, R. Page, *Curr. Protoc. Protein Sci.* **2010**, *Chapter 5*, Unit 5 24 21-29.
- [284] B. Zhao, X. Wang, H. Shang, X. Li, W. Li, J. Li, W. Xia, L. Zhou, C. Zhao, *Chem. Eng. Trans.* **2016**, *289*, 319-329.

- [285] W. Holzer, J. Shirdel, P. Zirak, A. Penzkofer, P. Hegemann, R. Deutzmann, E. Hochmuth, *Chem. Phys.* **2005**, *308*, 69-78.
- [286] M. A. Sheraz, S. H. Kazi, S. Ahmed, Z. Anwar, I. Ahmad, *Beilstein J. Org. Chem.* **2014**, *10*, 1999-2012.
- [287] J. P. Gallivan, D. A. Dougherty, *Proc. Natl. Acad. Sci. U.S.A.* **1999**, *96*, 9459-9464.
- [288] D. A. Dougherty, *J. Nutr.* **2007**, *137*, 1504S-1508S.
- [289] A. Anil Sushma, B. Zhao, I. B. Tsvetkova, C. Pérez-Segura, J. A. Hadden-Perilla, J. P. Reilly, B. Dragnea, *J. Phys. Chem. B* **2021**, *125*, 10494-10505.
- [290] F. Sherman, J. W. Stewart, S. Tsunasawa, *BioEssays* **1985**, *3*, 27-31.
- [291] C. Giglione, A. Boularot, T. Meinel, *Cell. Mol. Life Sci.* **2004**, *61*, 1455-1474.
- [292] G. vonHeijne, *Nature* **1989**, *341*, 456-458.
- [293] D. Milligan, D. Koshland Jr, *J. Biol. Chem.* **1990**, *265*, 4455-4460.
- [294] S. Peng, Y. Lee, C. Wang, H. Yin, S. Dai, S. Sun, *Nano Research* **2008**, *1*, 229-234.
- [295] M. J. Lach, *Construction of Highly Ordered Nanomaterials Composed of Protein Containers and Plasmonic Nanoparticles*, Cuvillier Verlag, **2020**.
- [296] S. K. Ghosh, S. Nath, S. Kundu, K. Esumi, T. Pal, *J. Phys. Chem. B* **2004**, *108*, 13963-13971.
- [297] M. Zahedian, X. Huang, I. B. Tsvetkova, V. M. Rotello, W. L. Schaich, B. Dragnea, *J. Phys. Chem. B* **2016**, *120*, 5896-5906.
- [298] S. F. Wuister, C. de Mello Donegá, A. Meijerink, *J. Am. Chem. Soc.* **2004**, *126*, 10397-10402.
- [299] Y. Liu, D. Kim, O. P. Morris, D. Zhitomirsky, J. C. Grossman, *ACS Nano* **2018**, *12*, 2838-2845.
- [300] D. A. Hines, P. V. Kamat, *J. Phys. Chem. C* **2013**, *117*, 14418-14426.
- [301] N. Meir, I. Pinkas, D. Oron, *RSC Adv.* **2019**, *9*, 12153-12161.
- [302] R. Hong, N. O. Fischer, A. Verma, C. M. Goodman, T. Emrick, V. M. Rotello, *J. Am. Chem. Soc.* **2004**, *126*, 739-743.
- [303] B. C. Mei, K. Susumu, I. L. Medintz, J. B. Delehanty, T. Mountziaris, H. Mattoussi, *Journal of Materials Chemistry* **2008**, *18*, 4949-4958.
- [304] F. Schulz, T. Vossmeier, N. G. Bastús, H. Weller, *Langmuir* **2013**, *29*, 9897-9908.
- [305] M. A. Aboudzadeh, A. Iturraspe, A. Arbe, M. Grzelczak, F. Barroso-Bujans, *ACS Macro Lett.* **2020**, *9*, 1604-1610.
- [306] Y. Cheng, A. C. Samia, J. D. Meyers, I. Panagopoulos, B. Fei, C. Burda, *J. Am. Chem. Soc.* **2008**, *130*, 10643-10647.
- [307] J. Ostermann, C. Schmidtke, C. Wolter, J.-P. Merkl, H. Kloust, H. Weller, *Beilstein J. Nanotechnol.* **2015**, *6*, 232-242.

- [308] C. Tortiglione, A. Quarta, M. A. Malvindi, A. Tino, T. Pellegrino, *PLoS One* **2009**, *4*, e7698.
- [309] A. V. Stoyanov, H. Ahmadzadeh, S. N. Krylov, *J. Chromatogr. B* **2002**, *780*, 283-287.
- [310] G. Ruyters, C. Betzel, in *Biotechnology in Space*, Springer, **2017**, pp. 11-26.
- [311] B. Rupp, *Acta Crystallogr. F* **2015**, *71*, 247-260.
- [312] S. Misyura, *AIChE Journal* **2020**, *66*, e16282.
- [313] K. Zhou, J. Zang, H. Chen, W. Wang, H. Wang, G. Zhao, *ACS Nano* **2018**, *12*, 11323-11332.
- [314] X. Zhao, *et al.*, *Anal. Chem.* **2022**, *94*, 4484-4494.
- [315] A. K. Zvezdin, V. a. c. A. Kotov, *Modern magneto-optics and magneto-optical materials*, CRC Press, **1997**.
- [316] M. Pohl, *et al.*, *New J. Phys.* **2013**, *15*, 075024.
- [317] D. M. Krichevsky, *et al.*, *Phys. Rev. B* **2020**, *102*, 144408.
- [318] V. Belotelov, *et al.*, *Nat. Nanotechnol.* **2011**, *6*, 370-376.
- [319] N. E. Sharpless, M. Flavin, *Biochemistry* **1966**, *5*, 2963-2971.
- [320] F. Teale, G. Weber, *Biochem. J.* **1957**, *65*, 476.
- [321] Y. Xiong, C. Shi, L. Li, Y. Tang, X. Zhang, S. Liao, B. Zhang, C. Sun, C. Ren, *New J. Chem.* **2021**.
- [322] A. D. Stephens, *et al.*, *PNAS* **2021**, *118*, e2020389118.
- [323] K. Tao, P. Makam, R. Aizen, E. Gazit, *Science* **2017**, *358*, eaam9756.
- [324] D. Pinotsi, L. Grisanti, P. Mahou, R. Gebauer, C. F. Kaminski, A. Hassanali, G. S. Kaminski Schierle, *J. Am. Chem. Soc.* **2016**, *138*, 3046-3057.
- [325] J. Zheng, C. Zhou, M. Yu, J. Liu, *Nanoscale* **2012**, *4*, 4073-4083.
- [326] J. Liu, P. N. Duchesne, M. Yu, X. Jiang, X. Ning, R. D. Vinluan III, P. Zhang, J. Zheng, *Angew. Chem.* **2016**, *128*, 9040-9044.
- [327] V. Karunakaran, D. D. Prabhu, S. Das, S. Varughese, *Phys. Chem. Chem. Phys.* **2015**, *17*, 18768-18779.
- [328] B. Shao, M. Baroncini, H. Qian, L. Bussotti, M. Di Donato, A. Credi, I. Aprahamian, *J. Am. Chem. Soc.* **2018**, *140*, 12323-12327.
- [329] C. A. Schneider, W. S. Rasband, K. W. Eliceiri, *Nature methods* **2012**, *9*, 671-675.
- [330] M. R. Willcott, ACS Publications, **2009**.
- [331] W. Kabsch, *Acta Crystallographica Section D* **2010**, *66*, 125-132.
- [332] A. J. McCoy, R. W. Grosse-Kunstleve, P. D. Adams, M. D. Winn, L. C. Storoni, R. J. Read, *J. Appl. Crystallogr.* **2007**, *40*, 658-674.
- [333] G. N. Murshudov, P. Skubak, A. A. Lebedev, N. S. Pannu, R. A. Steiner, R. A. Nicholls, M. D. Winn, F. Long, A. A. Vagin, *Acta Crystallogr. D* **2011**, *67*, 355-367.
- [334] M. D. Winn, *et al.*, *Acta Crystallogr. D* **2011**, *67*, 235-242.

- [335] P. Emsley, B. Lohkamp, W. G. Scott, K. Cowtan, *Acta Crystallogr. D* **2010**, *66*, 486-501.
- [336] E. Jurrus, *et al.*, *Protein Sci.* **2018**, *27*, 112-128.

10 Abbreviations

4-AP	4-Aminophenol
4-NP	4-Nitrophenol
AF488	Alexa Fluor 488
AF488Ftn ^(pos) -Cys	AF488 labeled Ftn ^(pos) -Cys
AgNP	Silver nanoparticles
Arg	Arginine
AS	Ammonium sulfate
Asp	Aspartic acid
AuEnc ^(neg)	Enc ^(neg) loaded with gold nanoparticles
AuEnc ^(pos)	Enc ^(pos) loaded with gold nanoparticles
AuEnc ^(wt)	Enc ^(wt) loaded with gold nanoparticles
AuFtn ^(neg)	Ftn ^(neg) loaded with gold nanoparticles
AuFtn ^(pos)	Ftn ^(pos) loaded with gold nanoparticles
AuNP	Gold nanoparticle
<i>B. linens</i>	<i>Brevibacterium linens</i>
BS3	Bis(sulfosuccinimidyl)suberate
BS(PEG) ₅	PEGylated bis(sulfosuccinimidyl)suberate
CaOAc	Calcium acetate
CdS	Cadmium sulfide
CdSe	Cadmium selenide
CeO ₂	Cerium oxide
CLP	Cargo-loading peptide
Cys	Cysteine
Da	Dalton
DHAP	2,5-Dihydroxyacetophenone
DHB	2,5-Dihydroxybenzoic acid
DHF	Dihydrofolate
DHFR-NST	Dihydrofolate reductase
DLS	Dynamic light scattering
EDTA	Ethylenediaminetetraacetic acid
EDX	Energy dispersive X-ray
eFtn ^(neg)	Empty Ftn ^(neg)
eFtn ^(pos)	Empty Ftn ^(pos)
eEnc ^(neg)	Empty Enc ^(neg)

Abbreviations

Enc	Encapsulin
Enc ^(neg)	Negatively surface charged <i>T. maritima</i> encapsulin
Enc ^(pos)	Positively surface charged <i>T. maritima</i> encapsulin
Enc ^(wt)	<i>T. maritima</i> wild type encapsulin
ESI	Electrospray ionization
FAD	Flavin adenine dinucleotide
FDTD	Finite-difference time-domain
FeO _x	Iron oxide
FLIM	Fluorescence lifetime imaging
FLP	Ferritin-like protein
FMN	Flavin mononucleotide
FRET	Förster resonance energy transfer
Ftn	Ferritin
Ftn ^(neg)	Negatively surface charged ferritin
Ftn ^(neg) -Cys	Ftn ^(neg) with additional cysteine (K53C)
Ftn ^(pos)	Positively surface charged ferritin
Ftn ^(pos) -Cys	Ftn ^(pos) with additional cysteine (K53C)
GFP	Green fluorescent protein
Glu	Glutamic acid
Gly	Glycine
gQD	Giant core/shell quantum dot
gQDEnc ^(neg)	Enc ^(neg) loaded with giant core/shell quantum dots
Gua	Guanidine hydrochloride
HEPES	4-(2-Hydroxyethyl)-1-piperazineethanesulfonic acid
HK97	Hong Kong 97
IEC	Ion-exchange chromatography
IPTG	Isopropyl-β-D-1-thiogalactopyranoside
LB	Lysogeny broth
Li ₂ SO ₄	Lithium sulfate
LSPR	Localize surface plasmon resonance
Lys	Lysine
MALDI-TOF	Matrix-assisted laser desorption ionization time-of-flight
Mg	Magnesium
MOF	Metal–organic framework
MPD	2-Methyl-2,4-pentanediol

Abbreviations

MS	Mass spectrometry
MUA	11-Mercaptoundecanoic acid
MUTAB	(11-Mercaptoundecyl)-N,N,N-trimethylammonium bromide
MW	Molecular weight
NaCl	Sodium chloride
NC	Nanocrystals
OA	Oleic acid
ODE	Ocatecane
PA	Photoacoustic
PCR	Polymerase chain reaction
PDB	Protein data bank
PEG	Polyethylene glycol
QD	Quantum dot
QY	Quantum yield
Rh3B	Rhodamine 3B
Rh3BFtn ^(pos) -Cys	Rh3B labeled Ftn ^(pos) -Cys
Rh6G	Rhodamine 6G
Rh6GFtn ^(pos) -Cys	Rh6G labeled Ftn ^(pos) -Cys
RhFtn ^(neg)	Ftn ^(neg) loaded with rhodamine
RhFtn ^(pos)	Ftn ^(pos) loaded with rhodamine
RT	Room temperature
SC	SpyCatcher
SDS-PAGE	Sodium dodecyl sulfate polyacrylamide gel electrophoresis
SEC	Size-exclusion chromatography
SEM	Scanning electron microscopy
SERS	Surface-enhanced Raman scattering
SOB	Super optimal broth
ST	SpyTag
Sulfo-SMCC	Sulfosuccinimidyl-4-(N-maleimidomethyl)-cyclohexan-1-carboxylat
<i>T. maritima</i>	<i>Thermotoga maritima</i>
TB	Terrific broth
TCA	Trichloroacetic acid
THFA	Tetrahydrofolate
TEM	Transmission electron microscopy
TOPO	Trioctylphosphine oxide

Abbreviations

VLP	Virus-like particles
ZnS	Zinc sulfide
ZnSe	Zinc selenide

11 List of figures

Figure 2.1: LAMER model for nanoparticle growth.....	3
Figure 2.2: Gold nanoparticle synthesis based on the TURKEVICH method.....	5
Figure 2.3: Schematic diagram of localized plasmon resonance in nanoparticles.....	6
Figure 2.4: Schematic JABLONSKI diagram used to illustrate electronic states of a molecule and the transition between them.....	8
Figure 2.5: Overview of certain fluorophores of the xanthene family.....	9
Figure 2.6: Schematic thiol-maleimide reaction pathway.....	10
Figure 2.7: Schematic comparison between insulator, conductor and semiconductor based on the energy gap between conduction and valence band.....	11
Figure 2.8: Illustration of the size dependent optical properties of QDs.....	11
Figure 2.9: Examples of protein containers with different sizes and morphology.....	14
Figure 2.10: Overview of structural features of encapsulin of the first family.....	15
Figure 2.11: Schematic illustration visualizing the peptide-directed encapsulation of gold nanoparticles into <i>T. maritima</i> encapsulin.....	17
Figure 2.12: Electron microscopy images of assembled gold nanoparticles.....	19
Figure 2.13: FDTD simulated field enhancement of 3D gold nanoparticle crystals.....	20
Figure 2.14: Illustration of the superfluorescence mechanism.....	21
Figure 2.15: Assembled lead halide perovskite nanocrystal superlattices and their fluorescence lifetime.....	21
Figure 2.16: A general strategy to assemble binary protein-nanoparticle crystals.....	22
Figure 2.17: General strategy for the assembly of protein-MOFs based on protein container, metal ions and organic linker.....	23
Figure 2.18: Schematic illustration of thin CCMV films loaded with gold nanoparticles and their catalytic activity to reduce 4-nitrophenol.....	24
Figure 2.19: Fluorescence spectra, decay curves and images of binary protein crystals.....	25
Figure 2.20: Confocal lifetime analysis of binary protein crystals with different AuNP loading.....	26
Figure 3.1: Schematic visualization of encapsulin surface supercharging based on the crystal structure model.....	29
Figure 3.2: Analytical data for the CLP-mediated encapsulation of gold nanoparticles.....	29
Figure 3.3: Purification and TEM images of gold nanoparticle-loaded ferritin.....	30
Figure 3.4: General strategy for the assembly of binary metal oxide nanoparticle-loaded protein crystals.....	31
Figure 4.1: Schematic overview of the fabrication of nanomaterials composed of gold nanoparticles and quantum dots.....	32
Figure 5.1: Electrostatic surface potential of oppositely charged Enc variants.....	35

Figure 5.2: Ion-exchange and size-exclusion chromatograms for negatively surface charged encapsulin.....	37
Figure 5.3: Overlay of three subsequent SECs of Enc ^(neg)	38
Figure 5.4: TEM images of Enc ^(neg) and corresponding histogram with size distribution.....	39
Figure 5.5: Ion-exchange and size-exclusion chromatograms for positively surface charged encapsulin.	41
Figure 5.6: TEM images of Enc ^(pos) and corresponding histogram with size distribution.	42
Figure 5.7: Overview of possible surface bound flavins and characteristic absorbance.	44
Figure 5.8: ESI MS spectra to distinguish which flavin is bound to encapsulin.....	46
Figure 5.9: Absorption spectra of Enc ^(pos) -Fla and Enc ^(pos)	48
Figure 5.10: Ion-exchange and size-exclusion chromatograms for positively supercharged ferritin with additional cysteine.	49
Figure 5.11: ESI MS spectrum of Ftn ^(pos) -Cys.	50
Figure 5.12: Investigation of the encapsulin disassembly via negative stained TEM images.	52
Figure 5.13: TEM images and histograms of synthesized AuNPs.....	54
Figure 5.14: Ligands applied on AuNPs for peptide-mediated encapsulation.	55
Figure 5.15: UV-Vis comparison between AuNPs of different sizes with different ligand shell composition.	56
Figure 5.16: ζ -potential measurements of AuNPs.....	58
Figure 5.17: Idealized cartoon representation of a MUTAB and CLP functionalized gold nanoparticle surface.	59
Figure 5.18: Schematic illustration of the encapsulation of AuNPs.	60
Figure 5.19: Negatively stained TEM images of AuNP-loaded Enc ^(pos)	61
Figure 5.20: AuNP encapsulation experiment with Enc ^(pos) visualized via TEM.	62
Figure 5.21: AuNP encapsulation experiment with Enc ^(neg) and Enc ^(pos) visualized via TEM.	62
Figure 5.22: Ion-exchange and size-exclusion chromatograms for negatively surface charged encapsulin loaded with AuNPs.	64
Figure 5.23: Ion-exchange and size-exclusion chromatograms for positively surface charged encapsulin loaded with AuNPs.	65
Figure 5.24: TEM image of gQDs with native ligand shell.....	66
Figure 5.25: Chemical structures of ligands used to functionalize gQDs.....	67
Figure 5.26: Normalized emission spectra of gQDs.....	68
Figure 5.27: TEM image of water soluble gQDs with MUA and CLP functionalization.	70
Figure 5.28: ζ -potential measurements of gQDs with different ligand shell composition.	70
Figure 5.29: Negative stained TEM images of initial gQD encapsulation test.	71

Figure 5.30: Normalized UV-Vis spectra of encapsulation test with gQDs into Enc ^(neg) prior to any protein purification.	72
Figure 5.31: Purification and characterization of gQDEnc ^(neg)	73
Figure 5.32: TEM images of gQDEnc ^(neg) after SEC.....	74
Figure 5.33: TEM images of gQDs functionalized with PEG ligands after ligand exchange. .	76
Figure 5.34: ζ -potential measurements of gQDs with PEG ligands.....	76
Figure 5.35: Purification of Enc ^(neg) gQDs encapsulation tests.	78
Figure 5.36: Overview of fluorophores used to label Ftn ^(pos) -Cys via thiol-maleimide reaction.	80
Figure 5.37: Schematic illustration of Ftn ^(pos) -Cys fluorophore labeling.	81
Figure 5.38: Comparison of two SECs of Rh3BFtn ^(pos) -Cys.	82
Figure 5.39: SECs of fluorophore-labeled-Ftn ^(pos) -Cys.	82
Figure 5.40: MALDI-TOF MS spectrum of AF488Ftn ^(pos) -Cys.....	84
Figure 5.41: Schematic illustration of a protein crystallization phase diagram.....	86
Figure 5.42: Protein crystals with different morphologies based on Enc ^(neg)	88
Figure 5.43: Crystal lattice and protein interfaces in Enc ^(neg) conditions.	90
Figure 5.44: Visualization of crystal lattice and protein interfaces in NaCl conditions.....	90
Figure 5.45: Electrostatic surface potential of one partially built protein container at the twofold interface in the NaCl condition of Enc ^(neg)	91
Figure 5.46: Crystallization screening with different buffers at different temperatures.....	92
Figure 5.47: Visualization of crystal lattice and protein interfaces in CaOAc condition at higher temperatures.	93
Figure 5.48: AuNP-loaded Enc ^(neg) crystals.....	93
Figure 5.49: SEM measurement of AuEnc ^(neg) crystal and EDX mapping.....	94
Figure 5.50: Protein crystals with different morphologies based on Enc ^(pos)	96
Figure 5.51: Visualization of crystal lattice and protein interfaces of Enc ^(pos) in Na citrate condition.....	97
Figure 5.52: Overview of crystallization conditions containing Enc ^(neg) and Enc ^(pos)	98
Figure 5.53: Schematic overview of available unitary crystal systems.	99
Figure 5.54: Schematic illustration for the assembly of hetero binary crystals.	100
Figure 5.55: Optical microscopy images of protein crystals with different nanoparticle cargo.	101
Figure 5.56: SEM image of a hetero binary AuEnc ^(neg) /eFtn ^(pos) crystal.	102
Figure 5.57: TEM images of a cubic AuEnc ^(neg) /eFtn ^(pos) crystal.	103
Figure 5.58: Hetero binary unit cell composed of Enc ^(neg) and Ftn ^(pos)	104
Figure 5.59: Optical microscopy images of protein crystals with fluorophore labeling and AuNP cargo.	105

Figure 5.60: Optical microscopy images of fluorophore and fluorophore-AuNP loaded crystals.	106
Figure 5.61: Optical microscopy images of cross-linked protein crystals.	108
Figure 5.62: Comparison between absorbance of AuEnc ^(neg) and emission and absorbance spectra of fluorophore-labeled Ftn ^(pos) -Cys.....	109
Figure 5.63: Emission spectra of hetero binary Enc ^(neg) /Ftn ^(pos) -Cys crystals with AuNPs and fluorophores.	110
Figure 5.64: Emission spectra of empty/fluorophore and AuNP/fluorophore protein crystals.	111
Figure 5.65: Lifetime curves for fluorophore and fluorophore-AuNP loaded protein crystals determined in confocal microscopy.....	113
Figure 5.66: Lifetimes curves for empty/fluorophore and AuNP/fluorophore protein crystals.	114
Figure 8.1: Supercharging of <i>T. maritima</i> Encapsulin towards positive charge based on a run with chain j.	133
Figure 8.2: Supercharging of <i>T. maritima</i> Encapsulin towards positive charge based on a run with chain i.	134
Figure 8.3: Supercharging of <i>T. maritima</i> Encapsulin towards negative charge based on a run with chain j.	134
Figure 8.4: Supercharging of <i>T. maritima</i> Encapsulin towards negative charge based on a run with chain i.	135
Figure 8.5: Aligned sequences of wild type encapsulin and positively supercharged encapsulin variants.....	140
Figure 8.6: Aligned sequences of wild type encapsulin and two encapsulin variants with a mutation at W90.	141
Figure 8.7: SDS gel of novel encapsulin variants.....	141
Figure 8.8: ESI MS spectra to characterize novel Enc variants.....	142
Figure 8.9: TEM images of novel Enc variants.....	142
Figure 8.10: Ion-exchange and size-exclusion chromatograms for Enc ^(neg) -Ala.....	142
Figure 8.11: Ion-exchange and size-exclusion chromatograms for wild type encapsulin.....	143
Figure 8.12: Ion-exchange and size-exclusion chromatograms for Enc ^(pos) -Ala.....	143
Figure 8.13: Ion-exchange and size-exclusion chromatograms for Enc ^(pos) -Fla.....	143
Figure 8.14: ESI MS spectra to distinguish which flavin is bound to encapsulin.....	144
Figure 8.15: UV-Vis calibration curves and linear fits to estimate flavin concentration.	144
Figure 8.16: Volume-weighted hydrodynamic diameters determined by DLS for AuNPs. ...	145
Figure 8.17: Native gel of Enc ^(wt) at different pH values to investigate disassembly behavior.	145

Figure 8.18: Salt screening for efficient AuNP encapsulation into supercharged Enc variants.	145
Figure 8.19: UV-Vis absorbance spectra of AuEnc ^(neg) after SEC.	146
Figure 8.20: IEC with a higher salt gradient to elute AuNPs from cation exchange column.	146
Figure 8.21: Size-exclusion chromatograms for positively surface charged encapsulin loaded with small AuNPs.	147
Figure 8.22: Volume-weighted hydrodynamic diameters determined by DLS for gQDs with different ligand shells.	147
Figure 8.23: Volume-weighted hydrodynamic diameters determined by DLS for gQDs with different PEG ligands.	148
Figure 8.24: SEC of Enc ^(neg) encapsulation test of gQDs functionalized TPEG-3 ligand.	148
Figure 8.25: UV-Vis spectrum featuring the characteristic absorption features of maleimide fluorophores.	149
Figure 8.26: MALDI-TOF MS spectra of fluorophore-labeled Ftn ^(pos) -Cys.	149
Figure 8.27: UV-Vis and emission spectra of purified fluorophore-labeled Ftn ^(pos) -Cys.	150
Figure 8.28: Visualization of crystal lattice and protein interfaces of Enc ^(pos) in citrate-HEPES condition.	150
Figure 8.29: Visualization of crystal lattice and protein interfaces of Enc ^(pos) in phosphate condition.	151
Figure 8.30: Overview of all introduced mutations in Enc.	151
Figure 8.31: Surface charge of Enc ^(pos) at different pH values.	155
Figure 8.32: Initial simulation of plasmonic interactions between two AuNPs.	155
Figure 8.33: SEM image of AuEnc ^(neg) crystal surface.	155
Figure 8.34: AFM images of a hetero binary crystal.	156
Figure 8.35: Optical microscopy images of protein crystals.	156
Figure 8.36: Overview of cross-linker and their length.	157
Figure 8.37: Normalized emission spectra of Enc ^(neg)	157

12 List of tables

Table 5.1: Overview of protein variants with or without flavin binding-site with their corresponding names.....	37
Table 5.2: Molecular mass determined via ESI MS for negatively supercharged encapsulin variants.....	39
Table 5.3: Hydrodynamic diameters and ζ -potential of negative encapsulin variants.....	40
Table 5.4: Molecular masses determined via ESI MS for positively supercharged encapsulin variants.....	42
Table 5.5: Hydrodynamic diameters and ζ -potential of positive encapsulin variants.	43
Table 5.6: Calculation of the number of riboflavin molecules attached to the encapsulin surface.	47
Table 5.7: Comparison of absorption ratios of encapsulin variants with and without flavin....	48
Table 5.8: Molecular mass determined via ESI MS for positively charged ferritin with additional cysteine.....	50
Table 5.9: Atomic absorption spectroscopy results to determine Au concentrations.	55
Table 5.10: DLS data for AuNPs of different sizes with altered ligand shell composition.	57
Table 5.11: Schematic overview of NaCl concentration screening for the encapsulation 13 nm large AuNPs.....	60
Table 5.12: Summary of DLS measurements on gQDs with different ligand shell composition.	69
Table 5.13: Summary of DLS measurements on gQDs with different PEG ligands.....	75
Table 5.14: Comparison of absorbance ratios to evaluate encapsulation of gQD into Enc ^(neg)	79
Table 5.15: Summary of absorbance and emission maxima for fluorophore-labeled Ftn ^(pos) -Cys.....	83
Table 5.16: Comparison of unlabeled and AF488 labeled Ftn ^(pos) -Cys charged ions in MALDI-TOF.....	85
Table 5.17: Crystallization conditions for Enc ^(neg)	89
Table 5.18: Comparison of lattice parameters of empty and AuNP loaded Enc ^(neg) crystal....	95
Table 5.19: Crystallization conditions for Enc ^(pos)	96
Table 5.20: Promising conditions for binary Enc crystals.....	98
Table 5.21: Comparison of single crystal X-ray data of empty and nanoparticle loaded protein crystals.....	103
Table 5.22: Summary of observed emission maxima of protein crystals composed of fluorophores and AuNPs.	112
Table 7.1: List of used <i>E. coli</i> strains.	119
Table 7.2: Native-PAGE gel composition.....	122

Table 7.3: Two-step PCR cycling protocol.....	127
Table 8.1: Weights used for the protein redesign in <i>Rosetta</i>	133
Table 8.2: Feasible positions for the supercharging of the encapsulin container based on <i>Rosetta</i> calculations.	135
Table 8.3: Sequence of primers used for the mutagenesis of Ftn ^(pos)	136
Table 8.4: Sequence of all primers used for the supercharging of <i>T. maritima</i> wild type encapsulin.	136
Table 8.5: Protein sequences for protein variants of this work.	137
Table 8.6: DNA sequences for protein variants of this work.....	138
Table 8.7: Absorption ratios for RhB3 labeled Ftn ^(pos) -Cys in SEC.	148
Table 8.8: Summarized MS results for fluorophore-labeled Ftn ^(pos) -Cys.....	150
Table 8.9: Data statistics and refinement details for unitary Enc ^(neg) crystals.....	152
Table 8.10: Data statistics and refinement details for unitary Enc ^(neg) crystal in CaOAc condition at higher temperature.	153
Table 8.11: Data statistics and refinement details for unitary Enc ^(pos) crystals.....	154
Table 8.12: Data statistics for nanoparticle loaded protein crystals.....	158
Table 8.13: Data statistics for hetero binary protein crystals.....	158

13 List of chemicals

Chemical	Supplier	H- and P- statements	GHS symbols
Acetic acid	VWR	H: 226-314 P: 210-243-280-301+330+331-304+340-308+310	GHS02; GHS05
Ammonium sulfate	AppliChem	H: 302-315-319-335-411 P: 261-264-270-271-273-280-301+312-302+352-304+340-305+351+338-312-321-330-332+313-337+313-362-391-403+233-405-501	-
Ampicillin sodium salt	AppliChem	H: 317-334 P: 261-272-280-284-321-302+352-304+341-333+313-342+311-362+364-501	GHS08
Acrylamide	AppliChem	H: 301-312+332-315-317-319-340-350-361f-372 P: 280-301+310-305+351+338-321-330-362+364-405-501	
Brilliant Blue G 250	Roth	-	-
Bromphenol blue	Merck	-	-
BS3	Fisher Scientific	H: 315-319-335 P: 280-261-264-304+340-312-302+352-362+364-332+313-305+351-337+313	GHS07
BS(PEG) ₅	Fisher Scientific	-	-
tert-Butylamine borane complex	Sigma Aldrich	H: 301-311-312-315-319-335-411 P: 261-264-270-271-273-280-301+310-302+352-304+340-305+351+338-312-321-322-330-332+313-337+313-361-362-363-391-403+233-405-501	GHS06, GHS09
Calcium acetate	Roth	-	-
Calcium chloride dihydrate	Sigma Aldrich	H: 319 P: 264-280-305+351+338-337+313	GHS07
Dichlormethane	Fisher Scientific	H: 315-319-335-336-351-373 P: 261-281-305+351+338	GHS08
Dithiothreitol	Sigma Aldrich	H: 302-315-319-335 P: 280-302+352-305+351+338-308+311	GHS07
Ethylenediaminetetraacetic acid	Roth	H: 309 P: 305+351+338	GHS07

List of chemicals

Ethanol	VWR	H: 225-319 P: 210-240-305+351+338-403+233	GHS02
Glutaraldehyde (25%)	Merck	H: 301-330-314-317-334-335-410 P: 260-280-304+340-310-305+351+338-403+233	GHS06, GHS08, GHS09, GHS05
Glycerol	VWR	-	-
Gold(III) chloride trihydrate	Sigma Aldrich	H: 314-317 P: 280-305+351+338-310	GHS01, GHS07
Guanidinium hydrochloride	Sigma Aldrich	H: 302+332-315-319 P: 261-280-301+312-330-304+340+312-305+351+338-337+313	GHS07
HEPES	Roth	H 315-319-335 P: 261-264-270-271-280-301+312-302+352-304+312-304+340-305+351+338-312-321-322-330-332+313-337+313-362-363-403+233-405-501	-
Hydrochloric acid (37%)	VWR	H: 290-314-335 P: 260-280-303+361+353-304+340+310-305+351+338	GHS05
Imidazole	Sigma Aldrich	H: 302-314-360d P: 260-280-301+312-303+361+353-304+340+310-305+351+338	GHS08, GHS07, GHS05
IPTG	Roth	H: 319-335-315 P: 280-302+352-304+340-305+351+338-312	GHS08, GHS07
LB-Medium	Roth	-	-
Lithium sulfate monohydrate	Sigma Aldrich	H: 302 P: 264-270-301+312+330	GHS07
(11-Mercaptoundecyl)- <i>N,N,N</i> -trimethylammoniumbromid	Sigma Aldrich	-	-
Magnesium chloride	Roth	-	-
Magnesium formate	Sigma Aldrich	-	-
MES monohydrate	AppliChem	H: 315-319-335 P: 261-305+351+338	GHS07
Methanol	VWR	H: 225-331-311-301-370 P: 210-233-280-302+352-304+340-308+310-403+235	GHS06, GHS02, GHS08
2-Methyl-2,4-pentanediol	Sigma Aldrich	H: 315-319-361d	GHS07

List of chemicals

		P: 202-264-280-302+352- 305+351+338-308+313	
N,N,N',N'- Tetramethylethylenediamine	AppliChem	H: 225-302+332-314 P: 280-303+361+353- 305+351+338-310-321-405-501	-
Oleic acid	Sigma Aldrich	H: 315-319-335 P: 261-264-271-280-302+352- 304+340-305+351+338-312-321- 332+313-337+313-362-403+233- 405-501	-
Oleylamine (70%)	Sigma Aldrich	H: 302-304-314-335-373-410 P: 260-280-303+361+353- 304+340+310-305+351+338	GHS08, GHS05, GHS09, GHS07
di-Potassium hydrogen phosphate trihydrate	Roth	-	-
Potassium dihydrogen phosphate	Roth	-	-
2-Propanol	VWR	H: 225-319-336 P: 210-280-305+351+338	GHS02, GHS07
SOB medium	Roth	-	-
Sodium chloride	Roth	-	-
Sodium dodecyl sulfate	Roth	H: 228-302+332-315-318-335-412 P: 210-261-280-301+312+330- 305+351+338+310-370+378	GHS02, GHS09, GHS07
Sodium hydroxide	Grussing	H: 290-314 P: 280-301+330+331- 305+351+338- 308+310	GHS05
Sulfo-SMCC	Fisher Scientific	H: 315-319-335 P: 280-271-261-264	GHS07
TB medium	Roth	-	-
Tetralin	Alfa Aeser	H: 304-315-319-351-411 P: 273-301+310-305+351+338- 331	GHS07, GHS09
Toluene	Fisher Scientific	H: 225-304-315-336-361d-373 P: 210-240-301+310+330- 302+352-314-403+233	GHS08, GHS02, GHS07
Trichloromethane	VWR	H: 331-302-315-319-351-361d- 372 P: 201-280-302+352-308+311	GHS08, GHS07
Trisodium citrate dihydrate	Sigma Aldrich	-	-
TRIS	Roth	-	-

List of chemicals

Uranyl acetate	Science Services	H: 300+330-373-411 P: 260-264-270-271-273-284- 301+310-304+340-310-314-320- 321-330-391-403+233-405-501	GHS06, GHS08, GHS09
----------------	------------------	------------------------------------------------------------------------------------------------------------------	------------------------

Danksagung

Ich bedanke mich bei meinem Doktorvater Prof. Tobias Beck für die Betreuung dieser Arbeit. Vom Anfang bis zum Ende habe ich es genossen an diesem spannenden Projekt gearbeitet zu haben. Insbesondere gilt mein Dank für umfangreiche Hilfe und zahlreiche Diskussionen, sowie wissenschaftlichen Freiheiten. Jedes Gespräch und jedes Feedback haben mich wissenschaftlich oder persönlich ein Stück weitergebracht. Während meiner Promotion war es mir immer möglich mich weiterzuentwickeln. Weiterhin bin ich auch für den Umzug aus Aachen nach Hamburg und den damit verbundenen Aufbau des Labors dankbar. So hatte ich die Möglichkeit an einem wissenschaftlich attraktiven Standort zu arbeiten, mich weiterzubilden und Verantwortung innerhalb der Arbeitsgruppe zu übernehmen.

Prof. Alf Mews gilt mein Dank für die freundliche Übernahme des Gutachtens der Dissertation. Ich danke Prof. Dr. Arwen Pearson und Dr. Tobias Vossmeier als Mitglieder der Prüfungskommission.

Des Weiteren danke ich Prof. Ulrich Schwanenberg für den Zugang zu seinen Laboren und Geräten während der Zeit in Aachen.

Mein Dank geht an Dr. Christian Strelow vom Institut für Physikalische Chemie in Hamburg für die Messungen am Konfokalmikroskop und der Optimierung des experimentellen Aufbaus. Weiterhin gilt mein Dank für folgende Mitarbeiter und Serviceabteilungen des Instituts für Physikalische Chemie in Hamburg für die Durchführungen von Messungen: Stefan Werner (TEM), Robert Schön (SEM), den Teams der Massenspektrometrie (ESI, MALDI) und Zentralen Element-Analytik (AAS).

Bei Gleb Bourenkov (Messtation P14, EMBL, Hamburg) möchte ich mich für die Unterstützung von Diffraktionsexperimenten an nanopartikel-beladenen Proteinkristallen bedanken.

Außerdem gilt mein Dank Dr. Thomas F. Keller (DESY) und seinem Team für Aufnahmen am HR-SEM und AFM.

Es gilt mein Dank bei den Arbeitsgruppen Mews, Weller und Abetz für zahlreiche und freundliche Hilfe bei möglichen Problemen und Fragen.

Außerdem möchte ich meiner Bachelorstudentin Lea Schmidtke und meinen Forschungsstudenten/Forschungsstudentinnen Sarah-Alexandra Hussak, Henrike Wagler, Niklas Mucke und Maximilian Ruffer, die mit ihren Arbeiten direkt oder indirekt zum Gelingen dieser Dissertation beigetragen haben, danken.

Meinen Arbeitskollegen/Arbeitskolleginnen Dr. Matthias Künzle, Dr. Marcel Lach, Dr. Made Budiarta, Dr. Brandon Seychell, Dr. Rafiga Masmaliyeva, Laurin Lang, und Varnika Yadav möchte ich für die freundschaftliche Arbeitsatmosphäre und für zahlreiche wissenschaftlichen

Diskussionen danken. Vor allem gilt mein Dank Hendrik Böhler, mit dem ich zahlreiche Stunden in der Bahn verbringen durfte. Nicht nur die Gespräche während der Pendelei, sondern auch all die wissenschaftlichen Diskussionen mit dir waren mir immer eine Freude. Des Weiteren habe ich in dir einen guten Freund gefunden, der mich während meiner Promotion begleitet hat.

Meinen Freunden aus der Heimat gilt mein Dank für die großartige, gemeinsame Zeit außerhalb der Promotion. Vor allem möchte ich mich bei Helena und Ike bedanken, auf deren Unterstützung und Hilfe ich jederzeit zählen kann.

Zum Schluss geht mein besonderer Dank meinen Großeltern Günter und Wilma und meiner Mutter Gabi, die mir schon als Kind ein Vorbild in Fleiß und Engagement war. Ich danke meinem Stiefvater Thomas, der mich wie seinen eigenen Sohn großzog und mir ein großartiger Vater war und ist. Ohne euch, wäre ich heute nicht hier. Außerdem gilt mein Dank meiner Partnerin, die immer für mich da ist. Trotz zwei Jahre Pandemie haben wir zusammen viel erlebt. Auf deine Unterstützung konnte und kann ich immer bauen. Mit dir zusammen, möchte ich jeden Star Wars und Marvel-Film sehen. Ohne dich, wäre alles nur halb so schön.

Ich werde euch allen immer dankbar sein, für das was ihr seid und für mich getan habt. Vielen lieben Dank.

Eidesstattliche Erklärung

Hiermit versichere ich an Eides statt, die vorliegende Dissertation selbst verfasst und keine anderen als die angegebenen Hilfsmittel benutzt zu haben. Die eingereichte schriftliche Fassung entspricht der auf dem elektronischen Speichermedium. Ich versichere, dass diese Dissertation nicht in einem früheren Promotionsverfahren eingereicht wurde.

23.12.2022



Michael Rütten

Curriculum Vitae

Personal

Name: Michael Rütten
Date of Birth: January 30, 1994
Place of Birth: Viersen, Germany
Nationality: German

Education

01/2020 – today	Doctoral studies Institute of Physical Chemistry University of Hamburg, Hamburg
10/2018 – 12/2019	Doctoral studies Institute of Inorganic Chemistry RWTH Aachen, Aachen
04/2018 – 09/2018	Master thesis Max-Planck-Institut für Kohlenforschung, Mülheim an der Ruhr
10/2016 – 09/2018	Master of Science in Chemistry Heinrich-Heine-Universität, Düsseldorf
10/2013 – 09/2016	Bachelor of Science in Chemistry Heinrich-Heine-Universität, Düsseldorf
08/2010 – 07/2013	Allgemeine Hochschulreife Anne-Frank Gesamtschule, Viersen

Do or do not. There is no try.

- Yoda -